UNIVERSITY OF OKLAHOMA

GRADUATE COLLEGE

ELECTROMAGNETIC MODELING METHODS FOR MICROSTRIP PATCH ANTENNAS UP TO THE MILLIMETER-WAVE AND SUB-TERAHERTZ BANDS

A DISSERTATION

SUBMITTED TO THE GRADUATE FACULTY

in partial fulfillment of the requirements for the

Degree of

DOCTOR OF PHILOSOPHY

By

NIM ROD CCOILLO RAMOS

Norman, Oklahoma

2022

ELECTROMAGNETIC MODELING METHODS
FOR MICROSTRIP PATCH ANTENNAS
UP TO THE MILLIMETER-WAVE AND SUB-TERAHERTZ BANDS

A DISSERTATION APPROVED FOR THE
SCHOOL OF ELECTRICAL AND COMPUTER ENGINEERING

BY THE COMMITTEE CONSISTING OF

Dr. Jorge L. Salazar-Cerreño, Chair

Dr. Pierre E. Kirstetter

Dr. Nafati A. Aboserwal

Dr. Hjalti H. Sigmarsson

Dr. Mark B. Yeary

Dr. Yan Zhang

To God,

For what I have each day.

To my mother: Luisa Elizabeth,

For what I am each day.

Acknowledgments

Completing this dissertation was only possible with the valuable support from different people and institutions. I am thankful to everyone who supported me and provided me with the tools and facilities to realize and culminate this work during my academic endeavor.

I start by thanking the sponsors of the research conducted during these 48 months of my academic journey: the U.S. Office of Navy Research, the U.S. Department of Commerce – National Oceanic and Atmospheric Administration, and the Department of Electrical and Computer Engineering of the University of Oklahoma.

I express my gratitude to Dr. Jorge Salazar, my Ph.D. advisor, and Doctoral Committee Chair, for the opportunity to join his dynamic and passionate research team, his permanent academic support, wise advice and orientation, and active supervision during my educational journey.

I thank the Doctoral Committee members, Dr. Hjalti Sigmarsson, Dr. Mark Yeary, Dr. Nafati Aboserwal, Dr. Pierre Kirstetter, and Dr. Rockee Zhang, for their membership acceptance, their time to administer the doctoral examinations, and their constructive feedback in reviewing this dissertation.

I acknowledge the Advanced Radar Research Center for the facilities and resources that allowed me to develop my research and for the fruitful interactions with valuable professionals who have worked there. It is my pleasure to high-

light Dr. Bob Palmer, Dr. David Schvartzman, Felipe Moncada, Gökhan Arıtürk, Hyeri Kim, Mariel Ávalos, Nawaf Almuqati, Reece Reinke, Dr. Robin Irazoqui, Dr. Rodrigo Lebrón, Russell Kenney, Sergio Rodríguez, Tom Brachtenbach, Tony Segalés, and Yoon Kim, for the productive discussions and for making my stay more enjoyable.

I appreciate the Phased Array Antenna Research and Development Group for the fruitful discussions, vast collaborative spirit, and peer support. Special thanks to Dr. Nafati Aboserwal, Dr. Zeeshan Qamar, and Syed Jehangir for the close collaborations and our numerous insightful discussions that enlightened my research pathway.

I am fortunate and deeply grateful to my friends, with a profound appreciation for their frank trust, loyalty, open minds, great chats and laughs, for accompanying me in celebrating each accomplishment and for supporting me in the adversity, and for allowing me to learn from them as well as allowing me to share my thoughts freely. In alphabetical order, I am honored to highlight César Salazar, Christian Beltrán, David Ortega, Deisy Mamedes, James Espichán, Jorge Alva, Joshua Ayala, Juliete Souza, Lizeth Castro, Mayde Aguilar, Rosalind Agasti, and Tanith Guerra.

To conclude, I want to express my deepest gratitude and heartfelt acknowledgment to my family, especially my mother, for their unlimited love, tireless efforts, unconditional support, and endless encouragement. I will eternally owe my parents the value of discipline they taught me, which has ultimately allowed me –and I am deeply honored– to be a first-generation Doctor of Philosophy in my family. I will do my best in my future life venture with the Grace of God.

Abstract

In the current world of highly integrated communications, reliable and robust systems will be required to develop the 6G networks. The millimeter-wave band (30 GHz–100 GHz) and the sub-terahertz band (100 GHz–300 GHz) have promising possibilities in radar and communication systems, such as broad bandwidth, device miniaturization, and high integration with electronic technology. As 6G communications will be the dominant technology in the coming years, highly-accurate antenna design is becoming essential to building systems that meet the expected performance standards. Despite the wide availability of antenna models working at frequencies below 10 GHz, they need to be in-depth reviewed and reformulated, especially in the sub-terahertz band. Thus, the work developed in this doctoral dissertation provides a framework of analytical methods for electromagnetic antenna modeling, enabling the design of microstrip patch antennae up to 300 GHz. This work covers unprecedentedly diverse models in frequency ranges from radiofrequency to the sub-terahertz band. The proposed model formulations consider the geometrical and electrical imperfections of materials used for antenna design. They show high accuracy in the modeled frequency response for measured antennas and transmission lines up to 110 GHz; and for simulated microstrip patch antennas up to 300 GHz, with thickness up to 5 % of the free-space wavelength, copper layers up to 35 μm thick, and with surface roughness up to 1 μm.

Contents

List of Tables **xv**

List of Figures **xvii**

List of Acronyms, Symbols, and Variables **xxi**

1 Introduction **1**

1.1 Preface 1

1.2 Motivation 2

1.3 Literature Review 5

1.4 Problem Formulation 10

1.4.1 Problem Statement 12

1.4.2 Research Questions 13

1.5 Justification 13

1.6 Hypothesis 13

1.7 Proposed Research 14

1.8 Contribution 18

1.9 Dissertation Overview 19

2 Overview on EM Modeling for Conventional Antennas **21**

2.1 Fundamentals 22

2.1.1 EM Theory equations 22

2.1.2 Relation between Fields and Circuits 23
2.1.3 The Electric and Magnetic Auxiliary Vector Potentials . . 25
2.1.4 The Electromagnetic Theorems 28
2.1.5 Computer-aided Modeling 31
2.2 Wired Antennas 33
2.2.1 Monopole 34
2.2.2 Dipole 38
2.3 Slot Antenna 43
2.3.1 Radiated Fields 45
2.3.2 Input Impedance 47
2.4 Microstrip Patch Antennas (MSPAs) 48
2.4.1 Cavity Model 49
2.4.2 Transmission Line Model 56
2.4.3 Modeling the Radiating Fields 60
2.4.4 Modeling the Input Impedance 65
2.4.4.1 Patch's Impedance: the RLC resonator 67
2.4.4.2 Direct-contact Feeding 71
2.4.4.3 Coupling-based Feeding 72
2.4.5 Modeling the Impedance Bandwidth 74
2.5 Summary 78

3 Advanced EM Modeling for Proximity-Coupled Microstrip Patch Antennas 79

3.1 Antenna Design 81
3.1.1 Geometry 81
3.1.1.1 Overlapping Feed-to-Patch Ratio 82
3.1.1.2 Substrate Thickness Ratio 83

3.1.2 Feeding Length 83
3.1.3 Substrate Thickness 85
3.1.4 Patch Dimensions 86
3.1.5 Design Guidelines 86
3.2 Bandwidth Estimation 87
3.2.1 Bandwidth Mathematical Formulation 88
3.2.2 Bandwidth over Feeding Substrate Thickness 90
3.2.3 Bandwidth over Substrate Thickness Ratio 90
3.2.4 Model assessment 91
3.2.5 Error analysis 94
3.3 Impedance Response 97
3.3.1 Previous Models for PC-MSPAs 98
3.3.2 Problem and Proposed Solution 100
3.4 Equivalent Electric Circuit Model 105
3.4.1 Patch RLC Resonator 106
3.4.2 Feeding Circuit 108
3.4.3 Feeding Equivalent Transmission Line 109
3.4.4 Model Assessment 111
3.4.4.1 Performance in Simulated PC-MSPAs 111
3.4.4.2 Assessment using Fabricated PC-MSPAs 114
3.4.5 PC-MSPA Radiation Patterns 117
3.5 Modeling PC-MSPAs with Differential Feeding 119
3.5.1 Proposed Model 122
3.5.1.1 Patch Resonant Frequency (f_{0p}) 122
3.5.1.2 Patch Quality Factor (Q_p) 123
3.5.1.3 Patch Resonant Resistance (R_p) 124

3.5.1.4 Feeding Circuit (L_T, C_T) . . . 124
3.5.1.5 Impedance Response . . . 127
3.5.2 Model Assessment . . . 128
3.6 Summary . . . 130

4 Challenges and Design Trade-offs for EM Modeling of Microstrip Patch Antennas up to the Sub-THz Band 133

4.1 Material Constitutive Parameters . . . 135
4.1.1 Electric Permittivity (ε) . . . 135
4.1.2 Magnetic Permeability (μ) . . . 136
4.1.3 Electric Conductivity (σ) . . . 138
4.2 Overview of mmWave and Sub-THz Antennas . . . 140
4.2.1 Materials . . . 143
4.2.1.1 Dielectrics . . . 144
4.2.1.2 Conductors . . . 145
4.2.2 Fabrication Techniques . . . 147
4.3 Effects of the Dielectric Electrical Characteristics on mmWave and Sub-THz MSPAs . . . 152
4.3.1 Anisotropy . . . 152
4.3.2 Frequency Dispersion . . . 154
4.3.3 Consequences in EM Modeling of mmWave and Sub-THz MSPAs . . . 155
4.4 Effects of the Conductor Geometrical Characteristics on mmWave and Sub-THz MSPAs . . . 158
4.4.1 Trace Thickness . . . 158
4.4.2 Surface Roughness . . . 163
4.4.2.1 Loss and Phase in Transmission Lines: A Review 165

4.4.2.2 Impact of the Surface Roughness in the Conductor Loss of Transmission Lines . . . 167
4.4.2.3 Impact of the Surface Roughness in the Phase of Transmission Lines . . . 171
4.4.3 Consequences in EM Modeling of mmWave and Sub-THz Antennas . . . 172
4.5 Equivalency Model to Assess the Impact of the Surface Roughness on Microstrip Lines and Striplines . . . 173
4.5.1 Equivalent Conductivity . . . 175
4.5.2 Equivalent Design Dielectric Constant . . . 178
4.5.3 Validation of the Proposed Model . . . 179
4.5.3.1 Validation Methodology . . . 179
4.5.3.2 Simulated Results . . . 180
4.5.3.3 Measurement Strategy . . . 183
4.5.3.4 Experimental Results . . . 187
4.6 Summary . . . 190

5 Enhanced EM Modeling for Microstrip Patch Antennas up to the Sub-THz Band 193

5.1 Modeling Capability up the Sub-THz Band . . . 195
5.1.1 Frequency Analysis . . . 196
5.1.2 Geometry Analysis . . . 201
5.1.2.1 Effect of MSPA Scaling in the Patch's Resonant Frequency . . . 204
5.1.2.2 Effect of MSPA Scaling in the Patch's Quality Factor 208
5.1.3 Modeling Strategy above 30 GHz . . . 216
5.2 Modeling Extension for Probe-fed MSPAs . . . 218

5.2.1 Patch Resonant Frequency 220
5.2.2 Patch Quality Factor 225
5.2.2.1 Conductor Quality Factor Q_c 225
5.2.2.2 Dielectric Quality Factor Q_d 227
5.2.2.3 Radiation and Surface-Wave Quality Factor Q_{rs} . 228
5.2.2.4 Assessment of the Patch's Quality Factor Q_p . . . 229
5.2.3 Patch Resonant Resistance 231
5.2.4 Probe Feeding 233
5.3 Modeling Extension for Proximity-coupled MSPAs 234
5.3.1 Patch Resonant Frequency 237
5.3.2 Patch Quality Factor 239
5.3.3 Patch Resonant Resistance 242
5.3.4 Proximity-coupled Feeding 243
5.4 Analysis of Model Accuracy up to 300 GHz 245
5.4.1 PF-MSPA Modeling Assessment 245
5.4.2 PC-MSPA Modeling Assessment 249
5.4.3 Rough-Conductor MSPAs Modeling Assessment 253
5.5 Summary 256

6 Conclusions **259**
6.1 Research Summary 260
6.2 Contribution Overview 263
6.3 Research Limitations 265
6.4 Research Findings 268
6.5 Future Research 269

References **271**

Appendix A EM Modeling Source Codes in MATLAB™ **287**

A.1 Design of a PC-MSPA in RF and Microwaves 287

A.2 Impedance Bandwidth of a PC-MSPA up to 30 GHz 291

A.3 Impedance Response of a PC-MSPA up to 30 GHz 293

A.4 Equivalency Model for Conductor Foil Surface Roughness 297

A.5 Impedance Response of a PF-MSPA up to 300 GHz 303

A.6 Impedance Response of a PC-MSPA up to 300 GHz 308

Appendix B List of Publications **314**

B.1 Journal Papers 314

B.2 Conference Papers 315

List of Tables

1.1 List of specific frequency intervals for 6G communications and radar systems in the sub-THz band (100 GHz–300 GHz). 2

1.2 Overview of the proposed research task groups and their scope. . 17

2.1 Fundamental equations for the EM theory. 23

2.2 E-field and input impedance for $\lambda/2$ and $5\lambda/4$ dipole antennas. . 41

3.1 Fabricated PC-MSPAs' specifications. 92

3.2 Errors between modeled, simulated and measured bandwidths. . . 92

3.3 A comparison between available models for PC-MSPA bandwidth. 97

3.4 Antennas' design specifications. 113

3.5 Performance of proposed model on simulated PC-MSPAs. 113

3.6 Fabricated S-band and C-band PC-MSPAs' specifications. 116

3.7 Performance of proposed model on fabricated PC-MSPAs. 117

3.8 Assessed antennas' specifications. 128

4.1 Dielectric materials used in mmWave and sub-THz antennas. . . . 145

4.2 Comparison of properties of different conductors for antennas. . . 147

4.3 Feeding width and impedance in PC-MSPAs up to 300 GHz. . . . 161

4.4 Impact of the conductor trace thickness in the patch's resonant frequency for PF-MSPAs and its geometrical modeling. 162

4.5 A comparison of insertion losses (in dB/mm) and unwrapped phase (in degrees/mm) in microstrip transmission lines between rough conductors and modeled smooth equivalent conductors. 182

4.6 A comparison of insertion losses (in dB/mm) and unwrapped phase (in degrees/mm) in strip transmission lines between rough conductors and modeled smooth equivalent conductors. 182

5.1 Accuracy of patch's resonant frequency in scaled MSPAs. 205
5.2 Accuracy of patch's quality factor in scaled MSPAs. 209
5.3 Accuracy of patch's dielectric quality factor in scaled MSPAs. . . 214
5.4 Accuracy of patch's conductor quality factor in scaled MSPAs. . . 215
5.5 Accuracy of patch's radiation quality factor in scaled MSPAs. . . 216
5.6 Assessment of accuracy estimation of the patch's resonant resistance for PF-MSPAs at different conductor thickness as a proportional relation with patch's parameters and dimensions. 232
5.7 Assessment of accuracy estimation of the patch's resonant resistance for PF-MSPAs at different operating frequencies as a proportional relation with patch's parameters and dimensions. 233
5.8 Assessment of accuracy estimation of the patch's resonant resistance for PC-MSPAs at different conductor thicknesses as a proportional relation with patch's parameters and dimensions. 244
5.9 Assessment of accuracy estimation of the patch's resonant resistance for PC-MSPAs at different operating frequencies as a proportional relation with patch's parameters and dimensions. 244
5.10 Sub-THz PF-MPSAs' design specifications. 246
5.11 Resonance modeling performance on sub-THz PF-MSPAs. 247
5.12 Sub-THz PC-MPSAs' design specifications. 250
5.13 Resonance modeling performance on sub-THz PC-MSPAs. 251
5.14 Resonance modeling performance on sub-THz PF-MSPAs under the presence of surface roughness in the patch and ground plane. . 254

List of Figures

1.1 Technical expectations for 6G [9]. 3

1.2 Schematic diagram for research problem formulation. 12

2.1 Electromagnetic theorems applied to antenna modeling. 29

2.2 Schematic of a cylindrical monopole. 34

2.3 Radiation patterns of a $\lambda/4$ monopole on an infinite ground plane. 38

2.4 Impedance response of a $\lambda/2$ and $5\lambda/4$ wired dipole antenna. . . . 41

2.5 Radiation patterns of a $\lambda/2$ and $5\lambda/4$ dipole antenna. 42

2.6 Radiation patterns for a $\lambda/2$ and $5\lambda/4$ slot antenna. 46

2.7 Impedance response of a $\lambda/2$ and $5\lambda/4$ slot antenna. 47

2.8 Cavity model for microstrip patch antennas. 49

2.9 Transmission line model for microstrip patch antennas. 57

2.10 Equivalent slots for a microstrip patch antenna. 61

2.11 Normalized radiation patterns for MSPA with probe feeding. . . . 65

2.12 MSPAs' feeding structures and their typical equivalent circuits. . . 66

2.13 MSPAs' input impedance with two different feeding structures. . . 68

2.14 Comparison of bandwidth models for MSPAs. 77

3.1 Geometry of a PC-MSPA. 82

3.2 Design guidelines for PC-MSPAs. 84

3.3 Impedance bandwidth model for PC-MSPAs. 89

3.4 Assessment of impedance-bandwidth behavior of PC-MSPAs. . . . 93
3.5 Bandwidth comparison with fabricated PC-MSPAs. 94
3.6 RMS model errors over feed substrate thickness h_1/λ_r. 95
3.7 Impedance reference position for PC-MSPAs. 98
3.8 Impedance trends in a PC-MSPA with different feed lengths. . . . 102
3.9 Equivalent circuit models of a PC-MSPA. 105
3.10 PC-MSPA circuit parameters over the feed's overlap ratio r_x. . . . 110
3.11 Model performance on simulated PC-MSPAs' frequency response. 112
3.12 Geometry, dimensions, and setup for fabricated PC-MSPAs. . . . 115
3.13 Model performance on fabricated PC-MSPAs' frequency response. 118
3.14 Normalized radiation patterns for fabricated PC-MSPAs. 119
3.15 Geometry and equivalent circuit for differentially fed PC-MSPAs. 120
3.16 Impact of the feeding structure for PC-MSPAs. 121
3.17 Patch resonator-parameter shifting factors for DF-PC-MSPAs from SF-PC-MSPAs at different substrate thicknesses and ratios at 3 GHz. 125
3.18 Patch resonator-parameter shifting factors for DF-PC-MSPAs from SF-PC-MSPAs at different dielectrics and patch squarenesses at 3 GHz. 126
3.19 Comparison between modeled and simulated impedance responses for PC-MSPAs in the S- and X-bands. 129

4.1 Radiating elements used in mmWave and sub-THz applications. . 140
4.2 Copper main foiling techniques and typical height distribution. . . 146
4.3 Dielectric polarization mechanisms and frequency dispersion [137]. 155
4.4 Variation of the dielectric properties along frequency for water. . . 156
4.5 Cross section of a multilayered microstrip line. Based on [107]. . . 158
4.6 Effect of the conductor thickness in microstrip lines. 160

4.7 Effects of the conductor surface roughness in microstrip lines [65]. 164
4.8 Geometrical roughness models for conductor foils. 170
4.9 Equivalent distribution of magnetic fields for 1 μm rough copper. 170
4.10 Impact of the conductor surface roughness in the phase delay. . . 172
4.11 Equivalence model for transmission lines with rough conductors. . 174
4.12 Variations of the equivalent conductivity over frequency. 177
4.13 Variations of the design dielectric constant over frequency. 179
4.14 Simulated results for rough microstrip lines and striplines. 181
4.15 Electrical setup for experimental validation of microstrip lines. . . 185
4.16 Measured results for rough microstrip lines up to 110 GHz. 188

5.1 Performance of the most recent EM modeling method in thick-conductor PC-MSPAs up to the mmWave band. 198
5.2 Performance of the most recent EM modeling method in zero-thickness-conductor PC-MSPAs up to the sub-THz band. 199
5.3 Effect of the conductor thickness in the modeling accuracy of the patch's resonant frequency in MSPAs up to the sub-THz band. . . 200
5.4 Patch's resonant frequency in scaled and thick MSPAs. 206
5.5 Patch's quality factor in scaled and thick MSPAs. 210
5.6 Geometrical formulation for modeling PF-MSPAs with thick conductors up to the sub-THz band. 221
5.7 Estimation accuracy of patch's resonant frequency in PF-MSPAs up to the sub-THz and with thick conductors. 224
5.8 Patch's conductor quality factor in thick MSPAs. 226
5.9 Estimation accuracy of patch's quality factor in PF-MSPAs up to the sub-THz and with thick conductors. 230

5.10 Geometrical formulation for modeling PC-MSPAs with thick conductors up to the sub-THz band. 236
5.11 Estimation accuracy of patch's resonant frequency in PC-MSPAs up to the sub-THz and with thick conductors. 238
5.12 Estimation accuracy of patch's quality factor in PC-MSPAs up to the sub-THz and with thick conductors. 241
5.13 Extended-model performance on PF-MSPAs up to 300 GHz. . . . 248
5.14 Extended-model performance on PC-MSPAs up to 300 GHz. . . . 252
5.15 Extended-model performance on sub-THz PF-MSPAs under the presence of surface roughness in the patch and ground plane. . . . 255

List of Acronyms, Symbols, and Variables

This list provides an overview of acronyms, symbols, and variables used across the different chapters of this dissertation.

Acronyms

EM:	electromagnetic.
CST:	computer simulation technology, a software trademarked by Dassault Systèmes SIMULIA Corp.
HFSS:	high-frequency structure simulator, trademarked by Ansys Inc.
PCAAD:	Personal Computer Aided Antenna Design software, trademarked by Antenna Design Associates, Inc.
PEC:	perfect electric conductor.
PMC:	perfect magnetic conductor.
PTFE:	Polytetrafluoroethylene, is an insulator material broadly known as the commercial brand Teflon™, used as substrate in MSPAs.
RLC:	resistance-inductance-capacitance paralell circuit.
MATLAB:	"matrix laboratory", a numeric computational environment, trademarked by The MathWorks Inc.
MSPA:	microstrip patch antenna.
PF-MSPA:	probe-fed microstrip patch antenna.
PC-MSPA:	proximity-coupled microstrip patch antenna.

mmWave: millimeter wave frequency band, defined in this work as the frequency interval from 30 GHz to 100 GHz. In a strict sense, this range goes from 30 GHz to 300 GHz. However, the research field is emphasizing the frequency band above 100 GHz as part of the sub-THz and THz bands for the developing 6G communication systems.

sub-THz: sub-terahertz frequency band, defined in this work as the frequency interval from 100 GHz to 300 GHz. In a strict sense, this range goes from 0.1 GHz to 1 THz. However, the research field is emphasizing the frequency band below 100 GHz as part of mmWave for 6G communication systems.

Symbols

$a|b$: Set a condition a, so that condition b is met.

$|S|$: magnitude or absolute value of the variable S.

$\angle S$: phase of the variable S.

$\mathbb{N}$: Set of natural numbers (0, 1, 2, ...).

∇: nabla operator for gradient, curl, divergence, and Laplacian.

Variables

α: attenuation constant, typically in Np/m.

β: phase constant, typically in rad/m.

δ: skin depth, typically in μm.

ΔL: fringe-field length extension in MSPAs, typically in mm.

ε: electric permittivity, in F/m.

ε_r:	relative electric permittivity, dielectric constant.
η:	characteristic impedance of a medium, in Ω.
θ:	spherical component of elevation, typically in rad.
λ_0:	free-space wavelength at a given frequency, in m.
μ:	magnetic permeability, in H/m.
μ_r:	relative magnetic permeability.
π:	numerical constant, equal to 3.141592...
σ:	electric conductivity, in S/m.
σ_{eq}:	rough-conductor equivalent electric conductivity, in S/m.
ϕ:	spherical component of azimuth, typically in rad.
ω:	angular frequency, typically in rad/s.
$\%BW$:	antenna's percent impedance bandwidth.
c_0:	speed of light at vacuum, approximated at 3×10^8 m/s.
C_p :	RLC-resonator capacitance in MSPA, typically in pF.
C_T:	feeding capacitance in PC-MSPA, typically in pF.
Dk:	design dielectric constant, in substrates with a conductive foil.
$\mathbf{E}$:	intensity of electric field, vector, in V/m.
f:	frequency, typically in GHz.
f_{0p}:	patch's resonant frequency in MSPAs, typically in GHz.
f_0:	antenna operating frequency, typically in GHz.
$\mathbf{H}$:	intensity of magnetic field, vector, in A/m.
h_{Cu}:	thickness of the copper foil, typically in μm.
h_T:	total thickness in MSPAs.
$\mathbf{J}$:	electrical current density, vector, in A/m^2.
k:	propagation constant in lossless media, wave number, in rad/m.
$\boldsymbol{\ell}$:	domain of length, in m.

L: patch length in MSPAs, typically in mm.

L_g: ground plane size in MSPAs, typically $2\lambda_0$.

L_p: RLC-resonator inductance in MSPA, typically in nH.

L_T: feeding inductance in PF-MSPAs and PC-MSPAs, typically in nH.

Q_p: patch's quality factor in MSPAs.

r: spherical component of radius, typically in m.

r_h: substrate thickness ratio in PC-MSPAs.

R_q: Surface roughness RMS value, typically in μm.

R_p: patch's resonant resistance in MSPAs, in Ω.

R_{pM}: patch-edge's resonant resistance in MSPAs, in Ω.

R_q: roughness RMS parameter value from, typically in μm.

r_x: feed-to-patch overlap ratio in PC-MSPAs.

$\mathcal{s}$: domain of surface, in m^2.

S_{11}: one-port antenna's reflection coefficient.

$\mathcal{v}$: domain of volume, in m^3.

$\tan\delta$: dielectric loss tangent.

t_f: feed thickness in PC-MSPAs, typically in μm.

t, t_p: patch thickness in MSPAs, typically in μm.

W: patch width in MSPAs, typically in mm.

X_{TF}: feeding reactance in MSPAs, in Ω.

Z_{11}: one-port antenna's input impedance, in Ω.

Z_0: characteristic impedance in transmission lines, in Ω.

Chapter 1

Introduction

Thoroughly conscious ignorance is the prelude to every real advance in science.

—James Clerk Maxwell

1.1 Preface

Nowadays, we live in a dynamically integrated world with advanced automated devices and high-speed communication systems. The fourth generation network, also known as 4G, is present worldwide [1–3]. The 5G technology is being massively implemented in the U.S., Europe, and Asia [1, 4, 5]. With the increasing necessity for faster, more reliable, and efficient devices, there is a significant motivation to innovate the current technology towards the sixth generation of communication systems, or 6G [6–8]. The mmWave band[1] (30 GHz – 100 GHz) and the sub-terahertz band[1] (100 GHz – 300 GHz) have both gained importance in the academia, industry, and government due to the intrinsic capability to support 6G communications and radar systems. As the carrier frequency increases, there is more deliverable bandwidth for data transfer [1, 7, 9]. This enhanced capabil-

[1]Some previous work defines the mmWave band from 30 GHz to 300 GHz, where the free-space wavelength is from 1 mm to 10 mm. Some others locate the sub-THz band from 100 GHz to 1000 GHz, covering frequencies below 1 THz. This work defines the mmWave and sub-THz bands in non-overlapping frequency ranges, where the mmWave band is defined from 30 GHz to 100 GHz; and the sub-THz band, from 100 GHz to 300 GHz.

ity enables high-precision radars for surveillance and biomedical purposes [7, 9]. Both frequency bands play a crucial role [4, 8] in the future of 6G communications since a small percent bandwidth is enough to provide data transfer speeds in the order of gigabits/second. Nowadays, the framework for the 6G era is intensively researched [1, 5, 8]. As more standards [10, 11], requirements [7, 12] and potential applications [13, 14] are found and released, new specific research fields are emerging [9, 15]. Table 1.1 lists specific frequency ranges in the sub-THz band that are expected for 6G communications and radar systems [10, 16].

Table 1.1: List of specific frequency intervals for 6G communications and radar systems in the sub-THz band (100 GHz–300 GHz).

6G communications		Radar systems	
Frequency (GHz)	Bandwidth (%)	Frequency (GHz)	Bandwidth (%)
116 - 123	5.9	136 - 148.5	8.8
174.8 - 182	4.0	151.5 - 155.5	2.6
185 - 190	2.7	231.5 - 235	1.5
244 - 246	0.8	238 - 248	4.1

1.2 Motivation

6G communication systems and radar applications in the mmWave and sub-THz bands are expected to perform superior to previous generations. 6G networks will have approximately 1000 times more simultaneous connections than in 5G and ultra-wide coverage up to 10 km in the sky and up to 37 km (20 nautical miles) in the sea [7, 12]. A similar improvement in the peak data rate, the maximum channel bandwidth, and area traffic capacity are anticipated [7, 8]. Also, sub-millisecond latency will be likely in 6G communications [7]. Due to the higher operating frequencies, radar applications await a spatial resolution of a few millimeters [9]. Fig. 1.1 [9] illustrates the scope of 6G performance metrics: peak data rate, latency, energy efficiency, radar resolution, error rate, and peak spec-

tral efficiency. Then, this upcoming technology motivates on researching in the mmWave and sub-THz bands.

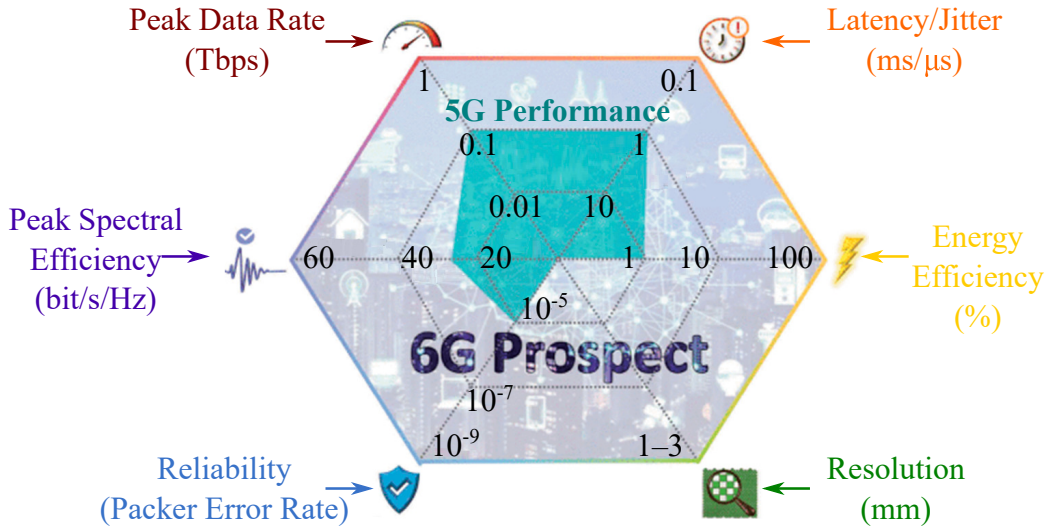

Figure 1.1: Technical expectations for 6G [9].
A significant improvement in the performance metric is expected, as 6G communications becomes the dominant technology.

The frequency band between 30 GHz and 300 GHz reveals diverse potential applications [13, 14], including but not limited to mobile wireless communications, information showers, centimeter-level positioning, HD-video resolution-like radar, advanced security body scan, and multipurpose applications such as joint communication links with radars and automated health systems.

Antennas play a crucial role in connecting electromagnetic (EM) devices through the transmission and reception of EM waves, even in the mmWave and the sub-THz bands. Extending known applications and devices at radio frequency to the sub-THz band is possible. There are examples, for instance, 140-GHz vector network analyzer-based frequency-modulated continuous-wave radar [17], 122-GHz imaging sensors, 145-GHz detectors, and 300-GHz wireless links [15]. Moreover, current software technology, both full-wave based [18, 19] and analytical-modeling based [20–22] provide significant support towards the design of the current antenna

technology. This solid growth of EM technology suggests that new EM devices will appear, and new hardware and software are contemplated to satisfy the higher requirements in the modeling, designing, and implementing these devices.

Thus, researching and contributing to antenna EM modeling in the mmWave and sub-THz bands will bring a new pathway for analysis and design. Modeling antennas at mm-Wave and sub-THz is a promising research opportunity and has challenges to address. As it will be more detailed in the literature review, the traditional antenna models [23, 24] work well up to 10 GHz, but not beyond, creating a room for discovery and innovation. Then, antenna modeling in the mmWave and the sub-THz band opens the opportunity to impact the development of diverse research fields positively, for instance, [1, 14], transceiver design, high-directivity beam alignment, MIMO antennas, 3D beamforming, mutual coupling, and terahertz antenna design.

Modeling the material characterization is a critical component of antenna EM modeling in the mmWave and sub-THz bands. Designing EM devices at such high frequencies brings challenges in the fabrication tolerances and sensitivity of material properties, which may impose constraints on their cost, reliability, and ultimately, viability [1, 25]. Also, the different research lines associated with these bands need to face potential challenges, and limitations [25, 26], such as short ranging due to high path loss, increasing interference with new services, power handling, strict fabrication tolerances, and high sensibility to the environment. Therefore, having an accurate material characterization constitutes the basis of quantifying the effects of EM wave propagation above 30 GHz on the material performance to set suitable strategies to overcome the limitations mentioned above.

1.3 Literature Review

A wide variety of antennas can be used for millimeter and sub-millimeter-wave applications. Antenna elements such as monopoles [27], printed dipoles [28–30], slots [31] and patches [15, 32] have been designed in applications in the sub-THz band. In addition, more sophisticated antennas [30, 31, 33, 34] for millimeter and sub-millimeter waves have been identified, among them integrated lenses, corrugated horns, reflectarrays, transmit arrays, and metasurface-based antennas. As noticed, antenna elements can be composed of metal, dielectric, or both. While microstrip antennas will be analytically studied and modeled in this work, Chapter 3 will provide more details about these antennas and their composting materials. The huge versatility of microstrip antennas in modeling and integrating different applications and their elementary architecture motivates doing structured research into modeling these antenna elements, from radio frequency to the sub-THz band.

The publication of Maxwell's equations in 1864 [35] settled down a firm basis for the electromagnetic theory and a fundamental stone to building the later antenna models. Microstrip patch antennas were initially proposed by Deschamps in 1953 [36] and patented by Gutton and Baissinot in 1955 [37]. From then, diverse model strategies and tools arose. The succeeding pages review previous work on these modeling topics: microstrip patch antennas (MSPAs), impedance-bandwidth broadening strategies for MSPAs, MSPAs in the sub-THz band, and material characterization. The mathematical formulations that describe the models mentioned in this review will be listed in the following chapters.

MSPAs are very popular due to their low profile, ease of fabrication, and easy integration with microwave circuits [38]. However, these antennas usually present challenges when the required bandwidth exceeds 10 %. Different strategies have been proposed in the literature to deal with these limitations [39],[40]. The

feeding technique of an MSPA plays a vital role in its frequency response. The probe-fed technique [41] produces a highly inductive impedance response. Due to the isolation between the feed and the patch, the aperture coupling feeding [23] produces low spurious radiation. The proximity coupling feeding [42] is more likely to behave with capacitive impedance. Also, MSPAs excited by proximity coupling feeding tend to produce broader bandwidth than MSPAs with probe feeding.

The first documented design guidelines and analytical models for MSPAs appeared in the early 80's [41, 43, 44]. The transmission-line and the cavity models [23] have provided the foundations for EM-modeling these antennas. Rigorous studies and analyses for rectangular and circular MSPAs employing probe-fed and inset-fed techniques were performed in [41] and [45], providing an equivalent RLC circuit for the patch. Sullivan et al. [46] presented an analysis of the aperture-coupled MSPA based on integral equations and Green's functions, constituting an initial step in developing circuit-based models. A detailed investigation of an electromagnetically coupled rectangular patch antenna was presented in [47], proposing an equivalent circuit based on the reciprocity theory. More recent models for the resonant frequency have been developed for a circular patch antenna [48] with less than 2 % of error. For rectangular patches, existing models [24, 49, 50] predict the patch resonant frequency with errors between 1.5 % and 5.5 % for substrate thicknesses in the range between $0.003\lambda_0$ and $0.05\lambda_0$.

Although there are models for MSPAs, the availability of reliable models for proximity-coupled MSPAs is limited. Modeling these antennas is challenging due to the complexity of the feeding mechanism and interaction with the patch voltage and current distribution. The impedance of the PC-MSPA cannot be directly determined under the end of the transmission line position unless considering the

fringing fields around the edge and the variable stripline characteristic impedance. In 1987, Pozar and Kaufman [42] obtained a numerical circuit model for the PC-MSPA. The model consisted of a capacitor in series with an RLC resonator. They found that the feeding behavior was predominantly capacitive when the overlapping section of the feed was low compared to the patch length.

During the last decade, Singh et al. [51] developed a circuit model for a circular PC-MSPA with a hybrid feed of an L-strip line. That model stated that the total feeding capacitance came from the electrostatic capacitances formed by the feed, the patch, and the ground plane, and the fringe-field equivalent capacitance coming from the open ends of these three surfaces. However, the values of these capacitances are so small –in the order of femtofarads– that modeling this antenna does not follow the expected impedance response. Limitations in the accuracy of the resonant frequency and resonant resistance in microstrip patches significantly affect the accuracy of the impedance response model in PC-MSPAs.

As noticed so far, previous work shows that the electromagnetic theorems can be applicable on microstrip antennas as long as the ground plane is vast (ideally infinite), behaving very closely to perfect electric conductors. The input impedance can be easily calculated once the circuit parameters are known using the cavity and transmission-line models. However, the substrate thickness range is limited to values usually less than 0.05 times the free-space wavelength. Also, the conductor thickness is considered negligible and usually omitted in the impedance models, affecting model accuracy.

PC-MSPAs [23, 42] have been widely used for a wide range of applications in the last decade [52, 53]. Compared with other conventional feeding techniques [23, 24, 54, 55], PC-MSPAs provide excellent features for enhancing impedance bandwidth. This benefit is due to the capacitance created by the patch, feed-layer,

and ground plane. However, the impedance bandwidth of an MSPA is typically very narrow, less than 5 %. Hence, broadening the impedance bandwidth in MSPAs has been a long-term research challenge that has led to innovating the geometrical design of MSPAs.

The first models for impedance bandwidth of patches in MSPAs [23, 56–58] suggest that by increasing the substrate thickness and decreasing the dielectric constant, the impedance bandwidth increases. However, with the increasing demand for miniaturized antennas, alternative strategies flourished. Adding a differential feed to PC-MSPAs enhances the bandwidth from 1 %-5 % to 20 % [24]. Differentially-feed MSPAs have outstanding stable impedance performance over large frequency operations and offer remarkable performance for high frequencies, including millimeter-waves [14, 32]. More recently, one of the best strategies to broaden bandwidth in MSPAs has been the inclusion of a modified ground plane as a metallic volume with an air cavity. By adding this backed cavity, the bandwidth could increase to 40 % [40]. Nonetheless, there is an absence of accurate models to estimate the impedance bandwidth and model broadband MSPAs. It is then observed that a panoramic assessment of the bandwidth as a behavioral parameter of PC-MSPAs would help develop more strategic designs for high-performance PC-MSPAs.

The traditional antenna models [23, 24] work up to 10 GHz. At this frequency and lower, the electrical properties of the materials are widely available in the manufacturers' data sheets and commercial simulators. Also, the impact of the conductor trace thickness and roughness in the impedance response is negligible. Nonetheless, as the operation frequency moves to higher values, the wavelength becomes smaller, and the material's geometrical imperfections get noticeable through variations in the electrical properties. It will be demonstrated in

Chapter 4 that the patch resonant frequency begins to be out of track at frequencies above 30 GHz. This inaccuracy is mainly because of assuming the conductor foil thickness and roughness as negligible, which is not valid in millimeter-wave frequencies and higher. Up to this review, no previous work provided antenna modeling in the mmWave and sub-THz bands that can tell more about these effects. However, there is relevant work [59–67] that report about increased losses in transmission lines. Therefore, further analysis is required to improve the model accuracy over frequencies up to 300 GHz.

It has been known since 1980 that the surface roughness increases the insertion losses of transmission lines [59]. From geometry-based empirical formulations [59, 60, 62, 64] to analytical models [61, 66], different strategies appeared, aiming to consider the roughness in transmission line design. From one side, the close forms [59, 60, 62, 64] offer an agile estimation of the impact of the conductor surface roughness. On the other hand, the analytical model of Gold and Helmreich [63, 67] gives accuracy and practicality, bringing a new concept of effective conductivity. Nonetheless, the accuracy in estimating the insertion losses is still limited.

In summary, there is a vast diversity of antenna models, counting formulations of different kinds: mathematical, geometrical, statistical, and physical derivations. The existing models usually consider perfect conductors, infinite ground planes, and other ideal assumptions to reduce the formulation complexity. Nevertheless, these assumptions begin to fail from the mmWave band and above. Thus, the existing models are limited to radio frequency bands, i.e., up to 10 GHz. In addition, this literature review reveals an opportunity to contribute with an unprecedented model for proximity-coupled MSPAs, which enables further research about this antenna up to the mmWave and sub-THz bands. In the subsequent pages, the research work for this dissertation will be formulated.

1.4 Problem Formulation

This work aims to address a problem concerning the analytical EM modeling of antennas for 6G communications and radar systems, expected to be in the mmWave and sub-THz bands. From the expressed motivations and the literature review, it is observed that EM models for MSPAs are functional in radio frequency but not above. The identified factors that surround this fact can be described in six aspects as follows:

- **Process:** Modeling antennas sometimes involves highly complex formulations, like the fringing field effect, and it usually requires analyzing many variables. Also, there are typical assumptions to reduce the modeling complexity, such as considering the conductors as perfect, with zero thickness and zero roughness.

- **Equipment:** Measured results are the main component of validating antenna models in radio frequency. However, industrial fabrication technology at sub-THz bands is currently under development to meet the strict fabrication tolerances that require antennas and electronic devices in this band. Also, feeding sub-THz antennas requires miniaturized connectors that may be available on the market in the coming years. In addition, the requirements for future applications set boundaries for the electromagnetic devices developed in the sub-THz band and above.

- **Materials:** Since antenna modeling in mmWave and sub-THz bands involves large frequency sweeps and smaller wavelengths; the material characterization needs to include advanced properties such as dielectric dispersion and anisotropy over frequency, conductor roughness in the interfaces with the dielectric and the air. The leading manufacturers, namely Rogers Corp., Isola Group., Taconic, etc., have started to list some of these advanced features.

However, they are still constrained to carrying accurate material characterization for mmWave and sub-THz modeling.

- **Research:** Full-wave simulations have been the base of most antenna designs for the last two decades, with little use of models for prototyping. This research trend has limited the number of new analytical models for antennas and their scope, especially for the mmWave and sub-THz bands.

- **Management:** Developing models involve an initial investment of computational resources or experiments to find the relations between the variables that compose them, e.g., antenna dimensions. This investment carries costs and delivery times, limiting the number of new models. Also, full-wave-based designs usually require heavy computation power, a significant amount of time, and their associated costs to produce antenna designs, mainly because of the high number of parametric analyses, frequency points, and meshing adjustments along with the EM device under simulation.

- **Environment:** The frequency band is the most significant variable that intervenes in modeling electromagnetic devices. Spectrum allocation dictates the frequency bands for every application created, and atmospheric attenuation limits the use of certain frequencies for specific applications. Both aspects combined constitute a boundary on the applications developed so far and, consequently, in the number of available models.

These aspects contribute to the lack of accurate EM models for antennas in the mmWave and sub-THz bands. The diagram of Fig. 1.2 summarizes the problem background. The upcoming subsection sentences the problem statement, which is also depicted in the red box on the right of Fig. 1.2.

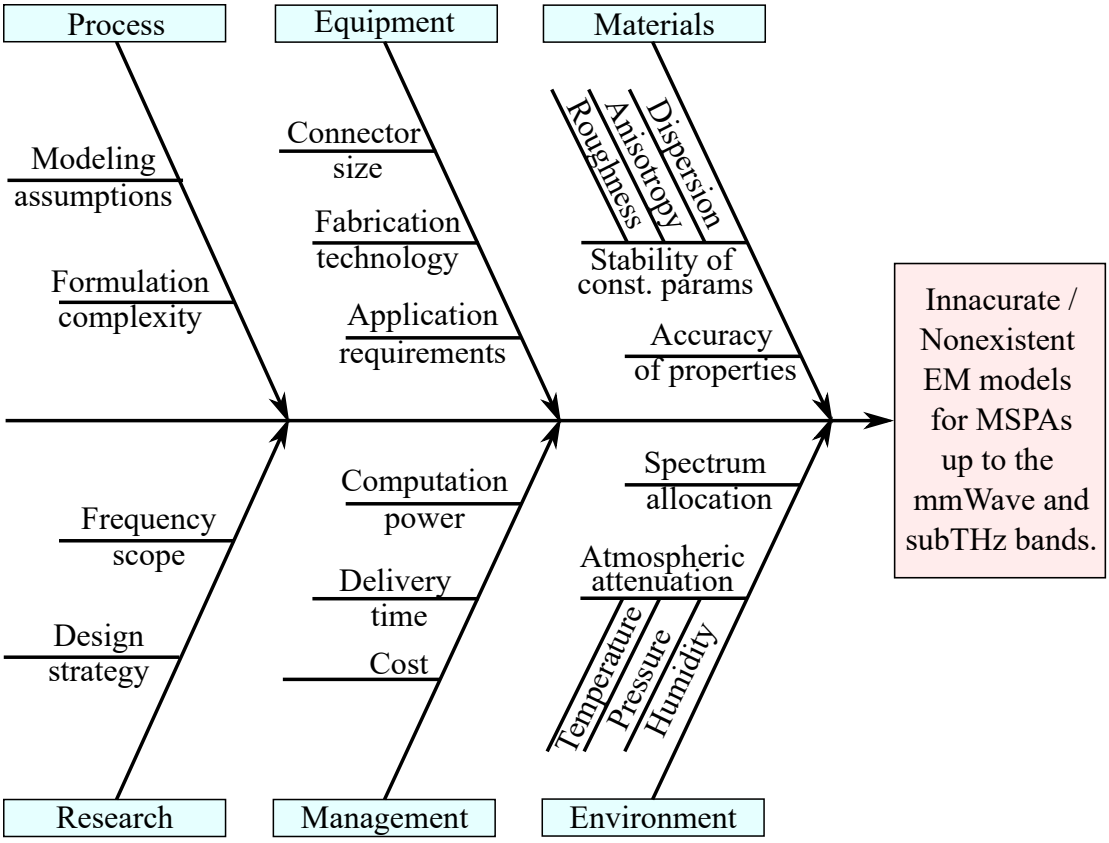

Figure 1.2: Schematic diagram for research problem formulation.
Many factors, e.g., modeling assumptions and limitations in material characterization, cause a lack of accurate MSPA models up to 300 GHz.

1.4.1 Problem Statement

After reviewing the problem background and previous work, the following statement is formulated: **To the best of my knowledge, the current models for MSPAs cannot be used up to the millimeter-wave and sub-terahertz bands for a highly-accurate characterization of the MSPAs' impedance response.** Therefore, the proposed solution is to investigate modeling strategies for MSPAs, from radio frequency up to 300 GHz.

1.4.2 Research Questions

The research in this work aims to answer the following questions:

1. How to accurately model proximity-coupled MSPAs?
2. What is the role of MSPAs in sub-THz radar and communication systems?
3. How to enhance the current EM models for MSPAs to become suitable in the mmWave and sub-THz bands?

Answering these questions will produce contributions, described in Section 1.8; while Section 1.7 discusses the strategy to answer these questions.

1.5 Justification

MSPAs will require higher operating frequencies to achieve the standards of the 6G communication systems. Therefore, future antenna engineering will demand new MSPA designs with lower dimensions and fabrication errors. Analytical modeling of MSPAs will be crucial for their development since it will enable instant prototyping while considering the material characterization (namely dielectric dispersion, the effect of the copper roughness, etc.) that takes place in the mmWave and sub-THz bands. Thus, electromagnetic modeling for broadband MSPAs has the potential to significantly impact the scientific community since it will constitute a brand-new framework for antenna design for an emerging technology that promises a substantial technological upgrade to our dynamic world.

1.6 Hypothesis

As discussed in the literature review, millimeter-wave frequencies are more comparable with the material imperfections, deemed negligible to radio frequency. Then, current models are limited to work to frequencies below millimeter waves,

and thorough analysis and reformulation are necessary to accurately model antennas above 30 GHz.

> This work hypothesizes that an electric circuit can accurately model the frequency response of MSPAs in the mmWave and sub-THz bands, provided a set of mathematical formulations that include the geometrical and electrical properties of their constitutive materials.

1.7 Proposed Research

The work developed in this dissertation aims to contribute analytical models for antennas that can be functional and suitable up to the frequency bands for future communication and radar systems. Therefore, the following goals are proposed as a baseline for the research that links to this work:

General goal:

To develop a mathematical framework for EM modeling of MSPAs up to the mmWave and sub-THz bands.

Specific goals:

1. To review, assess, and characterize EM modeling strategies for RF antennas.
2. To develop an analytical EM model for RF proximity-coupled MSPAs.
3. To provide an overview of the role of MSPAs in the mmWave and sub-THz bands, including trade-offs in materials and fabrication processes.
4. To build a mathematical formulation for accountability of antenna characterization for MSPAs, namely geometrical and electrical properties of dielectric substrates and conductor foils.
5. To synthesize EM models for MSPAs with high accuracy up to 300 GHz.

Then, the proposed research consists of exploration, description, correlative comprehension, and integration of analytical models of microstrip antennas from 300 MHz to 300 GHz. This research proposal can be divided into four task groups: overview of antenna modeling in radio frequency, EM modeling for proximity-coupled MSPAs, material characterization for mmWave and sub-THz antennas, and MSPA modeling in the mmWave and sub-THz bands. These task groups correlate to each chapter of this dissertation.

For antenna modeling in radio frequency and microwave (up to 10 GHz), the proposed research starts with exploring the currently used modeling strategies from a mathematical and physical perspective through fundamental subjects such as the EM theory and the electric circuit theory. This research will continue with an in-depth description of the modeling formulations to compute the impedance response and radiation patterns of wired antennas and MSPAs. EM models for wired dipoles in different orientations are presented. This fundamental research is detailed in Chapter 2, and correlates the first specific goal. Comprehending these models will provide the foundations towards proposing the new models for MSPAs in the next task groups.

As described in the literature review, there is a place to contribute with a new model for proximity-coupled microstrip patch antennas (PC-MSPAs). This research task starts by understanding the correlation between the antenna variables and its effect in the impedance frequency response and bandwidth, From them, new formulations are proposed to investigate. Then, this work will integrate MSPA models with different feedings, proposing, creating, and evaluating a circuit model for PC-MSPAs. This proposed task meets the dissertation research's second specific goal, and it will be presented in correlative order in the Chapter 3 of this dissertation.

Regarding material characterization for antennas in the mmWave and sub-THz bands, this research will start by diving into the literature for the foundations of materials and their constitutive parameters and attributes for wave propagation, phase delay, and attenuation. It will then explain current characterization methods, as well as the mathematical and physical formulations that quantify the impact of the substrate and conductor foil's imperfections on transmission lines. This research will discuss the effects of the dielectric dispersion and anisotropy and the conductor thickness and roughness. With this information, the following research task is to compile a detailed review of the trade-offs of materials that conform to antennas above 30 GHz. Also, this research will pursue a new concept of equivalent material that accounts for the conductor foil roughness. The second and third specific goals of this work and the Chapter 4 of this work connect to this research task group.

Researching antenna modeling in the mmWave and sub-THz bands will start from the synthesis of reformulations in the circuit models that account for microstrip antennas. The primary purpose of this research task group will be to model the effects of the irregular distribution of the geometrical and electrical properties of the materials that count in the antennas' impedance response and radiation patterns. With the integrated information obtained in the two previous research task groups, a set of new mathematical formulations will be proposed and evaluated. Then, the antenna models will be updated to preserve the equivalent circuit model and keep the proposed models as straightforward to replicate as possible. This research is integrated and presented in Chapter 5, and it relates to the fourth specific goal of this research work.

The data source comprises simulated impedance responses from diverse parametric analyses of the antennas under modeling. For antennas, the designs and

data are generated in Ansys™ HFSS [18], while the material characterization study is realized using Simulia™ CST software [19]. This data is exported as Z-parameters and S-parameters. The data importing and processing is carried out using MATLAB™ [68] by numerical inversion, i.e., by finding the values using the EM model that produces the results of the imported data. Then, the curve fitting technique [69] is applied to create the mathematical formulations of the variables that convey the EM model.

The formulated EM models for PC-MSPAs on the radio frequency spectrum, i.e., up to 10 GHz, have a double validation, with simulation and fabrication. The material characterization models which work up to the sub-THz band are also validated with simulation and measurement. However, due to equipment limitations, the antenna models up to the sub-THz band will not be validated through antenna fabrication but with simulations considering the most realistic conditions, including the variations of the materials' geometrical and electrical properties. Table 1.2 reviews the proposed research, with the research scope, frequency and validation scope for the four task groups described above.

Table 1.2: Overview of the proposed research task groups and their scope.

Research task group	Dissertation chapter	Research scope				Frequency scope			Validation scope	
		Exploratory	Descriptive	Comprehensive	Integrative	Up to 10 GHz	mmWave band	sub-THz band	Simulation	Fabrication
EM modeling overview in RF	2	✓	✓	✓		✓			✓	
PC-MSPA modeling in RF	3		✓	✓	✓	✓			✓	✓
Material characterization	4	✓	✓	✓	✓		✓	✓	✓	✓
Modeling in mmWave/sub-THz	5			✓	✓		✓	✓	✓	

1.8 Contribution

The main contribution of this work is an analytical-modeling framework for MSPAs up to the mmWave and sub-THz band, composed of diverse mathematical formulations of microstrip antennas and their materials. Based on the proposed research (Section 1.7) and the research questions (Section 1.4.2), the following specific contributions are identified:

1. A thorough overview of EM modeling techniques for wired and microstrip antennas in radio frequency, providing a brand-new analytical model for proximity-coupled MSPAs.

2. A panoramic review of the role of MSPAs in the mmWave and sub-THz bands, i.e., above 30 GHz, including trade-offs of architectures, materials, and fabrication techniques.

3. A mathematical-based concept of equivalent conductor and dielectric as a modeling formulation for the effect of the conductor roughness in the electromagnetic wave propagation in the mmWave and sub-THz bands.

4. A brand-new set of models for MSPAs in the mmWave and sub-THz bands, including the associated feeding techniques, such as probing, inset transmission line, aperture coupling, and proximity coupling.

These contributions add up new knowledge in the following research fields:

- **Antenna modeling,** with a framework composed of several models from 3 GHz to 300 GHz for microstrip antennas. All the published work from the research done in this dissertation contributes to this research field, namely [70–75].

- **Antenna design,** with a new set of guidelines for designing broadband proximity-coupled MSPAs, as well as a novel formulation to calculate its impedance bandwidth. The work in [70, 74] fits within this research subject.

- **Material characterization,** with a brand-new concept of equivalent conductivity and in-line dielectric constant as a mathematical formulation to count the effects of the conductor roughness in microstrip transmission lines. This research field links the paper [76] and its associated work.

- **6G communication systems,** with a compiled review of the trade-offs of MSPAs in 6G communications, including a new set of mathematical models for microstrip antennas, functional up to 300 GHz. The publication of [75] corresponds to this research line.

1.9 Dissertation Overview

This dissertation is organized into six chapters, covering different topics related to antenna modeling in radio frequency and microwaves, material characterization, and MSPA modeling up to the mmWave and sub-THz bands.

This chapter has settled the foundations of the research performed in this dissertation. Chapter 2 delivers an in-depth overview of the current electromagnetic modeling strategies for conventional antennas, which work for low-frequency applications such as radio, radars, and 2G-to-4G communication systems. Chapter 3 formulates and provides a brand-new model for proximity-coupled patch antennas, covering formulations for the impedance bandwidth, impedance response, and differential feeding. Chapter 4 contributes an insightful analysis of the impact of material constitutive characteristics on the performance of the analytical antenna model. This chapter illustrates the reasons for the limitations of the state-of-art

antenna models and provides new mathematical formulations to develop more accurate modeling. Moreover, and beyond the mainstream materials, this work also reviews non-conventional materials that are more suitable for sub-THz antenna fabrication. Chapter 5 supplies an enhanced set of models for probe-fed and proximity-coupled MSPAs up to 300 GHz. This contribution constitutes the base of a new framework for designing the new generation of antennas in the coming dynamic 6G communication systems. Finally, Chapter 6 will list the conclusions of this work, as well as new research lines for future work.

Chapter 2

Overview on EM Modeling for Conventional Antennas

Books permit us to voyage through time, to tap the wisdom of our ancestors.

—Carl Sagan, *Cosmos*

Antenna EM modeling involves a set of mathematical formulations considering the antenna architecture and setup to compute behavioral metrics, e.g., far-field radiation patterns and impedance response over frequency. This chapter delivers a thorough overview of EM models for wired antennas, slot antennas, and microstrip patch antennas (MSPAs). The fundamentals covered in the first sections give the most elementary tools for fully comprehending the derivations provided in the following sections. Modeling MSPAs involves analyzing and comprehending the effect of the three-dimensional structure under the patch on the field distribution, the impedance response, and the radiated fields. This understanding can be more effective by first studying more elementary antenna architectures. For this reason, this chapter reviews modeling strategies for wired antennas and slot antennas. Then, an in-depth study for MSPA EM models is performed and described, covering modeling strategies from the cavity model to computer-aid formulations, to compute the impedance bandwidth.

2.1 Fundamentals

Modeling antennas requires various mathematical tools that are functional and follow the physical laws that govern these electromagnetic devices. Maxwell's equations are the basis of electromagnetism and the starting point for this work regarding modeling. Equivalence principles –such as the relation between EM theory and circuits theory, the auxiliary potentials, and the EM theorems– are also crucial for effective modeling. These techniques bring computer-aided modeling as a direct application that enables antenna analysis and design. All these items are going to be covered in this section.

2.1.1 EM Theory equations

James Clerk Maxwell (1831-1879) settled the basis of the modern electromagnetic theory by compiling a set of four equations that relate the electric and magnetic fields with the spatial distribution of charges and currents in matter. In addition, two additional equations relate charges, voltages and currents, called "the continuity equation" and Ohm's Law [77]. These equations [77] can be written in their differential form for a given point in space; and in its integral form for a given volume or surface on a medium. For time-harmonic electromagnetic fields, these equations are listed in Table 2.1.

The variables described in Table 2.1 are defined as follows:

E is the electric field vector, in volt/meter (V/m).

H is the magnetic field vector, in ampere/meter (A/m).

J is the electric current density vector, in ampere/square-meter (A/m^2).

q_{ev} is the electric charge density, in coulomb/cubic-meter (C/m^3).

Q_{ev} is the electric charge in coulombs (C).

ω is the angular frequency of the EM fields, in radian/second (rad/s).

Table 2.1: Fundamental equations for the EM theory.

	Differential form	Integral form
Faraday's law	$\nabla \times \mathbf{E} = -j\omega\mu\mathbf{H}$	$\oint_{\boldsymbol{\ell}} \mathbf{E} \cdot d\boldsymbol{\ell} = -j\omega\mu \iint_{\boldsymbol{s}} \mathbf{H} \cdot d\boldsymbol{s}$
Ampere-Maxwell's law	$\nabla \times \mathbf{H} = \mathbf{J_{ic}} + j\omega\varepsilon\mathbf{E}$	$\oint_{\boldsymbol{\ell}} \mathbf{H} \cdot d\boldsymbol{\ell} = \iint_{\boldsymbol{s}} \mathbf{J_{ic}} \cdot d\boldsymbol{s} + j\omega\varepsilon \iint_{\boldsymbol{s}} \mathbf{E} \cdot d\boldsymbol{s}$
Gauss' law	$\nabla \cdot \mathbf{E} = q_{ev}/\varepsilon$	$\oiint_{\boldsymbol{s}} \mathbf{E} \cdot d\boldsymbol{s} = Q_{ev}/\varepsilon$
Magnetic Gauss' law	$\nabla \cdot \mathbf{H} = 0$	$\oiint_{\boldsymbol{s}} \mathbf{H} \cdot d\boldsymbol{s} = 0$
Continuity equation	$\nabla \cdot \mathbf{J_c} = -j\omega q_{ev}$	$\oiint_{\boldsymbol{s}} \mathbf{J_c} \cdot d\boldsymbol{s} = -j\omega Q_{ev}$
Ohm's law	$\mathbf{J_c} = \sigma\mathbf{E}$	

μ is the magnetic permeability of the medium, in farad/meter (F/m).

ε is the electric permittivity of the medium, in henry/meter (H/m).

σ is the electric conductivity of the medium, in siemen/meter (S/m).

$\boldsymbol{\ell}$ and $\boldsymbol{s}$ are the length and area domains of the medium sections where the EM fields are defined.

EM modeling is founded on these equations since the EM theory governs antenna radiation and field excitation inside them. Moreover, EM modeling is built from the electric-circuit theory through circuit components such as resistors, inductors, and capacitors. The following lines describe the relationship between the EM and electric-circuit theories.

2.1.2 Relation between Fields and Circuits

Since electric circuits carry electric currents and charges, their behavior is also governed by the EM theory. Three essential devices that carry electric current and voltage are the resistor, the capacitor, and the inductor. These devices are the basis of the electric-circuit theory, and their behavior is closely connected with the EM theory through Maxwell's equations. By rewriting the first two Maxwell's equations (voltages and currents) in the integral form, the following relations can be formulated [77]:

- Relation between EM constitutive parameters of matter and the circuit parameters: As observed in Table 2.1, the medium where the EM fields exist is characterized by three constitutive parameters: the electrical permittivity ε, the magnetic permeability μ, and the electrical conductivity σ. From an electric-circuit perspective, the matter can be electrically modeled by resistance R_i, inductance L_i, and capacitance C_i.

  By definition [77], the value of each circuit parameter is expressed as follows: the inductance L_i is the ratio of magnetic flux Ψ_m per unit of electric current I, the capacitance C_i is the ratio of electric charge Q_{ev} per unit of voltage V, and the resistance R_i is the ratio between voltage V and current I (from the Ohm's Law). Also, the flux counterparts in the EM theory are the electric flux density $\mathbf{D}$ and the magnetic flux density $\mathbf{B}$.

  The following relations [77] show a connection between the EM theory and the electric circuit theory through the constitutive relations of the matter:

$$\mathbf{J_c} = \sigma\mathbf{E} \qquad \longleftrightarrow \qquad I = G_i V = (1/R_i)V \tag{2.1a}$$

$$\mathbf{D} = \varepsilon\mathbf{E} \qquad \longleftrightarrow \qquad Q_{ev} = C_i V \tag{2.1b}$$

$$\mathbf{B} = \mu\mathbf{H} \qquad \longleftrightarrow \qquad \Psi_m = L_i I \tag{2.1c}$$

- Voltage in an inductor: from the integral form of Faraday's law, the voltage V in an inductor with inductance L_i can be written as [77]:

$$\oint_C \mathbf{E}.d\mathbf{l} = -j\omega\mu \iint_S \mathbf{H}.d\mathbf{s} = -j\omega\Psi_m \quad \longleftrightarrow \quad \sum V = -j\omega L_i I \tag{2.2}$$

  This circuit relation is also known as Kirchhoff's voltage law. The same relation can be acquired by using the electric displacement current formulation from Ampere-Maxwell's law.

- Current in a capacitor: from the Continuity equation, the current I on a capacitor with capacitance C_i can be expressed as [77]:

$$\oiint_s \mathbf{J_c}.d\boldsymbol{s} = -j\omega Q_{ev} \quad \longleftrightarrow \quad \sum I = -j\omega C_i V \tag{2.3}$$

  In this case, the circuit relation expressed above is known as Kirchhoff's current law. This relation can also be obtained using the mathematical concept of magnetic displacement current formulation, similar to the one from Ampere-Maxwell's law.

As observed, the EM theory is connected to the electric-circuit theory, which has significant consequences in antenna modeling. Electric circuits can be applied to characterize the antennas' impedance frequency response, being the basis for antenna circuit models. In addition, this modeled frequency response and the models for far-field antenna radiation can be used together to describe the antenna realized gain with accuracy.

2.1.3 The Electric and Magnetic Auxiliary Vector Potentials

As introduced in Section 2.1.1, Maxwell's equations are the basis for obtaining the EM fields. Simultaneously solving these equations, the EM fields can be obtained anywhere, including in the far-field region of antennas. From the distribution of currents and charges across the antenna geometry, the EM fields can be solved by using the wave equation, expressed as follows [77]:

$$\nabla^2\mathbf{E} = \gamma^2\mathbf{E} + \nabla \times \mathbf{M} + j\omega\mu\mathbf{J} + (1/\varepsilon)\nabla q_{ev} \tag{2.4}$$

$$\nabla^2\mathbf{H} = \gamma^2\mathbf{H} - \nabla \times \mathbf{J} + j\omega\varepsilon\mathbf{M} + (1/\mu)\nabla q_{mv}, \tag{2.5}$$

where $\gamma = j\omega\mu\sigma - \omega^2\mu\varepsilon$ is the wave propagation constant, q_{ev} and $\mathbf{J}$ are electric sources, and q_{mv} and $\mathbf{M}$ are equivalent magnetic sources. When γ is expressed as $\alpha + j\beta$, it includes the attenuation constant α and the phase constant β (also expressed as k). Also, the amplitudes of $\mathbf{E}$ and $\mathbf{H}$ are related through the wave impedance $\eta = |\mathbf{E}|/|\mathbf{H}|$.

These equations can be explicitly written depending on the coordinate system and analytically solved. The solutions may be exponential, cosinusoidal, Legendre's, or Bessel's functions [77]. Previous work [77] shows that waveguides and resonant cavities can be solved in this way. Also, the numerical solution of these equations over space, also known as full-wave solve, is what most commercial simulators perform. However, antennas have sources that need to be included in the formulations. Analytically solving Maxwell's equations for antennas can be intricate or impossible, depending on the mathematical complexity, because of the geometry and the radiating field zones.

The auxiliary vector potentials are a powerful mathematical tool that counts as an intermediate stage between Maxwell's equations and the solution of the generated differential and integral mathematical formulations.

The magnetic auxiliary potential $\mathbf{A}$ and the electric auxiliary potential $\mathbf{F}$ can be directly obtained from the antenna currents (electric currents $\mathbf{J}$ or equivalent magnetic currents $\mathbf{M}$) by the expressions (2.6)–(2.7) [77].

$$\nabla^2\mathbf{A} + \beta^2\mathbf{A} = -\mu\mathbf{J} \tag{2.6}$$

$$\nabla^2\mathbf{F} + \beta^2\mathbf{F} = -\varepsilon\mathbf{M} \tag{2.7}$$

The solution structure depends on the coordinate system, which will be exemplified from Section 2.2 to Section 2.4. From the equations listed above solutions, the EM fields can be calculated by analytical or numerical integration of the aux-

iliary potentials. The fields $\mathbf{E}$ and $\mathbf{H}$ are then computed as [77]:

$$\mathbf{E} = -j\omega\mathbf{A} - j\frac{1}{\omega\mu\varepsilon}\nabla(\nabla.\mathbf{A}) - \frac{1}{\varepsilon}\nabla\times\mathbf{F} \tag{2.8a}$$

$$\mathbf{H} = \frac{1}{\mu}\nabla\times\mathbf{A} - j\omega\mathbf{F} - j\frac{1}{\omega\mu\varepsilon}\nabla(\nabla.\mathbf{F}) \tag{2.8b}$$

Modeling far-field radiation is possible through analytical or numerical integration of the auxiliary potentials. Two important considerations are required for this procedure to be valid: the source's physical size needs to be small when seen from a distant point, and that observation point should be in the Fresnel's far-field zone, i.e., at a radial distance $R > 2D^2/\lambda$, where D is the source's most significant dimension, and λ is its operating wavelength. Then, the radiated fields can be computed as follows:

First, solving (2.6)–(2.7) along a source volume distribution $\mathcal{v}'$ in rectangular coordinates provide the following solutions [77]:

$$\mathbf{A}(x,y,z) = \frac{\mu}{4\pi}\int_{v'}\mathbf{J}(x',y',z')\frac{e^{-jkR}}{R}\,d\mathcal{v}' = (A_x, A_y, A_z) \tag{2.9}$$

$$\mathbf{F}(x,y,z) = \frac{\varepsilon}{4\pi}\int_{v'}\mathbf{M}(x',y',z')\frac{e^{-jkR}}{R}d\mathcal{v}' = (F_x, F_y, F_z), \tag{2.10}$$

where (x,y,z) represent the coordinates of the observation point, and (x',y',z') corresponds to the source's geometrical distribution ($\mathcal{v}'$, $\mathcal{s}'$, or $\boldsymbol{\ell}$). Then, the conversions of (2.11a)–(2.11b) deliver the components of $\mathbf{A}$ and $\mathbf{F}$ in spherical coordinates as [77]:

$$\begin{bmatrix} A_r \\ A_\theta \\ A_\phi \end{bmatrix} = \begin{bmatrix} \sin\theta\cos\phi & \sin\theta\sin\phi & \cos\theta \\ \cos\theta\cos\phi & \cos\theta\sin\phi & -\sin\theta \\ -\sin\phi & \cos\phi & 0 \end{bmatrix} \begin{bmatrix} A_x \\ A_y \\ A_z \end{bmatrix} \tag{2.11a}$$

$$\begin{bmatrix} F_r \\ F_\theta \\ F_\phi \end{bmatrix} = \begin{bmatrix} \sin\theta\cos\phi & \sin\theta\sin\phi & \cos\theta \\ \cos\theta\cos\phi & \cos\theta\sin\phi & -\sin\theta \\ -\sin\phi & \cos\phi & 0 \end{bmatrix} \begin{bmatrix} F_x \\ F_y \\ F_z \end{bmatrix} \tag{2.11b}$$

Consequently, the solutions for the radiated fields are expressed as [77]:

$$E_r \approx 0 \tag{2.12a}$$

$$E_\theta \approx (E_A)_\theta + (E_F)_\theta = -j\omega[A_\theta + \eta F_\phi] \tag{2.12b}$$

$$E_\phi \approx (E_A)_\phi + (E_F)_\phi = -j\omega[A_\phi - \eta F_\theta] \tag{2.12c}$$

$$H_r \approx 0 \tag{2.12d}$$

$$H_\theta \approx (H_A)_\theta + (H_F)_\theta = \frac{j\omega}{\eta}[A_\phi - \eta F_\theta] = \frac{-1}{\eta}E_\phi \tag{2.12e}$$

$$H_\phi \approx (H_A)_\phi + (H_F)_\phi = -\frac{j\omega}{\eta}[A_\theta + \eta F_\phi] = \frac{1}{\eta}E_\theta \tag{2.12f}$$

This procedure constitutes a crucial mathematical tool to determine radiating fields analytically. Despite being longer than the direct computation by using (2.4)–(2.5), the decoupling formulations of (2.6)–(2.7) that derive in the auxiliary potentials simplifies the mathematical complexity and computational resource usage to produce the same results. Following this structure, EM modeling utilizes different strategies to optimize calculations and still get an accurate estimation of antenna radiation.

2.1.4 The Electromagnetic Theorems

The EM theorems constitute an essential modeling basis for understanding antenna radiation since they provide a transformation in the geometrical and electrical configuration of an EM problem to an equivalent setup, which usually becomes easier to solve analytically. The following lines describe some of the most relevant

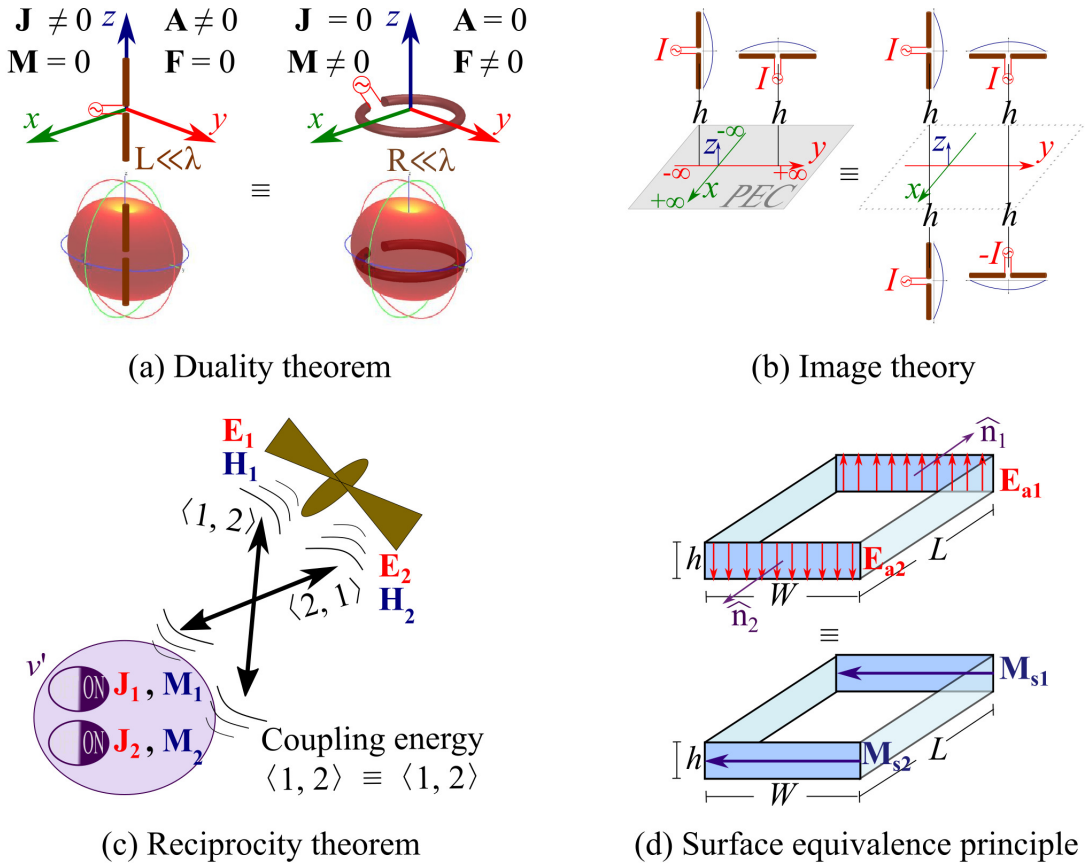

(a) Duality theorem (b) Image theory

(c) Reciprocity theorem (d) Surface equivalence principle

Figure 2.1: Electromagnetic theorems applied to antenna modeling.
(a) duality theorem, (b) image theory, (c) reciprocity theorem, and (d) surface equivalence principle. These theorems provide an essential basis for analytical modeling of the EM fields for radiating elements.

EM theorems related to antenna modeling: the duality theorem, the image theory, the reciprocity theorem, and the surface equivalence theorem, also known as Huygens's principle. An illustration summarizing these theorems is provided in Fig. 2.1.

- **Duality theorem:**

  Because of the symmetric distribution of mathematical terms in Maxwell's equations and the derived formulations, there are variable pairs that keep these equations if they are interchanged. The direct consequence of this duality is that an electrical problem can be reformulated as a magnetic problem and vice

versa. Moreover, the following variables can be interchanged when applying the duality theorem [77]: electric field **E** and magnetic field **H**, electric vector potential **F** and magnetic vector potential **A**, electric charge q_{ev} and a theoretical magnetic charge q_{mv}, electric current **J** and a theoretical magnetic current **M**, permittivity ε and permeability μ, and wave impedance η and wave admittance $1/\eta$.

- **Image theory:**

  The total EM fields of a source near an infinite plane made of perfect conductors can be calculated with an equivalent geometry formed by the original source with a virtual source –the image– that replaces the geometry of the infinite plane [77]. This image is located at a symmetrical distance to the infinite plane, with a magnitude of the same intensity and polarity that depends on the source's nature, either electric or magnetic. This equivalence is based on the existence of a unique solution having the boundary conditions near the infinite plane in both setups. This theorem is especially useful in the presence of antenna sources near ground planes of great size since calculating the radiated EM fields needs to consider the intricate reflections of such sources on the ground plane.

- **Reciprocity theorem:**

  This theorem considers a couple of sources (source 1 and source 2) and their associated EM fields (fields 1 and fields 2). Then, the reciprocity theorem states that the energy associated with fields 1 and source 2 is the same as if the energy is calculated by interchanging the EM fields and sources, i.e., fields 2 with source 1. This theorem becomes significant in antenna network analysis since it allows the characterization of the EM-field transmission and reception properties on different ports [77]. Another application is on mode analysis of

fields in waveguides, as the reciprocity theorem can be applied in the particular source-free case [77].

- **Surface equivalence theorem (Huygens's principle):**

  Let us define a set of EM fields over a closed region; produced by actual sources, e.g., an antenna and the surrounding space, where the EM fields need to be computed. This theorem states that this set of EM fields can be replaced with a list of equivalent sources over the same closed region where the original fields were distributed and with intensities to keep the produced fields over this region. This EM theorem is especially useful in modeling the radiation on indirect-contact-fed antennas since the EM fields at the feeding –produced by electric current sources– can be modeled by its equivalent physical model, reducing the calculation complexity of the associated radiated fields.

2.1.5 Computer-aided Modeling

Antenna modeling can be applied to computer-aided design by developing mathematical and computational tools. Diverse software exists nowadays to perform modeling, and they show a promising capability to deliver instant design with high accuracy. At a glance, the following examples are mentioned:

- **MATLAB™ Antenna Toolbox**

  The MATLAB™ Antenna toolbox is an application package that contains a set of functions related to RF antenna design, analysis, and plotting. The functions are based on the mathematical models available in the literature for mainstream antennas. This toolbox covers a variety of antenna geometries and material properties, e.g., dielectric constant. The workflow in the user interface begins by defining the antenna geometry and operating frequency, followed by dimensions and materials adjustments, and then, after a reasonable amount of

time –around a minute–, the results are ready to be listed and plotted. Up to the 2021b release, it has been observed that the models listed there consider flat and smooth foils for microstrip antennas, which make the models functional and accurate up to the RF and microwave bands (up to 10 GHz).

- **Ansys™ HFSS**

  The Ansys™-powered High-Frequency Simulation Software (HFSS) is a dedicated electromagnetic workspace inside the Ansys Electromagnetics Desktop environment. HFSS solves EM problems by full-wave simulation, processing Maxwell's equation in the differential form [78] along a tetrahedral meshing structure distributed in the geometrical design. HFSS primarily uses the Finite Element Method (FEM) [78]. Nevertheless, this software supplies in its last releases with more alternatives for solutions, such as transient mode, shooting and bouncing rays (SBR+), physical optics, and FEM transient. Up to the release of 2021 R2, HFSS includes the geometrical-based roughness models [59, 61] to analyze finite-conductivity materials to be included as a boundary condition in the EM designs. Also, Ansys Electromagnetics Desktop includes an antenna design tool, called Ansys Customization Toolkit, or ACT, in which designs can be exported to HFSS and then analyzed.

- **Simulia™ CST**

  The Computer Simulation Technology (CST) Studio Suite, powered by Simulia™, is an analysis software that provides a complete solution in EM, fluid dynamics, circuits, systems, and more areas, applied to a 3D geometrical design. For EM problems, CST makes a full-wave analysis of the design and its electrical properties. It solves Maxwell's equations in the integral form along a meshing structure similar to HFSS. CST mainly uses the Finite Integration Technique (FIT) [79], which can be applied in the time or frequency domains.

The 2021 version includes the gradient model [63] for the roughness analysis for conductive foils. This model is the most accurate approach to quantifying the effects of the foil surface roughness in fabricated transmission lines in the mmWave band. Therefore, this software has been used to analyze and synthesize the models proposed in Chapter 4 of this work.

- **Antenna Design Associates™ PCAAD**

  The Personal Computer Aided Antenna Designer app is a computational EM tool based on mathematical modeling of antenna elements, apertures, phased arrays, microstrip antennas, and transmission lines. This software provides instant antenna design and impedance matching, and it also supports a user interface that allows plotting the impedance response, return loss, and radiation patterns.

These tools provide reliable solutions using different computation strategies: full-wave solution of Maxwell's equations and analytical modeling. The work developed in this dissertation can provide brand-new modeling and design guidelines in the mmWave and sub-THz bands, expanding the current applicability of the models in RF and microwaves. This work is based on full-wave solutions, giving a set of equivalent circuits and geometrical models with the associated mathematical formulations.

2.2 Wired Antennas

This section aims to mathematically analyze wired antennas, namely monopoles and dipoles. The auxiliary vector potentials are used to get the electromagnetic fields in the far-field zone. This information also allows some antenna parameters, such as the directivity and input impedance. A simulation in MATLAB™ and

Ansys HFSS™ are performed to compare with the EM model.

2.2.1 Monopole

The monopole antenna is one of the most known and studied antennae, where its properties, such as directivity, beamwidth, and input impedance, are well known. This antenna's most basic shape and source configuration is a very thin cylindrical conductor with a current distribution density along this cylinder, which is above a huge ground plane, ideally infinite, of a perfectly electric conductor (PEC). This description is illustrated in Fig. 2.2 bellow.

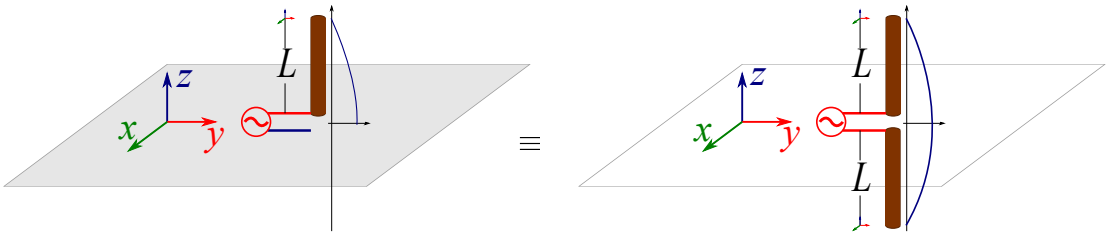

Figure 2.2: Schematic of a cylindrical monopole.
A monopole antenna (on the left) with a length L over an infinite ground plane can be modeled by its equivalent geometrical model (on the right).

The EM modeling of this antenna is based on:

- Image theory, considering the infinite plane constituted by a PEC. If it were not, the field equations would be different due to the diffraction of the eventual finite plane and due to the possible losses caused by the material's finite conductivity.
- Far-field zone approximations, assuming that the reference point for calculating the radiated fields are on the Fresnel's Far-field zone, at a distance $R \geq 2(l_f^2/\lambda)$, where $l_f = 2L$.
- Auxiliary vector potentials $\mathbf{A}$ and $\mathbf{F}$, which constitute an important step for getting the electromagnetic fields, avoiding more complex and unnecessary math computation while getting these fields, as described in Section 2.1.3.

Radiated Fields

According to the image theory, the monopole antenna placed on an infinite plane constituted of PEC is equivalent to a dipole antenna without the plane, as shown in Fig. 2.2. In consequence, the specifications of the current are analyzed, and it is seen in Fig. 2.2 that the expression of I_z is the same as at the initial setting, so the current distribution is:

$$I_z = I_0 \cos(kz') \; \forall z' \in [-L, L] \tag{2.13}$$

As seen in the source list in (2.13), there is no magnetic current source, so there is no electric vector potential $\mathbf{F}$, having uniquely the $\mathbf{A}$ or magnetic potential, which is going to be obtained as follows:

$$\mathbf{A}(x', y', z') = \frac{\mu}{4\pi} \int_{-L}^{L} I_0 \cos(kz') \frac{e^{-jkR}}{R} dl' \tag{2.14}$$

Considering the far-field zone, the expression (2.14) can be rewritten as:

$$\mathbf{A}(x', y', z') = \frac{\mu}{4\pi} \int_{-L}^{L} I_0 \cos(kz') \frac{e^{-jk\ (r - z'\cos\theta)}}{r} dz' \tag{2.15}$$

This formulation leads to the z-component of $\mathbf{A}$ as:

$$A_z = \frac{\mu I_0 e^{-jkr}}{4\pi r} \int_{-L}^{L} e^{jkz'\cos\theta} \cos(kz') dz' = \frac{\mu I_0 e^{-jkr}}{2\pi r k} \Big[\frac{\sin(kL - kL\cos\theta)}{\sin^2\theta} \Big] \tag{2.16}$$

By transforming from the rectangular coordinate system to the spherical coordinate system, then the angular component A_θ is expressed as:

$$A_\theta = -A_z \sin\theta = \frac{-\mu I_0\ e^{-jkr}}{2\pi r k} \Big[\frac{\sin(kL - kL\cos\theta)}{\sin\theta} \Big] \tag{2.17}$$

The angular component A_ϕ is zero, and the radial component A_r is irrelevant for far-field calculations as seen in (2.12a)–(2.12f). Therefore, the radiated E-

fields of a monopole antenna with an infinite ground plane are:

$$E_\theta \approx -j\omega A_\theta = \frac{j\eta I_0\ e^{-jkr}}{2\pi r}\ \Big[\frac{\sin(kL - kL\cos\theta)}{\sin\theta}\Big] \tag{2.18a}$$

$$E_\phi \approx -j\omega A_\phi = 0 \tag{2.18b}$$

Input Impedance

The input impedance of this antenna can be computed by first calculating the electromagnetic power density [24], then by decomposing its real and imaginary parts, and by comparing it with the circuits theory. Another way to get it is by numerically evaluating the integral equations for the current distribution and obtaining the impedance referred to at the maximum current. For a wired dipole of length $l_e = 2L$ and radius a, these expressions are [24]:

$$\begin{aligned} R_m = \frac{\eta}{2\pi}\Big\{ & C_\gamma + \ln(kl_e) - C_i(kl_e) \\ & + \frac{1}{2}\sin(kl_e)[S_{int}(2kl_e) - 2S_{int}(kl_e)] \\ & + \frac{1}{2}\cos(kl_e)[C_\gamma + \ln(kl_e/2) + C_{int}(2kl_e) - 2C_{int}(kl_e)]\Big\} \end{aligned} \tag{2.19}$$

$$\begin{aligned} X_m = \frac{\eta}{4\pi}\Big\{ & 2S_{int}(kl_e) + \cos(kl_e)[2S_{int}(kl_e) - S_{int}(2kl_e)] \\ & - \sin(kl_e)[2C_{int}(kl_e) - C_{int}(2kl_e) - C_{int}(\frac{2ka^2}{l_e})]\Big\}, \end{aligned} \tag{2.20}$$

where C_γ is the Euler's constant, C_{int} and S_{int} are the cosine and sine integrals for a given point, respectively. They are defined as:

$$C_\gamma = 0.5772 \tag{2.21}$$

$$C_{int}(x) = \int_0^x \cos(x)dx \tag{2.22}$$

$$S_{int}(x) = \int_0^x \sin(x)dx \tag{2.23}$$

Let us recall the monopole antenna with length L. Then, its input impedance is equal to the half of the corresponding to the equivalent dipole of length $l_e = 2L$, due to the electric model equivalency illustrated in Fig. 2.2 Also, the impedance related to the input is related to the one referred to at the maximum current through the factor $\sin^2(kl_e/2)$ [24]. Therefore, the input impedance Z_{in} of a monopole antenna with length L is defined as: [24]:

$$Z_{in} = R_{in} + jX_{in} = \frac{R_m}{2\sin^2(kl_e/2)} + j\frac{X_m}{2\sin^2(kl_e/2)} \tag{2.24}$$

Evaluation for a $\lambda/4$ monopole

For $\lambda/4$ monopole antennas, where $\theta \in [0, \pi/2]$, the E-fields are:

$$E_\theta \approx \frac{j\eta I_0\ e^{-jkr}}{2\pi r}\ \Big[\frac{\cos(\frac{\pi}{2}\cos\theta)}{\sin\theta}\Big] \tag{2.25a}$$

$$E_\phi \approx 0 \tag{2.25b}$$

The input impedance is computed from (2.24) as follows:

$$R_m = \frac{1}{2}\frac{\eta}{2\pi}[-C_{int}(\pi) + 0.5772 - \ln(2\pi)] = 36.56478 \approx 36.56\ \Omega \tag{2.26a}$$

$$X_m = \frac{1}{2}\frac{\eta}{4\pi}[2S_{int}(\pi) - 2S_{int}(\pi) + S_{int}(2\pi)] = 15S_{int}(2\pi) = 21.27\ \Omega \tag{2.26b}$$

$$Z_{in} = (R_m + jX_m)/\sin^2(\pi/2) = 36.56 + j21.27\ \Omega \tag{2.26c}$$

The radiation patterns of the $\lambda/4$ monopole over an infinite ground plane are displayed in Fig. 2.3. The overlapping plots between the model and simulation confirm the theory explained so far. As observed, modeling wired monopole antennas are possible using the auxiliary potential vectors and the image theory. Nonetheless, this model needs to be complemented with more powerful modeling strategies for finite ground planes, and thick wires, such as using the integral equations [80] and the diffraction theory [81].

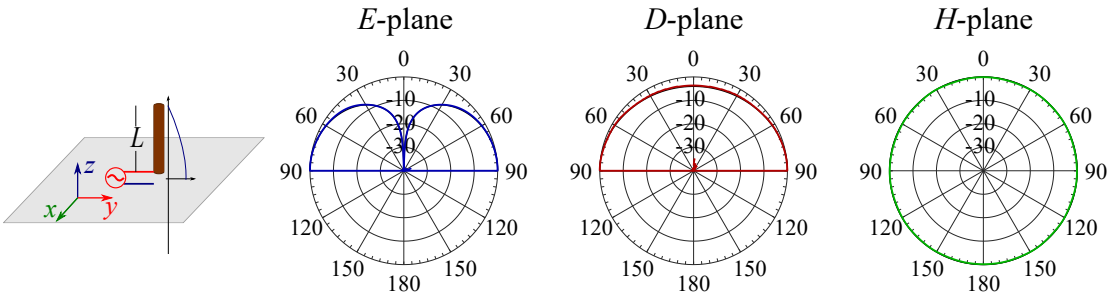

Figure 2.3: Radiation patterns of a $\lambda/4$ monopole on an infinite ground plane. The modeled (black) and simulated (colored) radiation patterns (E_θ) show a great agreement between them.

2.2.2 Dipole

The wired linear dipole is probably the most fundamental and studied antenna. Since the invention of wired telegraphy by Joseph Henry in 1842 [82], wired antennas have been gaining more relevance in radar and communication systems through the next decades. From the wired dipole, several variants have emerged, including reconfigurable dipole antennas [83], multiple-iteration fractal dipoles [84], wide-band tri-polarized antennas [85], and folded dipoles based on metamaterials [86]. Furthermore, there have been a progressive interest and necessity in deepening the dipole study [24, 87, 88] for a wide range of applications, e.g., ground-penetrating and vehicular radars, UWB communication systems, surveillance systems, imaging [88].

Modeling strategy

The current distribution of this antenna obeys the solution of solving the integral equation created from the statement that there is a charge distribution that creates a given electric potential, which is constant to 1 V in this case [24]. The mathematical solution of Pocklington's and Halle's integral equations for the current distribution over the wired configuration of the wired antenna provides a numerical solution to the charge distribution, which can be converted to the

current distribution. For very thin wired dipole antennas, (2.27) describes their current distribution I_z.

$$I_z = I_0 \sin\Big[k\Big(\frac{L}{2} - |z'|\Big)\Big] \;\forall z' \in \Big[-\frac{L}{2}; \frac{L}{2}\Big] \tag{2.27}$$

Radiated Fields

The dipole is conventionally oriented to the z-axis, and the formulation follows the same principle as the monopole formulation. However, when the dipole is horizontally oriented, i.e., aligned to the x-axis or y-axis, the mathematical formulations must follow the antenna's change of orientation by considering the coordinate system's unit vectors. Considering EM modeling for far-field zone, the approximations of (2.28a)–(2.28b) can be made [24]:

$$\text{Phase:} \qquad R \rightarrow \begin{cases} r - x' \;\sin\theta\cos\phi & \text{, for } x\text{-axis} \\ r - y' \;\sin\theta\sin\phi & \text{, for } y\text{-axis} \\ r - z' \;\cos\theta & \text{, for } z\text{-axis} \end{cases} \tag{2.28a}$$

$$\text{Amplitude:} \qquad R \rightarrow r \tag{2.28b}$$

For each dipole orientation, the radiated E-fields are calculated as follows:

- For the x-axis oriented dipole:

$$\mathbf{A}(x', y', z') = \frac{\mu}{4\pi}\int_{-L/2}^{L/2} I_0 \sin\Big[k\Big(\frac{L}{2} - |x'|\Big)\Big] \; \frac{e^{-jk\;(r - x'\sin\theta\cos\phi)}}{r}\, dx'$$

$$A_x = \frac{\mu I_0\; e^{-jkr}}{2\pi r k}\Big[\frac{\cos\Big(\frac{kL}{2}\sin\theta\cos\phi\Big) - \cos\Big(\frac{kL}{2}\Big)}{1 - \sin^2\theta\cos^2\phi}\Big] \tag{2.29}$$

$$\rightarrow A_\theta = \frac{\mu I_0\; e^{-jkr}}{2\pi r k}\Big[\frac{\cos\Big(\frac{kL}{2}\sin\theta\cos\phi\Big) - \cos\Big(\frac{kL}{2}\Big)}{1 - \sin^2\theta\cos^2\phi}\Big]\cos\theta\cos\phi \tag{2.30a}$$

$$A_\phi = -\frac{\mu I_0\; e^{-jkr}}{2\pi r k}\Big[\frac{\cos\Big(\frac{kL}{2}\sin\theta\cos\phi\Big) - \cos\Big(\frac{kL}{2}\Big)}{1 - \sin^2\theta\cos^2\phi}\Big]\sin\phi \tag{2.30b}$$

Therefore,

$$E_\theta \approx -\frac{j\eta I_0\ e^{-jkr}}{2\pi r}\ \Big[\frac{\cos\left(\frac{kL}{2}\sin\theta\cos\phi\right)-\cos\left(\frac{kL}{2}\right)}{1-\sin^2\theta\cos^2\phi}\Big]\cos\theta\cos\phi \tag{2.31a}$$

$$E_\phi \approx \frac{j\eta I_0\ e^{-jkr}}{2\pi r}\ \Big[\frac{\cos\left(\frac{kL}{2}\sin\theta\cos\phi\right)-\cos\left(\frac{kL}{2}\right)}{1-\sin^2\theta\cos^2\phi}\Big]\sin\phi \tag{2.31b}$$

- For the y-axis oriented dipole:

$$\mathbf{A}(x',y',z') = \frac{\mu}{4\pi}\int_{-L/2}^{L/2} I_0\sin\Big[k\big(\frac{L}{2}-|y'|\big)\Big]\ \frac{e^{-jk\ (r-y'\sin\theta\sin\phi)}}{r}\,dy'$$

$$A_y = \frac{\mu I_0\ e^{-jkr}}{2\pi rk}\ \Big[\frac{\cos\left(\frac{kL}{2}\sin\theta\sin\phi\right)-\cos\left(\frac{kL}{2}\right)}{1-\sin^2\theta\sin^2\phi}\Big] \tag{2.32}$$

$$\rightarrow A_\theta = \frac{\mu I_0\ e^{-jkr}}{2\pi rk}\ \Big[\frac{\cos\left(\frac{kL}{2}\sin\theta\sin\phi\right)-\cos\left(\frac{kL}{2}\right)}{1-\sin^2\theta\sin^2\phi}\Big]\cos\theta\sin\phi \tag{2.33a}$$

$$A_\phi = \frac{\mu I_0\ e^{-jkr}}{2\pi rk}\ \Big[\frac{\cos\left(\frac{kL}{2}\sin\theta\sin\phi\right)-\cos\left(\frac{kL}{2}\right)}{1-\sin^2\theta\sin^2\phi}\Big]\cos\phi \tag{2.33b}$$

$$\therefore E_\theta \approx -\frac{j\eta I_0\ e^{-jkr}}{2\pi r}\ \Big[\frac{\cos\left(\frac{kL}{2}\sin\theta\sin\phi\right)-\cos\left(\frac{kL}{2}\right)}{1-\sin^2\theta\sin^2\phi}\Big]\cos\theta\sin\phi \tag{2.34a}$$

$$E_\phi \approx -\frac{j\eta I_0\ e^{-jkr}}{2\pi r}\ \Big[\frac{\cos\left(\frac{kL}{2}\sin\theta\sin\phi\right)-\cos\left(\frac{kL}{2}\right)}{1-\sin^2\theta\sin^2\phi}\Big]\cos\phi \tag{2.34b}$$

- For the z-axis oriented dipole:

$$\mathbf{A}(x',y',z') = \frac{\mu}{4\pi}\int_{-L/2}^{L/2} I_0\sin\Big[k\big(\frac{L}{2}-|z'|\big)\Big]\ \frac{e^{-jk\ (r-z'\cos\theta)}}{r}dz',$$

$$A_z = \frac{\mu I_0\ e^{-jkr}}{2\pi rk}\ \Big[\frac{\cos\left(\frac{kL}{2}\cos\theta\right)-\cos\left(\frac{kL}{2}\right)}{\sin^2\theta}\Big] \tag{2.35}$$

$$\rightarrow A_\theta = \frac{-\mu I_0\ e^{-jkr}}{2\pi rk}\ \left[\frac{\cos\left(\frac{kL}{2}\cos\theta\right)-\cos\left(\frac{kL}{2}\right)}{\sin\theta}\right] \tag{2.36}$$

$$\therefore E_\theta \approx \frac{j\eta I_0\ e^{-jkr}}{2\pi r}\ \left[\frac{\cos\left(\frac{kL}{2}\cos\theta\right)-\cos\left(\frac{kL}{2}\right)}{\sin\theta}\right] \tag{2.37}$$

Input Impedance

As a linearly wired antenna, the model formulation for dipoles is the same as in monopoles, with the only difference of not being half as in the previous case. This means that the calculation of the input impedance can be computed as in (2.38) and (2.19)–(2.20), where $k = 2\pi/\lambda$, and $l_e = L$.

$$Z_{in} = R_{in} + jX_{in} = (R_m + jX_m)\csc^2(kL/2) \tag{2.38}$$

Evaluation for $\lambda/2$ and $5\lambda/4$ dipoles

The expressions for the E- and H-fields in the z-axis oriented dipole antennas can be reduced to the results shown in Table 2.2. The impedance response for both dipole antennas is plotted in Fig. 2.4.

Table 2.2: E-field and input impedance for $\lambda/2$ and $5\lambda/4$ dipole antennas.

Variable	Value for $\lambda = 0.5\lambda$	Value for $\lambda = 1.25\lambda$
E_θ	$\frac{j\eta I_0\ e^{-jkr}}{2\pi r}\left[\frac{\cos\left(\frac{\pi}{2}\cos\theta\right)}{\sin\theta}\right]$	$\frac{j\eta I_0\ e^{-jkr}}{2\pi r}\left[\frac{\cos\left(\frac{5\pi}{4}\cos\theta\right)-\frac{\sqrt{2}}{2}}{\sin\theta}\right]$
Z_{in}	73.13+j42.54 Ω	213-j374 Ω

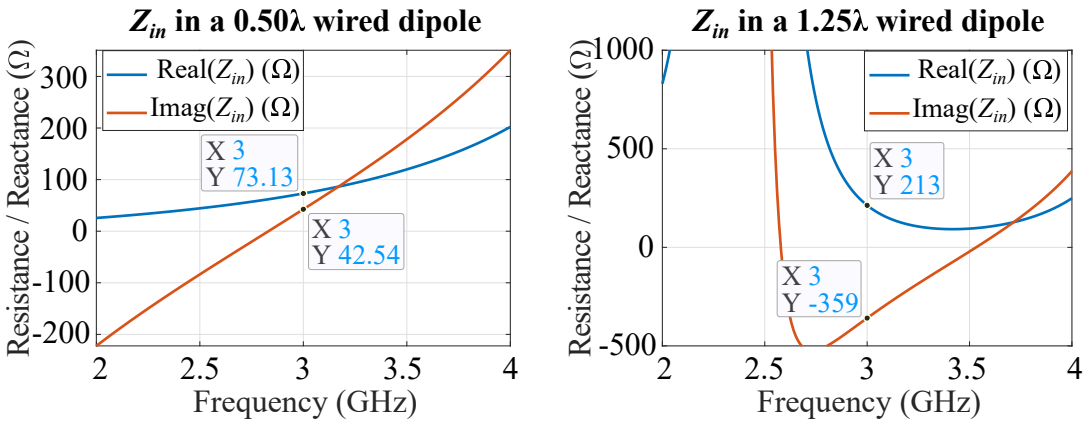

Figure 2.4: Impedance response of a $\lambda/2$ and $5\lambda/4$ wired dipole antenna. The dipoles' modeled impedance response is calculated for λ at 3 GHz.

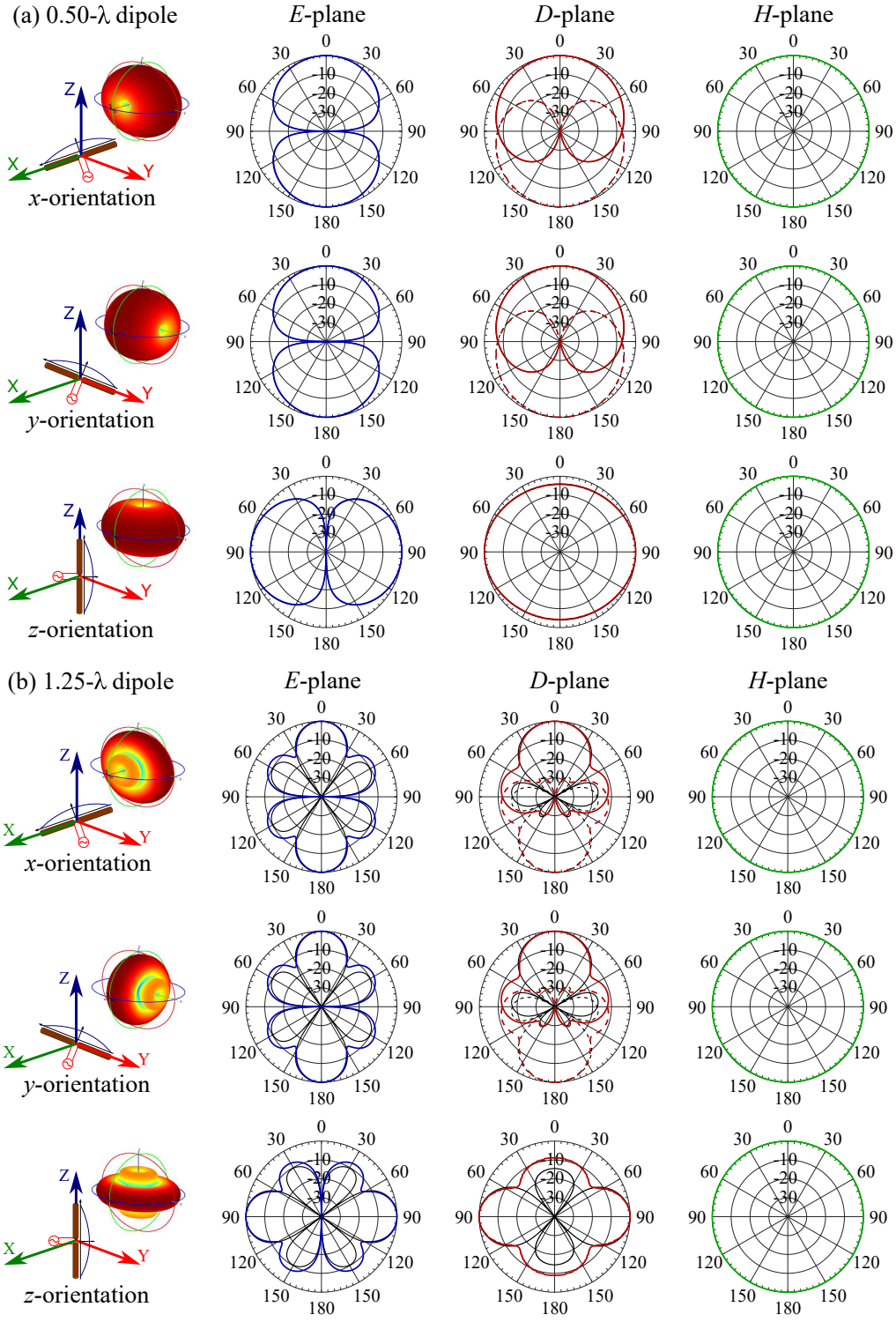

Figure 2.5: Radiation patterns of a $\lambda/2$ and $5\lambda/4$ dipole antenna. Comparison between modeled (black) and simulated (colored) radiation patterns (E_θ) in the E-, D-, and H- planes. The $\lambda/2$ (a) and $5\lambda/4$ (b) dipole antennas have x-, y-, and z- orientations. Wavelengths calculated at 3 GHz.

The two dipole antennas with different lengths produced the same three-dimensional radiation patterns, independently of the orientation, as observed in each case of Fig. 2.5. As expected from the equations, side lobes are present in dipole antennas with a length greater than λ. From the comparison between modeling and simulation, pictured in Fig. 2.5, it is noticed that the model matches the simulation in the direction of maximum propagation. However, it shows minor discrepancies in the side lobes, whose magnitudes are significantly lower than in the main lobe. Because of the uniform field distribution in the H-plane, the radiation patterns coincide perfectly as a circular shape and do not have side lobes. The presented EM models for linear wired antennas show the utility of the mathematical tools listed in Section 2.1. The expressed formulations will be further explored and analyzed for slot antennas.

2.3 Slot Antenna

Slot antennas are one of the most popular aperture antennas [24]. The easy fabrication, the tremendous capability for band broadening, and the light wind load make it very attractive in radar applications [31]. Modeling this antenna is supported on the formulations of wired antennas, especially on the impedance estimation, because of Babinet's principle [24]. The EM model for this antenna also constitutes the baseline for MSPA modeling, emphasizing the radiated fields and the geometrical equivalences from Huygens's principle [77]. Modeling this antenna is performed based on the equivalent model theorem, obtaining the equivalent superficial current densities $\mathbf{J}_s$ and $\mathbf{M}_s$. The x-polarized electric field $\mathbf{E}_{ax}$ over the aperture generated by a slot of length L and width W is defined as follows:

$$\mathbf{E_{ax}} = E_0\hat{\mathbf{i}}, \forall\ |x| \leq \frac{W}{2} \text{and}\ |y| \leq \frac{L}{2} \tag{2.39}$$

Based on the equivalent surface theorem [24], the electric field in the slot and magnetic and electric current densities can replace the geometry of the antenna, $\mathbf{M_s}$ and $\mathbf{J_s}$, respectively. They depend on the presence of electric or magnetic fields inside the aperture, respectively, and considering that outside the slot, there is an infinite perfect conductor, the image theory and the far-field equations can be applied. Thus, for the electric field $\mathbf{E_{ax}}$ inside the aperture, and assuming $\mathbf{H_{ax}} = 0$.

$$\mathbf{M_s} = -2\hat{\mathbf{n}} \times \mathbf{E_{ax}} = -2\hat{\mathbf{k}} \times E_0\hat{\mathbf{i}} = -2E_0\hat{\mathbf{j}} \tag{2.40a}$$

$$\mathbf{J_s} = \quad 2\hat{\mathbf{n}} \times \mathbf{H_{ax}} = 0 \tag{2.40b}$$

For the magnetic-current source derived in (2.40a), the electric auxiliary vector potential $\mathbf{F}$ is expressed as follows:

$$\mathbf{F}(x,y,z) = \frac{\varepsilon}{4\pi}\iint_{S'} \mathbf{J_s}(x',y',z')\frac{e^{-jkR}}{R}\,dS' \tag{2.41}$$

Then, the following far-field approximations are made: [24]

$$\begin{aligned} \text{Phase:} \qquad R &\to r - \mathbf{r'}\cdot\hat{\mathbf{r}} \\ &= r - (x',y',z')\cdot(\sin\theta\cos\phi, \sin\theta\sin\phi, \cos\theta) \\ &= r - (x'\sin\theta\cos\phi + y'\sin\theta\sin\phi) \end{aligned} \tag{2.42a}$$

$$\text{Amplitude:} \qquad R \to r \tag{2.42b}$$

Therefore,

$$\begin{aligned} \mathbf{F}(x,y,z) &= \frac{\varepsilon}{4\pi}\iint_{S'} \mathbf{M_s}(x',y',z')\frac{e^{-jk(r-\mathbf{r'}\cdot\hat{\mathbf{r}})}}{r}\,dS' \\ &= \frac{\varepsilon e^{-jkr}}{4\pi r}\iint_{S'} \mathbf{M_s}(x',y',z')e^{jkr'\mathbf{r'}\cdot\hat{\mathbf{r}}}\,dS' = \frac{\varepsilon e^{-jkr}}{4\pi r}\mathbf{L}(x,y,z) \end{aligned} \tag{2.43a}$$

The only component of $\mathbf{L}$ is expressed as:

$$L_y = \iint_{S'} M_y \; e^{jk\mathbf{r'}\cdot\hat{\mathbf{r}}} \, dS'$$
$$= (-2E_0)\frac{\sin\left(kW\frac{\sin\theta\cos\phi}{2}\right)}{kW\frac{\sin\theta\cos\phi}{2}}\frac{\sin\left(kL\frac{\sin\theta\sin\phi}{2}\right)}{kL\frac{\sin\theta\sin\phi}{2}} = (-2E_0) \;\; K_L \tag{2.44}$$

Rewriting to the spherical coordinate system:

$$L_\theta = \cos\theta\sin\phi \; L_y = -2E_0\cos\theta\sin\phi \; K_L \tag{2.45a}$$
$$L_\phi = \qquad \cos\phi \; L_y = -2E_0\cos\phi \; K_L \tag{2.45b}$$

Consequently, the radiated fields are:

$$E_\theta \approx -\frac{j\omega\eta\varepsilon e^{-jkr}}{4\pi r}L_\phi = \quad \frac{jke^{-jkr}}{2\pi r}E_0\cos\phi \; K_L \tag{2.46a}$$
$$E_\phi \approx \quad \frac{j\omega\eta\varepsilon e^{-jkr}}{4\pi r}L_\theta = -\frac{jke^{-jkr}}{2\pi r}E_0\cos\theta\sin\phi \; K_L \tag{2.46b}$$
$$H_\theta \approx -\frac{j\omega\varepsilon e^{-jkr}}{4\pi r} \; L_\theta = \quad \frac{jke^{-jkr}}{2\pi\eta r} \; E_0\cos\theta\sin\phi \; K_L \tag{2.46c}$$
$$H_\phi \approx -\frac{j\omega\varepsilon e^{-jkr}}{4\pi r} \; L_\phi = \quad \frac{jke^{-jkr}}{2\pi\eta r} \; E_0\cos\phi \; K_L \qquad , \tag{2.46d}$$

where:

$$K_L = \mathrm{sa}\left(kW\frac{\sin\theta\cos\phi}{2}\right)\mathrm{sa}\left(kL\frac{\sin\theta\sin\phi}{2}\right) \tag{2.47}$$
$$\mathrm{sa}(x) = \frac{\sin x}{x} \tag{2.48}$$

2.3.1 Radiated Fields

Since the slot antenna is placed in the xy plane, the E-field components E_θ and E_ϕ are not zero. Then, a polarization definition needs to be applied to transform E_θ and E_ϕ into new values E_{co} and E_{cr}. They represent the co-polar and cross-polar components of the E-field, respectively. Among the various polarization

definitions in the literature [89], the third Ludwig's definition [90] is one of the most popular formulations used to quantify polarization. According to this definition, the values of E_{co} and E_{cr} are expressed as [90]:

$$E_{co} = E_\theta \cos\phi - E_\phi \sin\phi \tag{2.49a}$$

$$E_{cr} = E_\theta \sin\phi + E_\phi \cos\phi \tag{2.49b}$$

A 3-GHz x-oriented slot antenna is designed with a 1.7-mm thick FR4 substrate on an infinite ground plane and aperture dimensions of 2.5 mm (0.025λ) by 50 mm (0.5λ). The excitation is located around 17 mm from the $-y$-axis side, getting contact between the 50-mm sides. The radiation patterns are computed and compared with simulated antennas in Ansys™ HFSS, all normalized from -40 dB to 0 dB. This comparison is provided in Fig. 2.6. The main planes considered are: E- ($\phi = \pi/2$), H- ($\phi = 0$) and D- ($\phi = \pi/4$).

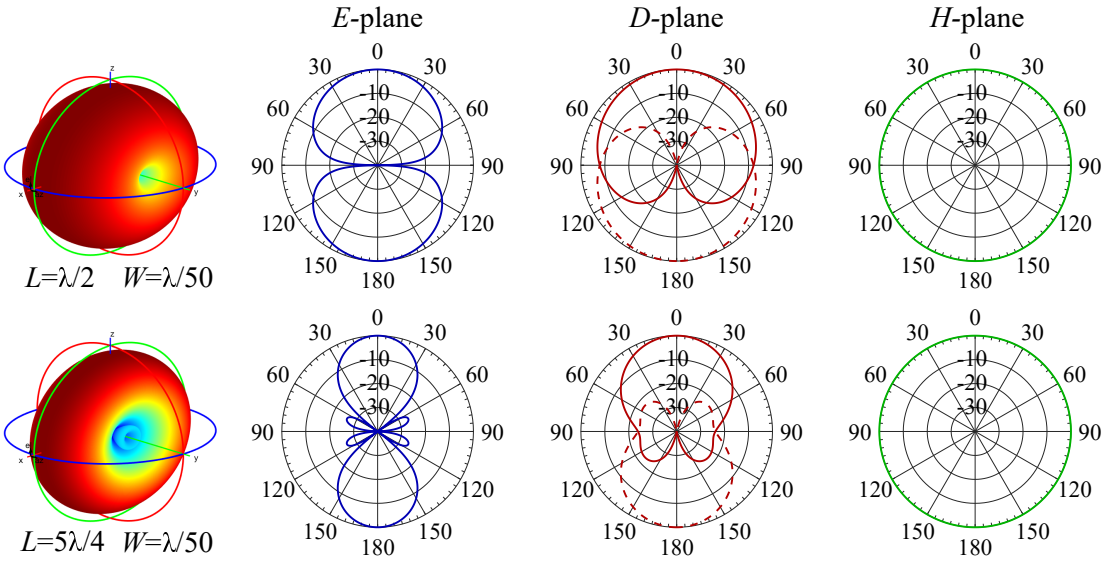

Figure 2.6: Radiation patterns for a $\lambda/2$ and $5\lambda/4$ slot antenna.
Modeled radiation patterns for a y-oriented slot antenna with x-polarized inner E-fields. The wavelengths and the radiation pattern in 3D, and in the E-, D- and H-planes are calculated at 3 GHz. Substrate thickness set to 1.7 mm.

2.3.2 Input Impedance

From Babinet's principle [24], the slot antenna is complementary to the wired linear dipole. The impedance of a slot antenna Z_s is related to the impedance of a wired dipole antenna Z_d. The complementary dipole has the same length as the slot's largest dimension, while the slot's shortest dimension is paper-thin, as in the wire width of the dipole. Then, the input impedance of a slot antenna Z_s is expressed as in (2.50), where Z_d can be calculated from (2.38). This relation is restricted for flat and very thin conductors, where the ground plane's dimensions are at least several times the slot's length.

$$Z_s = \frac{1}{4}\frac{\eta^2}{/}Z_d \tag{2.50}$$

Then, the input impedance of a $\lambda/2$ slot antenna is $363 - j211\ \Omega$. For the $5\lambda/4$ slot, the impedance is $51.8 + 77.2\ \Omega$. The impedance response of both antennas is plotted in Fig. 2.7.

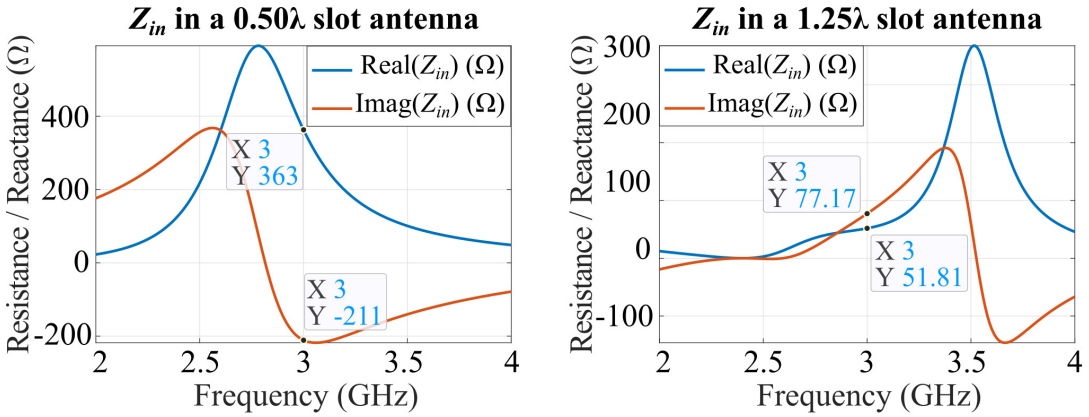

Figure 2.7: Impedance response of a $\lambda/2$ and $5\lambda/4$ slot antenna.
The modeled impedance response of slot antennas is related to the electrically complementary dipole of the same size. Antenna designed in the S-band.

2.4 Microstrip Patch Antennas (MSPAs)

MSPAs have been widely used in several applications, including mobile phones, radar, and base stations [15, 32]. Their compactness, lightweight, low profile, polarization diversity, and easy fabrication make this antenna appealing, despite the low power handling capability and the likelihood of warpage in PTFE substrates. Besides, the typically narrow (1 %–5 %) impedance bandwidth of MSPAs has been improved up to around 40 % by developing geometrical and electrical strategies [40, 55].

An MSPA comprises a small conductive surface over a dielectric substrate and a ground plane, as depicted in Fig. 2.9. This conductive surface is called *patch* and can have various shapes. A rectangular MSPA is characterized by the patch of dimensions L (length) and W (width), a substrate with thickness h and dielectric constant ε_r, and a perfectly conductive and infinite ground plane. For practical effects, the patch length is typically around $0.5\lambda/\sqrt{\varepsilon_r}$, and the ground plane is many times larger than the patch. In addition, lossy materials are present in real MSPA, which are described by the substrate's loss tangent $\tan\delta$ and the patch's bulk conductivity σ. The feeding is positioned at the coordinate point (x_0, y_0).

Modeling this antenna involves several equivalences, for instance, Huygens's principle, the image theory, and the geometrical reductions due to symmetry. Also, modeling MSPA requires accurate characterization of the impact of the field distribution over the volume on the radiating fields and impedance response. Then, this section covers diverse models and formulations available from previous work that have provided advances in EM modeling for MSPAs in RF and microwaves.

2.4.1 Cavity Model

This model [24, 41, 91] states that the rectangular patch of dimensions L and W, and the ground plane, are the top and bottom faces of a resonant cavity, which sides are determined by the perimeter of the patch. An illustration of this cavity can be found in Fig. 2.8. Because of the charge distribution on the patch, the side walls can be modeled as perfect magnetic conductors (PMC) [24]. The top and bottom faces are considered perfect electric conductors (PEC). These boundaries define the propagation modes and their respective resonant frequency inside the cavity. Finite conductivity is then considered as a loss factor, expressed in the cavity's quality factor.

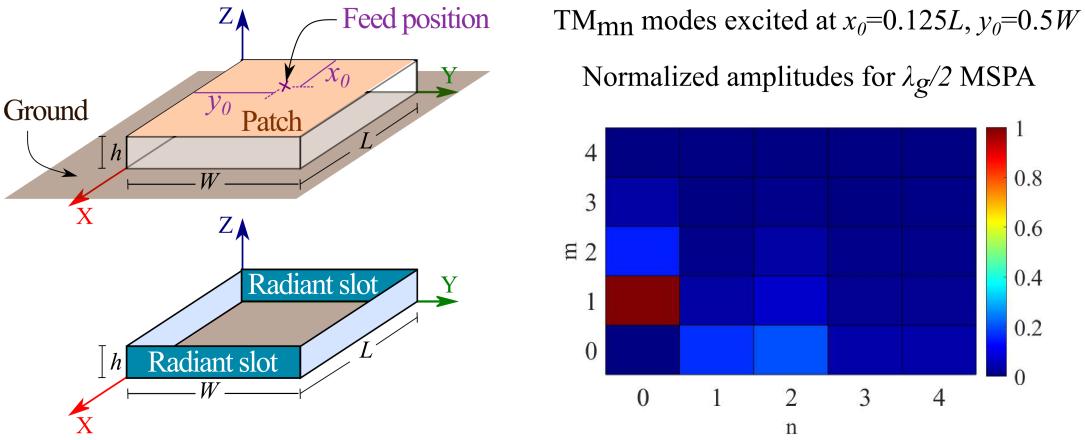

Figure 2.8: Cavity model for microstrip patch antennas.
The patch and the ground plane form a resonant cavity, where the patch perimeter determines the sides. This model explains the field propagation modes, the radiation mechanism, and the patch resonance.

This physical model explains the field distribution inside the volume created by the cavity under the patch and mathematically characterizes the resonance of the dominant propagation mode TM_{01}. Modeling the fields inside the cavity requires using the boundary conditions at the PEC and PMC walls and solving the auxiliary vector potentials. Defining the cavity's resonant frequency and quality factor gives its characterization.

Modeling the EM fields inside the cavity

The formulation of the EM fields can be written in full extension from (2.8a)–(2.8b) for a given set of potentials $\mathbf{A}$ and $\mathbf{F}$. By decomposing the fields in rectangular coordinates, they are expressed as:

$$E_x = -j\omega A_x - j\frac{1}{\omega\mu\varepsilon}\left(\frac{\partial^2 A_x}{\partial x^2} + \frac{\partial^2 A_y}{\partial x \partial y} + \frac{\partial^2 A_z}{\partial x \partial z}\right) - \frac{1}{\varepsilon}\left(\frac{\partial F_z}{\partial y} - \frac{\partial F_y}{\partial z}\right) \tag{2.51a}$$

$$E_y = -j\omega A_y - j\frac{1}{\omega\mu\varepsilon}\left(\frac{\partial^2 A_x}{\partial x \partial y} + \frac{\partial^2 A_y}{\partial y^2} + \frac{\partial^2 A_z}{\partial y \partial z}\right) - \frac{1}{\varepsilon}\left(\frac{\partial F_x}{\partial z} - \frac{\partial F_z}{\partial x}\right) \tag{2.51b}$$

$$E_z = -j\omega A_z - j\frac{1}{\omega\mu\varepsilon}\left(\frac{\partial^2 A_x}{\partial x \partial z} + \frac{\partial^2 A_y}{\partial y \partial z} + \frac{\partial^2 A_z}{\partial z^2}\right) - \frac{1}{\varepsilon}\left(\frac{\partial F_y}{\partial x} - \frac{\partial F_x}{\partial y}\right) \tag{2.51c}$$

$$H_x = -j\omega F_x - j\frac{1}{\omega\mu\varepsilon}\left(\frac{\partial^2 F_x}{\partial x^2} + \frac{\partial^2 F_y}{\partial x \partial y} + \frac{\partial^2 F_z}{\partial x \partial z}\right) + \frac{1}{\mu}\left(\frac{\partial A_z}{\partial y} - \frac{\partial A_y}{\partial z}\right) \tag{2.51d}$$

$$H_y = -j\omega F_y - j\frac{1}{\omega\mu\varepsilon}\left(\frac{\partial^2 F_x}{\partial x \partial y} + \frac{\partial^2 F_y}{\partial y^2} + \frac{\partial^2 F_z}{\partial y \partial z}\right) + \frac{1}{\mu}\left(\frac{\partial A_x}{\partial z} - \frac{\partial A_z}{\partial x}\right) \tag{2.51e}$$

$$H_z = -j\omega F_z - j\frac{1}{\omega\mu\varepsilon}\left(\frac{\partial^2 F_x}{\partial x \partial z} + \frac{\partial^2 F_y}{\partial y \partial z} + \frac{\partial^2 F_z}{\partial z^2}\right) + \frac{1}{\mu}\left(\frac{\partial A_y}{\partial x} - \frac{\partial A_x}{\partial y}\right) \tag{2.51f}$$

Due to the geometrical placement of the patch in the xy plane, the fields are TM^z, meaning that the z component of the magnetic field is zero. Hence, (2.51f) terms have to accomplish the following conditions to achieve $H_z = 0$, without annulling the other components, in (2.51a)–(2.51e). Therefore, the vector potentials have the form $\mathbf{A} = A_z\,\hat{\mathbf{k}}$ and $\mathbf{F} = \mathbf{0}$.

Since the potential $\mathbf{A}$ has a single component, A_z can be found by solving (2.52) by following the separate-variable function technique [77]. The function A_z and the propagation constant k are then defined in (2.53)–(2.54).

$$\nabla^2 A_z + k^2 A_z = 0 \tag{2.52}$$

$$A_z(x, y, z) = a_{z_1}(x) a_{z_2}(y) a_{z_3}(z) \tag{2.53}$$

$$k^2 = k_x^2 + k_y^2 + k_z^2 \tag{2.54}$$

The solution of (2.52) is expressed as:

$$A_z = (C_1\cos(k_x x) + D_1\sin(k_x x))(C_2\cos(k_y y) + D_2\sin(k_y y)) \\ (C_3\cos(k_z z) + D_3\sin(k_z z)) \quad (2.55)$$

Thus, replacing (2.55) in (2.51a)–(2.51f) the following expressions are obtained for the EM fields inside the cavity:

$$E_x = -j\frac{1}{\omega\mu\varepsilon}\frac{\partial^2 A_z}{\partial x\partial z} = -j\omega\frac{k_x k_z}{k^2}(-C_1\sin(k_x x) + D_1\cos(k_x x)) \\ (C_2\cos(k_y y) + D_2\sin(k_y y))(-C_3\sin(k_z z) + D_3\cos(k_z z)) \quad (2.56a)$$

$$E_y = -j\frac{1}{\omega\mu\varepsilon}\frac{\partial^2 A_z}{\partial y\partial z} = -j\omega\frac{k_y k_z}{k^2}(C_1\cos(k_x x) + D_1\sin(k_x x)) \\ (-C_2\sin(k_y y) + D_2\cos(k_y y))(-C_3\sin(k_z z) + D_3\cos(k_z z)) \quad (2.56b)$$

$$E_z = -j\omega A_z - j\frac{1}{\omega\mu\varepsilon}\frac{\partial^2 A_z}{\partial z^2} = j\omega\left(\frac{k_z^2}{k^2} - 1\right)(C_1\cos(k_x x) + D_1\sin(k_x x)) \\ (C_2\cos(k_y y) + D_2\sin(k_y y))(C_3\cos(k_z z) + D_3\sin(k_z z)) \quad (2.56c)$$

$$H_x = \frac{1}{\mu}\frac{\partial A_z}{\partial y} = \frac{k_y}{\mu}(C_1\cos(k_x x) + D_1\sin(k_x x)) \\ (-C_2\sin(k_y y) + D_2\cos(k_y y))(C_3\cos(k_z z) + D_3\sin(k_z z)) \quad (2.56d)$$

$$H_y = -\frac{1}{\mu}\frac{\partial A_z}{\partial x} = -\frac{k_x}{\mu}(-C_1\sin(k_x x) + D_1\cos(k_x x)) \\ (C_2\cos(k_y y) + D_2\sin(k_y y))(C_3\cos(k_z z) + D_3\sin(k_z z)) \quad (2.56e)$$

$$H_z = 0 \quad (2.56f)$$

Considering the cavity shown in Fig. 2.8, the boundary conditions are applied for the electric field components and the cavity faces. The top and bottom faces are made of perfect electric conductors (PEC), and the lateral sides are made of perfect magnetic conductors (PMC), or at least very near these ideal materials.

Then, $\hat{\mathbf{n}} \times \mathbf{E} = 0$ in PEC and $\hat{\mathbf{n}} \times \mathbf{H} = 0$ in PMC, where $\hat{\mathbf{n}}$ is the normal vector to each face and $\mathbf{E}$, $\mathbf{H}$ are the EM fields in these boundaries, at an infinitesimal distance from each face. Then, the condition equations are the following:

- Bottom (PEC): $z = 0 : -\hat{\mathbf{k}} \times \mathbf{E} = 0 \rightarrow E_x = E_y = 0$

$$E_x|_{z=0} = 0 \text{ and } E_y|_{z=0} = 0 \rightarrow D_3 = 0 \tag{2.57}$$

- Top (PEC): $z = h : \quad \hat{\mathbf{k}} \times \mathbf{E} = 0 \rightarrow E_x = E_y = 0$

$$E_x|_{z=h} = 0 \text{ and } E_y|_{z=h} = 0 \rightarrow C_3 \sin(k_z h) = 0 \therefore k_z = \frac{p\pi}{h} \tag{2.58}$$

- Left (PMC): $y = 0 : -\hat{\mathbf{j}} \times \mathbf{H} = 0 \rightarrow H_x = H_z = 0$

$$H_x|_{y=0} = 0 \rightarrow D_2 = 0 \tag{2.59a}$$

$$H_z|_{y=0} = 0, \quad \text{Already satisfied by TM}^z \tag{2.59b}$$

- Right (PMC): $y = W : \quad \hat{\mathbf{j}} \times \mathbf{H} = 0 \rightarrow H_x = H_z = 0$

$$H_x|_{y=W} = 0 \rightarrow C_2 \sin(k_y W) = 0 \rightarrow k_y = \frac{n\pi}{W} \tag{2.60a}$$

$$H_z|_{y=W} = 0, \quad \text{Already satisfied by TM}^z \tag{2.60b}$$

- Front (PMC): $x = 0 : \quad \hat{\mathbf{i}} \times \mathbf{H} = 0 \rightarrow H_y = H_z = 0$

$$H_y|_{x=0} = 0 \rightarrow D_1 = 0 \tag{2.61a}$$

$$H_z|_{x=0} = 0, \quad \text{Already satisfied by TM}^z \tag{2.61b}$$

- Back (PMC): $x = L : -\hat{\mathbf{i}} \times \mathbf{H} = 0 \rightarrow H_y = H_z = 0$

$$H_y|_{x=L} = 0 \rightarrow C_1 \sin(k_x L) = 0 \rightarrow k_x = \frac{m\pi}{L} \tag{2.62a}$$

$$H_z|_{x=L} = 0, \quad \text{Already satisfied by TM}^z \tag{2.62b}$$

Now, the electromagnetic field is completely defined inside. Rewriting the field components in (2.56a)–(2.56f) by using the constraints in (2.57)–(2.62b), and considering $C_{mnp} = C_1C_2C_3$, the field components are:

$$E_x = -j\omega\frac{k_xk_z}{k^2}C_{mnp}\sin(k_xx)\cos(k_yy)\sin(k_zz) \tag{2.63a}$$

$$E_y = -j\omega\frac{k_yk_z}{k^2}C_{mnp}\cos(k_xx)\sin(k_yy)\sin(k_zz) \tag{2.63b}$$

$$E_z = -j\omega\left(1-\frac{k_z^2}{k^2}\right)C_{mnp}\cos(k_xx)\cos(k_yy)\cos(k_zz) \tag{2.63c}$$

$$H_x = -\frac{k_y}{\mu}C_{mnp}\cos(k_xx)\sin(k_yy)\cos(k_zz) \tag{2.63d}$$

$$H_y = \frac{k_x}{\mu}C_{mnp}\sin(k_xx)\cos(k_yy)\cos(k_zz) \tag{2.63e}$$

$$H_z = 0 \tag{2.63f}$$

In these equations, k_x, k_y, k_z have been calculated in (2.58),(2.60a),(2.62a) and making $(m,n,p) = \mathbb{N}^3 - (0,0,0)$. Furthermore, it is observed that the field expressions can have different response ways or configurations, called *modes*. Depending on the dimensions of the cavity, these modes can have different resonant frequencies, as shown in (2.64).

The resonant frequency is influenced by the squared inverse of each dimension, so as a greater dimension is had, the less resonant frequency is produced.

$$f_{r_{mnp}} = \frac{1}{2\pi\sqrt{\mu\varepsilon}}\sqrt{\left(\frac{m\pi}{L}\right)^2+\left(\frac{n\pi}{W}\right)^2+\left(\frac{p\pi}{h}\right)^2} \tag{2.64}$$

The propagation mode with the lowest resonant frequency is also known as *dominant mode*, which is the mode TM^z_{100} $(m=1, n=0, p=0)$ in the MSPA cavity model. Since the resonant frequency of this mode is mostly influenced by the cavity's greatest dimension, L, then the propagation constants per axis are expressed as $k_x = \pi/L$, and $k_y = k_z = 0$.

Consequently,

$$E_x = E_y = H_x = H_z = 0 \tag{2.65a}$$

$$E_z = -j\omega\left(1 - \frac{k_z^2}{k^2}\right) C_{mnp} \cos(k_x x) \cos(k_y y) \cos(k_z z) = E_a \cos\left(\frac{\pi x}{L}\right) \tag{2.65b}$$

$$H_y = \frac{k_x}{\mu} C_{mnp} \sin(k_x x) \cos(k_y y) \cos(k_z z) = H_a \sin\left(\frac{\pi x}{L}\right) \tag{2.65c}$$

These EM fields are defined and valid inside the cavity. A complete formulation for the fields can be acquired by considering higher-order modes described in the following lines. Also, the expressions obtained above will be used in Section 2.4.3 to model the radiating fields for MSPAs.

Characterizing the cavity as a resonator

Making a generalization of the field distribution over the cavity and considering a feeding excitation point (x_0, y_0) and a probe of effective cross-sectional dimensions d_x and d_y, the following expression can be written [41]:

$$E_z(x, y) = jI_0 Z_0 k \sum_{m=0} \sum_{n=0} \frac{\Psi_{mn}(x, y)\Psi_{mn}(x_0, y_0)}{k^2 - k_{mn}^2} G_{mn}, \tag{2.66}$$

where $k = \omega\sqrt{\mu\varepsilon}$, $k_m = m\pi/L$, $k_n = n\pi/W$, $k_{mn}^2 = k_m^2 + k_n^2$, and the functions G_{mn}, Ψ_{mn}, and χ_{mn} are defined as follows [41]:

$$G_{mn} = \mathrm{sa}\left(\frac{m\pi d_x}{2L}\right) \mathrm{sa}\left(\frac{n\pi d_y}{2W}\right) \tag{2.67}$$

$$\Psi_{mn} = \frac{\chi_{mn}}{\sqrt{LW}} \cos k_m x \cos k_n y \tag{2.68}$$

$$\chi_{mn} = \sqrt{2}^{\,\mathrm{sign}(m+n)}, \ \forall\ m, n \in \mathbb{N} \tag{2.69}$$

This formulation provides an overview of the propagation modes of a patch and the corresponding intensities. An illustration of this overview is provided in the normalized-amplitude mesh plot in Fig. 2.8 for an excitation point at $x_0 = L/8$, and $y_0 = W/2$, and probe with diameter $d_x = d_y = \lambda/100$. The amplitudes of the

different modes are dependent on the feeding location. The best predominance of the mode TM_{10} occurs where the feed is located along the patch's length and when $y_0 = W/2$.

A direct consequence of modeling the patch as a cavity is its characterization through the resonant frequency and the quality factor through mathematical definitions. They are listed as follows:

- Resonant frequency

  A cavity with length L, width W and height h, where $L > W > h$, has a resonance frequency for the TM_{10} that can be calculated by evaluating (2.64) with $m = 1, n = 0, p = 0$. Nonetheless, the resonance of the dominant mode in a patch antenna occurs at a higher frequency. This frequency shift is due to the effect of the fringing fields that exist on the patch edges. To accurately this shift, a factor q_f is included, so the resonant frequency can be rewritten as in (2.70) [41]. As seen in Section 2.4.2, the transmission line model includes a more detailed formulation of the effect of the fringing fields that supports this frequency shift.

  $$f_r = q_f \frac{c_0}{2L\sqrt{\varepsilon_r}}, \tag{2.70}$$

- Quality factor

  In the cavity model, the losses are considered by introducing the concept of effective loss-tangent $\tan\delta_{eff}$. This loss parameter is slightly higher than the substrate's loss-tangent $\tan\delta$, and includes the losses done by the finite conductivity of the patch, the patch radiation, and the surface waves. Then, the quality factor Q_p of the resonant cavity can be obtained as in (2.71). The transmission line model explains more about the ohmic losses; thus, it provides more formulation about the quality factor of a patch.

  $$Q_p = (\tan\delta_{eff})^{-1} \tag{2.71}$$

As observed, the cavity model provides a realistic characterization of the propagation mode properties, gives the foundations to model the radiation of this antenna, and establishes the modeling basis for the patch as a resonator. Nonetheless, this model is limited in estimating the impedance response since the cavity does not radiate power, and the model predicts energy storage, i.e., purely reactive impedance. The transmission line model addresses this limitation, as seen in the following lines in Section 2.4.2.

2.4.2 Transmission Line Model

Considering the MSPA geometry of Fig. 2.9, the transmission line (TL) model [24, 41, 43] postulates that a rectangular patch can be modeled as a couple of microstrip TLs terminated in admittance loads. The characteristic impedance of these TLs is defined by the patch width W, substrate thickness h, and dielectric constant ε_r. Also, the length of both lines is equivalent to the patch's length L. An overview of this model is illustrated in Fig. 2.9. This model delivers a unique insight into the antenna's impedance as a behavioral parameter that can be modeled using the electric circuit theory. This section explains the formulation of the patch's edge conductance and the inclusion of the patch's fringing fields in the resonant frequency.

Patch edge conductance

As demonstrated later in Section 2.4.3, the radiation of an MSPA effectively comes from the two faces below the patch edges facing each other and separates a distance L. They are illustrated in Fig. 2.8 and 2.9, which are known as *radiating slots*. In the transmission line model, they are represented as edge admittances $G + jB$, considered loads in a circuit made of microstrip lines.

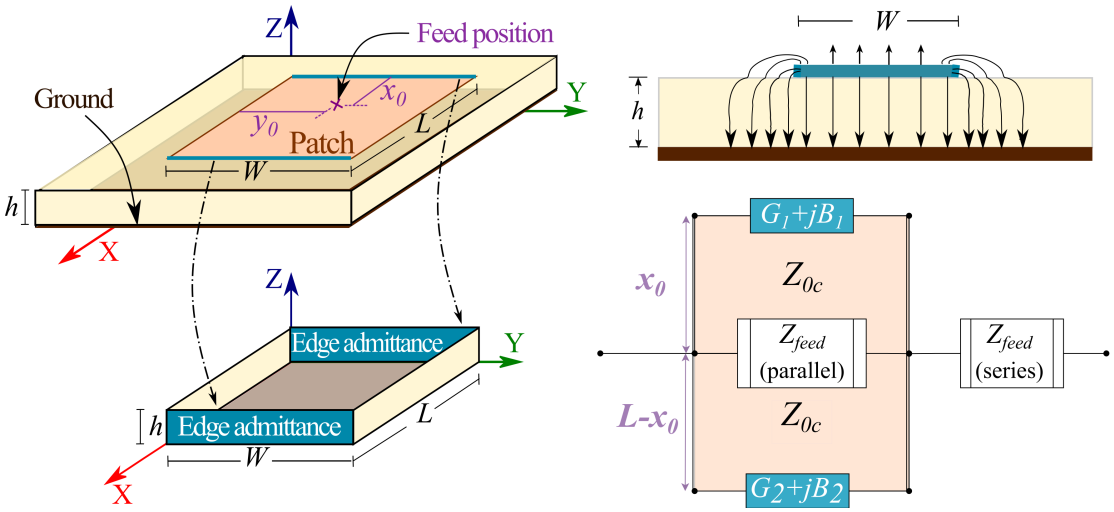

Figure 2.9: Transmission line model for microstrip patch antennas.
The two radiating slots form the longitudinal delimiters of a microstrip transmission line, where the characteristic impedance is determined by the patch width and substrate electrical properties. This model explains the patch's edge resistance and the effects of the fringe fields, and it considers an impedance contribution from the antenna feed.

Given two edge admittances, they can be written as $Y_1 = G_1 + jB_1$ and $Y_2 = G_2 + jB_2$. Since they are congruent, then $Y_2 = Y_1, G_2 = G_1, B_2 = B_1$. Previous work shows that these admittances can be calculated as [24]:

$$G_1 = \frac{W}{120\lambda_0}\left[1 - \frac{1}{24}(k_0 h)^2\right], \qquad \frac{h}{\lambda_0} < \frac{1}{10} \tag{2.72a}$$

$$B_1 = \frac{W}{120\lambda_0}[1 - 0.636 \ln k_0 h], \qquad \frac{h}{\lambda_0} < \frac{1}{10} \tag{2.72b}$$

Depending on the feeding type and location, these two admittances can be processed differently. The feed can have an impedance connected in parallel or series with the transmission lines. This is illustrated in Fig. 2.9. As it will be explored in Section 2.4.4, an inset feeding contributes with an inductance in series with the transmission lines and no parallel components. Therefore, the two admittances can be processed directly by the distance they are separated.

Typically, the patch length L is designed to be around 180 degrees in electrical length, i.e., half of the guided wavelength. This setup can be considered to compute the patch impedance Z_p^i from the two edge admittances as follows:

$$Z_p^i = \frac{1}{Y_p^i} = \frac{1}{Y_1^i + Y_2^i} = \frac{1}{Y_1 - Y_2} = \frac{1}{2G_1} \tag{2.73}$$

However, since the two slots are coupled [24], then a term G_{21} can be included to update the patch impedance value to Z_p as:

$$Z_p(x_0 = 0) = \frac{1}{2(G_1 + G_{21})} \tag{2.74}$$

$$Z_p(x_0) = Z_p(x_0 = 0) f(x_0) \tag{2.75}$$

This formulation introduces the concept of patch input impedance, while the equivalent circuit considers the feed's impedance. The function $f(x_0) \in [0; 1]$ makes the patch impedance a variable over the feeding position and compared with its maximum value $Z_p(x_0 = 0)$. A more detailed discussion of the patch impedance estimation is provided in Section 2.4.4.

Fringing effects

Since the patch dimensions are finite and small compared with the ground plane, the E-field lines get fringed near the edges. Also, some of the E-field lines departing from the patch's top face travel through the air before passing through the dielectric and hitting the ground plane.

The cavity model showed that the patch resonates at a frequency higher than the one produced with the physical dimensions of the patch's cavity because of the fringing fields. An effective length and permittivity are required to account for this effect. Different models have been developed [24, 92, 93]. The most common are the ones expressed in (2.76)–(2.77) [24].

- Effective dielectric constant (ε_{eff}):

  The concept of effective dielectric constant [24, 92] was defined to account for the effect of the E-field mixture along the air and substrate layers. For a given patch of width W over a substrate of thickness h and dielectric constant ε_r, the value of ε_{eff} is between 1 and ε_r, expressed as:

$$\varepsilon_{eff} = \frac{\varepsilon_r + 1}{2} + \frac{\varepsilon_r - 1}{2}\left[1 + 12\frac{h}{W}\right]^{-1/2} \tag{2.76}$$

- Additional length to account for the effect of the fringing fields (ΔL):

  The fringing effects can be considered by including an additional length ΔL that adds to the patch's physical length L. The value of ΔL using the Hammerstad's model is given in (2.77), and the patch's effective length L_e is then written in (2.78).

$$\Delta L = h\left[0.412\frac{(\varepsilon_{eff} + 0.300)(\frac{W}{h} + 0.264)}{(\varepsilon_{eff} - 0.258)(\frac{W}{h} + 0.800)}\right] \tag{2.77}$$

$$L_e = L + 2\Delta L \tag{2.78}$$

  Consequently, the patch's resonant frequency can be reformulated from the cavity model and rewritten with the effective dielectric constant and patch length. Thus, (2.70) can now be expressed as:

$$f_r = \frac{c_0}{2L_e\sqrt{\varepsilon_{eff}}}, \tag{2.79}$$

  Even though these equations are easy to implement and provide a fast estimate with errors of less than 5 %, they are limited to paper-thin substrates, less than 0.05 times the free-space wavelength, RF frequencies usually less than 10 GHz, and for a limited range of permittivity and relation W/h. More complex and

complete models for calculating these two parameters (effective permittivity and fringing-effect additional length) will be discussed in Section 2.4.4.

As discussed, the transmission line model gives a complementary understanding of the behavior of MSPAs, providing explanations not found in the cavity model. Even though this model is less accurate than the cavity model [24], it provides essential formulations that are nowadays included in modern models. This model introduced the effective patch length and permittivity to account for the effect of the fringe fields and included the patch resistance and the feed impedance in an equivalent circuit. Hence, the transmission line model supplies the foundations of impedance response modeling, further explained in Section 2.4.4.

2.4.3 Modeling the Radiating Fields

Modeling MSPA radiation is based on the equivalent model theorem and the image theory (Section 2.1.4). From the inner fields in the patch neighborhoods, calculated in Section 2.4.1, it is possible to compute the superficial current densities $\mathbf{J}_s$ and $\mathbf{M}_s$ and then apply the far-field formulations (Section 2.1.3) to model the radiated fields.

Let us define the coordinate values (x', y', z') for the field source (antenna) and (x, y, z) for the free space. The four side slots are labeled and pictured in Fig. 2.10. Since the ground plane is infinite, the equivalent current densities $\mathbf{J}_s$ and $\mathbf{M}_s$ get doubled. Also, the normal vector $\hat{\mathbf{n}}$ is defined as the unit vector that points outside the cavity and is perpendicular to the corresponding slot. For the TM_{10} mode, the values of $\mathbf{J}_s$ and $\mathbf{M}_s$ are formulated for each slot as follows:

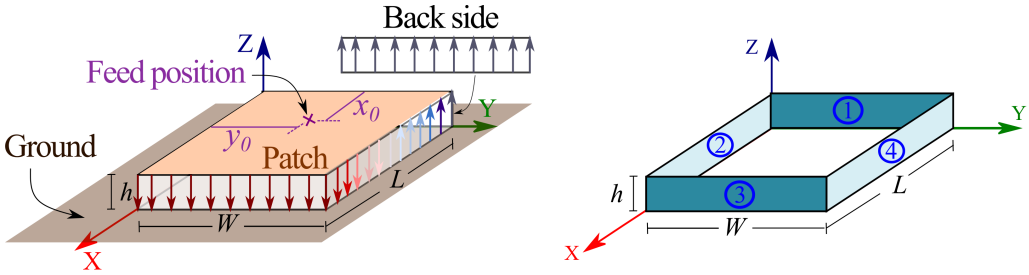

Figure 2.10: Equivalent slots for a microstrip patch antenna.
The field distribution (on the left) is defined from the cavity model, and the equivalent slots (on the right) define the radiating EM fields for MSPAs.

– Back slot ①: $x' = 0, \quad 0 \le y' \le W, \quad 0 \le z' \le h$

$$\mathbf{E}_{a1} = E|_{(x',y',z')\in①} = E_a\hat{\mathbf{k}} \tag{2.80a}$$

$$\mathbf{H}_{a1} = H|_{(x',y',z')\in①} = 0\hat{\mathbf{j}} \tag{2.80b}$$

$$\mathbf{M}_{s1} = -2\hat{\mathbf{n}} \times \mathbf{E}_{a1} = \quad 2\hat{\mathbf{i}} \times E_{a1}\hat{\mathbf{k}} = -2E_a\hat{\mathbf{j}} \tag{2.80c}$$

$$\mathbf{J}_{s1} = \quad 2\hat{\mathbf{n}} \times \mathbf{H}_{a1} = -2\hat{\mathbf{i}} \times 0\hat{\mathbf{j}} \quad = \quad \mathbf{0} \tag{2.80d}$$

– Left slot ②: $0 \le x \le L, \quad y = 0, \quad 0 \le z \le h$

$$\mathbf{E}_{a2} = E|_{(x',y',z')\in②} = E_a \cos\left(\frac{\pi x'}{L}\right)\hat{\mathbf{k}} \tag{2.81a}$$

$$\mathbf{H}_{a2} = H|_{(x',y',z')\in②} = H_a \sin\left(\frac{\pi x'}{L}\right)\hat{\mathbf{j}} \tag{2.81b}$$

$$\mathbf{M}_{s2} = -2\hat{\mathbf{n}} \times \mathbf{E}_{a2} = \quad 2\hat{\mathbf{j}} \times E_{a2}\hat{\mathbf{k}} \quad = 2E_a \cos\left(\frac{\pi x'}{L}\right)\hat{\mathbf{i}} \tag{2.81c}$$

$$\mathbf{J}_{s2} = \quad 2\hat{\mathbf{n}} \times \mathbf{H}_{a2} = -2\hat{\mathbf{j}} \times H_{a2}\hat{\mathbf{j}} \quad = \mathbf{0} \tag{2.81d}$$

– Front slot ③: $x = L, \quad 0 \le y \le W, \quad 0 \le z \le h$

$$\mathbf{E}_{a3} = E|_{(x',y',z')\in③} = -E_a\hat{\mathbf{k}} \tag{2.82a}$$

$$\mathbf{H}_{a3} = H|_{(x',y',z')\in③} = 0\hat{\mathbf{j}} \tag{2.82b}$$

$$\mathbf{M}_{s3} = -2\hat{\mathbf{n}} \times \mathbf{E}_{a3} = -2\hat{\mathbf{i}} \times E_{a3}\hat{\mathbf{k}} = -2E_a\hat{\mathbf{j}} \tag{2.82c}$$

$$\mathbf{J}_{s3} = \quad 2\hat{\mathbf{n}} \times \mathbf{H}_{a3} = \quad 2\hat{\mathbf{i}} \times 0\hat{\mathbf{j}} \quad = \quad \mathbf{0} \tag{2.82d}$$

– Right slot ④: $\quad 0 \le x \le L, \quad y = W, \quad 0 \le z \le h$

$$\mathbf{E}_{a4} = E|_{(x',y',z')\in④} = E_a \cos\left(\frac{\pi x'}{L}\right)\hat{\mathbf{k}} \tag{2.83a}$$

$$\mathbf{H}_{a4} = H|_{(x',y',z')\in④} = H_a \sin\left(\frac{\pi x'}{L}\right)\hat{\mathbf{j}} \tag{2.83b}$$

$$\mathbf{M}_{s4} = -2\hat{\mathbf{n}} \times \mathbf{E}_{a4} = -2\hat{\mathbf{j}} \times E_{a4}\hat{\mathbf{k}} \quad = -2E_a \cos\left(\frac{\pi x'}{L}\right)\hat{\mathbf{i}} \tag{2.83c}$$

$$\mathbf{J}_{s4} = \quad 2\hat{\mathbf{n}} \times \mathbf{H}_{a4} = \quad 2\hat{\mathbf{j}} \times H_{a4}\hat{\mathbf{j}} \quad = \quad \mathbf{0} \tag{2.83d}$$

Since the expressions above have the same shape as in the formulations for the slot antenna, modeling the radiating fields for MSPAs will follow a similar procedure. Therefore, the expression (2.43a) for the electric auxiliary potential $\mathbf{F}$ will be used. Moreover, the far-field approximations of (2.42a)-(2.42b) will be applied, adjusting them for the vertical structure of the slots. Then, the value of R in the far-field zone to phase corrections are:

$$\begin{aligned} R &\to r - (x', y', z').(\sin\theta\cos\phi, \sin\theta\sin\phi, \cos\theta) \\ &= \begin{cases} r - (x'\sin\theta\cos\phi + z'\cos\theta) & \text{, for slots ② and ④} \\ r - (y'\sin\theta\sin\phi + z'\cos\theta) & \text{, for slots ① and ③} \end{cases} \end{aligned} \tag{2.84a}$$

As the geometry of MSPAs for radiation purposes is equivalent to two pairs of vertical slot antennas, the number of calculations can be reduced to half if each pair is considered an antenna array. Let us define two identical antennas with separation vector $\mathbf{r}_\mathrm{s}$, where the main antenna is located at a position vector **r'**, then the position of the replicated antenna is expressed as in (2.85). Thus, the resulting relation between fields can then be expressed as in (2.86), which will be included in the upcoming formulations of the radiated fields.

$$\mathbf{r'}_\mathrm{i} = \mathbf{r'} + \mathbf{r}_\mathrm{s} \tag{2.85}$$

$$e^{-jkR} \approx e^{-jk(r-\mathbf{r'}_\mathrm{i}\cdot\hat{\mathbf{r}})} = e^{jk\mathbf{r}_\mathrm{S}\cdot\hat{\mathbf{r}}} e^{-jk(r-\mathbf{r'}\cdot\hat{\mathbf{r}})} \to \mathbf{E}_{(r_i)} = e^{jk\mathbf{r}_\mathrm{S}\cdot\hat{\mathbf{r}}}\mathbf{E}_{(r)} \tag{2.86}$$

Let us define the variables P_L, P_W, P_h, and $\Phi_T = P_L + P_W + P_h$, which relate the spherical coordinates and the MSPA dimensions:

$$P_L = (kL/2)\sin\theta\cos\phi \tag{2.87a}$$

$$P_W = (kW/2)\sin\theta\sin\phi \tag{2.87b}$$

$$P_h = (kh/2)\cos\theta \tag{2.87c}$$

Calculation of the electromagnetic fields

- For the slots (1) and (3): Length: W, height h.

$$\mathbf{M}_{s1} = \mathbf{M}_{s3} = \mathbf{M_s} = -2E_a\hat{\mathbf{j}} \tag{2.88a}$$

$$\mathbf{r_s} \;.\; \mathbf{r} = L\sin\theta\cos\phi \tag{2.88b}$$

The single component of the vector L, L_y is:

$$L_y = (1 + e^{j2P_L}) \iint_{S'} M_{sy}\; e^{jkr'\cos\psi}\, dS' = E_{A1}\cos(P_L)\,\mathrm{sa}(P_W)\,\mathrm{sa}(P_h) \tag{2.89a}$$

where $E_{a1} = -4E_aWhe^{j\mathbf{\Phi_T}}$.

These components in spherical coordinates have the following expressions:

$$L_\theta = \cos\theta\sin\phi L_y = E_{A1}\;\cos\theta\sin\phi\;\cos(P_L)\;\mathrm{sa}(P_W)\;\mathrm{sa}(P_h) \tag{2.90a}$$

$$L_\phi = \quad \cos\phi \quad L_y = E_{A1} \quad \cos\phi \quad \cos(P_L)\;\mathrm{sa}(P_W)\;\mathrm{sa}(P_h) \tag{2.90b}$$

Then, from (2.46a)–(2.46b), the far-field E-fields are expressed as listed:

$$E_{1\theta} \approx -\frac{jke^{-jkr}}{4\pi r}E_{A1}\;\cos\phi\;\cos(P_L)\;\mathrm{sa}(P_W)\;\mathrm{sa}(P_h) \tag{2.91a}$$

$$E_{1\phi} \approx \quad \frac{jke^{-jkr}}{4\pi r}E_{A1}\;\cos\theta\sin\phi\;\cos(P_L)\;\mathrm{sa}(P_W)\;\mathrm{sa}(P_h) \tag{2.91b}$$

- For the slots (2) and (4): Length: L, height h.

$$\mathbf{M}_{s2} = -\mathbf{M}_{s4} = \mathbf{M_s} = 2E_a \cos\Big(\frac{\pi x'}{L}\Big)\hat{\mathbf{i}} \tag{2.92a}$$

$$\mathbf{r_s} \;.\; \mathbf{r} = W \sin\theta \sin\phi \tag{2.92b}$$

The component L_x of the vector L in rectangular coordinates is:

$$L_x = (1 - e^{j2P_W}) \iint_{S'} M_{sx}\; e^{jkr' \cos\psi}\, dS' = E_{A2} \cos(P_L) \sin(P_W)\, \mathrm{sa}(P_h) \tag{2.93a}$$

where $E_{A2} = 4e^{j\mathbf{\Phi_T}} E_a h L P_L/[P_L^2 - (\pi/2)^2] = 4e^{j\mathbf{\Phi_T}} E_a h L^*$. The variable L^* is an equivalent length defined for representation purposes.

The conversion to spherical coordinates delivers:

$$L_\theta = \cos\theta\cos\phi L_x = \quad E_{A2}\;\; \cos\theta\cos\phi\;\; \cos(P_L)\;\; \sin(P_W)\;\; \mathrm{sinc}(P_h) \tag{2.94a}$$

$$L_\phi = \quad -\sin\phi L_x = -E_{A2} \quad \sin\phi \quad \cos(P_L)\;\; \sin(P_W)\;\; \mathrm{sinc}(P_h) \tag{2.94b}$$

Therefore, the far-field EM fields are expressed as listed:

$$E_{2\theta} \approx \quad \frac{jke^{-jkr}}{4\pi r} E_{A2}\;\; \sin\phi\;\; \cos(P_L)\;\; \sin(P_W)\;\; \mathrm{sinc}(P_h) \tag{2.95a}$$

$$E_{2\phi} \approx \quad \frac{jke^{-jkr}}{4\pi r} E_{A2}\;\; \cos\theta\cos\phi\;\; \cos(P_L)\;\; \sin(P_W)\;\; \mathrm{sinc}(P_h) \tag{2.95b}$$

The next step is to sum the E-fields from both slot pairs. From (2.91a)–(2.91b) and (2.95a)–(2.95b), the factor $E_a L$ can be expressed as V_0.

Consequently, combining all these fields and performing the factorization where necessary, the following expressions are gotten for the E-field:

$$E_\theta \approx \frac{jke^{-jkr} V_0 e^{j\mathbf{\Phi_T}}}{\pi r}(L^* \sin\phi \sin P_W + W\cos\phi\, \mathrm{sa}\, P_W)\cos P_L\, \mathrm{sa}\, P_h \tag{2.96a}$$

$$E_\phi \approx \frac{jke^{-jkr} V_0 e^{j\mathbf{\Phi_T}}}{\pi r}(L^* \cos\phi \sin P_W - W\sin\phi\, \mathrm{sa}\, P_W)\cos P_L\, \mathrm{sa}\, P_h \cos\theta \tag{2.96b}$$

In these expressions, the first term of the sum corresponds to the fields produced by the slots ② and ④, while the second one to the slots ① and ③, as they also have the coefficients L^* and W, respectively. Then, by applying the polarization definitions of (2.49a)–(2.49b), the radiation patterns for this antenna are obtained, as displayed in Fig. 2.11.

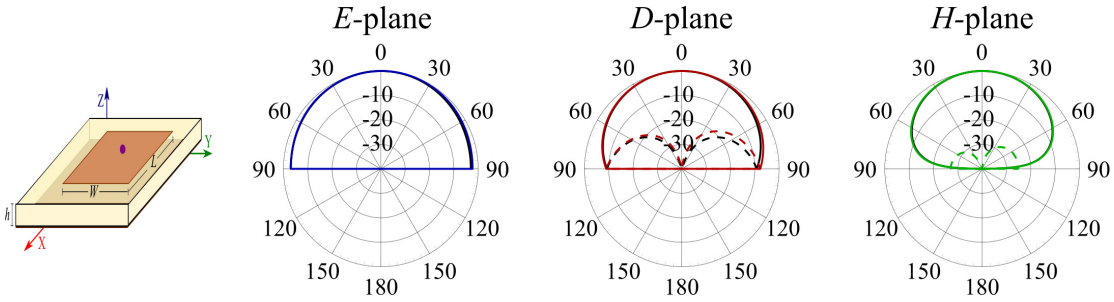

Figure 2.11: Normalized radiation patterns for MSPA with probe feeding. The third Ludwig polarization definition [90] has been used to plot the above radiation patterns. The formulations in (2.96a)–(2.96b) and the simulated radiation patterns have a good agreement in the three main planes.

2.4.4 Modeling the Input Impedance

The impedance response for MSPAs can be modeled using both the cavity model and the transmission line model, which have been enhanced for increased accuracy. Associating the impedance response modeling with the electric circuit theory provides a powerful way to characterize this antenna in terms of formulation, reduced complexity, easy implementation, and more efficient inclusion of the physics that govern MSPAs.

Modeling the input impedance response involves analyzing the impedance produced by both the patch and the feeding structure. For MSPAs, there are four main feeding techniques; namely, probe [41], inset transmission line [45], aperture coupling [46], and proximity coupling [47]. These feeding structures are illustrated in Fig. 2.12 with their typically associated circuit models.

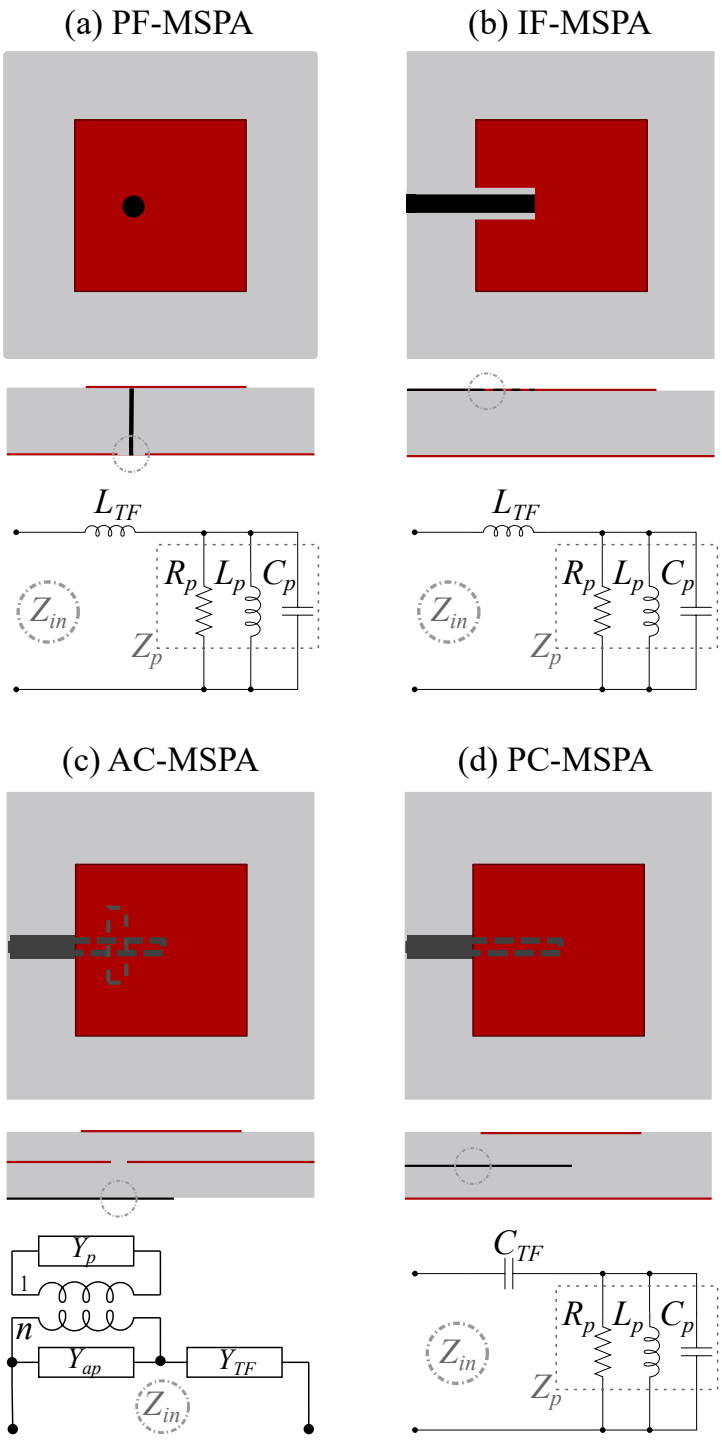

Figure 2.12: MSPAs' feeding structures and their typical equivalent circuits. Direct-contact feeding structures include the coaxial probe and the inset transmission line. The aperture-coupled and proximity-coupled feedings are contactless mechanisms. The former is the easiest to fabricate, and the latter is useful to minimize spurious radiation, despite the complex fabrication.

From the cavity model and the formulation in Section 2.4.1, it is observed that the patch is electromagnetically modeled as a resonator. Then, the impedance model is widely chosen [23, 24, 41, 42] to be a parallel RLC circuit, which is the resonator model in the electric circuits' theory.

The feeding contribution to the MSPA's input impedance depends on the associated geometry and electrical properties. How the feed is connected or coupled with the patch, and the ground plane plays an important role in modeling them. The following lines provide more details about the patch RLC resonator and the impedance models for direct-contact and coupling-based feeding structures.

For direct-contact feeding structures, such as probe feeding (PF) and inset feeding (IF), the impedance is typically modeled as an inductor in series with the RLC resonator [24, 41]. For coupled-based feeding structures, modeling the impedance is significantly more complex. Modeling the aperture-coupled (AC) feeding includes transformer conversion of admittances obtained from the transmission line model [23]. The feeding structure for proximity-coupled (PC) MSPAs is typically modeled as a capacitor connected in series with the patch's RLC resonator. However, as shown in Chapter 3, this capacitor is not enough to model this feeding mechanism accurately. Fig. 2.13 illustrates the impedance response for direct-contact and coupling-based MSPAs. It shows current models' capability to analytically characterize the input impedance of MSPAs from their geometry and electrical properties as input information.

2.4.4.1 Patch's Impedance: the RLC resonator

The patch RLC circuit is fully defined by the resonant resistance R_p, the resonant frequency f_{0p}, and the quality factor Q_p. The value of R_p is related to the maximum resonant resistance R_{pM} and the feed position x_0. Knowing the antenna

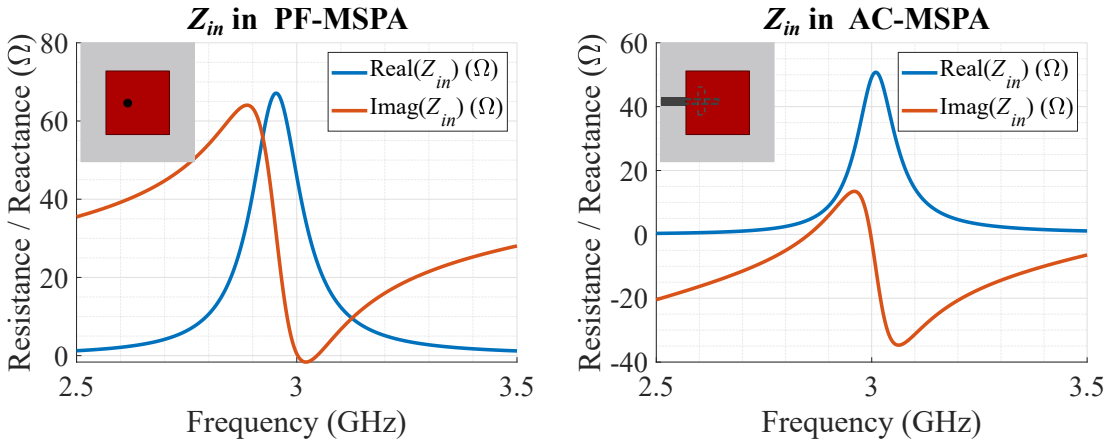

Figure 2.13: MSPAs' input impedance with two different feeding structures. (a) PF-MSPA with $L = W = 30.85$ mm, $\varepsilon_r = 2.2$, $h = 62$ mil, $x_0 = L/3$. (b) AC-MSPA with $L = W = 31.10$ mm, $\varepsilon_{ra} = 2.2$, $h = 60$ mil, aperture $L_a = 9$ mm $\times$ $W_a = 1.55$ mm, feed $x_0 = L/2$, $\varepsilon_{rf} = 3.66$, $h_f = 31$ mil, and stub $L_s = 9$ mm. The input reactance of MSPAs with direct-contact feeding structures is typically very inductive. For coupling-based MSPAs, the reactance can be inductive or capacitive.

dimensions considering the geometry of Fig. 2.8 and Fig. 2.9, the parameters f_{0p}, Q_p and R_{pM} can be obtained as follows:

Considering the patch as a microstrip transmission line of width W, over a substrate with thickness h and relative permittivity ε_r, the effective relative permittivity ε_{re} can be calculated as in (2.76) [24]. However, the effective value ε_{rep} used in patch design has been empirically determined to be:

$$\varepsilon_{rep} = 0.5\varepsilon_r + 0.5\varepsilon_{re}, \tag{2.97}$$

being this expression used in this proposed model henceforth. It is worth noting that (2.97) has been slightly modified from the original formulation $\varepsilon_{rep} = 0.7\varepsilon_r + 0.3\varepsilon_{re}$ [50] to get more accurate resonant frequencies compared with simulated PF-MSPAs, being the errors less than 2 % in both cases.

The value of the length extension ΔL to account for the effect of the fringe fields can be computed as on (2.77). However, a precise expression of ΔL is found

in [93] and listed in (2.98) as:

$$\Delta L = h\ \zeta_1\zeta_3\zeta_5/\zeta_4, \tag{2.98}$$

where

$$\zeta_1 = 0.4349\ \frac{\varepsilon_{rep}^{0.81} + 0.260}{\varepsilon_{rep}^{0.81} - 0.189}\ \frac{(W/h)^{0.8544} + 0.236}{(W/h)^{0.8544} + 0.870} \tag{2.99a}$$

$$\zeta_2 = 1 + \frac{(W/h)^{0.371}}{(1 + 2.358\varepsilon_r)} \tag{2.99b}$$

$$\zeta_3 = 1 + 0.5274\frac{\arctan\left[0.084(W/h)^{1.9413/\zeta_2}\right]}{\varepsilon_{rep}^{0.9236}} \tag{2.99c}$$

$$\zeta_4 = 1 + 0.0377\arctan\left(0.067(W/h)^{1.456}\right)[6 - 5e^{0.036(1-\varepsilon_r)}] \tag{2.99d}$$

$$\zeta_5 = 1 - 0.218e^{-7.5(W/h)} \tag{2.99e}$$

In addition, the value of ΔW can be obtained by using (2.98) where ζ_1 through ζ_5 can be calculated using (L/h_T) instead of (W/h_T). For square patch, $\Delta W = \Delta L$. Then, the effective length (L_e) and effective width of the patch (W_e) can be expressed as $L_e = L + 2\Delta L$ and $W_e = W + 2\Delta W$.

Thus, the resonant frequency of the RLC resonator is:

$$f_{0p} = \frac{c_0}{2L_e\sqrt{\varepsilon_{rep}}}, \tag{2.100}$$

where c_0 is the free-space speed of light. Hence, the wavelength (λ_{0p}) and the wave number (k_{0p}) at resonance are:

$$\lambda_{0p} = c_0/f_{0p} \tag{2.101a}$$

$$k_{0p} = 2\pi/\lambda_{0p} \tag{2.101b}$$

The resonator quality factor Q_p [49] can be calculated as in (2.102), considering the losses of the dielectric, the conductor, the radiation, and the surface waves through Q_d, Q_c, Q_{rad} and Q_{sw} in the following terms:

$$
\begin{aligned}
Q_p &= [Q_d^{-1} + Q_c^{-1} + (Q_{rad}^{-1} + Q_{sw}^{-1})]^{-1} \\
&= \left[\tan\delta + \frac{1}{h_T\sqrt{\pi f_{0p}\mu\sigma}} + \frac{16}{3}\frac{pc_1}{\varepsilon_r}\frac{h_T}{\lambda_{0p}}\frac{W_e}{L_e}\frac{1}{e_r^{hed}} \right]^{-1},
\end{aligned} \tag{2.102}
$$

where $\tan\delta$, μ, and σ are the substrate loss tangent, substrate relative permeability, and copper conductivity, respectively. The values of p, c_1 and e_r^{hed} in (2.102) are expressed as [49]:

$$
\begin{aligned}
p = 1 - \frac{1}{10^3}\big[&16.605(k_{0p}W_e)^2 - 0.229(k_{0p}W_e)^4 \\
&+ 18.283(k_{0p}L_e)^2 - 0.217(k_{0p}W_e)^2(k_{0p}L_e)^2\big]
\end{aligned} \tag{2.103a}
$$

$$
c_1 = 1 - 1/(\varepsilon_r\mu_r) + 0.4/(\varepsilon_r^2\mu_r^2) \tag{2.103b}
$$

$$
e_r^{hed} = \left[1 + \frac{3}{4}\pi\frac{k_{0p}h_T}{c_1}\Big(1 - \frac{1}{\varepsilon_r}\Big)^3\right]^{-1} \tag{2.103c}
$$

The resonant resistance R_p [49] is related to its maximum value R_{pM} [49] and the effective feed position $L_{0e} = L_0 + \Delta L$ along the patch effective length L_e, as expressed in (2.104b).

$$
R_{pM} = 4/\pi(\mu_r\eta_0)Q_p(L_e/W_e)(h_T/\lambda_{0p}) \tag{2.104a}
$$

$$
R_p = R_{pM}\cos^2\left(\pi\frac{L_{0e}}{L_e}\right) = R_{pM}\cos^2\left(\pi\frac{L_0 + \Delta L}{L + 2\Delta L}\right) \tag{2.104b}
$$

Therefore, the RLC components [49] for a rectangular patch are given as:

$$
R_p = R_{pM}\cos^2(\pi L_{0e}/L_e) \tag{2.105a}
$$

$$
L_p = \frac{R_p}{2\pi f_{0p}Q_p} \tag{2.105b}
$$

$$
C_p = \frac{Q_p}{2\pi f_{0p}R_p} \tag{2.105c}
$$

Then, the impedance of the patch Z_p can be calculated through the expression of (2.106). The impedance at resonance is $R_p + j0$. On the extremes of the

bandwidth, the impedance is $R_p/2 \pm jR_p/2$, happening at the frequencies $f_{0p}K_f^{\pm 1}$ where $K_f = 0.5[(1/Q_p) + \sqrt{4 + (1/Q_p)^2}]$.

$$Z_p = \frac{1}{{R_p}^{-1} + (j\omega L_p)^{-1} + j\omega C_p} \tag{2.106}$$

2.4.4.2 Direct-contact Feeding

For PF-MSPAs, the feeding probe adds an inductive reactance jX_{TF} that sums the impedance produced by the RLC resonator. The value of X_{TF} is expressed for a probe of radius a_f along a range of frequencies f as [94]:

$$X_{TF} = \frac{\eta k h_T}{2\pi}\Big[\ln\Big(\frac{2}{ka_f}\Big) - \gamma\Big]\cos^2\Big(\pi\rho(L_0, L, \Delta L)\Big) \tag{2.107}$$

where $\eta = 120\pi\sqrt{\mu_r/\varepsilon_r}\ \Omega$, $k = 2\pi f\sqrt{\varepsilon_r\mu_r}/c_0$, $\gamma = 0.5772$ and the function $\rho(L_0, L, \Delta L) = |L_0 - L/2|/(L + 2\Delta L)$. Thus, the inductance L_{TF} (Fig. 2.12a) can be calculated as in (2.108).

It is important to indicate that the formulas of (2.107)–(2.108) assume that the probe is electrically thin and the upper and lower planes are infinite.

$$L_{TF} = 200\mu_r h_T\Big[\ln\Big(\frac{2}{ka_f}\Big) - \gamma\Big]\cos^2\Big(\pi\rho(L_0, L, \Delta L)\Big)\text{nH} \tag{2.108}$$

Consequently, the impedance response Z_{in} of a PF-MSPA is expressed as:

$$Z_{in} = Z_p + j\omega L_{TF} = Z_p + jX_{TF} \tag{2.109}$$

For IF-MSPAs, the impedance response is computed by transforming Z_p with the inset feed of length L_f and characteristic impedance Z_{0T} as:

$$Z_{in} = Z_{0T}\frac{Z_p + jZ_{0T}\tan kl}{Z_{0T} + jZ_p\tan kl} \tag{2.110}$$

2.4.4.3 Coupling-based Feeding

For AC-MSPAs, modeling the impedance response is highly complex because of the non-uniform coupling effect between the aperture and the patch and between the aperture and the feed. The most accepted model nowadays is based on the modal expansion of the transmission line model. As shown in Fig. 2.12c, the equivalent circuit includes lumped admittances for the patch and aperture, an electric transformer, and a stub admittance conversion with transmission lines.

As seen in Fig. 2.12c, the feed ends in an open-circuit stub at a distance from the point on the same reference level as the coupling aperture. The reference level is illustrated in the dotted circle in the antenna geometry in Fig. 2.12c. Let us define the feed parameters –a microstrip transmission line– as follows: it has a width W_f, a length L_f, a stub of length L_s, and a characteristic impedance Z_{0f}. Then, the admittance of the stub seen from the reference level is expressed as [23]:

$$Z_{TF} = -jZ_{0s}\cot(kL_s + \Delta L) + 1/G_{0s}, \tag{2.111}$$

where ΔL is the field-fringing length increase, as expressed in (2.78) or (2.98), and G_{0s} is the open-end conductance, which can be computed by using (2.72a).

The coupling aperture presents an impedance that considers the effect of the magnetic-field coupling and the aperture's equivalent planar waveguide. Thus, the aperture admittance Y_{ap} is written as:

$$Y_{ap} = \frac{1}{2}\sum_{p,n}^{'} y_{pn}\frac{\left[\int_{s_a} f(y)\psi_{pn}\,dx\,dy\right]^2}{\int_s \psi_{pn}^2\,dy\,dz}, \tag{2.112}$$

where the notation $\sum_{p,n}^{'}$ means that the sum term for $p = 0, n = 0$ is not considered. The region s_a covers the aperture's surface of length L_a and width W_a, while the domain s encompasses the planar waveguide's effective width W_{ae} and height h. The patch is assumed to be placed on the xy plane for the integral

terminology. The functions y_{pn}, $f(y)$, and Ψ_{pn} are defined as:

$$y_{pn} = j\frac{k_0^2\varepsilon_{rfe} - (n\pi/W_{ae})^2}{\omega\mu\alpha_{pn}} \tag{2.113a}$$

$$f(y) = \begin{cases} \dfrac{1}{W_a} & \text{for } |y-y_0| \leq \dfrac{W_{ae}}{2} \\ \dfrac{1}{W_a}\dfrac{\sin[k_s(L_a/2 - |y-y_0|)]}{\sin[k_s(L_a - W_e/2)]} & \text{for } \dfrac{W_{ae}}{2} \leq |y-y_0| \leq \dfrac{L_a}{2} \end{cases} \tag{2.113b}$$

$$\psi_{pn} = \cos\left[\frac{p\pi}{h_f}(z+h+h_f)\right]\cos\left[\frac{n\pi}{W_{ae}}\left(y - y_0 + \frac{W_{ae}}{2}\right)\right] \tag{2.113c}$$

given an antenna substrate defined by its thickness h and dielectric constant ε_{ra}, and a feeding substrate characterized by its thickness h_f and dielectric constant ε_{rf}. By using (2.76), the corresponding effective dielectric constants can be expressed as ε_{rfa} and ε_{rfe}. The wave number k_0 considers propagation in the vacuum, while k_s is expressed as in (2.114a). The function α_{pn} is expressed as in (2.114b).

$$k_s = k_0\sqrt{\frac{\varepsilon_{ra} + \varepsilon_{rf}}{2}} \tag{2.114a}$$

$$\alpha_{pn} = \sqrt{\left(\frac{p\pi}{h_f}\right)^2 + \left(\frac{n\pi}{W_{ae}}\right)^2 - k_0^2\varepsilon_{rfe}} \tag{2.114b}$$

The patch's admittance Y_p can be evaluated as in (2.115), including the associated functions in (2.116)–(2.119):

$$\begin{aligned} Y_p = {} & \frac{1}{j\omega\mu}\frac{2W_a^2}{L_eW_e}\left[\frac{\omega^2\alpha_{m=0}^2}{2h}\sin^2\left(\frac{\pi x_0}{L_e}\right)\left\{\frac{1}{\omega_{01}'(\omega - \omega_{01}')} - \frac{1}{2\omega_{01}'^2}\right\}\right. \\ & \left. + \sum_{m,n}\frac{k_0^2\varepsilon_{rae} - (m\pi/W_e)^2}{\delta_m}\sin^2\left(\frac{n\pi x_0}{L_e}\right)\frac{\alpha_m^2\cos(k_zh)}{k_z\sin(k_zh)}\right], \\ & \forall(m,n) \in \mathbb{N}^2 - (0,1) \end{aligned} \tag{2.115}$$

$$\alpha_m = \int_0^{W_e} f(y)\cos(m\pi y/W_e)dy \tag{2.116}$$

$$\omega_{01}^{'} = \frac{c\pi}{a_e\sqrt{\varepsilon_{rae}}}\left(1 + \frac{1}{2Q_p}\right) \tag{2.117}$$

$$k_z = \sqrt{k_0^2\varepsilon_{rae} - (m\pi/b_e)^2 - (n\pi/a_e)^2} \tag{2.118}$$

$$\delta_m = 0.5^m, m \in \mathbb{N} \tag{2.119}$$

where ω is the angular frequency, $c = 3 \times 10^8$ m/s is the light speed at vacuum, and Q_p is the patch's quality factor (2.102) [49].

Therefore, the impedance response for AC-MSPAs is given by:

$$Z_{in} = \frac{T_{TF}(Y_{ap} + Y_p/n^2)}{T_{TF} + Y_{ap} + Y_p/n^2} \tag{2.120}$$

As observed in the mathematical formulation above, modeling the impedance for AC-MSPA is convoluted and is the only one that does not follow the structure RLC-feed in series, as with the other cases.

For PC-MSPAs, the feeding structure has been typically modeled as a capacitance in series with the RLC resonator that characterizes the patch. Previous work [24, 42, 51] states that this capacitance C_{TF}, as in Fig. 2.12d, comes from the parallel plates between the feed, the patch, and the ground plane. This concept will be analyzed in Chapter 3. As discussed in Section 3.2, the capacitance C_{TF} is not enough to accurately model these antennas.

2.4.5 Modeling the Impedance Bandwidth

Impedance matching results are crucial to maximize the realized gain in antennas, and MSPAs is not the exception. It is known that MSPAs typically have narrow bands, limiting their usage in broadband applications unless modifying the design to increase the impedance bandwidth. Modeling this parameter is relevant in antenna design since it allows the development of suitable design strategies to fit the antenna's bandwidth with its intended application.

The impedance bandwidth $\%BW$ for any antenna is related with its impedance response Z_{in} through the reflection coefficient or the S_{11} parameter. For a given complex impedance Z_{in} over frequency and a reference impedance Z_0, the complex value of S_{11} is expressed as [95]:

$$S_{11} = \frac{Z_{in} - Z_0}{Z_{in} + Z_0} \tag{2.121}$$

For MSPAs, Z_0 is typically set to 50 Ω by designing the feeding structure (coaxial line for PF-MSPAs, microstrip line for IF-MSPAs and AC-MSPAs, or embedded microstrip line for PC-MSPAs). Then, the logarithmic magnitude value of S_{11} (in decibels) is processed as $|S_{11}|$ (dB)$= 20\log_{10}|S_{11}|$. Since MSPAs are passive devices, the magnitude values of S_{11} do not exceed unity, meaning that the logarithmic value of its magnitude keeps negative over frequency. The impedance bandwidth can be then defined as the frequency interval where $|S_{11}|$ is less than -10 dB divided by the center frequency of such interval. Let be the frequencies f_1 and f_2 where $|S_{11}| < -10$ dB. Then, the percentage impedance bandwidth $\%BW$ is expressed as:

$$\%BW = \frac{f_2 - f_1}{(f_2 + f_1)/2} 100\% \tag{2.122}$$

Previous work shows different strategies to analytically model the impedance bandwidth for MSPAs as a behavioral parameter that depends on the antenna's geometrical and electrical properties. The upcoming lines review these strategies, while a more profound discussion is provided in Chapter 3, including a new modeling method to estimate the impedance bandwidth for PC-MSPAs.

Given a MSPA with the geometry of Fig. 2.8, with length L, width W, substrate thickness h and dielectric constant ε_r, operating at a frequency f with

efficiency e_r. Then, the wavelength and wave number can be calculated as in (2.101a)–(2.101b). The physical constants p and c_1 can be computed from (2.103a)–(2.103c). Then, the percent bandwidth can be estimated as follows:

- **Method 1: Non-linear with the patch squareness [58]**

$$\%BW = A_{BW} h/(\lambda_0\sqrt{\varepsilon_r})\sqrt{W/L} \tag{2.123a}$$

$$A_{BW} = \begin{cases} 180, & \text{if } h/(\lambda_0\sqrt{\varepsilon_r}) \leq 0.045 \\ 200, & \text{if } h/(\lambda_0\sqrt{\varepsilon_r}) \in [0.045, 0.075] \\ 220, & \text{if } h/(\lambda_0\sqrt{\varepsilon_r}) \geq 0.075 \end{cases} \tag{2.123b}$$

- **Method 2: Linear with the patch squareness [56]**

$$\%BW = \frac{16}{3\sqrt{2}} \frac{pc_1}{e_r \varepsilon_r} \frac{h}{\lambda_0} (W/L) \tag{2.124}$$

- **Method 3: Independent from the patch squareness [57]**

$$BW(\text{MHz}) = 4f(\text{GHz})^2 \frac{h(\text{in})}{1/32} \tag{2.125a}$$

$$\%BW = 12.8 f(\text{GHz})\ h(\text{in}) \tag{2.125b}$$

The average of these three formulations is computed. Then, a ratio between the percent bandwidth delivered by each method and the methods' average is calculated. A comparison of the average percent bandwidth estimation with these three methods is provided in Fig. 2.14 together with the normalized ratio for each method. A square MSPA is considered, having a size of 3 cm, at 6 GHz, over a substrate with dielectric constant $\varepsilon_r = 3.66$ and variable thickness up to 300 mils, and assuming 100 % efficiency. An increasing difference is observed with thicker substrates, which is not convenient for an accurate estimation of the impedance bandwidth of MSPAs. Besides, the feed plays an essential role in the bandwidth

performance of MSPAs. However, establishing a single formulation for MSPAs with any feeding structure is not accurate. Then, this work addresses this issue by providing a new formulation for the impedance bandwidth for PC-MSPAs, which have the best broadband capabilities.

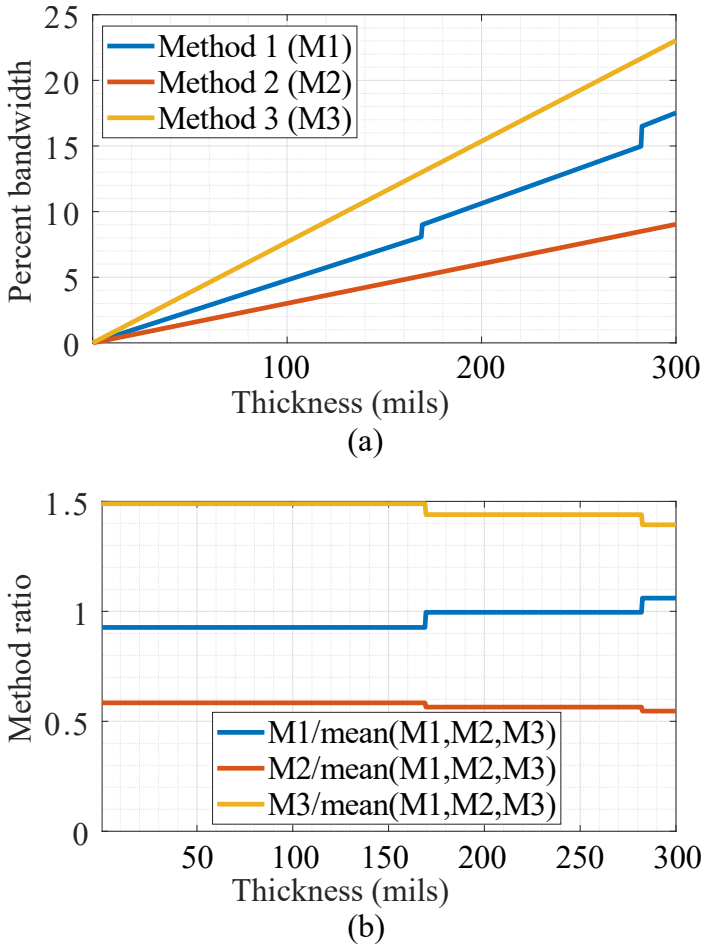

Figure 2.14: Comparison of bandwidth models for MSPAs.
Three methods from the available literature are evaluated and compared for 6-GHz square MSPA. (a) Computed values of the percentage impedance bandwidth with three methods from previous work [56–58]. (b) Comparison by ratio between each method's bandwidth and the average bandwidth from the three methods. The estimations diverge with the substrate thickness, having errors up to 50 % from the average.

2.5 Summary

This chapter has reviewed the essential formulations and previous work regarding EM modeling for MSPAs, including a review of the fundamental background in EM, wired antennas, and slot antennas. As explored, modeling MSPAs requires analyzing and formulating several phenomena that occur to these antennas, including the interaction with the feeding structure.

The pros and cons of current MSPA models can be listed as follows:

✓ The EM theorems can be applied as long as the ground plane behaves like a perfect electric conductor.

✓ The input impedance becomes straightforward to calculate once the circuit parameters are known.

✓ The impedance models based on electric circuits are intuitive and easy to be implemented on a computational program.

✗ The substrate thickness range is limited to values usually less than 0.05 times the free-space wavelength.

✗ The formulation complexity depends on the feeding structure and the interaction (by contact or by coupling) with the patch.

✗ The conductor thickness is considered negligible, and it is usually omitted in the impedance models. This assumption is not a problem for modeling in RF or microwaves, but the accuracy gets compromised in the mmWave and sub-THz bands.

The following chapter provides a new model for estimating the bandwidth and impedance response of narrow-band and broadband PC-MSPAs in RF and microwaves. A reformulated model for PF-MSPAs and PC-MSPAs is provided in Chapter 5, increasing the functionality up to 300 GHz.

Chapter 3

Advanced EM Modeling for Proximity-Coupled Microstrip Patch Antennas

We will always have STEM with us. Some things will drop out of the public eye and will go away, but there will always be science, engineering, and technology. And there will always, always be mathematics. —Katherine Johnson

Proximity-coupled microstrip patch antennas (PC-MSPAs) were introduced in the early 70's [41]. One of the most outstanding features of the PC-MSPA is the broader bandwidth that it can provide compared to MSPAs with other feeds ([24, 54]) such as the aperture, inset, and probe feeds. This broader band is traditionally justified due to the capacitive nature of the feeding structure and its intermediate location between the patch and the ground planes. The percentage bandwidth of an MSPA with probe feed is typically very narrow, less than 5 %. This bandwidth shortage motivates designers to perform geometrical modifications, and several computational optimizations [40] to enhance this behavioral parameter.

Diverse models for MSPAs with different feeds are available in the literature, from analytical approaches ([41],[23], [96]) such as the transmission line model and the cavity model, to the full-wave ones such as the use of the Green's functions [97], and the Method of Moments (MoM) [42]. However, analytical models are usually limited to thin substrates, and full-wave models normally require a long time for

implementation and computation. Moreover, despite the very few and mostly full-wave models for PC-MSPA, [44] proposed a design procedure for square and circular PC-MSPA using MoM-derived curves, but it seems not to have a complete bandwidth assessment that relates to the antenna substrate thicknesses. Then, this chapter provides an advanced EM model for PC-MSPAs, covering from design guidelines to a computer-aided mathematical framework for impedance response.

First, this chapter describes a new strategy to design and estimate the impedance bandwidth of a two-layer and single-material PC-MSPA through a mathematical close-form. As it will be shown in the upcoming sections, the simulated and experimental results present great agreement with the bandwidth model presented. The proposed model enables the evaluation of a PC-MSPA bandwidth that allows the development of a framework for more effective designs.

Then, this chapter presents a fully analytical model to assess the impedance response of a proximity-coupled microstrip patch antenna (PC-MSPA). An improved formulation of the patch resonant frequency is used to calculate the quality factor, resonant resistance, and the feeding circuit parameters of the antenna. The proposed model also assesses the PC-MSPA impedance response while considering the fabrication constraints. For the proposed model's validation, the antennas are first simulated for S-, C- and X-bands. Two prototypes are fabricated and measured. It will be shown that the proposed model predicts the antenna resonant frequency and impedance bandwidth with less than 1 % error. In addition, an unprecedented model for PC-MSPAs with differential feeding is introduced and formulated up to the X-band.

3.1 Antenna Design

This section proposes a mathematically-based analysis and an alternative design procedure for PC-MSPAs. The following aspects are detailed: geometry, design of the feeding length, design of the substrate thickness for bandwidth maximization, and a summary with design guidelines.

3.1.1 Geometry

PC-MSPAs are also known by its feeding structure as electromagnetically coupled (EMC) MSPAs. This feeding technique comes under a non-contacting scheme as there is no physical contact between the radiating patch and the feed line. Two substrates are used such that the feed line terminated with an open circuit is between the two substrates, the radiating patch with dimensions L_p and W_p is on top of the upper substrate, and the lower (feed) substrate is grounded. The microstrip feed line of width W_f is centered to the patch width and is inset a distance L_0 from the edge of the patch.

Since there is no direct contact between the microstrip feed line and the radiating patch in this feeding mechanism, the radiating patch on the upper substrate (patch layer) is excited by an open-ended microstrip feed line printed on the lower substrate (feed layer) through capacitive coupling. Matching is possible by controlling the feed line (feeding stub) length and the width-to-length ratio of the patch.

The geometry of a PC-MSPA is shown in Fig. 3.1, having two substrate layers, the patch, the ground plane, and a feeding transmission line between the layers. The bottom substrate (h_1, ε_1) supports the feed at the top and the ground plane on the bottom, while the top substrate (h_2, ε_2) supports the patch on the top. Both substrates are stacked together so that they form a compact structure, as

shown in the antenna's side view of Fig. 3.1. For this study, both substrates are of the same material and the same thickness, i.e. $\varepsilon_1 = \varepsilon_2 = \varepsilon_r$ and $r_h = 1$. The patch length, which determines the patch resonant frequency (f_{0p}), is set to $L \approx \lambda_r/2 = \lambda_0/(2\sqrt{\varepsilon_r})$. The ground plane size is set to $L_g = W_g = 2\lambda_0$ to make the impedance response less dependent on the antenna cell size. The transmission line with length L_f, used as a feed, has a section x_0 that overlaps the patch.

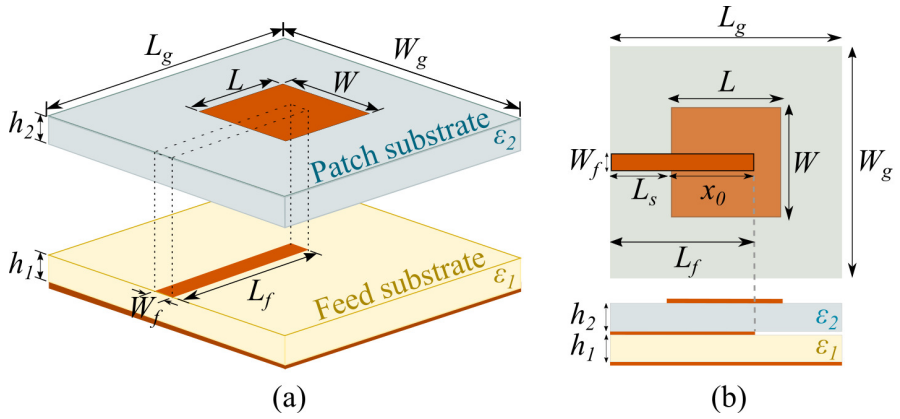

Figure 3.1: Geometry of a PC-MSPA.
The stack-up (a) and the orthogonal projections (b) provide an overview of the dimensions and material properties used in PC-MSPAs.

Two geometry relations are crucial to effectively model the feeding mechanism in PC-MSPAs: the overlapping feed-patch ratio, and the substrate thickness ratio. Both quantities are defined in the upcoming lines.

3.1.1.1 Overlapping Feed-to-Patch Ratio

Considering the PC-MSPA geometry of Fig. 3.1, where the patch length is L, and the overlapping portion of the proximity-coupled feeding transmission line is x_0, then:

$$r_x = \frac{x_0}{L}, \tag{3.1}$$

where r_x is defined as the overlapping feed-patch ratio.

3.1.1.2 Substrate Thickness Ratio

From the same geometry, a substrate thickness ratio r_h can be defined as:

$$r_h = \frac{h_2}{h_1}, \tag{3.2}$$

where h_2 is the thickness of the substrate associated with the patch (top layer), and h_1 is the thickness of the substrate and linked to the feed and the ground plane (bottom layer).

3.1.2 Feeding Length

Impedance matching is produced by having a feeding transmission line with the appropriate width and length since these dimensions are directly related to the characteristic impedance and electrical length, respectively.

The width of the feeding line (W_f) can be set by following the design procedure of [98] to get characteristic impedance Z_0 of 50 Ω, as Z_0=$f(W_f/h_1,\varepsilon_r)$. Moreover, the feed length L_f can be calculated as:

$$L_f = L_s + x_0 = 0.5(L_g - L) + r_x L \tag{3.3}$$

The antenna matching can be set around the operating center frequency f_o if the length portion of the feeding transmission line L_0 is a certain optimum fraction of the patch length L, i.e., if $r_x = r_{x-opt}$. This optimum fraction r_{x-opt} can be calculated as in (3.4). This formulation is illustrated in Fig. 3.2a with HFSS-simulated data and using the materials: Rogers™ 5880 Duroid (ε_r=2.2), Rogers™ 4350B (ε_r=3.66) and Rogers™ 6006 (ε_r=6.15).

$$r_{x-opt} = \kappa_3 \left(\frac{h_1}{\lambda_r}\right)^3 + \kappa_2 \left(\frac{h_1}{\lambda_r}\right)^2 + \kappa_1 \left(\frac{h_1}{\lambda_r}\right) + \kappa_0 \tag{3.4}$$

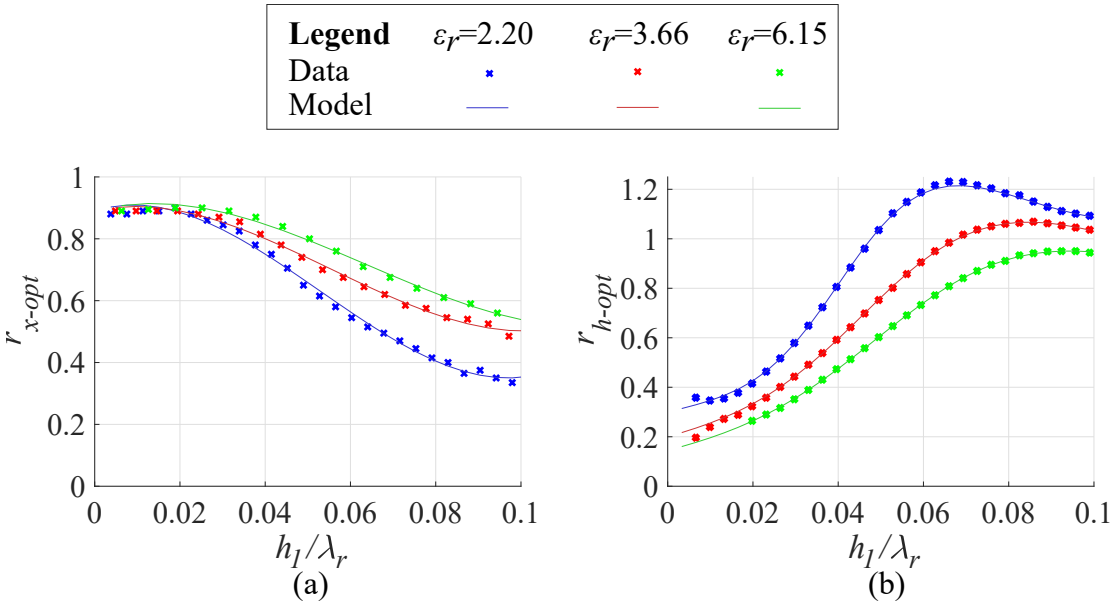

Figure 3.2: Design guidelines for PC-MSPAs.
Comparison between modeled and simulated optimum values of (a) overlapping feed-patch ratio r_{x-opt}, and (b) substrate thickness ratio r_{h-opt}. The proposed formulations of (3.4)-(3.7) permit analytical design of PC-MSPAs.

where κ_3, κ_2, κ_1 and κ_0 are defined as:

$$\kappa_3 = 73.75\varepsilon_r^2 - 834.9\varepsilon_r + 3129 \tag{3.5a}$$

$$\kappa_2 = -149.9 - 257.1e^{-0.1708\varepsilon_r^2} \tag{3.5b}$$

$$\kappa_1 = 0.2772\varepsilon_r^2 - 2.489\varepsilon_r + 8.502 \tag{3.5c}$$

$$\kappa_0 = 0.89 \tag{3.5d}$$

These equations are primarily valid for substrate dielectric constants between 2.2 and 6.15 and feed substrate thickness less than $0.1\lambda_r$ (265 mils in Rogers™ 5880 Duroid, 205 mils in Rogers™ 4350B, and 158 mils in Rogers 6006™ all at 3 GHz). In all the cases, it has been verified that $W_f < W$ and $W_f < 0.25\lambda_r$ when simulating the antenna geometry at S-band (2–4 GHz).

From the above equations and Fig. 3.2a, it is found that the overlapping portion between the feed length and the patch length is more than half of the patch

length. This feed length tends to reduce as thicker are the substrates. It is also observed that the variation of r_x per h_1/λ_r length unit is decreased as ε_r increases. For dual-port applications with differential feeding, r_x will need to be less than 0.5, which results optimum when using thicker substrates and feed substrates with less dielectric constant.

3.1.3 Substrate Thickness

The total thickness h_T of the antenna can be expressed in function of the feed substrate thickness h_1 and the substrate thickness ratio r_h as:

$$h_T = h_1 + h_2 = h_1\Big(1 + \frac{h_2}{h_1}\Big) = h_1(1 + r_h), \tag{3.6}$$

where the ratio r_h can be set to an optimum value for bandwidth maximization. This optimum value, r_{h-opt} is modeled in (3.7). Fig. 3.2b provides an illustration of these equations.

$$r_{h-opt} = \tau_1 + \tau_2 \tanh\Big[\tau_3\Big(\frac{h_1}{\lambda_r} - \tau_4\Big)\Big] + \tau_5 \cos\Big(\tau_6\ \frac{h_1}{\lambda_r}\Big) \tag{3.7}$$

where τ_1, τ_2, τ_3, τ_4, τ_5 and τ_6 can be obtained as follows:

$$\tau_1 = 1.379e^{-0.7\varepsilon_r} + 0.3682 \tag{3.8a}$$

$$\tau_2 = 0.5182e^{-0.4078\varepsilon_r} + 0.6912 \tag{3.8b}$$

$$\tau_3 = 128e^{-0.925\varepsilon_r} + 25.4 \tag{3.8c}$$

$$\tau_4 = -\,0.0446e^{-0.6077\varepsilon_r} + 0.05295 \tag{3.8d}$$

$$\tau_5 = 0.2694e^{-0.15\varepsilon_r} + 0.2903 \tag{3.8e}$$

$$\tau_6 = 96.43e^{-0.9577\varepsilon_r} + 16.98 \tag{3.8f}$$

From this formulation, most design cases get the best coupling when $r_h < 1$, thus for $h_2 < h_1$. Since the actual substrate thicknesses h_1 and h_2 used in a design may be related by a ratio r_h different than the optimum value r_{h-opt}, the coupling

might then be reduced, mainly affecting the impedance bandwidth. Besides, this optimum ratio can get a maximum value at a specific feed substrate thickness h_1, and this peak is inversely dependent on the permittivity. The cases where $h_2 > h_1$ for maximum bandwidth are only possible for $\varepsilon_r < 5.38$, according to the presented equations. It is also possible to have equal substrates (h_2=h_1) for maximum bandwidth as lower dielectric constants have both layers, which may be helpful in fabrication and logistics. As observed so far, this work contributes to the completion of the design of a PC-MSPA through the closed forms of the patch substrate thickness and the feeding structure dimensions.

3.1.4 Patch Dimensions

The design of a square patch begins from the rectangular patch dimensions (L_{po},W_{po}) as a start point. For a given pair of substrates with dielectric constants ε_r, total thickness h_T, and a desired operating center frequency f_c, then the dimensions L_o and W_o are expressed as [24]:

$$W_{po} = \frac{c_0}{2f_c}\sqrt{\frac{2}{\varepsilon_r + 1}} \tag{3.9a}$$

$$L_{po} = \frac{c_0}{2f_c\sqrt{\varepsilon_{re}}} - 2\Delta L, \tag{3.9b}$$

where c_0 is the speed of light at vacuum. The values for ε_{re} and ΔL can be computed from (2.76) and (2.77), respectively. Then, the patch dimensions can be squared by making L=W=L_{po}.

3.1.5 Design Guidelines

The formulations mentioned above allow to synthesize the following design guidelines for impedance bandwidth maximization at a specified center frequency for PC-MSPAs:

1. Set the ground plane size as $L_g = W_g = 2\lambda_c$ at a desired center frequency f_c. Also, define a dielectric constant for both substrates ε_r and the feed substrate thickness h_1 as an initial start point.

2. Compute the patch dimensions L and W by following the procedure of Section 3.1.4 by starting with a rectangular patch and then making it square.

3. Follow the formulation of (3.4)-(3.5d) or the curves shown on Fig. 3.2a to get $r_x = r_{x-opt}$ and then the feed transmission line length L_f as in (3.3). The corresponding width W_f is adjusted for a 50-Ω characteristic impedance.

4. Follow the formulation of (3.7)-(3.8f) or the plots displayed in Fig. 3.2b to get $r_h = r_{h-opt}$. Then, calculate the patch substrate thickness by $h_2 = h_1 r_h$ to maximize bandwidth.

3.2 Bandwidth Estimation

The impedance bandwidth is typically defined as the range of frequencies f_l (lower frequency), f_u (upper frequency) over which the return loss is more than 10 dB ($|S_{11}| < -10$ dB). The percentage fractional bandwidth is determined by the ratio between the impedance bandwidth and the central frequency f_c. Then, the percentage bandwidth is defined as:

$$\%BW = 100\frac{f_u - f_l}{f_c} = 200\frac{f_u - f_l}{f_u + f_l} \tag{3.10}$$

This work proposes a close form to compute $\%BW$ for PC-MSPAs. The expression (3.10) is reformulated by using the antenna geometry and considering the design procedure of Section 3.1.5. The upcoming lines describe more about estimating the impedance bandwidth for PC-MSPAs.

3.2.1 Bandwidth Mathematical Formulation

It can be estimated from the substrates' thicknesses and dielectric constants, considering that the patch and the transmission line feed are set to match the designed frequency ($f_c \approx f_\circ$) by using $x_0{=}r_{x-pt}L$. Then, the percentage bandwidth of the PC-MSPA with linear polarization can be predicted to be:

$$\%BW = A_{BW}\sqrt{1-(Y_8/K_8)^2} \tag{3.11}$$

The equation for estimating the percentage bandwidth of the PC-MSPA presents three components: bandwidth amplitude A_{BW}, allowable range of substrate thickness ratio K_8, and the normalized value Y_8 of substrate thickness ratio over its optimum value for a given feed substrate. The graphical representation of these components is illustrated in Fig. 3.3. Further description of A_{BW} is provided in Section 3.2.2, while detailed formulation for K_8 and Y_8 is listed in Section 3.2.3.

Therefore, the bandwidth close-form of (3.11) produces a family of semi-elliptical curves, where the families are determined by h_1/λ_r variations, and each semi-ellipse has a height A_{BW}, a width $2K_8$, and they are centered in Y_8.

This formulation may be physically interpreted as the substrate's relative permittivity and thickness change. As ε_r increases, the bandwidth tends to reduce, and it is observed in the A_{BW} term, which also has a second-degree polynomial growth as the feeding substrate becomes thick. Meanwhile, the shape parameter K_8 represents the range of substrate thickness ratio where bandwidth can exist. Besides, Y_8 represent the deviation of substrate ratio from r_h. Hence, if an antenna with a certain feeding substrate thickness h_1 has patch substrate thickness $h_2{=}r_{h-opt}h_1$, then it would have the maximum bandwidth, as $Y_8{=}0$.

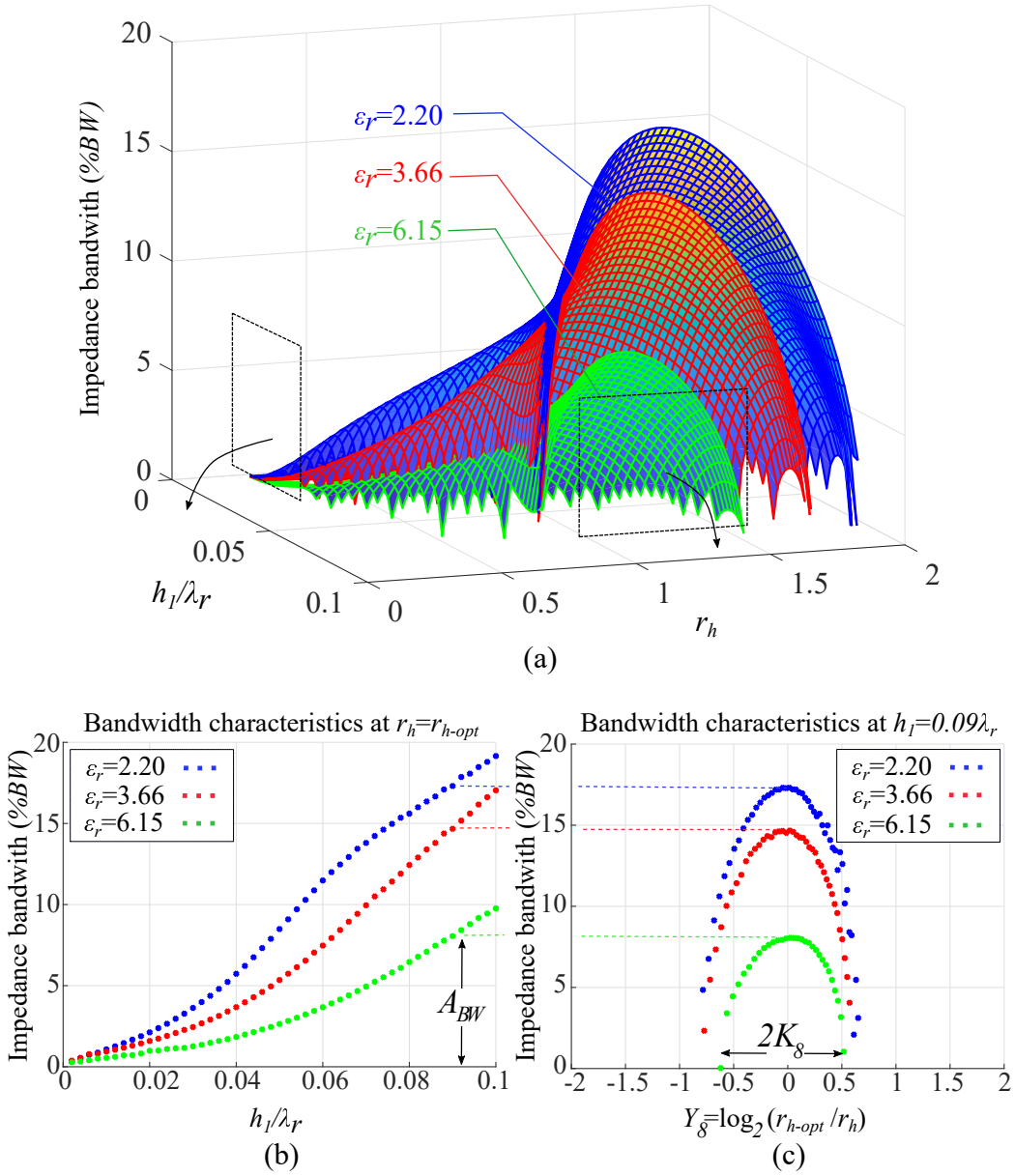

Figure 3.3: Impedance bandwidth model for PC-MSPAs.
(a) Three-dimensional distribution of the percent impedance bandwidth ($\%BW$), (b) side projection over feeding substrate electrical thickness h_1/λ_r, (c) side projection over substrate thickness ratio. The value of $\%BW$ for PC-MSPAs is characterized by the amplitude component A_{BW}, the logarithmic distance Y_8 between the substrate thickness ratio r_h and its optimum value r_{h-opt}, and the associated distance amplitude K_8 where a bandwidth exists.

3.2.2 Bandwidth over Feeding Substrate Thickness

Given the feed substrate with a thickness h_1, and patch substrate with thickness $h_2 = h_1 r_{h-opt}$, and assuming congruent substrates (ε_1=ε_2=ε_r), then, the maximum possible bandwidth is expressed as:

$$A_{BW} = a_1 \left[\left(\frac{h_1}{\lambda_r} \right)^2 - \frac{1}{2} \left(1 + \tanh \frac{h_1/\lambda_r - a_2}{10^{-3}} \right) \left(\frac{h_1}{\lambda_r} - a_2 \right)^2 \right] \tag{3.12}$$

where $a_1 = 98840e^{-2.145\sqrt{\varepsilon_r}} + 533.6$ and $a_2 = -0.3252e^{-0.8037\sqrt{\varepsilon_r}} + 0.1231$. This formulation was obtained by applying the curve-fitting technique [69] from the bandwidth trends in Fig. 3.3a, and it is illustrated in Fig. 3.3b.

3.2.3 Bandwidth over Substrate Thickness Ratio

The following parameters can be defined for a given patch substrate thickness h_2 independently chosen from h_1:

$$Y_8 = \log_2(r_h / r_{h-opt}) \tag{3.13}$$

$$K_8 = \log_2 \left[\frac{K_a}{r_h} + \sqrt{4 + \left(\frac{K_a}{r_h} \right)^2} \right] - 1 \tag{3.14}$$

where K_a can be obtained as follows:

$$K_a = k_1 + k_2 \tanh \left[k_3 \left(\frac{h_1}{\lambda_r} - k_4 \right) \right] + k_5 \cos \left(k_6 \, \frac{h_1}{\lambda_r} \right) \tag{3.15a}$$

$$k_1 = 0.7682e^{-0.3526\varepsilon_r} + 0.4086 \tag{3.15b}$$

$$k_2 = 2.299e^{-0.5975\varepsilon_r} + 0.2538 \tag{3.15c}$$

$$k_3 = 80.32e^{-1.028\varepsilon_r} + 42.36 \tag{3.15d}$$

$$k_4 = -0.06715e^{-0.771\varepsilon_r} + 0.04963 \tag{3.15e}$$

$$k_5 = 1.271e^{-0.5736\varepsilon_r} + 0.07257 \tag{3.15f}$$

$$k_6 = 311.6e^{-1.406\varepsilon_r} + 18.96 \tag{3.15g}$$

This formulation was also acquired by applying the curve-fitting technique [69] from the bandwidth trends in Fig. 3.3a. The bandwidth $\%BW$ can be then maximized to A_{BW} for a given feed substrate h_1. If the patch substrate thickness h_2 is set out of the optimum value $r_{h-opt}h_1$, then $\%BW$ follows (3.11), where K_8 is pictured in Fig. 3.3c.

3.2.4 Model assessment

Full wave simulations of PC-MSPAs as of Fig. 3.1 were performed at f_o=3 GHz, considering three different materials and changing h_1 from 0.002 λ_r to 0.1λ_r, h_2 from 0.275h_1 to 2h_1. The feeding line length was calculated as in (3.3), where r_x was obtained and calculated in (3.4). The results are shown in Fig. 3.4, as follows: the first row describes the normalized central frequency (f_c/f_o); the second row shows the return loss at the simulated value of f_c=$(f_u + f_l)/2$ where $[f_l; f_u]$ is the interval where $|S_{11}|< -10$ dB; and then the third and fourth rows display the simulated and modeled percentage bandwidth of (3.10) and (3.11), respectively. For the three different materials, the model results of the percentage bandwidth in Fig. 3.4d are in good agreement with the corresponding simulated ones shown in Fig. 3.4c.

In addition, four antenna configurations have been fabricated and measured using two different materials and different design frequencies in the S-, C-, and X-bands. These cases have been labeled as 'Case 1', 'Case 2', 'Case 3' and 'Case 4', which specifications are listed in Table 3.1, noticing that r_h=1 in all the cases. The simulated and measured reflection coefficients of these antennas are expressed in decibels (dB) and plotted in Fig. 3.5 . The antenna in Case 1 and Case 4 has a ground plane size of $\lambda_o/2$ x $\lambda_o/2$ where λ_o is the free space wavelength of the design frequency. The PC-MSPA ground plane in Case 2 and Case 4

has been extended to 5 cm ($\lambda_o/2$ at 3 GHz) to facilitate the connections for measurements. From Fig. 3.5, it is clear that the measured results mostly agree with and validate the results produced via simulations for all cases. A small discrepancy between the simulated and measured results may result from antenna fabrication and assembling defects.

Furthermore, this work also provides an analysis of model errors. The plot in Fig. 3.6a shows the percentage RMSE of the central frequency relative to the intended central frequency from several simulated antennas with $h_1/\lambda_r < 0.1$, which is expressed as $\Delta f_c/f_c$. Meanwhile, Fig. 3.6b shows the bandwidth error, which is calculated as $\Delta\ \%BW = |\%BW_{(model)} - \%BW_{(simulation)}|$ from Fig. 3.4. Table 3.2 quantifies the errors between modeled, simulated, and measured impedance bandwidth of the four cases, using the central frequency (f_c) for each prototype.

Table 3.1: Fabricated PC-MSPAs' specifications.

Specification	Unit	Case 1	Case 2	Case 3	Case 4
f_o	GHz	3	6	6	10
$\varepsilon_1, \varepsilon_2$	-	2.20	3.48	3.48	2.20
h_1, h_2	mm	3.175	1.524	1.524	0.790
L, W	mm	29.40	11.82	11.80	9.070
L_g, W_g	mm	50.00	50.00	2.000	50.00
r_x	-	0.686	0.687	0.721	0.760
L_f	mm	27.87	13.27	12.68	11.50
W_f	mm	10.00	3.350	3.350	2.420
x_0	mm	20.56	7.680	7.100	4.530

Table 3.2: Errors between modeled, simulated and measured bandwidths.

Case	f_c	$\%(\Delta f_c)/f_c$		$\Delta\ \%BW$	
		Measured	Simulated	Measured	Simulated
Case 1	3 GHz	0.17	0.04	1.41	0.18
Case 2	6 GHz	1.91	0.99	0.80	0.98
Case 3	6 GHz	0.09	0.76	0.15	1.46
Case 4	10 GHz	1.00	1.30	0.65	0.39

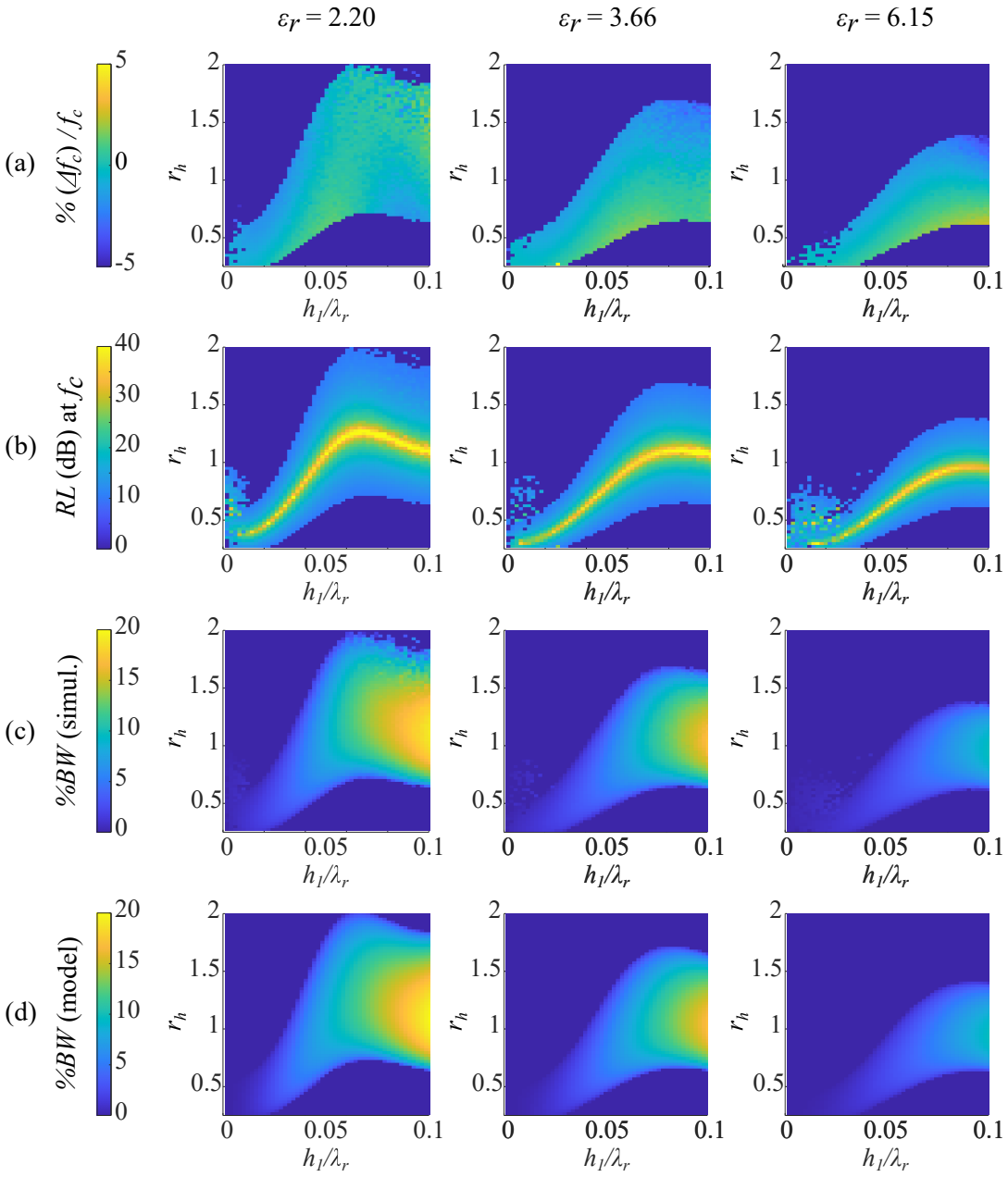

Figure 3.4: Assessment of impedance-bandwidth behavior of PC-MSPAs. Operating frequency and impedance bandwidth for PC-MSPAs made of different materials: Rogers™ 5880 Duroid (left column), Rogers™ 4350B (middle column) and Rogers™ 6006 (right column). All the variations are simulated at 3 GHz in $\lambda_\circ/2$ unit cell (L_g =5 cm). (a) Percentage deviation of designed central frequency, (b) Return loss at the central frequency (f_c), (c) Simulated percentage bandwidth, and (d) Modeled percentage bandwidth. The results indicate a high accuracy in the design guidelines and bandwidth formulation proposed in this work and for different dielectric substrates.

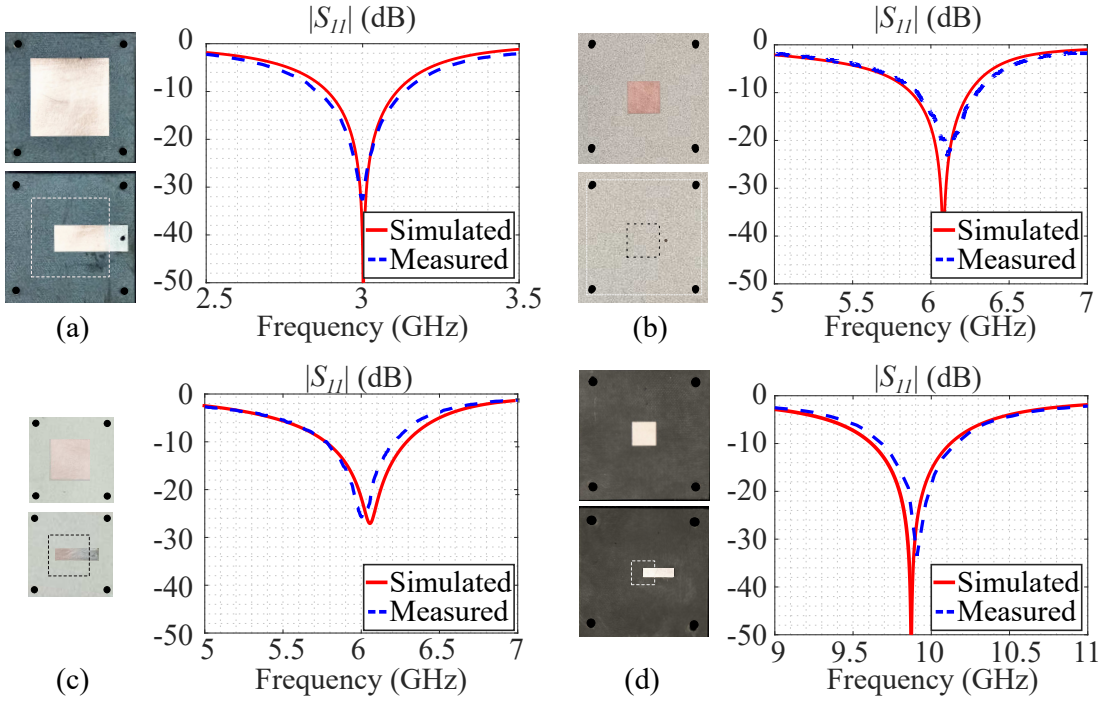

Figure 3.5: Bandwidth comparison with fabricated PC-MSPAs.
Measured and simulated S_{11} frequency response for PC-MSPAs: (a) Case 1: S-band (3 GHz), (b) Case 2: C-band (6 GHz), (c) Case 3: C-band (6 GHz), and (d) Case 4: X-band (10 GHz). The overlapping bandwidths indicate agreement between simulation and measurement, providing a double validation for the proposed model, which bases on simulated PC-MSPA designs.

3.2.5 Error analysis

The operating central frequency f_c in all simulated cases is around the design operation frequency f_o, having a root mean square error (RMSE) less than 3 %. This means having errors less than 1.34 % in Rogers™ 5880 ($\varepsilon_r = 2.20$), 1.45 % in Rogers™ 4350 ($\varepsilon_r = 3.66$), and 2.76 % in Rogers™ 6006 ($\varepsilon_r = 6.15$), as noticed in the color space in the first row of Fig. 3.4. This agreement is due to the accurate design from (3.3). However, it is also seen that designing very thin antennas ($h_1 < 0.03\lambda_r$, $h_2/h_1 < 0.75$) may produce frequency f_c 5 % below f_o. This effect is visible in the dark blue colored points in the bottom left corner of the first row that are not present in the other rows. Consequently, this frequency

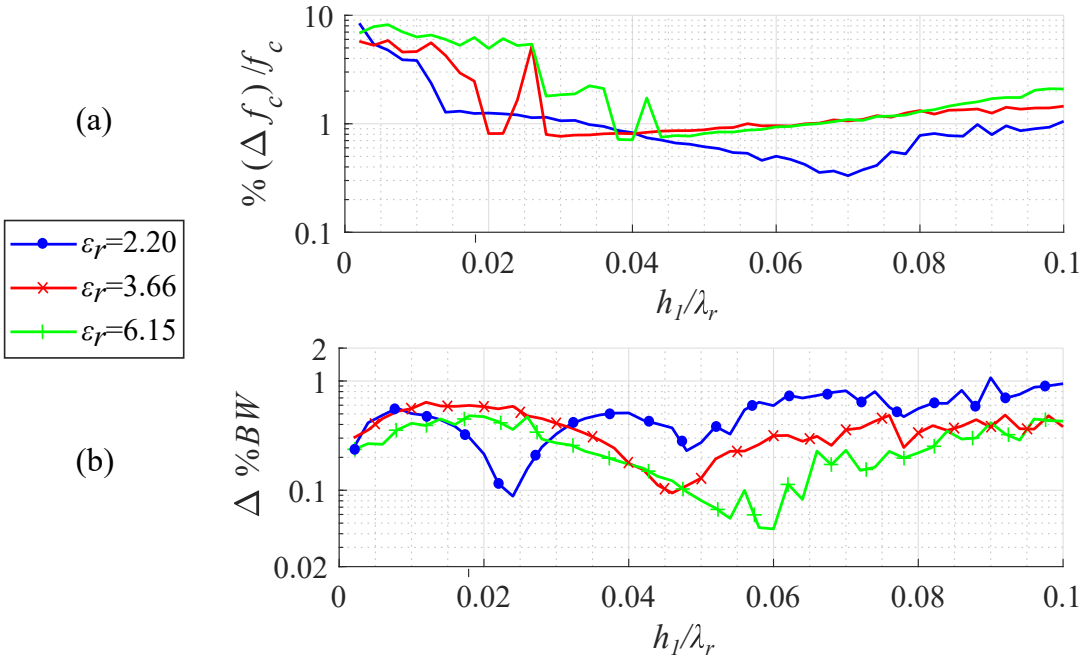

Figure 3.6: RMS model errors over feed substrate thickness h_1/λ_r.
(a) Central frequency fluctuations, (b) Percentage bandwidth term $\%\Delta BW$.
The modeling errors keeps lower than 2 % for $0.03 < h_1/\lambda_r < 0.1$.

downshifting is reflected as higher RMSE as shown in Fig. 3.6a. These fluctuations are primarily due to the numerical simulation errors for substrates where $h_1/\lambda_r < 0.03$. Moreover, as the feed thickness h_1 increases ($h_1 > 0.03\lambda_r$), the simulated PC-MSPAs converge with less numerical errors, providing percentage RMSEs less than 5 %. Meanwhile, according to Table 3.2, the measured central frequency in the four cases also has an excellent agreement, having slightly more errors in Case 2 and Case 4 due to fabrication imperfections.

The maximum return loss, related to the maximum predicted bandwidth across different values of r_h, are obtained when the parameter $Y_8 = 0$ in (3.11), which takes place when $h_2 = h_1 r_{h-opt}$. This trend is observed by comparing the simulations of Fig. 3.4b and the frequency responses of Fig. 3.5. Considering Case 1 and Case 3, which do not have a ground plane extension, the values of $|Y_8|$ are 0 and 0.17, meaning that the return loss would be stronger in Case 1 than in Case 3.

This behavior is observed in the simulation and experiment as shown in Fig. 3.5a and Fig. 3.5c.

Regarding the antenna bandwidth, the RMSE of the term $\%\Delta BW$ is less than 2 %, as observed in Fig. 3.6b, showing high accuracy of the model in comparison with the simulation. These errors remain consistent over h_1/λ_r, but they represent a bigger relative error when h_1/λ_r is small, i.e. less than $0.03\lambda_r$. This increase is observed, for instance, in the spotty area at the bottom left corners in the plots of Fig. 3.4b, where the predicted bandwidth is zero. Due to numerical simulation fluctuations, the term Δ $\%BW$ may be higher at $Y_8 \approx K_8$, where the expected percentage bandwidth goes to zero. In addition, from the experimental results, it is observed in Table 3.2 that the bandwidth has an error term up to 1.46 %. Overall, the expression of the bandwidth can get a good estimation of the bandwidth, but it should be considered only as a reference value, as it may differ from measured values due to fabrication errors and limitations, as well as numerical errors, especially in ultra-thin antennas.

Those results mean that the proposed feed-to-patch ratio model $r_x = r_{x-opt}$ allows having a PC-MSPA with a stabilized central frequency f_c and around the design frequency of the antenna f_o. The maximum return loss and bandwidth results show that the model and prediction have good agreement with the results, but the model errors may increase as the antenna thickness is reduced and as $r_h = h_2/h_1$ is far away from the optimum value r_{h-opt}. Designing PC-MSPAs outside the optimum guidelines may affect the maximum return loss and bandwidth. Also, feed substrates with higher thickness would increase the bandwidth as long as the patch substrate thickness h_2 has the appropriate dimension related to r_{h-opt} to maximize coupling.

In addition, the proposed model is compared with previous work available in literature [56], [58], [57]. The calculated percentage bandwidths for PC-MSPAs are compared with those from simulated designs and close-forms from previous work. The analysis covers electrically thin and thick PC-MSPAs between the S-band and the X-band. Four study cases, listed in Table 3.3, are defined. They consider the simulated value of the PC-MSPA bandwidth as a reference. It is seen from Table 3.3 that when the error between the simulated and predicted bandwidth is less than 0.5 % using the new model. This model provides superior performance compared to previous models, with errors that round up to 9 %.

Table 3.3: A comparison between available models for PC-MSPA bandwidth. The study cases for this comparison consider $h_1 = h_2$, and $L = W$.

Parameters	Reference (HFSS)	Bandwidth (Error)	Theoretical Bandwidth Estimation			
			Proposed Model	Previous Work		
				Ref. [56]	Ref. [58]	Ref. [57]
f_o=3 GHz, ε_r=2.20 h_1=125 mils, W=29.40 mm	7.430	$\%BW$ (Δ_{BW})	**7.610** (**0.180**)	6.433 (0.997)	7.706 (0.276)	9.600 (2.170)
f_o=10 GHz, ε_r=6.15 h_1=50 mils, W=4.85 mm	10.28	$\%BW$ (Δ_{BW})	**10.37** (**0.090**)	4.323 (5.959)	6.145 (4.317)	12.80 (2.518)
f_o=10 GHz, ε_r=3.48 h_1=60 mils, W=6.28 mm	16.38	$\%BW$ (Δ_{BW})	**16.32** (**0.060**)	7.963 (8.417)	10.89 (5.487)	15.36 (1.020)
f_o=6 GHz , ε_r=2.20 h_1=125 mils, W=12.19 mm	17.79	$\%BW$ (Δ_{BW})	**18.17** (**0.385**)	13.64 (4.149)	18.84 (1.052)	19.20 (1.415)

3.3 Impedance Response

As described in Chapter 2, the impedance response of an MSPA can be computed using either the cavity model or the transmission line model. Also, from the geometry defined in Section 3.1.1, it is important to notice that the overlapping feed-to-patch ratio $r_x = x_0/L$ and the substrate thickness ratio $r_h = h_2/h_1$ play an important role in modeling PC-MSPAs. The feeding location under the left

edge of the patch is the reference location where Z_{in} is obtained. In Fig. 3.7a, this position is labeled at the coordinate origin. Thus, at $x = 0$ is located the Z_{in} model reference, as depicted in Fig. 3.7b. The non-overlapping portion of the feeding is an embedded microstrip line, characterized from now with an impedance Z_{0u}. In contrast, the overlapping portion can be considered a stripline, with a characteristic impedance defined from now as Z_{0s}. This section provides an in-depth study of previous work and the problem with estimating the impedance response of PC-MSPAs.

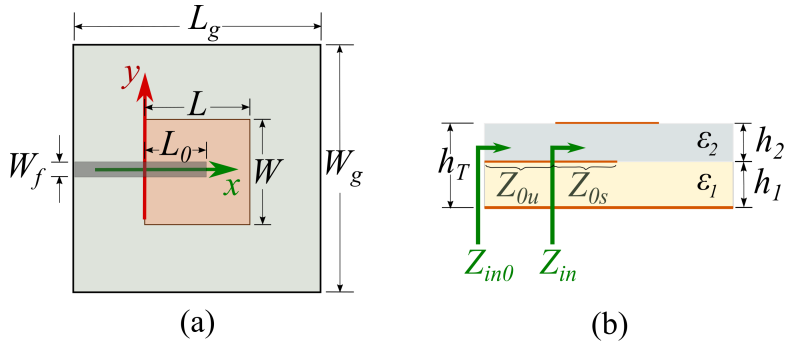

Figure 3.7: Impedance reference position for PC-MSPAs.
(a) Top view and coordinate system, (b) Side view, impedance references.
The reference position for Z_{in} is considered at the position $(x, y) = (0, 0)$, i.e., at the beginning of the overlapping section of the feeding line.

3.3.1 Previous Models for PC-MSPAs

The input impedance Z_{in} of an MSPA with any feed includes the patch impedance Z_p (2.106) in addition to the impedance corresponding to the feeding mechanism. In the PF-MSPA, the probe adds a frequency-dependent reactance (2.107) to the patch impedance (2.106). Because of the direct contact between the feed (probe) and the patch, the feed impact adds up to the patch's impedance, as expressed in (2.109). Although there are models for MSPAs available in the literature, the particular case of PC-MSPA is very limited in quantity and accuracy, primarily

due to the complexity of modeling the feeding mechanism that interacts with the patch voltage and current distribution.

In contrast to the PF-MSPA, where the impedance directly relates to the feed position, the impedance in the PC-MSPA can not be directly determined under the end of the transmission line position unless complex considerations around the edge are taken into consideration, e.g., fringe fields, the variable characteristic impedance of the stripline depending on the length of the overlapping portion of the feed. Therefore, the impedance's reference position needs to be relocated, for instance, under the patch's left edge, i.e., at $x = 0$. The existing models and the proposed one in this work consider the location $x = 0$ to determine Z_{in}.

Then, having the PC-MSPA impedance Z_{in}, the input impedance Z_{in0} [95] at any port located outside the overlapping section of the feed can be computed by using (3.16), where γ and β are the propagation constant and the wave number, respectively.

$$Z_{in0} = Z_{0u}\frac{Z_{in} + Z_{0u}\tanh\gamma l}{Z_{0u} + Z_{in}\tanh\gamma l} \approx Z_{0u}\frac{Z_{in} + jZ_{0u}\tan\beta l}{Z_{0u} + jZ_{in}\tan\beta l} \tag{3.16}$$

where Z_{0u} is the characteristic impedance of the embedded microstrip line outside the feed's overlapping section, which has a length $L_s = L_f - x_0$.

A numerical circuit model [42] for PC-MSPA was obtained, consisting of a capacitor in series with an RLC resonator, where the capacitor counted for the reactance produced by the feeding, and the resonator aimed to model the patch impedance response. That model showed the antenna's equivalent circuit when measuring the feed's impedance at $x = 0$ (Fig. 3.7a). Although the model was derived for a specific design, it showed that the behavior of a PC-MSPA was predominantly capacitive when the overlapping section of the feed was low compared to the patch length. Also, that model computed a resonant resistance of 40 Ω,

showing that having non-zero resonant resistance is possible in PC-MSPA even though the feeding is ending strictly under the middle of the patch ($x_0 = 0.5L$), which would not be the case when applying (2.105a) for PF-MSPA.

A circuit model [51] for a circular MSPA with a hybrid feed of an L-strip line was developed more recently. The input impedance of a PC-MSPA, also under the left edge of the patch ($x = 0$ in Fig. 3.7a), was proposed using expression (3.18). The vertical portion of an L-strip feeding must not be considered to compare this model with PC-MSPAs. So, let us only consider the horizontal portion as a transmission line; thus, $R_s = L_s = 0$ in (3.18). Hence, the model of [51] becomes equivalent to the capacitor C_T of (3.17) in series with the patch RLC resonator of (2.106), where R_p of (2.105a) used the normalized Bessel function instead of the squared cosine function, as circular patch was used. The total capacitance of (3.17) resulted from the direct capacitances (C_{pg}, C_{pp}) between the overlapping portions of the feed and the plates above and below it (patch and ground plane), as well as the fringe capacitances (C_{fg}, C_{fp}) in the open ends of the feed and the patch, and it is given by:

$$C_T{}^{-1} = (C_{pg} + C_{fg})^{-1} + (C_{pp} + 2C_{fp})^{-1} \tag{3.17}$$

$$Z_{in} = R_s + j\omega L_s + 1/(j\omega C_T) + Z_p \tag{3.18}$$

3.3.2 Problem and Proposed Solution

Despite of the limited availability of PC-MSPA models in the literature, there is an evolution of complexity in the feed's equivalent circuit while preserving the patch's impedance nature as an RLC resonator. Both models discussed above agree on the strongly capacitive nature of proximity-coupled feeding. Nonetheless, there are still limitations in predicting the impedance behavior in the PC-MSPA for different lengths of the feed's overlapping portion.

To illustrate these limitations, let us recall the feed-to-patch overlap ratio $r_x = x_0/L$. Fig. 3.8 shows the variation of the reflection coefficient (Γ) along different overlap ratios ($0 < r_x < 1$) applied to the antenna Design 1 (Table 3.4). Fig. 3.8a illustrates Γ of the resonator impedance Z_p (2.106) with resonant resistance of (2.105a). Fig. 3.8b plots Γ from the resonator adding a 1 pF capacitor. Then, Fig. 3.8c displays the impedance transferred from the feed position $x = x_0$ to $x = 0$ by using (3.16) , and Fig. 3.8d shows the actual variation (simulated) of Γ, having the phase reference set at $x = 0$, i.e. under the left edge of the patch.

The advantage of plotting Γ in the Smith chart is that the patch RLC resonator and feeding parameters can be observed in a single picture. For instance, if looking at Fig. 3.8d, the trend of the radiation resistance can be noticed through the maximum distance between each curve and the edge of the chart along the curves. Also, the loop diameter of the Γ response is determined by the quality factor and the feeding equivalent capacitance, being more prominent as both parameters get high values. The effect of the transmission line length can be noticed in the phase rotation of Γ in the chart, but it is better observed in the impedance plots of Fig. 3.8e-f.

The limitations on the resonant-resistance modeling function can be observed by comparing the plots of Fig. 3.8c with Fig. 3.8d. For example, exciting the patch underneath its center ($r_x = 0.5$) would produce all-zero input impedance as $R_p = 0$ according to (2.105a) and Fig. 3.8c, which is not true as observed in Fig. 3.8d. For lower overlap ratios, it is observed in Fig. 3.8d that the antenna response is predominantly capacitive, as already observed in [42], being feasible to represent it as an RLC-C circuit.

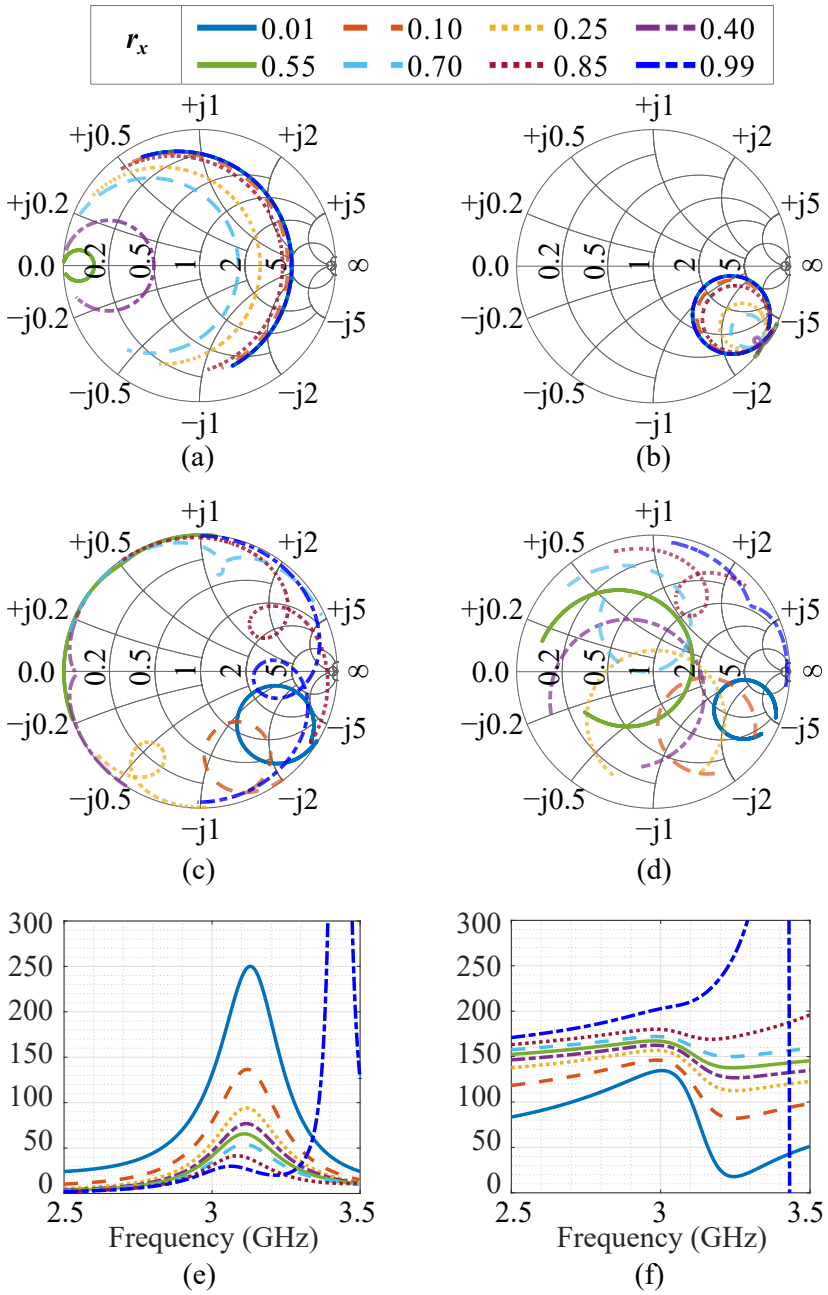

Figure 3.8: Impedance trends in a PC-MSPA with different feed lengths. Variation of the reflection coefficient (Γ) in a PC-MSPA. (a) Synthesized patch resonator using (2.105a); (b) adding a 1 pF capacitor; (c) rotating with (3.16); (d) actual trend from simulation; (e) impedance real part; and (f) imaginary part, with different feeding lengths embedded to the position $x = 0$. Source of R_{pM}, f_p and Q_p: simulation of an square PC-MSPA with $L = W = 27.7$ mm, $h_1 = 3.175$ mm, $r_x = 0.25, r_h = 1, \varepsilon_1 = \varepsilon_2 = 2.20$. These trends suggest modeling PC-MSPAs as a in-series electric circuit between the patch RLC resonator and the feed impedance load.

For high overlap ratios, the response looks more inductive, looking in the Smith chart like a phase rotation of the previous responses with lower overlaps but with an increasing reactance as the feed becomes longer. It is also noticed in Fig. 3.8d that the loop diameter decreases as r_x increases, which is different from the profile of Fig. 3.8c. All these observations suggest considering an alternative profile of the radiation resistance instead of the squared cosine profile of (2.105a), e.g., by considering effective feed positions rather than the physical feeding positions or by developing a new curve model from scratch. This work proposes a new curve model, which will be detailed in Section 3.4.

The effect of the feeding circuitry is also noticed by comparing Fig. 3.8a with Fig. 3.8b. Because of the small capacitance, the highly negative reactance produces a significant rotation of the Γ curve of Fig. 3.8a anti-clockwise to the one of Fig. 3.8b. However, as the capacitance increases, this rotation reduces up to the point that the capacitance is high enough to produce a Γ curve more likely than that of Fig. 3.8a, not having a rotation clockwise as expected and observed in Fig. 3.8d, suggesting the existence of inductance and a transmission line rotation. Fig. 3.8e-f shows the impedance variation in both real and imaginary parts, aiming better to illustrate the impact of inductive reactances and phase rotation.

The curves of the real part in Fig. 3.8e show a decaying resonant resistance as the feed extends, but without getting zero at $r_x = 0.5$ as happens with PF-MSPAs. The patch resonant frequency and quality factor change slightly across the feed lengths, being these changed more pronounced when $r_x < 0.25$ and $r_x > 0.75$. Also, very high resistances and shifts in the patch resonant frequency are observed when $r_x > 0.90$, behavior due to a phase rotation, suggesting the effect of a transmission line length in such lengthy feedings.

Furthermore, the curves of the imaginary part in Fig. 3.8f indicate that the reactances are composed of the imaginary parts of the patch resonator, adding reactances much less than zero and then towards zero and more as long the feed is. In the same way, as in Fig. 3.8e, no phase rotation is perceived in the response while $r_x < 0.75$, indicating that larger capacitances and inductances produce the increase of the reactance. If only the capacitances are considered, then the response would be limited because the maximum reactance value would be half of the resonant resistance, which is not valid, especially when $r_x > 0.70$.

Hence, modeling the feeding as a circuit structure composed of an inductor and a capacitor connected in series is proposed to overcome this limitation. This structure would then connect in series with the patch RLC resonator. In summary, the behavior of a PC-MSPA can be dependent on r_x as follows:

- Short overlaps ($r_x < 0.25$): The impedance response has capacitive reactance, and the resonant resistance dramatically changes with slight variations of the feed length. An equivalent capacitor in series with the RLC resonator fits very well in this case.

- Moderate overlaps ($0.25 \leq r_x \leq 0.75$): The impedance response has capacitive and inductive reactance. The resonant resistance decreases as the feed becomes longer with less sensitivity. An LC circuit in series with the patch RLC resonator fits very well in this overlapping range.

- Large overlaps ($r_x > 0.75$): The patch resonant frequency gets shifted, and open-circuit impedances appear at the upper frequencies of the interval analysis as a phase rotation occurs. An equivalent transmission line in series with the LC-RLC series is required to model the behavior of the PC-MSPA better.

Therefore, the proposed solution consists of a new model to obtain the impedance of a PC-MSPA with feed lengths in the range of moderate overlaps. The model comprises a set of equations for the patch resonator and the feeding inductance and capacitance, integrating them in a hybrid model structure of a transmission line in series with an LC-RLC circuit.

3.4 Equivalent Electric Circuit Model

This section presents a new model for a PC-MSPA. The model is divided into a patch RLC resonator, a feeding circuit, and a feeding equivalent transmission line. Notice that the equivalent transmission line can be ignored for moderate overlaps on which this work focuses. An equivalent circuit of the proposed model is presented in Fig. 3.9b. The input impedance of the PC-MSPA Z_{in} is given by (3.19). The real part of Z_{in} only depends on the patch resonator, while the imaginary part depends on both the patch resonator and the feeding.

$$Z_{in} = Z_p + Z_{feed} = \mathrm{Re}(Z_p) + j\mathrm{Im}(Z_p + Z_{feed}), \tag{3.19}$$

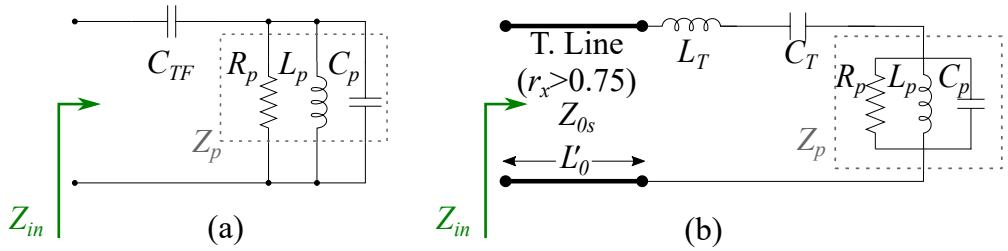

Figure 3.9: Equivalent circuit models of a PC-MSPA.
(a)Traditional model, (b)Proposed model. This work proposes a more accurate model for the patch and the feed. For feed-to-patch ratio $r_x = x_0/L \leq 0.75$, a PC-MSPA can be electrically modeled as a LC series load in series with the RLC patch resonator.

3.4.1 Patch RLC Resonator

The parameters f_{0p}, Q_p, and R_{pM} can be calculated considering the average relative permittivity of the two substrates ε_r, the total thickness $h_T = h_1 + h_2$, and the length of the patch L. For R_p, the length of the overlapping section of the feed x_0 is also required for the calculation. Because the coupling mechanism in the PC-MSPA depends on the substrates thickness ratio, the expressions (2.100), (2.102), (2.104a) and (2.104b) of f_{0p}, Q_p, R_{pM} and R_p is reformulated in this section.

The RLC resonant frequency in PC-MSPAs (f_{0p}) tends to shift upwards from the RLC resonant frequency of the same patch but with probe feeding. To consider this shift and use (2.100), a factor F_{f0} is applied as expressed in (3.20). In order to avoid any confusion, the RLC resonant frequency calculated in (2.100) is renamed to f_{0r}, thus the corresponding wavelength (2.101a) is also renamed to λ_{0r}. Then, f_{0p} is expressed as:

$$f_{0p} = f_{0r}F_{f0} = f_{0r}(F_0 + (h_T/\lambda_{0r} - 0.005)F_1), \tag{3.20}$$

where $F_0 = 1.02 - 0.045/\sqrt{\varepsilon_r}$ and $F_1 = (0.7376/r_h + 0.4754)/\sqrt{\varepsilon_r}$. The result of (3.20) has an error less than 1 % with simulated data of square PC-MSPA designs, and over the range $\varepsilon_r \in [1.7; 3.66]$, $r_h \in [0.75; 1.25]$ and $h_T \leq 0.1\lambda_{0r}/\sqrt{\varepsilon_r}$. After f_{0p} is calculated, (2.101a) - (2.101b) can be used to obtain λ_{0p} and k_{0p} which will be used to get Q_p and R_p.

Following the patch cavity model, its effective length L_e can be calculated using (3.21), where f_{0p} has been calculated in (3.20). Hence, the value of ΔL for PC-MSPAs can be rewritten as in (3.22).

$$L_e = \frac{c_0}{2f_{0p}\sqrt{\varepsilon_{rep}}} \tag{3.21}$$

$$\Delta L = 0.5(L_e - L) \tag{3.22}$$

The RLC quality factor Q_p in a patch is a function of the resonant frequency, the relative permittivity, and the effective patch dimensions (L_e, W_e). By comparison with simulated data, it was observed that a value of W_e as in (3.23) enables the prediction of the quality factor of the square PC-MSPA with errors less than 10 %. It is important to indicate that this value of W_e only represents a mathematical estimate.

$$W_e = W + 2\Delta W \approx W + 2(0.25\Delta L) \tag{3.23}$$

Consequently, the RLC quality factor of PC-MSPAs can be calculated using (2.102) considering the resonant frequency f_{0p} of (3.20) and the effective dimensions of (3.21) and (3.23).

The RLC resonant resistance R_p of PC-MSPAs can be rewritten as in (3.25). The value of R_{pM} was obtained from (2.104b) using $x_0 = 0$ and a square patch, and it can be calculated as in (3.24). The shape curve F_{Rp} is expressed in (3.26) for different values of r_x and r_h.

$$R_{pM} = \frac{4}{\pi}(\mu_r \eta_0) Q_p \Big(\frac{h_T}{\lambda_{0p}}\Big) \cos^2\Big(\frac{\pi \Delta L}{L + 2\Delta L}\Big) \tag{3.24}$$

$$R_p = R_{pM} F_{Rp} \tag{3.25}$$

$$F_{Rp} = p_0 e^{-p_1 r_x} + (1 - p_0) e^{-p_2 r_x} \tag{3.26}$$

In (3.26), the terms p_0, p_1, and p_2 are defined as:

$$p_0 = \sqrt{r_h}(-0.66 e^{-97.13 \frac{h_T}{\lambda_{0r}}} + 0.74 e^{-4.505 \frac{h_T}{\lambda_{0r}}}) \tag{3.27a}$$

$$p_1 = \frac{1.544}{\frac{h_T}{\lambda_{0r}} + 0.01456} \tag{3.27b}$$

$$p_2 = r_h^{0.75}\Big[1.456 - 1.698 e^{-32.18 \frac{h_T}{\lambda_{0r}}}\Big] \tag{3.27c}$$

A simplified expression of F_{Rp} is provided in (3.28) for short and moderate overlaps assuming $h_1 = h_2$.

$$F_{Rp} = 32.38(1 - r_x^{0.005}) + 0.14 \tag{3.28}$$

These terms are illustrated in Fig. 3.10a, and they include a fast-decay exponential shape, dictated by p_1; and a slow-decay exponential shape, dictated by p_2. Typical values of p_1 are around several tens, while p_2 is a value between 0.5 and 1.5. For moderate overlap ratios, the first term of (3.26) can be ignored to calculate F_{Rp}.

3.4.2 Feeding Circuit

The feeding structure can be modeled as an in-series LC circuit as pictured in Fig. 3.9b. Hence, the values of the feeding inductance L_T and feeding capacitance C_T can be expressed as in (3.31a) and (3.31b) for moderate overlap ratios as demonstrated below.

First, for $\varepsilon_{r1} = 2.2$, $\mu_{r1} = 1$, $f_{0p1} = 2.945$ GHz, the values of L_T and C_T were obtained by selecting the combination (L_{T1}, C_{T1}) that produced the least reactance errors between modeled and simulated results of Z_{in}.

$$L_{T1} = 0.1587e^{4.551r_x} \text{ nH} \tag{3.29a}$$

$$C_{T1} = -11(r_x - 0.4534)^2 + 1.797 \text{ pF}, \tag{3.29b}$$

Since the patch is designed to have a length of $L = \lambda_r/2$ and the overlapping length of the feeding x_0 depends on L to have r_x constant, then (3.29a) and (3.29b) can be generalized as:

$$L_T = L_{T1}\frac{f_{0p1}}{f_{0p}} \text{ nH} \tag{3.30a}$$

$$C_T = C_{T1}\frac{f_{0p1}}{f_{0p}} \text{ pF} \tag{3.30b}$$

Thus, replacing (3.30a)–(3.30b) in (3.29a)–(3.29b) for a given f_{0p} in GHz:

$$L_T = \frac{0.4674}{f_{0p}} e^{4.551 r_x} \text{ nH} \tag{3.31a}$$

$$C_T = \frac{32.395}{f_{0p}} [0.1634 - (r_x - 0.4534)^2] \text{ pF, for } r_x \leq 0.05 \tag{3.31b}$$

As observed in (3.31a)–(3.31b), the feeding inductance is negligible at short overlaps, but it becomes significant as the overlap ratio increases. Also, the equivalent capacitance increases to a maximum at $r_x = 0.45$ and decreases as the r_x increases. The variation of the feeding inductance and capacitance (L_T, C_T) are shown in Fig. 3.10b,c as a function of the overlapping ratio r_x.

3.4.3 Feeding Equivalent Transmission Line

For short and moderate overlaps, the transmission line of Fig.3.9b can be ignored since the response does not get shifted and the input reactance increases almost linearly with the frequency, i.e., having an inductance. However, for large overlaps, an equivalent transmission line of length $x_0^{'}$ needs to be added to the LC feed circuit model, where $x_0^{'} \leq x_0$. Physically, this line may be due to the proximity between the open ends and the non-planar feature of the structure, which is more noticeable at large overlaps. Because the overlapping portion of the feeding is between the patch and the ground plane, the equivalent transmission line takes the form of a stripline (with impedance Z_{0s}) [99] instead of an embedded microstrip line (with impedance Z_{0u}) [98, 100]. Notice that the equivalent resonant resistance may be less than that plotted in Fig. 3.10a when including this equivalent transmission line. The feeding inductance and capacitance may not continue following the pattern pictured in Fig. 3.10b,c, as $r_x \to 1$, Q_p may decrease and R_p may get close to zero.

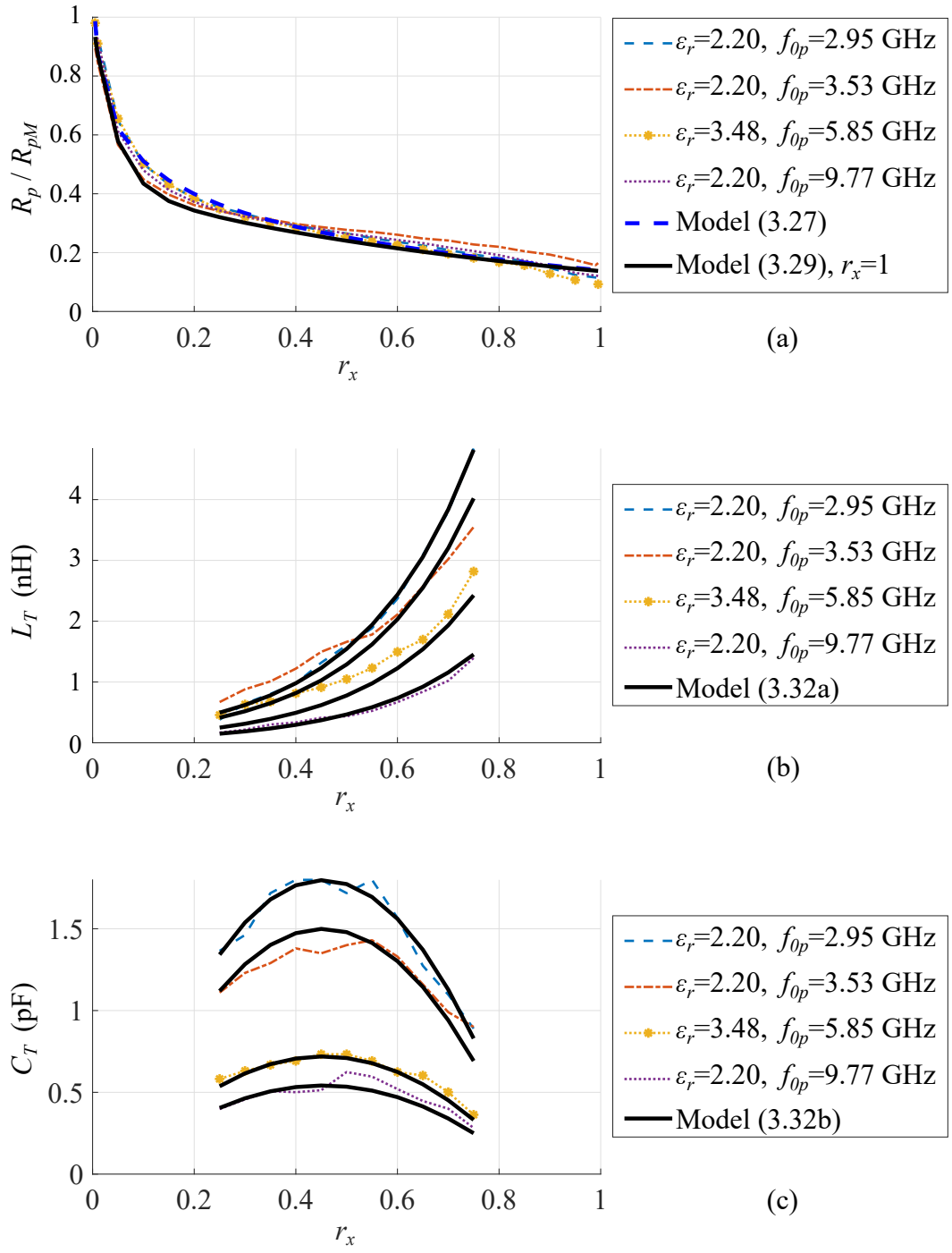

Figure 3.10: PC-MSPA circuit parameters over the feed's overlap ratio r_x. Family of curves for: (a) Normalized radiation resistance (R_p/R_{pM}). (b) Feeding inductance (L_T). (c) Feeding capacitance (C_T). The data points (colored plots) were obtained from simulated PC-MSPAs operating between 3 GHz and 10 GHz. The modeled traces (black plots) illustrate the characterization of the circuit feeding parameters for these PC-MSPAs.

3.4.4 Model Assessment

The proposed model is validated with simulated and measured results of the impedance of PC-MSPAs designed at 3 GHz (Design 1 or D1), 3.5 GHz (Design 2 or D2), 5.4 GHz (Design 3 or D3), and 9.4 GHz (Design 4 or D4). The proposed antenna design is shown in Fig. 3.7a,b and the dimensions of the proposed designs are listed in Table 3.4. In order to show the generalized capability of the proposed model, the proposed designs differ from those used to get the model equations. Different overlap ratios r_x are used to show the model assessment, regardless of the maximum return loss that the antenna gets at f_o. An assessment in both Z_{in} and S_{11} parameters is presented.

3.4.4.1 Performance in Simulated PC-MSPAs

The model performance using the de-embedded wave port in HFSS (ideal condition) is illustrated in Fig. 3.11 through a comparison between modeled and simulated responses of the input impedance and the S_{11} parameter. The results were obtained considering an ideal wave port in the simulated designs and de-embedding the port from the position $x = -(L_f - x_0)$ to $x = 0$. In addition, the values of the patch RLC resonator parameters are compared in Table 3.5 between the modeled and simulated values.

The plots in Fig. 3.11 show excellent agreement between modeled and simulated impedance responses when the model is validated using the de-embedded wave port in HFSS (ideal condition). A frequency shift is more perceptible in D2 as it has the lowest thickness. A resonant resistance shift is observed in D1, the electrically thickest design. Minimum errors are observed when comparing the modeled and simulated real parts of the design responses. Errors are slightly more perceptible in D2, primarily due to the frequency shift. The S_{11} plots of

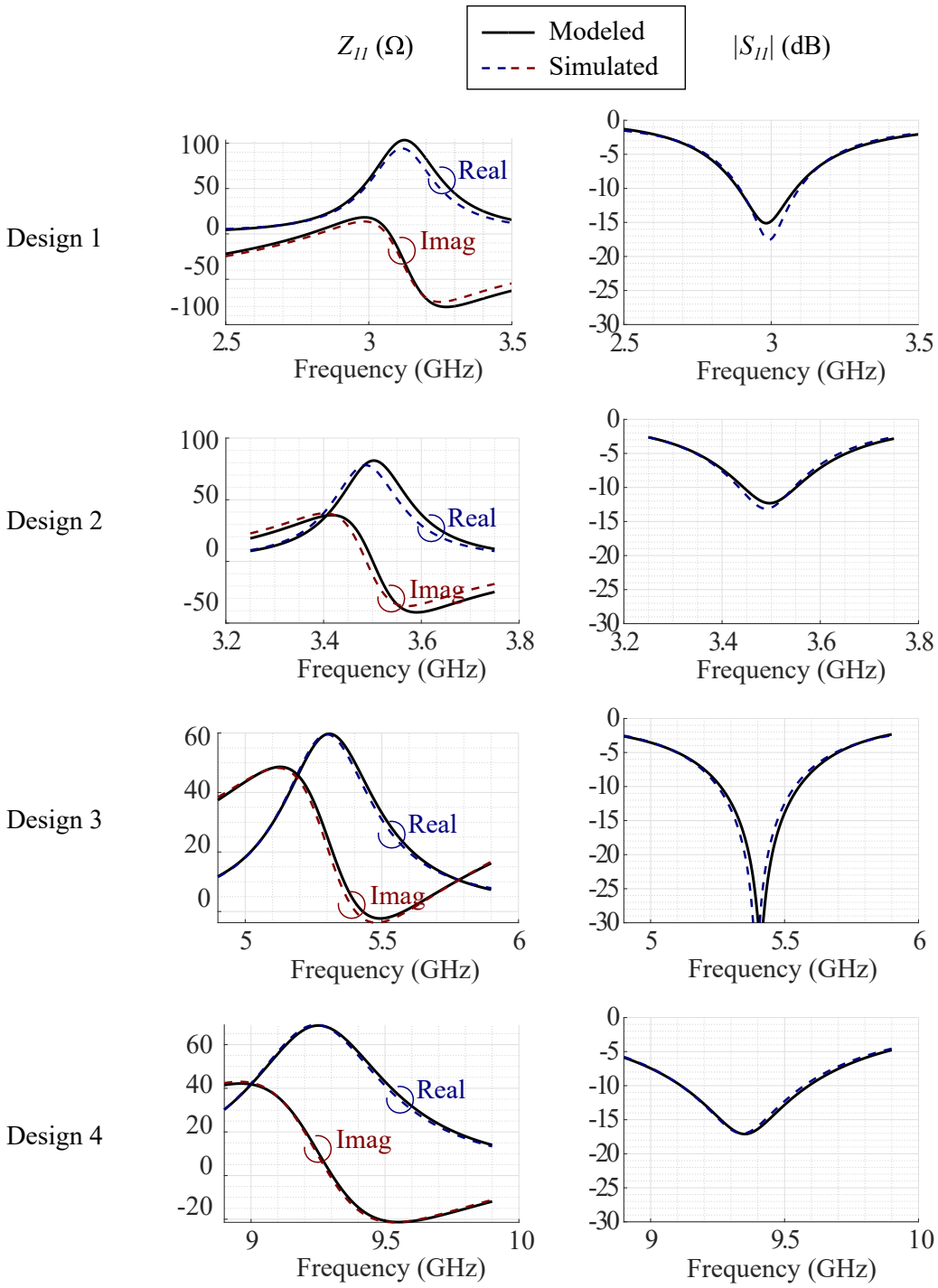

Figure 3.11: Model performance on simulated PC-MSPAs' frequency response. Comparison between modeled and simulated impedance responses $Z_{11}(\Omega)$, on the left column; and S_{11} (dB), on the right column. It shows an excellent agreement between modeled and simulated frequency responses of the designed PC-MSPAs along a wide range of frequencies.

Table 3.4: Antennas' design specifications.

Specification	Unit	D1 [70]	D2 [42]	D3 (this work)	D4 (this work)
f_o	GHz	3.0	3.5	5.4	9.4
$\varepsilon_1, \varepsilon_2$	-	2.2	2.2	2.2	2.2
h_1, h_2	mm	3.175	1.575	1.575	0.787
L, W	mm	27.7	26.1	16.6	9.65
r_x	-	0.25	0.50	0.70	0.60
L_f	mm	93.08	90	59.32	32.72
W_f	mm	9.00	4.55	4.55	2.30
L_g, W_g	mm	200	180	112	63.5
h_T	λ_0	0.063	0.037	0.057	0.049

Table 3.5: Performance of proposed model on simulated PC-MSPAs. Comparison between modeled and simulated patch parameters from the RLC resonator equivalent circuit. The proposed model delivers accurate characterization of the patch circuit properties in PC-MSPAs.

RLC parameter	Source	D1 [70]	Error (%)	D2 [42]	Error (%)	D3 (this work)	Error (%)	D4 (this work)	Error (%)
f_{0p}	Model	3.125	-	3.503	-	5.308	-	9.252	-
	Simul.	3.120	0.15	3.490	0.37	5.300	0.15	9.240	0.13
Q_p	Model	10.46	-	19.53	-	12.60	-	14.57	-
	Simul.	10.75	2.70	20	2.35	13	3.08	14.95	2.54
R_p	Model	103	-	81.7	-	59.7	-	68.8	-
	Simul.	94.1	9.88	78.0	4.78	59.5	0.28	69.1	0.39

"-" means *no data*. The errors consider the simulation data as references.

the second row of Fig. 3.11 show that the -10 dB bandwidth is well predicted, as is the resonant frequency of the four antenna designs, although some difference in the coupling level due to calculation errors in the R_p is observed in D1. The inductance L_T has a critical role in the accuracy of the feed reactance, especially in D3, which has a reactance response above $j0\ \Omega$. This accuracy would not have been possible if the model considered only a capacitor, as seen in the third row of Fig. 3.11.

The comparison of patch RLC parameters listed in Table 3.5 shows that the resonant frequency f_{0p} presents errors less than 0.5 %. This high accuracy is necessary because it is used as part of the required variables to calculate the other

two parameters (Q_p, R_p) and the feeding parameters (L_T, C_T). The quality factor presented errors less than 3.5 %, not showing the dependency of these errors on substrate thickness. However, the resonant resistance can be more accurately determined for antennas with thinner substrates.

3.4.4.2 Assessment using Fabricated PC-MSPAs

The assessment of the model performance using a coaxial probe feed (real condition) is performed through the comparison between the modeling, simulations, and measurements of antenna designs 2 and 3 of Table 3.4. Even though the antenna fabrication was intended to replicate the same specifications during the fabrication process, an air gap h_a and a slight displacement on the patch p_m occurred. The effect of fabrication imperfections is illustrated in Fig. 3.12. The model needs to consider this effect to have more accurate results. The air gap h_a is included in the model by reformulating the effective thickness used for the patch substrate h_2' (3.32) instead of the physical thickness h_2. Thus, the thickness ratio and the total thickness are also affected by h_2' in (3.33)–(3.34).

$$h_2' = h_2 + h_a \tag{3.32}$$

$$r_h' = h_2'/h_1 \tag{3.33}$$

$$h_T' = h_2' + h_1 \tag{3.34}$$

Moreover, the average relative permittivity [101] ε_r' is calculated as:

$$\frac{h_T'}{\varepsilon_r'} = \sum_{i=1}^{n} \frac{h_i}{\varepsilon_{r,i}} \tag{3.35}$$

The patch longitudinal displacement p_m along the $x-$axis is also considered in the model, especially to determine the overlap ratio. This value is a meaningful parameter needed to accurately determine the resonant resistance R_p. In

Fig. 3.12c, this shift is positive if the patch moves as indicated in the arrows, and negative if in the opposite direction. The inclusion of p_m in the model is done with an effective overlap ratio of l'_{0n} calculated from the expected overlap ratio r_x as in (3.36). These dimensions are listed in Table 3.6. The specifications not mentioned were already listed in Table 3.4. The modeled impedance Z_{in} from the reference position at $x = 0$ is transformed to the measurement position as Z_{in0}, as pictured in Fig. 3.12, located under the ground plane and connected through a 50 Ω coaxial cable and a probe.

$$r'_x = \frac{r_x L - p_m}{L} \tag{3.36}$$

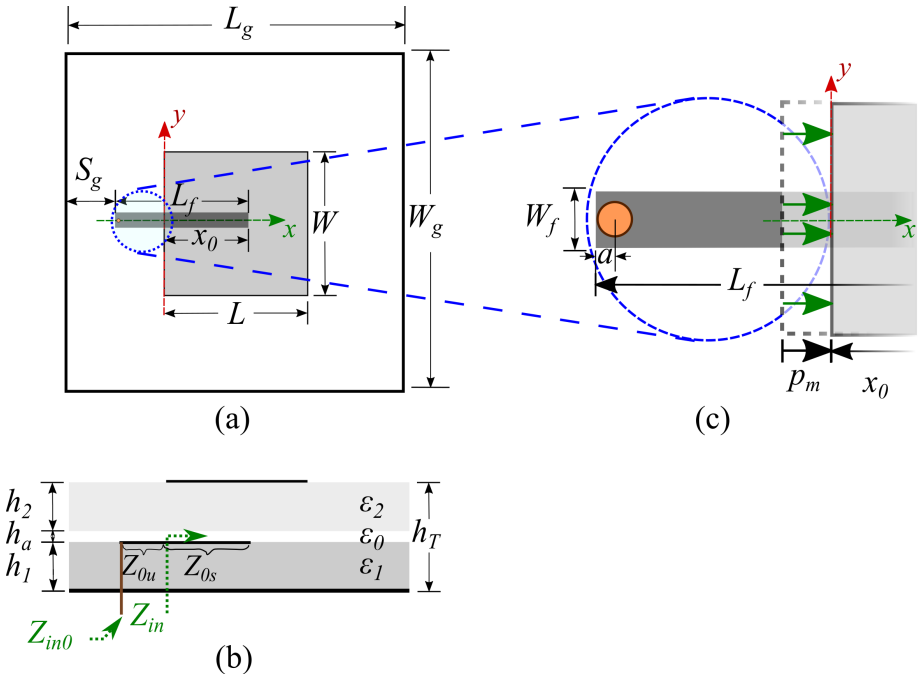

Figure 3.12: Geometry, dimensions, and setup for fabricated PC-MSPAs.
(a) PC-MSPA top view, (b) side view, with an air gap h_a between the substrates.
(c) An illustration of the patch longitudinal displacement p_m.
A coaxial probe has been placed under the proximity-coupled feeding for electrical connection with the vector network analyzer used in the experimental validation. The validation was performed by evaluating Z_{in0}.

Table 3.6: Fabricated S-band and C-band PC-MSPAs' specifications.

Specification		Unit	D2 [42]	D3 (this work)
Avg. relative permittivity	ε'_r	-	1.954	2.086
Estimated air gap	h_a	mm	0.37	0.15
Measured patch size	L, W	mm	26.3± 0.1	16.55 ± 0.1
Estimated patch displacement	p_m	mm	-2.00	0.85
Effective overlap ratio	r'_x	-	0.576	0.751
Space to antenna border	S_g	mm	65.71	40.60
Feeding length	L_f	mm	24.29	18.71

Hence, Fig. 3.13 provides a comparison between modeled, simulated, and measured values of the impedance and S_{11} parameter when the antennas include a coaxial connector under the specific location $x = -(L_f - x_0)$. This 50-Ω connector has an inner and outer radius of 0.65 mm and 2.10 mm, respectively, and the dielectric is Teflon-based material ($\varepsilon_r = 2.0$). Table 3.7 lists a comparison between measured, simulated, and modeled resonant frequencies f_o, in-bandwidth minimum f_l and maximum f_u frequencies, and the impedance bandwidth of the antenna designs from the S_{11} parameter data.

The model validation using a coaxial probe also presents good agreement despite the additional calculations from the transmission line transformations. The line transformations converted the impedance response from $x = 0$ to the actual port location. As seen in Fig. 3.13, the impedance response and the reflection coefficient are very well predicted. A slight difference is noticed, but a good match in the resonant frequency and the bandwidth is obtained.

The model predicted the resonant frequency in both cases with errors less than 0.2 %. The measurement uncertainty was also counted in the model computation, as the patch length directly affects f_{0p}. Considering the frequency interval where $|S_{11}| < -10$ dB, the model can predict the impedance bandwidth with errors less than 1 %, as listed in the last rows of Table 3.7.

Table 3.7: Performance of proposed model on fabricated PC-MSPAs.
The comparison between modeled, simulated and measured values of the impedance bandwidth and resonant frequencies shows a great performance of the impedance model in fabricated PC-MSPAs in the S- and C- bands.

PC-MSPA bandwidth information	Source	D2 [42]	Error (%)	D3 (this work)	Error (%)
Resonant frequency (f_o)	Modeled	3.655	-	5.517	-
	Simulated	3.648	0.18	5.509	0.15
	Measured	3.650	0.12	5.508	0.16
Minimum frequency in bandwidth (f_l)	Modeled	3.578	-	5.400	-
	Simulated	3.565	0.36	5.378	0.41
	Measured	3.561	0.48	5.374	0.48
Maximum frequency in bandwidth (f_u)	Modeled	3.731	-	5.628	-
	Simulated	3.729	0.05	5.629	0.02
	Measured	3.728	0.07	5.632	0.07
Impedance bandwidth ($\%BW$)	Modeled	4.19 %	-	4.13 %	-
	Simulated	4.50 %	0.31	4.56 %	0.42
	Measured	4.58 %	0.40	4.68 %	0.55

"-" means *no data*. The errors consider the simulation and measurement data as references.

3.4.5 PC-MSPA Radiation Patterns

The expressions of the far-field radiation patterns of a PC-MSPA over a theoretical infinite ground plane are given in (3.37a)–(3.37b) using the patch dimensions and substrate thickness [102].

$$E_\theta \propto -\frac{\cos\phi \cos P_L \operatorname{sinc} P_W \operatorname{tanc} P_h}{1 + j\tan(P_h)} \tag{3.37a}$$

$$E_\phi \propto \frac{\cos\theta \sin\phi \cos P_L \operatorname{sinc} P_W \operatorname{tanc} P_h}{1 + j\tan(P_h)} \tag{3.37b}$$

where $P_L = kL/2 \sin\theta\cos\phi$, $P_W = kW/2\sin\theta\sin\phi$, $P_h = kH_T\cos\theta$, $\operatorname{sinc}\alpha = (\sin\alpha)/\alpha$ and $\operatorname{tanc}\alpha = (\tan\alpha)/\alpha$ are defined in [102]. The directivity D for MSPAs is typically around 7 dBi, and the realized gain G can be calculated from the antenna's impedance response as $G = D(1 - |S_{11}|^2)$, where S_{11} can be estimated from Z_{in} as in (2.121). This relation connects the MSPA's impedance response modeled in this work with its radiation properties.

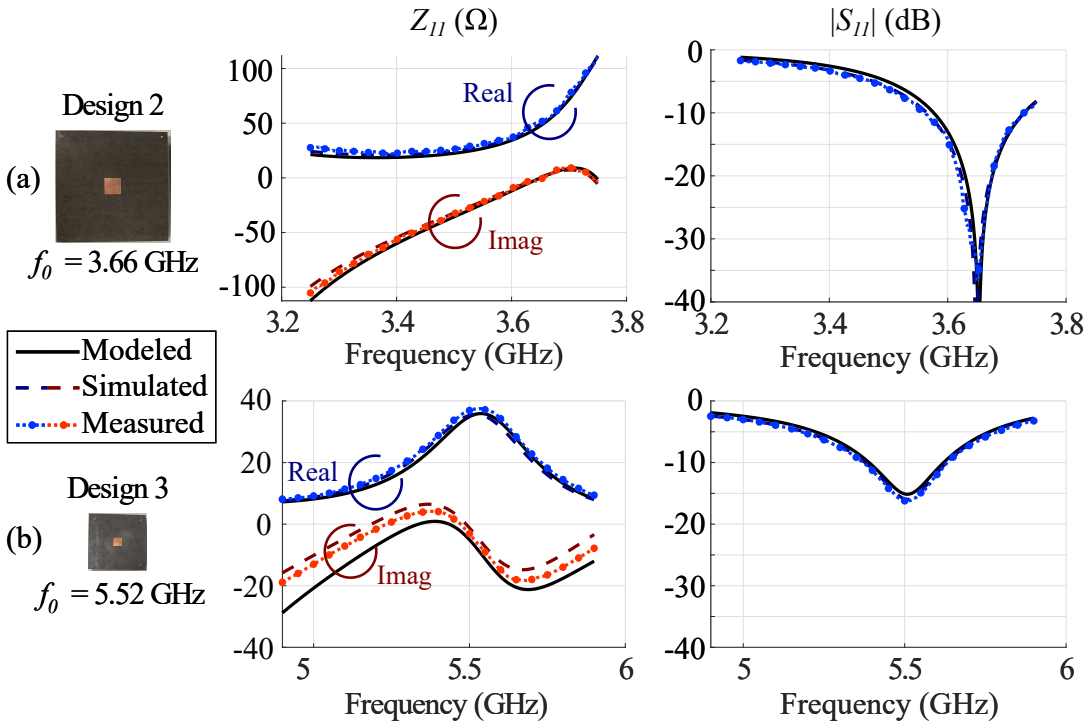

Figure 3.13: Model performance on fabricated PC-MSPAs' frequency response. Comparison between modeled, simulated and measured impedance (Z_{11}) and reflection coefficient (S_{11}) over frequency. Experimental validation performed for the fabricated antennas Design 2 (S-band) and Design 3 (C-band). These overlapping plots successfully validate the proposed model with experiment.

The radiated fields produced by the PC-MSPA can be obtained using the equivalent radiating slots using the patch cavity model [24]. The length of each slot is represented by the width of the patch (W). The patch length (L) dictates the separation between slots. In the previous expressions, the term sinc Z can be ignored since $\sin(Z)$ can be approximated to Z when electrically-thin substrates are used. The modified second Ludwig's definition of cross-polarization is used [89, 90]. According to [89], there are two variants of this definition, depending on the feeding orientation. The variant 2-I [89] is used for patches fed along the x-axis, as pictured in Fig. 3.12. The normalized simulated and measured radiation patterns of antenna designs 2 and 3 are shown in Fig. 3.14, where a good agreement between them is found for the E-, H-, and D- planes.

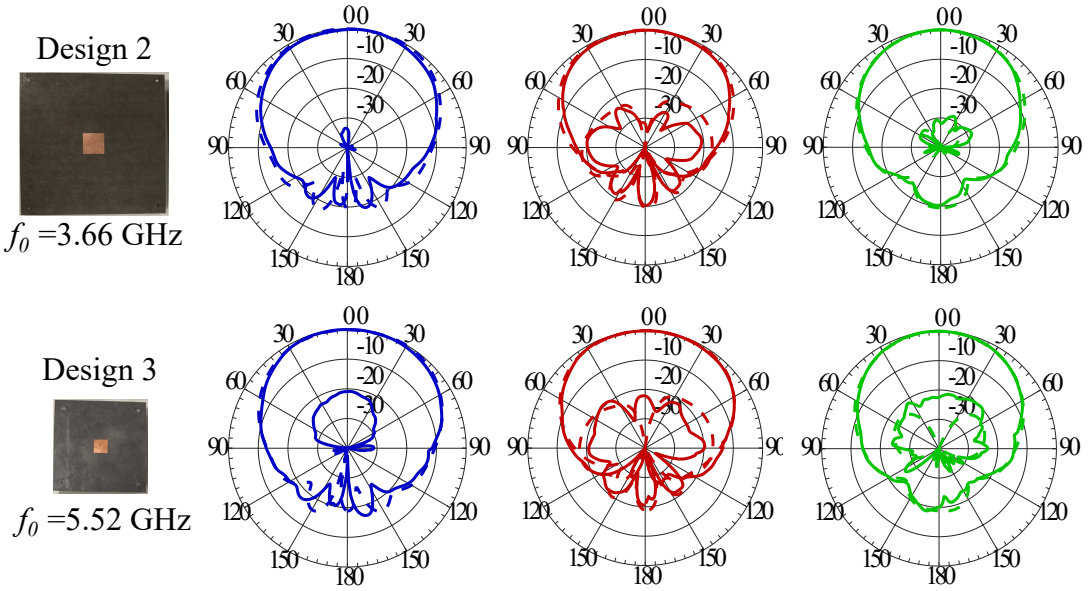

Figure 3.14: Normalized radiation patterns for fabricated PC-MSPAs.
The traces correspond to the co- and cross-polarized components in the *E*-, *D*- and *H*-planes, from left to right. The dashed traces are linked to simulated PC-MSPAs, and the measured patterns are depicted with solid lines. The antennas used for this comparison correspond to Design 2 and Design 3 of Table 3.4, which are in the S- and C- bands, respectively.

3.5 Modeling PC-MSPAs with Differential Feeding

Differential feeding (DF) has the intrinsic feature of broadening bandwidth due to its topology [103]. The geometry of a DF-PC-MSPA is shown in Fig. 3.15, and it comprises of three conductor layers on two substrates. The feed is composed of two transmission lines, which are excited with the same signal amplitude but with a phase difference of 180 degrees, i.e. a differential feeding setup is established in this antenna. The patch ratios r_p (3.1) and r_h (3.2) are also crucial to model DF-PC-MSPAs.

Mathematically modeling DF-PC-MSPAs in this work will contribute on a novel strategy to evaluate its performance, e.g. an estimation of its impedance behavior. The previous section listed an analytical formulation to model single-

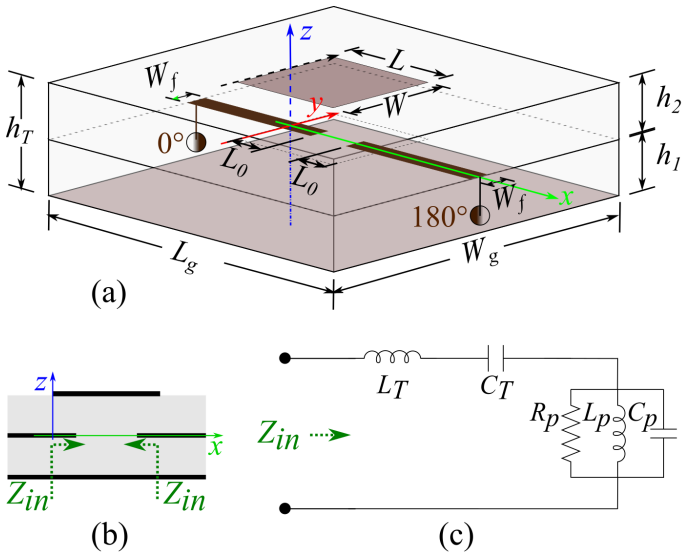

Figure 3.15: Geometry and equivalent circuit for differentially fed PC-MSPAs. (a) 3D geometry, (b) front view, (c) equivalent circuit. Since the feeding transmission lines have an overlapping section of less than half of the patch's length, the equivalent model for DF-PC-MSPAs is simplified to an LC-RLC electric circuit at each port.

fed (SF) PC-MSPAs. Nonetheless, due to the different field distributions under the patch, as shown in Fig. 3.16c,d, an inspection of the impedance response of SF-PC-MSPAs and DF-PC-MSPAs is performed.

The impedance behavioral trends of differentially fed PC-MSPAs compared with the one with single feeding can be illustrated in Fig. 3.16a,b. A PC-MSPA was designed and simulated to show the feeding difference. This antenna consists of two Rogers™ 5880 substrates ($\varepsilon_r = 2.2, \tan\delta = 0.0009$, $h_1 = h_2 = 125$ mils), a square patch of 32 mm, 50-Ω transmission lines, and a square ground plane set to 200 mm each side. Different feeding positions have been included to observe the trends. By comparing the bold and thin lines in Fig. 3.16a, it can be noticed that the patch resonant frequency, i.e. the frequency where the maximum of the real part of the impedance occurs, shifts to higher values. Besides, the frequency intervals with the half of the maximum resistance become narrower, i.e. the

patch quality factor gets higher. Also, the maximum resistance, which occurs at resonance, increases. Similar trends are seen in the imaginary parts of the antenna impedance.

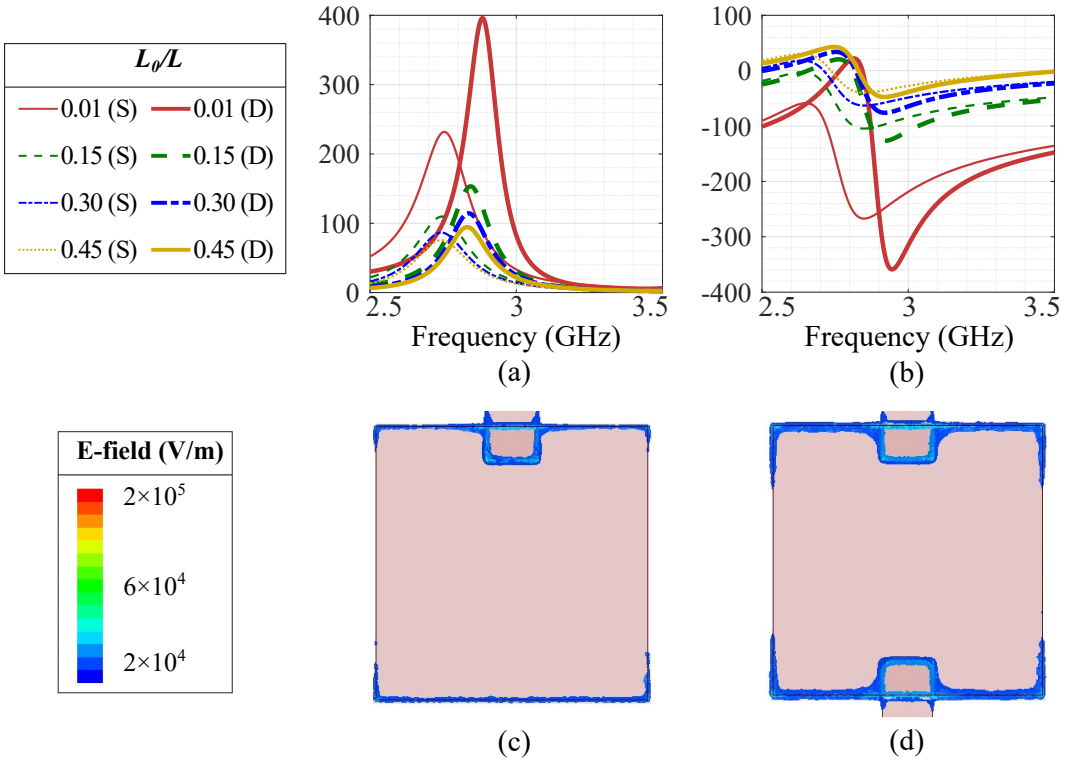

Figure 3.16: Impact of the feeding structure for PC-MSPAs.
Variations of impedance response of a PC-MSPA with different feed lengths and feeding setups: (a) Real part of Z_{in}, (b) Imaginary part of Z_{in}, (c) Fields in SF-PC-MSPAs, and (d) Fields in DF-PC-MSPAs. From these differences compared with PC-MSPAs with single feeding, a reformulated circuit model is proposed, containing ratio formulations for the patch's RLC parameters.

The analytical model for PC-MSPAs provided in Section 3.4 enables an accurate analysis of this single-fed antenna. This section provides an analytical model for DF-PC-MSPAs. Section 3.5.1 delivers the mathematical formulation of the equivalent electric circuit of DF-PC-MSPAs. Section 3.5.2 illustrates the model accuracy by assessing the reflection coefficients between modeled and simulated DF-PC-MSPAs at 3 GHz and 9 GHz.

3.5.1 Proposed Model

The impedance response of a PC-MSPA can be modeled by an equivalent electric circuit composed by a RLC parallel resonator [24], in series with a LC in-series segment (Section 3.4.2). By this means, the patch follows the impedance pattern of the RLC resonator, while the impedance contribution from the feeding comes from the LC segment. This work provides new equations for the shifting factors in the patch resonant frequency and in the patch quality factor, as well as a reformulation of the patch resonant resistance for SF-PC-MSPAs. In the next lines, a set of mathematical equations will be provided, which complete the description of this proposed model.

3.5.1.1 Patch Resonant Frequency (f_{0p})

Considering that the feeding transmission lines end along the patch length and on the middle of its width, as shown in Fig. 3.15, then the dominant propagation mode can be excited for radiation. For SF-PC-MSPAs, the patch's resonant frequency f_{0p} follows the formulations in (3.20), which are based on the cavity model [41] and consider the substrate thickness ratio r_h (3.2). Then, the value of f_{0p} can be calculated for DF-PC-MSPAs as follows:

$$f_{0p} = f_{0r} F_{f0} \frac{f_{0p}^{(D)}}{f_{0p}^{(S)}} = \frac{c_0}{2L_e\sqrt{\varepsilon_{rep}}} F_{f0} \frac{f_{0p}^{(D)}}{f_{0p}^{(S)}}, \tag{3.38}$$

$$\frac{f_{0p}^{(D)}}{f_{0p}^{(S)}} = 1 + \left(\frac{h_T}{\lambda_{0r}}\right)^2 \left[21.17e^{-0.75r_h} + 4.83e^{-7.3r_x}\right] \tag{3.39}$$

where $c_0 = 3\times10^8$ m/s, $L_e = L + 2\Delta L$ and ε_{rep} are defined in (2.98)[93] and (2.97), respectively. The factor F_{f0} is defined in (3.20) as a shifting multiplier from the equivalent resonant frequency of the same patch with a single probe feeding to the one with single proximity-coupled feeding. The factor $f_{0p}^{(D)}/f_{0p}^{(S)}$ introduced in

(3.39) counts the frequency shift of PC-MSPAs due to the differential proximity-coupled feeding, in accordance to the trends observed in Fig. 3.16. This factor is illustrated in Fig. 3.17a,d, and in Fig. 3.18a,d.

3.5.1.2 Patch Quality Factor (Q_p)

The quality factor of the modeled RLC resonator that accounts for the patch (Q_p) [49] comes from the dielectric, the conductor, the radiation, and the surface waves. Thus, Q_p can be computed as in (2.102), and comprises the dielectric loss Q_d, conductor loss Q_c, radiation Q_{rad}, and surface waves Q_{sw}. Since Q_{rad}, the portion of Q_p that comes from radiation, generally possesses the lowest value among the other values (Q_d, Q_c, Q_{sw}), a reformulation has been performed to provide more accuracy. This reformulation has been done by comparing the quality factors from the real part of impedance responses of SF-PC-MSPAs with lossless materials, so that $Q_p = (Q_{rad}^{-1} + Q_{sw}^{-1})^{-1}$. Then, Q_p can be rewritten for DF-PC-MSPAs as:

$$Q_p = \left[\tan\delta + \frac{1}{h_T\sqrt{\pi f_{0p}\mu\sigma}} + \frac{Q_{rp}^{(S)}}{Q_{rp}^{(D)}} {r_h}^{0.24} \frac{16}{3}\frac{pc_1}{\varepsilon_r}\frac{h_T}{\lambda_{0p}}\frac{W}{L}\frac{1}{e_r^{hed}}\right]^{-1}, \tag{3.40}$$

$$\frac{Q_{rp}^{(D)}}{Q_{rp}^{(S)}} = 1 + \frac{4.32}{100}\frac{e^{36h_T/\lambda_{0r}}}{{r_h}^{1.25}}\left(\frac{L}{W}\right) + \frac{1.54}{100}\frac{e^{60h_T/\lambda_{0r}}}{r_h}\left(\frac{25L}{44W} + \frac{19}{44}\right)e^{-10r_x} \tag{3.41}$$

where the factor ${r_h}^{0.24}$ counts for the influence of the substrate thickness ratio in PC-MSPAs. The variables $\tan\delta$, μ and σ are the substrate loss tangent, the substrate permeability, and the substrate's foil conductivity. The values of p, c_1, and e_r^{hed} are defined with more detail in [49]. Besides, the factor $Q_{rp}^{(D)}/Q_{rp}^{(S)}$ (3.41) multiplies Q_{rad} when the PC-MSPA presents a differential feeding setup. This shifting factor is pictured in Fig. 3.17b,e, and in Fig. 3.18b,e.

3.5.1.3 Patch Resonant Resistance (R_p)

The resonant resistance R_p in square PC-MSPAs is expressed as in (3.42). By including the variations on the substrate's dielectric constant, then the normalization factor K_R and the shape curve F_{Rp} are expressed as in (3.43) and (3.44), respectively.

$$R_p = \frac{4}{\pi}\mu_r\eta_0 Q_p \frac{h_T}{\lambda_{0p}} K_R F_{Rp} \tag{3.42}$$

$$K_R = 1.1\varepsilon_r^{-0.02\lambda_{0p}/h_T}(W/L)^{0.75} r_h^{-0.8+4.44\sqrt{h_T/(\varepsilon_r\lambda_{0p})}} \tag{3.43}$$

$$F_{Rp} = Ae^{-p_1 r_x} + (1-A)e^{-p_2 r_x}, \tag{3.44}$$

where

$$A = 0.58 - 1.8e^{-270\frac{h_T}{\lambda_{0r}}\frac{1}{\varepsilon_r}} + \Big[0.1732 + 130.8\Big(\frac{h_T}{\lambda_{0r}}\frac{1}{\varepsilon_r} - 0.03135\Big)^2\Big]\ln r_h \tag{3.45}$$

$$p_1 = \frac{2}{(h_T/\lambda_{0r})\sqrt{\varepsilon_r} + 0.035} \tag{3.46}$$

$$p_2 = 1.35 r_h^{0.75}\Big[1 - 1.25e^{-50\frac{h_T}{\lambda_{0r}}\varepsilon_r^{-0.63}}\Big] \tag{3.47}$$

The variations made included total thicknesses (from 31.25 mils to 250 mils at 3 GHz), patch length over width ratio (0.75 to 1.25), relative permittivity (1.1, 2.2, and 4.4), and substrate thickness ratio (from 0.67 to 1.50). The shifting factor $R_p^{(D)}/R_p^{(S)}$ is built by the ratio of calculating R_p (3.42) for DF-PC-MSPAs and SF-PC-MSPAs. This factor is plotted in Fig. 3.17c,f, and in Fig. 3.18c,f.

3.5.1.4 Feeding Circuit (L_T, C_T)

The impact of the feeding on the impedance response of PC-MSPAs can be evaluated by the reactances produced by an inductor and a capacitor connected in series. Let be the feeding inductor named L_T, and the feeding capacitor, C_T. Then, the values of L_T, C_T are expressed as in (3.31a) and (3.31b), respectively.

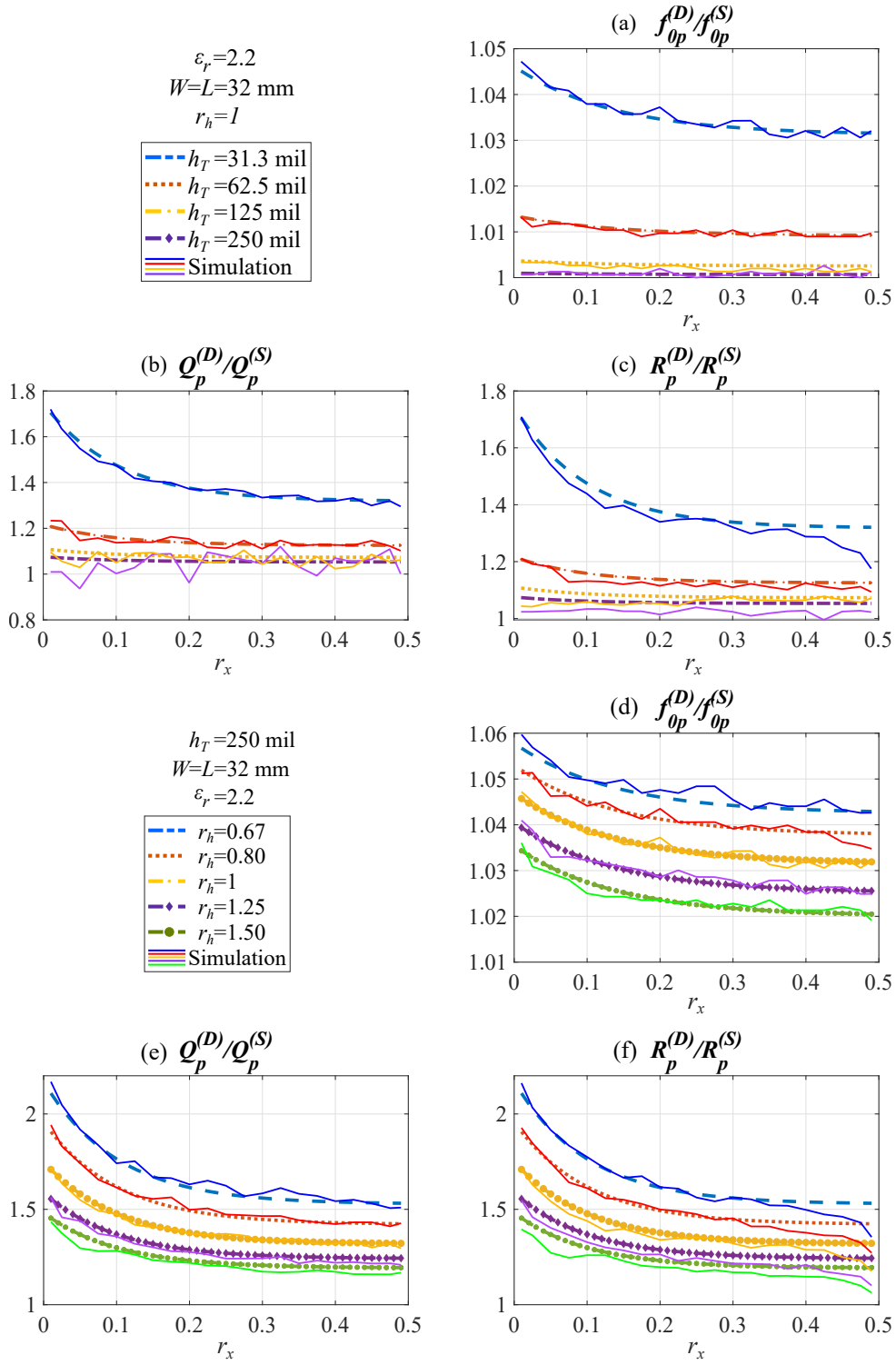

Figure 3.17: Patch resonator-parameter shifting factors for DF-PC-MSPAs from SF-PC-MSPAs at different substrate thicknesses and ratios at 3 GHz.
The dashed lines show high model accuracy for simulated DF-PC-MSPAs at different dielectric thicknesses. Simulated values are plotted in solid lines.

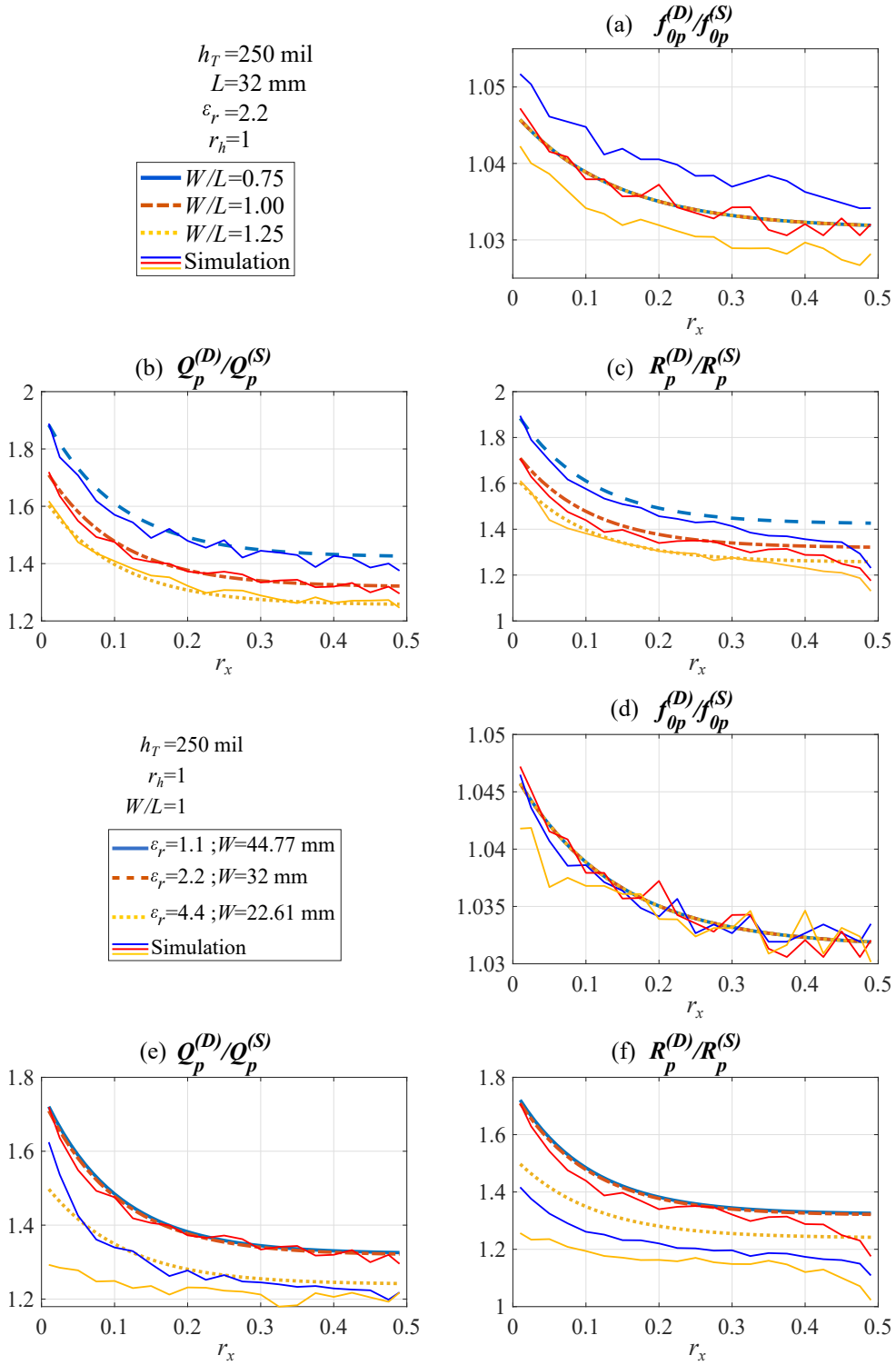

Figure 3.18: Patch resonator-parameter shifting factors for DF-PC-MSPAs from SF-PC-MSPAs at different dielectrics and patch squarenesses at 3 GHz.
The dashed lines show high model accuracy for simulated DF-PC-MSPAs at different dielectric thicknesses. Simulated values are plotted in solid lines.

3.5.1.5 Impedance Response

For each port, the input impedance at the origin of the overlap between the patch and the feed can be written from the electric circuit of Fig. 3.15c as:

$$Z_{11} = Z_p + Z_f = \Big(\frac{1}{1/R_p + 1/j\omega L_p + j\omega C_p}\Big) + \Big(j\omega L_T + \frac{1}{j\omega C_T}\Big), \tag{3.48}$$

where Z_p and Z_f are the impedances of the patch resonator, and of the feed, respectively. Also, the values of L_p, and C_p can be obtained by replacing the values from (3.38), (3.40), and (3.42) in the expressions (2.105b)-(2.105c).

From the theory of differential feeding setup [104, 105], the assessment of these antennas is made through the differential input impedance Z_{11d}. Let be the ports named "1" and "2", one in front of the other one along the PC-MSPA, and configuring differential feed. Then, the impedance parameters generated in this bi-port network are: Z_{11}, Z_{12}, Z_{21}, and Z_{22}. In each port there is one self impedance (Z_{11}, Z_{22}), and one mutual impedance (Z_{12}, Z_{21}). For symmetrically-fed microstrip antennas:

$$Z_{11} = Z_p + Z_f \tag{3.49a}$$

$$Z_{12} = -Z_p \tag{3.49b}$$

$$Z_{21} = -Z_p \tag{3.49c}$$

$$Z_{22} = Z_p + Z_f, \tag{3.49d}$$

Then, applying the definition of differential input impedance Z_{11d} [105]:

$$\begin{aligned} Z_{11d} &= Z_{11} - Z_{21} - Z_{12} + Z_{22} \\ &= 2(Z_p + Z_f) - 2(-Z_p) \\ &= 4Z_p + 2Z_f \end{aligned} \tag{3.50}$$

Thus, the impedance response of a DF-PC-MSPA can be evaluated by the expression derived in (3.50). Furthermore, previous work already has demonstrated that the contribution of a patch in differential feeding gets multiplied by four [105], which is noticed in the first term of (3.50).

3.5.2 Model Assessment

To assess the formulations made in this work, different variations have been made. In Fig. 3.17, the proposed shifting factors of (3.39) and (3.41) are evaluated and compared with the observed shifting factors from simulated antenna variations in total thickness, substrate thickness ratio, patch size ratio, and permittivity. Also, the differential impedance of two antennas in S- and X-band is evaluated to assess the accuracy of the impedance model. The antenna specifications are listed in Table 3.8, and the impedance responses are pictured in Fig. 3.19. Future work will aim to experimentally validate this model.

Table 3.8: Assessed antennas' specifications.

Specification		Unit	Design 1	Design 2
Relative permittivity	ε_r	-	2.2	2.2
Loss tangent	$\tan\delta$	mm	0.0009	0.0009
Patch size	L, W	mm	24.2	8
Total substrate thickness	h_T	mm	3.175	1.575
Substrate thickness ratio	r_h	mm	1.00	1.00
Feed-to-patch overlap ratio	r_x	-	0.125	0.125
Cell size	L_g	mm	200	50

The plots in Fig. 3.17 suggest that the proposed shifting factors $f_{0p}^{(D)}/f_{0p}^{(S)}$ and $Q_{rp}^{(D)}/Q_{rp}^{(S)}$ follow accurately the observed shifts in DF-PC-MSPAs. As shown in Fig. 3.17a–c, the proposed model allows the prediction the impact of the differential feeding in PC-MSPAs in a wide range of thickness, from $0.008\lambda_0$ (31.25 mils at 3 GHz) to $0.064\lambda_0$ (250 mils at 3 GHz). Moreover, the proposed model follows

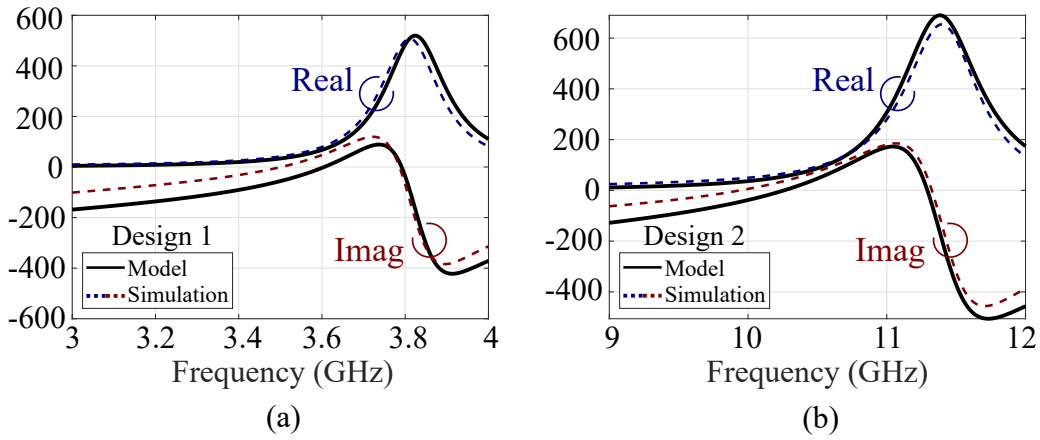

Figure 3.19: Comparison between modeled and simulated impedance responses for PC-MSPAs in the S- and X-bands.
The proposed model allows accurate estimation of the real part of the input impedance of DF-PC-MSPAs up to 12 GHz. Future work on modeling the differential feeding will further enhance the accuracy of the imaginary part.

the perceived variations in the RLC parameters when the substrate thickness ratio varies, as noticed in Fig. 3.17d–f. This is an important finding since the main variable that affects the performance of PC-MSPAs is this substrate ratio, which even sets the limits of maximum bandwidth that it can get, as found in [70]. The plots in Fig. 3.18a–c illustrate the accuracy of the proposed model on following the shifts in the patch resonator parameters. Despite that the model does not include a variation in patch length over width ratio, it does not produce deviations more than 0.5 % in the estimation. Furthermore, it is observed that the proposed model can follow accurately the variations in the patch resonant frequency. It is also observed that the proposed model works best with dielectric constants around 2.2, as suggested in Fig. 3.18d–f. This optimization is advantageous since many broadband antennas are developed with materials with similar dielectric constants.

Fig. 3.13 shows that the model accurately predicts the impedance response of the simulated S-band and X-band antennas. The real part is followed almost

completely, while the imaginary part has some slight variations outside the resonance. These results suggest that the proposed shifting factors allow getting accurate estimation of the RLC resonator parameters. They also suggest that the proposed work can be enhanced by including a further analysis of the impact of the differential feeding on the LC-series feed.

Consequently, the equivalent electrical circuit of a PC-MSPA can still be modeled as an RLC parallel circuit in series with a LC series circuit. However, this circuit model required additional reformulation to be accurate for DF-PC-MSPAs. The proposed model enables an estimation of the differential impedance response of DF-PC-MSPAs proving an accuracy less than 1 % in the patch resonance frequency. Also, the shifting factors in the patch quality factor and resonant resistance show a very good agreement between analytical model estimation and simulation in Ansys™ HFSS. Finally, the validations in the S- and X-bands showed a high accuracy in the estimation of the impedance response of DF-PC-MSPAs.

3.6 Summary

This chapter has provided several analytical models for PC-MSPAs. These models include new analytical guidelines to geometrically design PC-MSPAs, an advanced formulation to estimate its impedance bandwidth, an improved equivalent electric circuit to model the impedance response of these antennas. A new model for PC-MSPAs with differential feed has been also introduced.

The proposed guidelines to design a PC-MSPA with optimum bandwidth has been proposed. Two fundamental geometrical variables identified in this study are the feed-to-patch ratio and the substrate thickness ratio. Keeping the appropriate feed-to-patch ratio and patch dimensions ensures the antenna resonance in the user's desired operation frequency. Moreover, an optimum substrate thickness

ratio has been found to maximize the impedance bandwidth for a given feed substrate.

The proposed bandwidth model assumes a two-layered (thin or thick) PC-MSPA with the design procedure guidelines provided in this chapter. An extensive mathematical analysis of this antenna has been undertaken at several levels of design complexity to evaluate the robustness of proposed expressions. Generic expressions used to calculate the impedance bandwidth of edge, and probe-fed microstrip patch antennas have been discussed and compared with the proposed model. Although those expressions from previous work can be used for PC-MSPAs, they do not provide an accurate estimation of the bandwidth of a PC-MSPA.

Several PC-MSPA antennas were designed and fabricated with different materials, thicknesses, bandwidth requirements, and frequency bands. In all cases, simulated and measured results agree very well with results obtained from the proposed analytical model. Errors between the proposed analytical model and simulation and measurement are less than 3.1 %. The proposed models are primarily valid for dielectric constants between 2.2 and 6.15 and feed substrate thickness less than $0.1\lambda_r$.

Besides, an updated and accurate EM model of the PC-MSPA has been proposed and validated. It consisted of an electric circuit with the corresponding mathematical formulations for the circuit parameters. The relative position of the feed along the patch was defined by the ratio r_x. This ratio was used to develop an exponential-based equation for the resonant resistance and a frequency-based equation for the feeding capacitance and inductance.

The proposed equivalent circuit and equations allowed a simple but accurate model to be built for the PC-MSPA. The model was validated with antenna

designs on S-, C-, and X-bands. In all cases, the feed and patch had a moderate overlap ratio. Thus, the calculated -10 dB frequency interval and bandwidth presented errors of less than 1 % when comparing simulated and measured results, despite the differences in the coupling level at frequencies near the resonance. The differences in the coupling level may be decreased by adjusting the equation of the patch's resonant resistance. Also, the far-field radiation patterns presented high symmetry and moderately high cross-polarization isolation levels, showing that the PC-MSPA model can help build a design with a highly accurate predicted impedance response.

Furthermore, this chapter introduced an analytical model to estimate the impedance response of PC-MSPAs with differential feeding. This model includes several formulations to quantify the impact of the differential feeding in the patch resonator parameters. These formulations were expressed as shifting factors, which are geometry dependent. With this formulation, the proposed model accurately estimate the real part of the impedance response. Future work aims to analyze the impact of the differential feeding in the circuit parameters L_T and C_T, and in the antenna's input reactance.

Chapter 4

Challenges and Design Trade-offs for EM Modeling of Microstrip Patch Antennas up to the Sub-THz Band

> *In some strange way, any new fact or insight that I may have found has not seemed to me as a "discovery" of mine, but rather something that had always been there and that I had chanced to pick up.* —Subrahmanyan Chandrasekhar

Characterizing antenna materials' electrical and geometrical properties is necessary for modeling and design at mmWave and sub-THz bands. The dielectrics and conductors can no longer be considered constant, flat, and smooth at such frequencies. Moreover, as the frequencies approach the mmWave band and above, the material dimensions are more comparable with the free-space wavelength. Then, having an advanced material characterization over frequency becomes imperative to acquire reliable antenna designs.

As demonstrated in Chapter 2 and Chapter 3, it is possible to model MSPAs below 30 GHz. The antenna materials' geometry and electrical properties are the input information on these models. Then, the current theories, physical models, and mathematical formulations transform the above input data into EM-related variables, such as the resonant frequency, quality factor, and resonant resistance. The models then deliver a minute description of the antenna behavior as impedance frequency response.

This chapter thoroughly reviews antenna materials' geometrical and electrical properties, the challenges, design trade-offs that traditional EM modeling faces, and several strategies to make antenna modeling functional up to the sub-THz band. In the first section, the constitutive parameters of matter are reviewed, showing a perspective of the electrical properties that will be analyzed in the following sections. Then, an overview of antennas commonly used between 30 GHz and 300 GHz is given, including an overview about materials and fabrication techniques.

The second half of this chapter focuses on analyzing the effects of the material imperfections above 30 GHz, including an equivalence model that enables better modeling up to 300 GHz. The effects of material anisotropy and frequency dispersion in antennas are discussed for dielectrics, and the effects of the material thickness and RMS surface roughness are analyzed for conductors. In both cases, this work describes the consequences of these imperfections to EM modeling and proposes modeling strategies that will be applied in Chapter 4 and Chapter 5. At a glance, these strategies cover an equivalency roughness model by including the frequency-dependent equivalent conductivity and a brand-new set of modifications to the cavity model for MSPAs.

This chapter provides an equivalency model to account for the effects of the conductor surface roughness in the insertion losses and phase delays. This work analyzes diverse mathematical roughness models from previous work and proposes an improved formulation to quantify the losses in rough conductors as a frequency-dependent equivalent conductivity. The phase delays in rough conductors are also analyzed. A new formulation for the design dielectric constant is presented to model the effect of the conductor roughness in the phase delay of transmission lines.

4.1 Material Constitutive Parameters

The electrical behavior of a material depends on the intensity of the EM fields applied through it and on the atomic properties of the composing matter. The effects of applying an EM field on the matter impacts both microscopic and macroscopic level. On a microscopic level, each atom or its fundamental particles get arranged in the direction of the applied field. The sum of all the atomic arrangements creates electric and magnetic flows and electric currents on a macroscopic level. This section reviews the constitutive parameters of matter, namely the electric permittivity (ε), the magnetic permeability (μ), and the electric conductivity (σ). The primary bibliographic source used to describe this section is found in [77].

4.1.1 Electric Permittivity (ε)

A material may support a higher electric flux than the vacuum when an electric field is applied since its atomic positive and negative charges can have a directional arrangement. The phenomenon of arranging these fundamental particles is known as *electric polarization*. Let be an electric field $\mathbf{E_0}$, then the associated electric flux density $\mathbf{D_0}$ in the vacuum is written as:

$$\mathbf{D_0} = \varepsilon_0 \mathbf{E_0} \tag{4.1}$$

The term ε_0 is the electric permittivity of vacuum, which is 8.85 pF/m. At a macroscopic level, the electric polarization is quantified by the polarization vector $\mathbf{P}$. Consequently, the electric flux density increases to $\mathbf{D}$ as in (4.2).

$$\begin{aligned} \mathbf{D_0} + \mathbf{P} &= \varepsilon_0 \mathbf{E_0} + \mathbf{P} \\ \mathbf{D} &= \varepsilon_0 \mathbf{E_0} + \mathbf{P} \end{aligned} \tag{4.2}$$

The polarization vector $\mathbf{P}$ is related to the electric field $\mathbf{E_0}$ through the electric susceptibility χ_e, or $\mathbf{P}= \varepsilon_0\chi_e\mathbf{E_0}$. Then, (4.2) can be rewritten as:

$$\begin{aligned}\mathbf{D} &= \varepsilon_0\mathbf{E_0} + \varepsilon_0\chi_e\mathbf{E_0} \\ &= \varepsilon_0(1+\chi_e)\mathbf{E_0} = \varepsilon\mathbf{E_0}\end{aligned} \tag{4.3}$$

From this equivalency, it is seen that any material can be characterized by a physical parameter ε, known as *electric permittivity*, and has units farad/meter. It relates the electric flux density and the input electric field intensity inside it. The value of ε is typically expressed in terms of ε_0 through the term ε_r known as relative permittivity or dielectric constant, as expressed in (4.4).

$$\frac{\varepsilon}{\varepsilon_0} = 1 + \chi_e = \varepsilon_r \text{ (dimensionless)} \tag{4.4}$$

As ε increases, the material can keep more electric flux inside it. Therefore, it is desirable to use materials with low values of ε_r for antenna design. Also, for such low dielectric constants, the guided wavelength increases since $\lambda_g = \lambda_0/\sqrt{\varepsilon_r}$, making a planar antenna electrically thinner with a given physical thickness than with higher values of ε_r.

4.1.2 Magnetic Permeability (μ)

A material can support a magnetic field intensity depending on its atomic directional arrangement capabilities when a magnetic flux density is applied, in which phenomenon is called *magnetic polarization*. Let be a magnetic flux $\mathbf{B_0}$, thus its effect on the magnetic field $\mathbf{H_0}$ at vacuum is expressed as:

$$\mathbf{H_0} = \frac{\mathbf{B_0}}{\mu_0} \tag{4.5}$$

The term μ_0 is the magnetic permeability of vacuum and is 1.26 μH/m. Considering the orbital model of atoms, where the electrons (negative charges) orbit the nucleus (positive charges), the material can be physically modeled as an array of randomly oriented magnetic dipoles. In a macroscopic level, the magnetic polarization is quantified by the magnetization vector $\mathbf{M}$, which adds up to the former field $\mathbf{H_0}$, creating a new magnetic flux density $\mathbf{B}$ as:

$$\begin{aligned} \mathbf{H_0} + \mathbf{M} &= \frac{\mathbf{B_0}}{\mu_0} + \mathbf{M} \\ \mathbf{H_0} + \mathbf{M} &= \frac{\mathbf{B}}{\mu_0} \end{aligned} \tag{4.6}$$

Since the magnetization vector $\mathbf{M}$ is proportional to the magnetic field $\mathbf{H_0}$ as $\mathbf{M}= \chi_m \mathbf{H_0}$, then:

$$\begin{aligned} \mathbf{H_0} + \chi_m \mathbf{H_0} &= \frac{\mathbf{B}}{\mu_0} \\ \mathbf{H_0} \mu_0 (1 + \chi_m) &= \mathbf{B} = \mu \mathbf{H_0} \end{aligned} \tag{4.7}$$

It is then noticed that any material can be characterized by a physical parameter μ, known as *magnetic permeability*, and has units henry/meter. This constitutive parameter links the magnetic field intensity and the input magnetic flux density. The value of μ is typically expressed as μ_0 through the term μ_r known as relative permeability, as expressed in (4.8).

$$\frac{\mu}{\mu_0} = 1 + \chi_m = \mu_r \text{ (dimensionless)} \tag{4.8}$$

As opposed to dielectrics, where χ_e can achieve values much greater than zero, the typical behavior of χ_m is close to zero on both sides, positive and negative, up to the order of millionths. For values $\chi_m \to 0^-$, the material is considered as *diamagnetic*; then $\mu_r \to 1^-$, and $\mathbf{M}$ has opposite direction to $\mathbf{B_0}$. For values

$\chi_m \to 0^+$, the material is considered as *paramagnetic*; then $\mu_r \to 1^+$, and $\mathbf{M}$ has the same direction as $\mathbf{B_0}$. Typical materials used in antennas fall in any of both categories, so μ_r can be set to unity for modeling purposes, which can make errors up to 0.05 % in calculating the guided wavelength $\lambda_g = \lambda_0/\sqrt{\varepsilon_r \mu_r}$ if evaluating $\lambda_g = \lambda_0/\sqrt{\varepsilon_r}$ as discussed in Section 4.1.1.

4.1.3 Electric Conductivity (σ)

A material can support a current flow of electric charges when an electric field is applied, and valence electrons are available to migrate between consecutive atoms. This phenomenon is called *electric conduction*. Let us define a small volume $\Delta v = \Delta \ell \Delta s$ where $\Delta \ell$ is the length that electric charges flow during an instant of time Δt. For a given volumetric charge density q_{ev}, the electric charges are computed as $\Delta Q_e = q_{ev} \Delta v$ and flow through a cross-section of area Δs. In a macroscopic level, electric charges drift with a speed $\mathbf{v_e} = \Delta \ell / \Delta t$ much slower than electron speed. Then, the current density $\mathbf{J}$ is expressed as:

$$\mathbf{J} = \frac{\Delta Q_e / \Delta t}{\Delta s} = \frac{1}{\Delta s} \frac{q_{ev} \Delta \ell \Delta s}{\Delta t} = q_{ev} \mathbf{v_e} \tag{4.9}$$

Since the current flow is created from a given field $\mathbf{E_0}$, then:

$$\mathbf{v_e} = \mu_e \mathbf{E_0}, \tag{4.10}$$

where μ_e is the electron mobility, a quantity proportional to the electron charge, and considers the mechanical dynamics of charges. This quantity has a negative sign, and despite being noted with the Greek letter μ, it should not be confused with the magnetic permeability μ. Replacing (4.10) into (4.9):

$$\mathbf{J} = q_{ev} \mu_e \mathbf{E_0} = \sigma \mathbf{E_0} \tag{4.11}$$

where σ is known as *electric conductivity*, and has units siemen/meter (S/m). Both

the electric charge density q_{ev} and electric mobility μ_e in (4.11) have a negative sign, ensuring that σ is a positive number. This material constitutive parameter has a value over a wide range, from orders of μS/m to MS/m. Depending on its relation with the electrical permittivity ε and the frequency, a material can be considered a good conductor or a good dielectric. More discussion is provided in Section 4.4.2.1.

It is seen in (4.11) that the capability of a material to transport a current is proportional to the electric field applied. However, if the electric charge density is vast, as in good conductors such as metals, then the required value of the electric field is less important to support an electric current. In fact, for very good conductors, where σ is in the order of Megasiemem per meter, the current density $\mathbf{J}$ gets finite for negligible values of electric field $\mathbf{E}$.

In addition to having a high electric charge density from atomic valence electrons, another characteristic that can make a material a very good conductor is the electron mobility. It is an intrinsic physical property of materials. As later shown in Section 4.2.2, carbon-based materials such as graphene and nanotubes have superior electron mobility in their internal structure. This enhanced property has opened the opportunity to explore new materials for mmWave, and sub-THz applications [32].

Since the material constitutive parameters depend on the temperature, this work assumes room temperature (around 70°F or 21°C) in the analysis and proposed models related to material characterization. For non-ferromagnetic materials in antenna modeling and design, the approximation $\mu_r = 1$ is assumed. Furthermore, Section 4.3 and Section 4.4 provide a discussion of the frequency-dependent effects of ε and σ, covering topics such as dielectric frequency dispersion and conductor surface roughness.

4.2 Overview of mmWave and Sub-THz Antennas

Diverse research work has been done in the mmWave, sub-THz, and higher frequency bands for different purposes since the beginning of this century. Jamshed et al. [14] presented a condensed overview of the antennas used in applications in the frequency range between 100 GHz and 10 THz. This work identifies the radiating elements used in the mmWave and sub-THz bands (30 GHz - 300 GHz), shown at a glance in Fig. 4.1 and are reviewed in the upcoming lines.

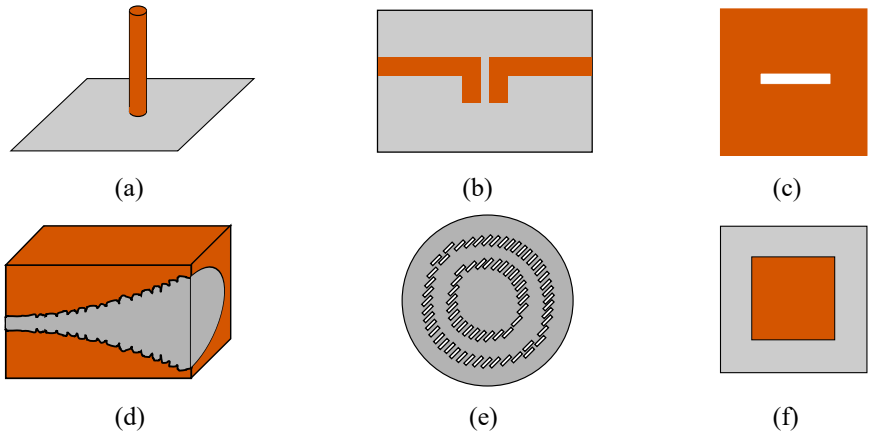

Figure 4.1: Radiating elements used in mmWave and sub-THz applications. (a) Wired monopole, (b) printed dipole, (c) rectangular slot, (d) corrugated horn, (e) dielectric lens, and (f) microstrip patch. Antenna references based on [15, 30, 106] . Among these devices, MSPAs can be used above 30 GHz. Modeling MSPAs will help optimizing its design and analysis.

(a) Monopole [27]

This antenna has been used as a plasmon nanoantenna for future wireless communications. Wired monopoles are easy to design, have non-sensitive impedance variation for frequencies around resonance, the fabrication is low-cost compared to lithography of similar metal structures, and has enhanced output power. However, it is single-polarized, and its frequency response strongly depends on the material size, especially above 300 GHz.

(b) Planar dipole [28–30]

It has been developed to show its capability in wireless communications for 5G networks and beyond. These antennas are compact and lightweight, low profile, conformal, and easy to design and fabricate compared to other antennas in the same frequency range. Planar dipoles are low-cost compared to lithography of similar metal structures and are electrically balanced. In addition, they have non-sensitive impedance variation for frequencies around resonance and may have large impedance bandwidth when adequately designed. Nevertheless, planar dipoles are big in electrical size and have low gain compared to other antennas. They have single polarization and are lossy, especially when coupling to CMOS components. Even so, it is possible to overcome this drawback by modifying the antenna structure. It is recommended to have a thickness less than $0.01\lambda_0$ to get efficiency close to unity.

(c) Rectangular slot [31]

This radiating element is complementary to the dipole antenna because of Babinet's principle. It is used in radars and as an array fed by a waveguide. These antennas are very straightforward to fabricate and have high power handling capability. Also, their low wind load makes this antenna especially favorable for radar. Besides, slot antennas possess ultra-high impedance bandwidth capabilities, peculiarly in the tapered slot, also known as *Vivaldi antenna*. Even so, they are challenging to match and have high cross-polarization levels. In addition, the increased presence of surface waves makes them lossy. It is recommended to have a thickness less than $0.04\lambda_0$ to get an efficiency close to 1.

(d) Horn [30, 31, 34]

These antennas are the most used elements in THz systems, including in the sub-THz range. There are different shapes: pyramidal, conical, diagonal, and corrugated. Horn antennas have several benefits: low losses, low cross-polarization levels in the corrugated horn, low side lobes, massive impedance bandwidth, low VSWR, high Gaussian coupling efficiency, excellent beam circularity, and easy integration with photo-diodes. However, horn antennas are difficult and costly to design and fabricate, especially corrugated horns. They possess a non-symmetrical beamwidth and undesirable side lobes in the specific case of pyramidal horns, but multi-mode excitation can overcome these drawbacks. Horn antennas may also be incompatible with multi-pixel arrays.

(e) Dielectric lens [30, 31, 34]

These radiating elements are often used as collimating antennas, usually with other antennas, e.g., horns, co-planar waveguides, etc. These antennas are the best preferable at sub-mm wave frequencies (beyond 300 GHz), and they have also been used in the mmWave and sub-THz bands. Nagatsuma et al. [34] designed two lenses for transmission and reception. The transmitter lens with 2.3 degrees of beamwidth, -24 dB side lobes, and 37.1 dBi of directivity. The reception antenna parameters were 0.47 degrees, -22.5 dB, and 52.1 dBi, respectively. The high directivity, low loss, low cost, and low side lobes –similar to Gaussian beam– make this antenna very attractive to be used in frequencies above 30 GHz. Also, dielectric lenses have more relaxed fabrication tolerances than horns. Nonetheless, they have a narrow impedance bandwidth and complex integration with electronics.

(f) Microstrip patch [15, 32]

MSPAs are widely used in several applications, including mobile phones, radar, and base stations. Chapter 2 and Chapter 3 have provided a profuse discussion on these antennas, and they will be mathematically modeled up to 300 GHz in Chapter 5 based on the observations and trade-offs found in this chapter. The pros for this antenna are abundant: compact and lightweight, low profile, conformal, polarization diversity, easy fabrication, and integration. Although they typically present a narrow impedance bandwidth, modern strategies are available in the literature to enhance the bandwidth [32, 40]. The low power handling capability and susceptibility to warpage are other limitations in MSPAs, especially in fragile Teflon-based substrates.

4.2.1 Materials

Antennas in the mmWave and sub-THz bands require to be made of materials that allow maximum efficiency and minimum loss to compensate for the atmospheric attenuation that is present, especially in the sub-THz region. From the identified radiating elements of Fig. 4.1, there are metallic-only antennas (monopole, slot, horn), dielectric-only antennas (lens), and mixed antennas (printed dipole, patch). In sub-THz antennas, it is more common to use multiple layers, more than two, since it is more compatible with antenna-on-chip technology. Also, various layers may help reduce the losses more effectively, and the expansion coefficient can be better controlled [107]. This section identifies and describes different materials (dielectrics and conductors). Also, this section lists and describes diverse fabrication techniques for the antennas reviewed above.

4.2.1.1 Dielectrics

Dielectrics for high-frequency antennas (mmWave band and above) are preferred to meet the following qualities: low loss tangent, low dielectric constant, good power handling capability, stable behavior over varying environmental conditions and the working bandwidth, and compatibility with hybrid constructions. [108].

Most of the common dielectrics used in RF antennas, such as Rogers 4350B, FR4 epoxy, etc., are still used in the mmWave band but not preferred in sub-THz antennas because the above qualities are less satisfactory. Even so, the well-known Rogers 5880 Duroid was found in an antenna at 130 GHz as part of an imaging system [109]. Other conventional materials used are Indium phosphide (InP) [110], benzocyclobutene (BCB) [110] –including the Cyclotene™ 3000/4000-series [111]–, and polyamides [112] are mostly used. The printed dipole antenna developed by Vettikalladi et al. [29] is a good example of using InP and BCB substrates.

Non-conventional materials such as electromagnetic band-gap materials (EBG) [107] and low-temperature co-fired ceramic materials (LTCC) [15, 113] are also used to fabricate sub-THz antennas. LTCC materials can have a loss tangent of less than 0.006 in the sub-THz region, thicknesses as low as 12.5 μm, and they can be integrated into micro-electro-mechanical systems (MEMS). Some examples of these materials are Ferro A6-M [113] and DuPont 951 and 951 [114]. Besides, EBG are customizable materials since an electromagnetic bandgap material *is fabricated by periodically embedding the conductors in the host material, which may reduce an effective dielectric permittivity and magnetic permeability of the composite material to even the negative value.* [107]. Thus, adding conductive structures in the top layer can purposely modify the dielectric properties of EBGs. Table 4.1 summarizes the dielectric materials discussed in this section, including its electrical properties. As later detailed in Section 4.3.2, the loss tangent $\tan\delta$

is related to the complex permittivity of the material, $\varepsilon = \varepsilon' - j\varepsilon''$, where ε'' accounts for the losses in the dielectric. Then, $\tan\delta = \varepsilon''/\varepsilon'$ gets typical values near zero.

Table 4.1: Dielectric materials used in mmWave and sub-THz antennas.

Material	At frequency	ε_r	$\tan\delta$
Rogers™ 5880 Duroid	10 GHz	2.20	0.0009
Rogers™ 4350	10 GHz	3.66	0.0040
Rogers™ 3006	10 GHz	6.15	0.0020
Indium Phosphide (InP)	300 GHz	12.5	0.0020
Benzocyclobutene (BCB)	300 GHz	2.50	0.0050
Cyclotene™ 3000	10 GHz	2.65	0.0020
Polyamide	10 GHz	2.50	0.0017
Ferro A6-M	200 GHz	6.00	0.0020
DuPont 951	79 GHz	6.00	0.0047

4.2.1.2 Conductors

Copper has been widely used in RF antennas due to its high bulk conductivity, only behind silver. It has a nominal conductivity of 58 MS/m at a temperature of 300 K, an atmospheric pressure of 101 MPa, and at DC frequency. Its low cost and high compatibility with manufacturing make this material versatile. It is practically the default conductor in antennas and printed circuits in RF and microwave.

Printed circuit boards are composed of a dielectric substrate and a copper foil, which may be located at the top, bottom, or both. The most common thickness for cladding is performed with a surface mass density of 0.5, 1, and 2 ounces per square foot. Since these weights are equivalent to a defined volume, considering a density of 8830 kg per cubic meter, the cladding weights are equal to 17.5, 35, and 70 μm in thickness, respectively.

Diverse foiling techniques can be applied to copper adherence to the dielectric substrate underneath. Fig. 4.2 illustrates the two main foiling techniques: rolled

and electrodeposited. The surface roughness for these two types of foil usually is several times different. A typical RMS value for electrodeposited copper rounds 1.8 μm, while for rolled copper, this value decreases to 0.3 μm. An in-depth discussion of the effect of the copper thickness and roughness is provided in Section 4.4.1 and Section 4.4.2, respectively.

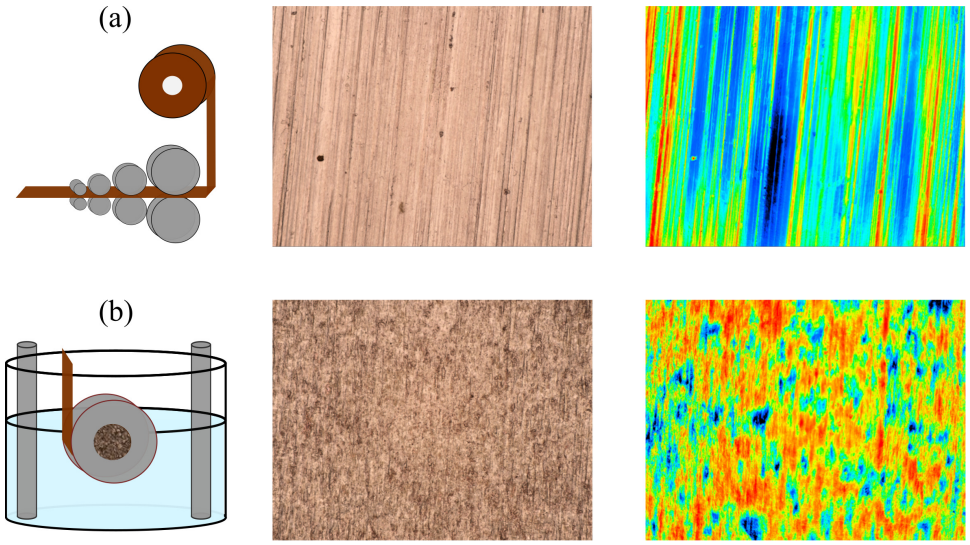

Figure 4.2: Copper main foiling techniques and typical height distribution.
(a) Mechanically rolled copper [115], identifiable by the directional strips.
(b) Chemically electrodeposited copper [115] can be recognized by the presence of bright and dark spots randomly located across the surface. Under the microscope, the digital elevation map samples the roughness profiles for both foiling techniques, typically smoother for the rolled copper.

As the frequency increases, the assumption of the almost perfect electric conductor (PEC) with conventional material such as copper becomes less accurate since $(\sigma/(\omega\varepsilon))^2 \gg 1$ gets closer to unity. However, this relation is still valid at sub-THz frequencies, with errors of 0.1 % or less. Despite the excellent conductivity of copper, it becomes lossy in mmWave and beyond, as later discussed in Section 4.3. Then, more conductive, thinner, and stronger materials are strongly preferred. Good alternatives such as carbon-based materials (graphene and nanotubes or CNT) have shown better properties than copper, as listed in Table 4.2.

Table 4.2: Comparison of properties of different conductors for antennas.

Property	Unit	Copper	Graphene	Carbon nanotube
Electric mobility	$cm^2V^{-1}s^{-1}$	32	2×10^5	8×10^4
Current density	Acm^{-1}	10^6	10^9	10^9
Tensile strength	MPa	587	1.5×10^6	$(50 - 500) \times 10^3$
Thermal conductivity	$Wm^{-1}K^{-1}$	400	5000	3000

Non-conventional conductors such as graphene and CNT also show good miniaturization capabilities in metallic-based antennas. A PC-MSPA was designed by Varshney et al. [32] with graphene traces and silicon-dioxide layers, delivering a bandwidth over 100 % for frequencies above 1 THz. Dash and Patnaik [116] have designed a wired dipole at 1 THz with copper, graphene, and CNT. The copper dipole's size was set to $\lambda_0/2$, as also studied in Section 2.2.2). However, the necessary height to replicate the same radiation pattern was $\lambda_0/3$ for CNT and $\lambda_0/4.4$ for graphene. The radiation characteristics for $\theta > 30°$ remained the same, while the directivity grew from 2.16 dB for the copper wired-dipole to 3 dB for CNT and 3.3 dB for graphene.

Isolated graphene has static conductivity of 10–100 MS/m [117–119], up to about 70 % more than copper. However, this material can have a variable conductivity according to the fields applied and the temperature, making it favorable to design reconfigurable antennas. Also, graphene is highly anisotropic, having in-plane conductivity (which can be higher than copper) and out-of-plane conductivity, which can be of several orders less than copper [118].

4.2.2 Fabrication Techniques

Antenna fabrication in the sub-THz band requires high precision. Fortunately, the technology is progressively more sophisticated, and there is work with conductor line widths down to 2 μm and RMS roughness up to 0.35 μm. Conven-

tional fabrication techniques such as 3D printing, milling, Potassium Hydroxide (KOH) etching, photolithography, and micro-machining are available and used in RF antennas. However, since sub-THz antennas require sub-millimeter fabrication tolerances, only some of these techniques can still be applied. Besides, non-conventional fabrication techniques are applied for sub-THz antenna fabrication. This section provides an overview of different fabrication techniques for sub-THz antennas.

Printed-circuit board (PCB) prototyping [120, 121]

Antenna fabrication in PCB with mechanical and laser milling techniques has been widely used in RF antennas because of its practicality and accuracy. LPKF-branded laser machines use a scanner-guided 20 μm ultraviolet laser capable of structuring, engraving, and cutting materials in a short time [121].

The most meaningful advantage is its high control capability, allowing antenna fabrication up to the R-band (220 GHz–325 GHz) [120]. The LPKF™ Proto Laser S machine has a minimum track width of 50 μm and minimum gap width of 25 μm. The LPKF™ Proto Laser U4 has the same minimum track width as its predecessor and minimum gap width of 20 μm. For more strict tolerances, high-end computer numerical machining (CNC) milling machine [122] is preferable, with tolerances in the order of single-digit micrometers.

Three-dimensional printing [120, 123]

Three-dimensional (3D)-printing, also known as *additive manufacturing* [106], is a conventional fabrication technique that builds 3D objects by physically depositing the material layer by layer. Current technology allows printing with 10 μm or vertical resolution. This process is cost-effective and easy to perform since it only

needs a computer design model, the material to use, and a setup that reflects the user's needs. Nonetheless, it has the drawback of being susceptible to physical defects such as deformation due to temperature.

The most common 3D printing processes for dielectric and metal are polymer jetting 3D printing and metal binder jetting (MBJ), respectively. The 3D Stratasys™ Objet 30 Scholar has a resolution of 28 μm $times$ 42 μm $times$ 42 μm while the Stratasys™ Form 2 has a laser spot width of 140 μm and thickness resolution of 25 μm. As in the case of PCB antenna fabrication, 3D printing can be used up to 325 GHz since the tolerances become severe at higher frequencies.

Silicon-based fabrication process

Silicon technology has been widely used for sub-THz antennas and optical devices. It offers a high-level integration with electronic and optical devices despite providing low gain, less than 10 dBi, and low efficiency, less than 10 in on-chip antennas [124]. Even so, improving these drawbacks is currently an active research topic, and alternative advanced SiGe BiCMOS technology is in use, allowing the fabrication of antennas up to 500 GHz. Also, antenna-in-package technology constitutes a powerful alternative for sub-THz antennas.

There are different fabrication techniques based on Silicon technology, being mostly used in micro-electro-mechanical systems (MEMS) [125]:

- High-density plasma etching, such as the Deep reactive ion etching (DRIE).
- Bonding: anodic bonding between metals and glasses and thermal bonding between silicon wafers.
- Surface Sacrificial Layer Technique: This is a membrane-based fabrication technique that refines poly-silicon membranes by physical and chemical synthesis stages.

Direct Write Lithography (DWL) [126, 127]

Direct Write Lithography (DWL) is a *maskless, 3D, high-resolution photolithography technique which relies on the local solidification of a photoresist at the focus of a laser beam to "draw"* in the material [127]. This technique, also known as Direct Laser Writing (DLW), is mainly used in optomechanical micro tools. It uses the combination of a tightly focused laser beam properly modulated and scanned over the substrate, with the displacement of a high precision XYZ stage [126]. This technology allows writing the patterns directly on the substrate with a resolution of 0.1 μm $\times$ 0.1 μm $\times$ 0.3 μm.

Low-Temperature Co-fired Ceramic (LTCC) prototyping [15, 128]

Fabrication in LTCC is widely used for antennas in-package, i.e., encapsulated and integrated into other electronic and optical devices. Among its advantages, LTCC materials have low losses, good thermal conductivity, and excellent integration, but it is expensive. Its high handling capability of layers is attractive for developing stepped profiles, such as in the corrugated horn antenna.

This fabrication process uses layers of unfired green ceramic tapes (whose main constituent is weakly bound clay material) and metal pastes (copper, silver, or gold). The ceramic tapes have relative permittivity between 4 and 75, loss tangent from 0.0004 to 0.006, and thicknesses between 12.5 μm and 250 μm. This process involves screen printing of metal layers onto the unfired green material, staking, pressing, and firing at 900 °C. The conductor line width and spacing can be as low as 100 μm.

Other alternatives to LTCC are also used in antenna-in-package technology to reduce costs. High-density interconnects (HDI) prototyping uses industry-standard materials in massive production, and HDI-based fabrication involves

blind and buried microvias, sequential lamination, and conductor wiring. Since HDI also refers to PCB technology, HDI prototyping uses the steps involved in PCB prototyping.

Deep reactive ion etching (DRIE) [106, 128, 129]

This non-conventional fabrication process has been used for MEMS. A wafer is located inside a DRIE machine that contains plasma and an RF antenna. This etching technique uses high-density plasma generated by inductive coupling between the plasma and the DRIE machine RF antenna. The DRIE machine antenna creates an oscillating magnetic field that produces the ionization of gas molecules and atoms at low-pressure [129]. According to [129], a separate RF power source is connected to the cathode to generate DC bias and attractions to the wafer. Thus, it becomes possible to decouple ion current and ion energy applied to the wafer, completing the etching process.

Among its advantages are high etch rate (etched height over a short time), smooth surface (tolerance of ± 5 μm), and high selectivity (etching rate difference between materials exposed to the same plasma [130]). However, this process is expensive and very complex, and it is usually complemented with another process, such as diffusion bonding [106]. A side effect of this process is the introduction of unwanted undulations on the side walls [131] that may affect performance.

Diffusion bonding process [128, 132]

This non-conventional fabrication technique is based on the atomic diffusion of elements in the interface between two consecutive layers. This technology is capable of joining two metallic parts without using any sticking material or tightening elements. However, since a combination of high temperatures and pressure is ap-

plied, the contacting surfaces must be as flat as possible to obtain a good bond and prevent voids in the interface. Despite the high cost, weight, and complexity, it offers several advantages, such as high accuracy ($\pm 20\mu$m), high capability to handle small objects in the order of hundredths of millimeters, high robustness, and low wall roughness. This fabrication process can be complemented with CNC machining to cut multiple layers and DRIE for conductor plating to achieve even higher accuracy.

4.3 Effects of the Dielectric Electrical Characteristics on mmWave and Sub-THz MSPAs

Dielectrics are characterized by permittivity, which can be a complex number when they become lossy. The real part of this value is greater than the electric permittivity of vacuum $\varepsilon_0 = 8.85$ pF/m. Conversely, the imaginary part of the complex permittivity is intended to be as closest to zero as possible. The complex permittivity is a property that depends –although very slightly– on the geometrical orientation and the frequency. Below 30 GHz, both properties are usually ignored, but as the frequency increases, the material imperfections become more noticeable in antenna modeling and design. This section reviews the effects of anisotropy and frequency dispersion on modeling antennas in the mmWave and sub-THz bands.

4.3.1 Anisotropy

Anisotropic materials such as liquid-crystal polymers and graphene are used in sub-THz antennas. Anisotropy can be seen in dielectric properties but also in conductors.

The electric flux density vector is related to the electric vector by [77]:

$$\mathbf{D} = \boldsymbol{\varepsilon}\mathbf{E}$$
$$\begin{bmatrix} D_x \\ D_y \\ D_z \end{bmatrix} = \begin{bmatrix} \varepsilon_{xx} & \varepsilon_{xy} & \varepsilon_{xz} \\ \varepsilon_{yx} & \varepsilon_{yy} & \varepsilon_{yz} \\ \varepsilon_{zx} & \varepsilon_{zy} & \varepsilon_{zz} \end{bmatrix} \begin{bmatrix} E_x \\ E_y \\ E_z \end{bmatrix}, \tag{4.12}$$

where $\boldsymbol{\varepsilon}$ is the tensorial electric permittivity. Typically, the non-diagonal components are conjugated ($\varepsilon_{xy} = \varepsilon_{yx}^*$,$\varepsilon_{xz} = \varepsilon_{zx}^*$,$\varepsilon_{yz} = \varepsilon_{zy}^*$). Some materials [133] that experience anisotropy only in the main axis ($\varepsilon_{xy} = \varepsilon_{yx} = \varepsilon_{xz} = \varepsilon_{zx} = \varepsilon_{yz} = \varepsilon_{zy} = 0$). Moreover, there are materials [134, 135] that experience uni-axial anisotropy, which means that from the diagonal, only one axis presents a different value of the permittivity than the other two, which are congruent. A typical example of uni-axial anisotropy takes place in Rogers™ 3010 [134], where $\varepsilon_{xx} = \varepsilon_{yy} = 11.9$ (horizontal), and $\varepsilon_{zz} = 11$ (vertical).

Conductors can also be anisotropic. That is the case of graphene when in the presence of magnetic bias. Also, graphene is a mono-atomic-layer material, i.e., a thickness can be obtained by stacking layers one above another. Then, the surface conductivity tensor can be defined from Ohm's law as [77, 136]:

$$\mathbf{J} = \boldsymbol{\sigma}\mathbf{E}$$
$$\begin{bmatrix} J_x \\ J_y \end{bmatrix} = \begin{bmatrix} \sigma_{xx} & \sigma_{xy} \\ \sigma_{yx} & \sigma_{yy} \end{bmatrix} \begin{bmatrix} E_x \\ E_y \end{bmatrix} \tag{4.13}$$

where $\boldsymbol{\sigma}$ is the tensorial static conductivity of an anisotropic material. For the specific case of graphene, its anisotropic conductivity [136] is defined as $\sigma_{xx} = \sigma_{yy} = \sigma_d$, and $\sigma_{xy} = \sigma_{yx} = \sigma_0$. In this redefinition, σ_d is the conductivity component along a given direction, while σ_0 is the component for the per-

pendicular direction. Since the conductivity of graphene is highly dependent on temperature, excitation energy, and operating frequency, its anisotropic properties can also change.

4.3.2 Frequency Dispersion

For a given angular frequency $\omega = 2\pi f$ and considering $\varepsilon = \varepsilon' - j\varepsilon''$, a material is considered a good dielectric if $(\sigma/(\omega\varepsilon'))^2 \ll 1$. The real part of the permittivity ε' is related to the design dielectric constant Dk by $Dk \geq \varepsilon'/\varepsilon_0$, while the loss tangent is calculated as $\tan\delta = \varepsilon''/\varepsilon'$. Debye [137] found that the dielectric properties are variable over the frequency in an extensive perspective, i.e., from 1 Hz to 1 PHz, illustrating this variation in Fig. 4.3. An equation was formulated to describe the behavior of the dielectric parameters $(\varepsilon', \varepsilon'')$ over the angular frequency $\omega = 2\pi f$, which are expressed as follows:

$$\varepsilon = \varepsilon' - j\varepsilon'' \tag{4.14}$$

$$\varepsilon(\omega) = \varepsilon_\infty + \frac{\varepsilon_{DC} - \varepsilon_\infty}{1 + j\omega\tau} \tag{4.15}$$

$$\varepsilon'(\omega) = \varepsilon_\infty + \frac{\varepsilon_{DC} - \varepsilon_\infty}{1 + \omega^2\tau^2} \tag{4.16a}$$

$$\varepsilon''(\omega) = \frac{(\varepsilon_{DC} - \varepsilon_\infty)\omega\tau}{1 + \omega^2\tau^2}, \tag{4.16b}$$

where ε_{DC} is the permittivity at DC (0 Hz), and ε_∞ is the permittivity at a frequency high enough to be considered infinite, normally above optical ranges. τ is the material relaxation time, i.e., the times it takes to polarize, being this variable dependent not only on the material but also on the temperature. The relaxation frequency can be also defined as $f_c = 1/(2\pi\tau)$ [138]. An example of this dispersive response is provided in Fig. 4.4. It is then seen that the permittivity, the dielectric constant, and the loss tangent at sub-THz frequencies are different from the values at RF frequencies lower than 10 GHz. Even though antenna materials

present a much less drastic variation than the presented in Fig. 4.4 because of the loss tangent, this example shows that material characterization at sub-THz frequencies needs to be performed, as ε' and ε'' may present changes along these high frequencies.

Another consequence of the equation presented above is that the permittivity varies in frequencies through a plot ε'-versus-ε'' in the xy Cartesian plane drawn as a circle, as seen in Fig. 4.4. This plot is called the Cole-Cole diagram [138]. This diagram can be used to estimate the permittivity at a given frequency, similarly to the Smith chart, to calculate the input impedance in transmission lines.

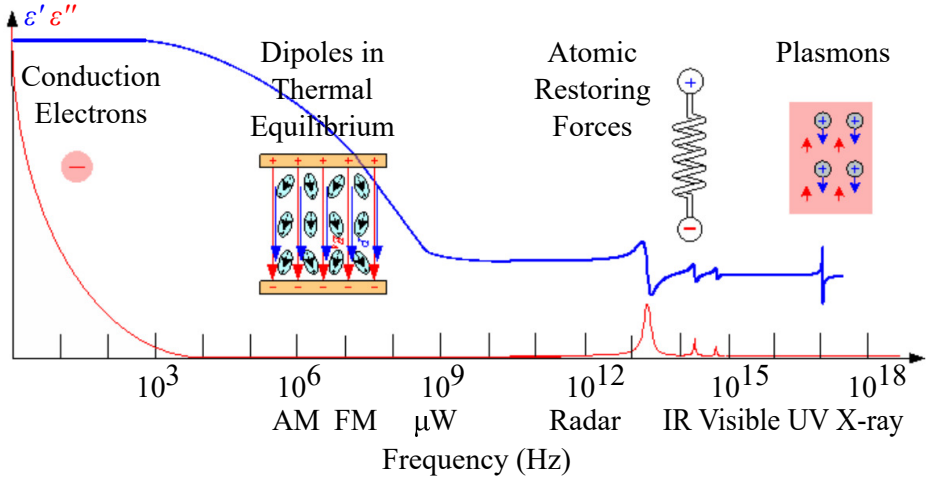

Figure 4.3: Dielectric polarization mechanisms and frequency dispersion [137]. Variations of the real and imaginary components of the electric permittivity versus frequency, with a regional estimate of the dominating dielectric mechanisms. In the mmWave and sub-THz bands, there is a polarization mixture between electric dipoles and atomic forces.

4.3.3 Consequences in EM Modeling of mmWave and Sub-THz MSPAs

This section has shown that anisotropy and frequency dispersion may be present in materials used for antennas in the mmWave and sub-THz bands. The following strategies consider both phenomena in modeling MSPAs:

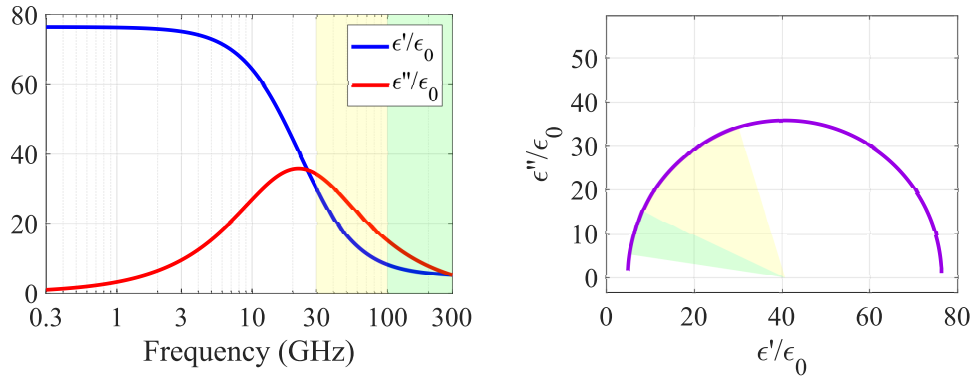

Figure 4.4: Variation of the dielectric properties along frequency for water. In this example, the dielectric constant significantly decreases in the mmWave band (indicated in yellow), up to minimum values in the sub-THz band (indicated in green). Diagram build using (4.15) and the following parameters [138]: $\varepsilon_{DC} = 76.47$, $\varepsilon_\infty = 4.9$, and $\tau = 7.2$ picoseconds.

- Directional modeling: Considering the formulations of the cavity model (Fig. 2.8), the E- fields inside the patch cavity are oriented to the $z-$axis. Then, this strategy proposes considering the z direction of the permittivity to model the resonator components. More studies need to be performed to confirm this hypothesis, which is beyond the scope of this work.

- Frequency-dependent effective permittivity: for broadband modeling, the frequency dispersion of dielectrics can be considered by calculating the effective dielectric constant, but now with a frequency dependency. For each resonant mode, one dielectric constant value can be evaluated at the center frequency of the interval analysis.

Regarding the frequency-dependent variation of the effective permittivity, Jha [107] proposed a detailed formulation for microstrip transmission lines. This formulation combines the frequency-dependent variation of the effective permittivity [139] and its average value in multilayered transmission lines [140]. According to this approach and considering the geometry of Fig. 4.5, the effective average

permittivity $\varepsilon_e(f)$ as a function of the frequency f in GHz is presented in (4.17) through the following steps [107, 141]:

1. The frequency-independent average permittivity ε_{rc} can be calculated from several substrate layers of relative permittivity ε_{ri}, and thicknesses h_i that sum in total h_T as in (3.35) in Chapter 3.

2. The frequency-dependent effective permittivity $\varepsilon_e(f)$ can be expressed as:

$$\varepsilon_e(f) = \varepsilon_{rc} - \frac{\varepsilon_{rc} - \varepsilon_{e0}}{1 + (f/f_a)^m} \tag{4.17}$$

where:

$$\varepsilon_{e0} = \frac{\varepsilon_{rc}+1}{2} + \frac{\varepsilon_{rc}-1}{2}\Big(1 + \frac{12h}{w}\Big)^{-1/2} + F(\varepsilon_{rc}, h) - \frac{0.217t}{\sqrt{wh}}(\varepsilon_{rc}-1) \tag{4.18a}$$

$$F(\varepsilon_{rc}, h) = \begin{cases} 0.02(\varepsilon_{rc}-1)(1-w/h)^2, & \text{for } w/h < 1 \\ 0, & \text{for } w/h \geq 1 \end{cases} \tag{4.18b}$$

$$f_a = \frac{f_b}{0.75 + (0.75 - 0.332\varepsilon_{rc}^{-1.73})w/h} \tag{4.18c}$$

$$f_b = \frac{47.746}{h\sqrt{\varepsilon_{rc} - \varepsilon_e(0)}} \arctan\left(\varepsilon_{rc}\sqrt{\frac{\varepsilon_e(0)-1}{\varepsilon_{rc}-\varepsilon_e(0)}}\right) \tag{4.18d}$$

$$m = m_0 m_c, \ m < 2.32 \tag{4.18e}$$

$$m_0 = 1 + \frac{1}{1+\sqrt{w/h}} + 0.32(1+\sqrt{w/h})^{-3} \tag{4.18f}$$

$$m_c = \begin{cases} 1 + \frac{1.4}{1+w/h}(0.15 - 0.235e^{-0.45f/f_a}), & \forall\ w/h \leq 0.7 \\ 1, & \forall\ w/h > 0.7 \end{cases} \tag{4.18g}$$

Since only one value of ε_e is required for the PC-MSPA model, the average frequency of the interval analysis is considered to perform the above mentioned calculations. Then, as stated in (2.97), the effective permittivity used for the patch is the average between ε_e and ε_{rc}.

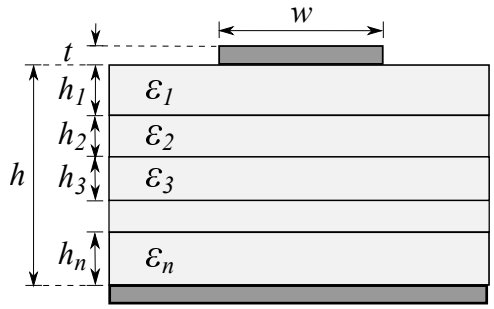

Figure 4.5: Cross section of a multilayered microstrip line. Based on [107]. This structure also represents the stack-up of a multilayered MSPA in mmWave and sub-THz bands, and the effective dielectric constant can be computed by following the formulations in (3.35), (4.17), and (2.97).

4.4 Effects of the Conductor Geometrical Characteristics on mmWave and Sub-THz MSPAs

Conductors usually are present in metallic traces, principally copper. These traces are typically some microns thick and present an RMS surface roughness in the order between tenths of a micron to about 1 μm. Modeling MSPAs consider three assumptions: the trace has an infinitesimal thickness, the feeding line impedance is 50 Ω, and the input impedance location is defined before modeling. Even assuming the bulk conductivity constant over frequency at room temperature, the thickness and roughness are geometrical characteristics that need to be analyzed and included in modeling mmWave and sub-THz MSPAs. This section discusses the effects of the conductor trace thickness and surface roughness on modeling MSPAs, especially at frequencies between 30 GHz and 300 GHz.

4.4.1 Trace Thickness

A trace thickness of 17.5 μm is the most likely to be used in MSPAs in RF and microwaves. Because of its small electrical thickness –in the order of up to 0.002 λ_0– the physical thickness is deemed zero, allowing less complex modeling.

However, this assumption starts to be inaccurate in the mmWave band and higher frequencies. The effects of the trace thickness on modeling MSPAs above 30 GHz can be primarily observed in the characteristic impedance of microstrip lines and on the resonant frequency of the patch's RLC resonator.

Let us define a microstrip transmission line of width W over a dielectric with thickness h and relative permittivity ε_r. Its characteristic impedance can be calculated as in (4.19). The variables in this expression comes from computing the calculations in (4.20b)–(4.20f) [23].

$$Z_0 = \frac{\eta_0}{2\pi\sqrt{\varepsilon_{re}}} \ln\left[\frac{F_1}{u} + \sqrt{1+\frac{4}{u^2}}\right], \tag{4.19}$$

where:

$$F_1 = 6 + (2\pi - 6)e^{-(30.666/u)^{0.7528}} \tag{4.20a}$$

$$\eta_0 = 120\pi\ \Omega \tag{4.20b}$$

$$u = W/h \tag{4.20c}$$

$$\varepsilon_{re} = \frac{\varepsilon_r + 1}{2} + \frac{\varepsilon_r - 1}{2}\left(1 + \frac{10}{u}\right)^{-ab} \tag{4.20d}$$

$$a = 1 + \frac{1}{49}\ln\left[\frac{u^4 + (u/52)^2}{u^4 + 0.432}\right] + \frac{1}{18.7}\ln\left[1 + \left(\frac{u}{18.1}\right)^3\right] \tag{4.20e}$$

$$b = 0.564\left(\frac{\varepsilon_r - 0.9}{\varepsilon_r + 0.3}\right)^{0.053} \tag{4.20f}$$

The equations expressed above follow a more accurate computation of the characteristic impedance of microstrip lines, with errors less than 1 % in Z_0, and less than 0.2 % in ε_{re}, for $\varepsilon_r < 128$ and $u \in [0.01, 100]$.

The expression (4.20d) is a generalization of (2.76) in Chapter 2. Using this sophisticated formulation is necessary to account accurately for the effects of trace thickness in the upcoming lines.

When a trace thickness t is considered, the value of u (4.20c) needs to be updated to u'' as in (4.22) following these additional steps:

$$u' = u + \frac{1}{\pi}\frac{t}{h}\ln\left(1 + \frac{4e}{(t/h)\coth^2\sqrt{6.517u}}\right) \tag{4.21}$$

$$u'' = u + \frac{u'-u}{2}\left(1 + \frac{1}{\cosh\sqrt{\varepsilon_r - 1}}\right) \tag{4.22}$$

Fig. 4.6 illustrates the effect of the conductor trace thickness t in the impedance of microstrip lines in the sub-THz band.

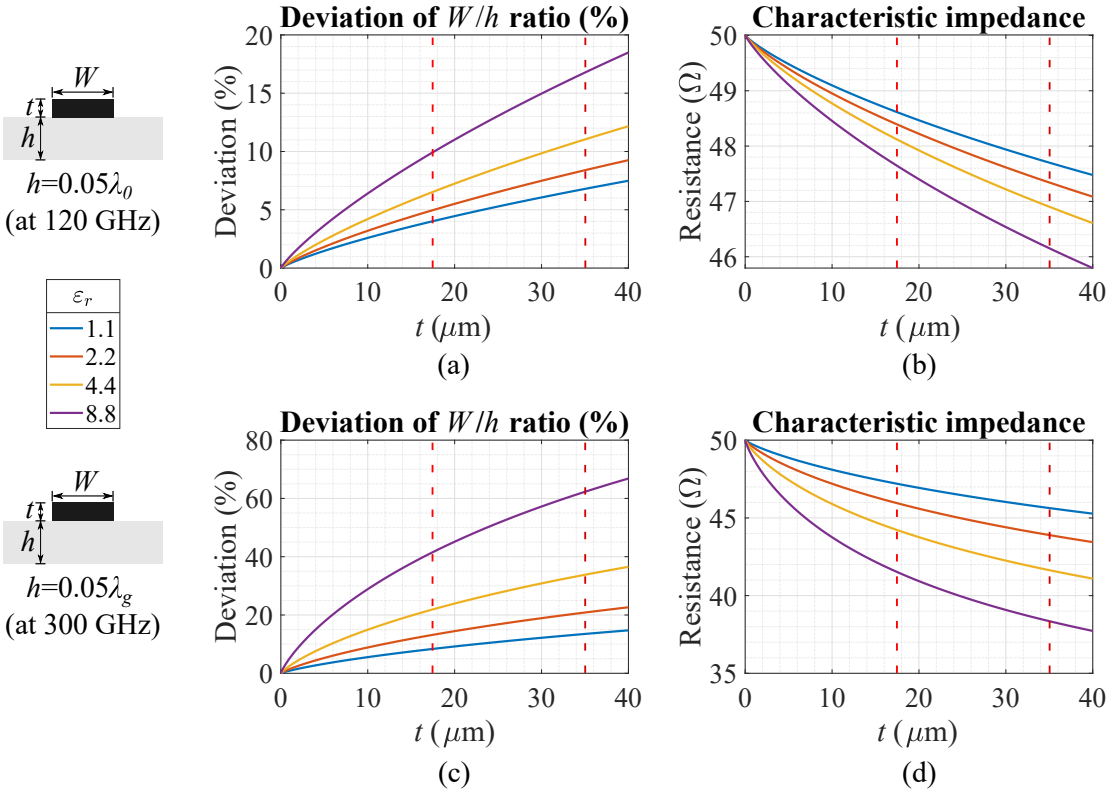

Figure 4.6: Effect of the conductor thickness in microstrip lines.
As the frequency, conductor trace thickness, and dielectric constant increase, the assumption of a zero-thickness conductor becomes more inaccurate (a,c), and the characteristic impedance decreases below 50 Ω (b,d).

As mentioned above, the value u'' in (4.22) considers a non-zero value of t. If using u (4.20c), then the model incurs a deviation error that increases as the

trace becomes thick, as plotted in Fig. 4.6a,c. This deviation increases with permittivity and frequency since the electrical thickness is bigger for smaller guided wavelengths. Because of the deviation of u'' from u, the characteristic impedance deviates from 50 Ω. Then, a smaller value of W must be chosen to keep MSPA modeling valid under the assumption of matching feed.

For modeling PC-MSPAs, it is also assumed that the feeding transmission line is designed for a characteristic impedance of is 50 Ω. The feeding's characteristic impedance is verified, considering two Rogers 5880 substrates ($\varepsilon_r = 2.20, h_1 = h_2 = 1.575$ mm). The line impedance values are listed in Table 4.3. As the operating frequency increases, the up-scaled feeding width W_f produces line impedances below 50 Ω, increasing errors. This downshifting effect of the impedance is noticed one more time in microstrip lines, as seen in Fig. 4.6. Then, the values of W_f need to be adjusted in addition to the up-scaling to get a 50-Ω characteristic impedance in the embedded microstrip lines over frequency, as shown in the fifth column of Table 4.3.

Table 4.3: Feeding width and impedance in PC-MSPAs up to 300 GHz.
Similarly to microstrip lines, the characteristic impedance gets affected by the conductor thickness in embedded microstrip lines, which feed PC-MSPAs.

Scale factor	f_0 (GHz)	W_f (mm)	Z_{0u} (Ω)	New W_f (mm)	New Z_{0u} (Ω)
1	3.5	4.55	50.01	4.55	50.01
2	7	4.55/2	50.14	4.55/2	50.14
4	14	4.55/4	49.38	4.48/4	50.15
8	28	4.55/8	48.65	4.40/8	49.88
16	56	4.55/16	48.08	4.25/16	49.96
28.57	100	4.55/28.6	47.06	4.10/28.6	49.89

Another substantial effect of the conductor trace thickness in modeling mmWave and sub-THz MSPAs is an upwards shifting in the patch's RLC resonant frequency f_{0r}. So far, the models for MSPAs described in Section 2.4 consider flat traces without thickness. For frequencies up to 30 GHz, this assumption can still be

deemed valid, as the design errors between 3D and 2D geometry are less than 0.5 %, and the mathematical modeling errors are less than 1 %. At mmWave frequencies and above, the design errors for f_{0r} increase to around 2 %, as noticed in the third column of Table 4.4. The modeling errors get up to 4 % error, as seen in the fourth column in Table 4.4.

Table 4.4: Impact of the conductor trace thickness in the patch's resonant frequency for PF-MSPAs and its geometrical modeling.

f_0 (GHz)	Simulation (Ansys ™ HFSS)		Model		
	f_{0r} (GHz) (3D copper)	f_{0r} (GHz) (2D copper)	f_{0r} (GHz) ($h_T = h$)	f_{0r} (GHz) ($h_T = h + t/2$)	f_{0r} (GHz) ($h_T = h + t$)
3.5	3.450	3.453 (+0.1 %)	3.433 (-0.6 %)	3.434 (-0.5 %)	3.435 (+0.0 %)
7.0	6.890	6.860 (-0.4 %)	6.862 (+0.0 %)	6.866 (-0.3 %)	6.870 (+0.1 %)
14	13.77	13.81 (+0.3 %)	13.71 (-0.7 %)	13.72 (-0.4 %)	13.74 (+0.2 %)
28	27.51	27.61 (+0.4 %)	27.36 (-0.9 %)	27.42 (-0.3 %)	27.48 (+0.4 %)
56	54.86	55.20 (+0.6 %)	54.48 (-1.3 %)	54.73 (-0.2 %)	54.98 (+0.9 %)
119	115.8	117.2 (+1.2 %)	114.7 (-2.2 %)	115.8 (-0.0 %)	116.9 (+1.9 %)
140	136.2	137.9 (+1.3 %)	134.5 (-2.5 %)	136.0 (-0.1 %)	137.6 (+2.3 %)
175	169.7	172.3 (+1.5 %)	167.3 (-3.0 %)	169.6 (-0.1 %)	172.0 (+2.8 %)
245	236.5	241.1 (+2.0 %)	231.9 (-3.9 %)	236.2 (-0.1 %)	240.9 (+3.8 %)

In addition to the frequency shifts described above, another trend is found when the geometrical model is modified. When the trace thickness t is considered in the current cavity model, i.e., for $h_T = h + t$, the errors also increase, but with a positive sign, as observed in the last column of Table 4.4. Two modeling scenarios are then revealed. When the thickness is not considered, the value of f_{0r} is underestimated. Conversely, when the thickness is included, there is an overestimation of f_{0r}. This evidence suggests an intermediate thickness value where the errors get minimum over frequency, which is confirmed in the low errors on the fifth column of Table 4.4 for half-thickness.

4.4.2 Surface Roughness

The effects of surface roughness are notorious in the mmWave and sub-THz bands. Coonrod [65] performed an experimental study of the conduct roughness in the Rogers™ 3003 material with rolled and electrodeposited copper layers. Fig. 4.7 shows experimental results of the effects of the surface roughness in the insertion loss on transmission lines.

From Fig. 4.7a, it is noticed that the roughness increases the total loss; also, thinner substrates are more roughness-lossy than thicker ones. Fig. 4.7b expands the roughness analysis up to 100 GHz, seeing a difference of loss expected to be more than 1.5 dB/in in the sub-THz band if the lines continue beyond 100 GHz. Moreover, the conductor roughness affects the design dielectric constant in microstrip lines (Dk), which is greater than the actual relative permittivity $\varepsilon_r = 3$ for this material. From 1 to 100 GHz, it is observed from Fig. 4.7c that the roughness influences Dk, and Fig. 4.7d shows that the substrate thickness also influences Dk. From this evidence, it is expected that future models of the conductor roughness be more accurate in following the experimental trends.

As observed, the effects of the surface roughness in conductive foils need to be considered in MSPA design, significantly above 30 GHz, i.e., in the mmWave band and above. This section provides a thorough overview of analytical models that explain the role of the conductor surface roughness in the performance of transmission lines.

The conductor surface roughness can be numerically described by diverse statistical parameters, such as R_z, R_q, R_a, and more [142]. These parameters can be obtained from digital elevation models acquired through remote-sensing means, e.g., interferometric microscopes. In this work, the multi-line root means square surface roughness R_q [142] is used to develop, apply and compare the proposed

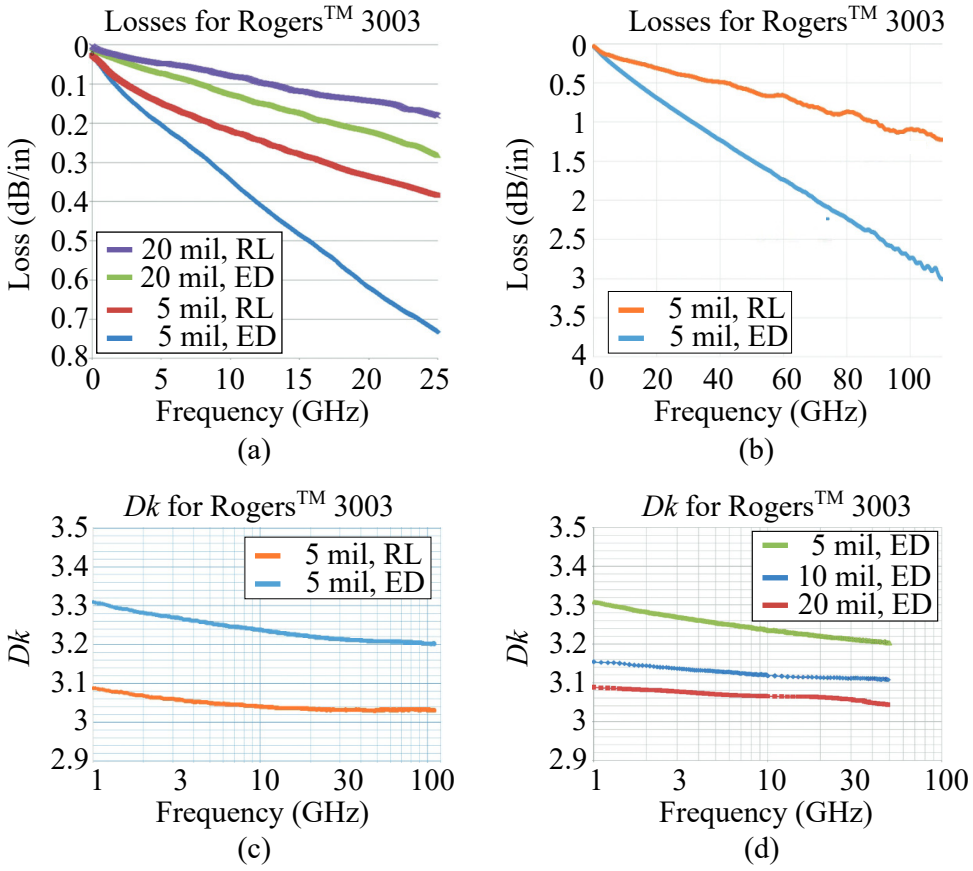

Figure 4.7: Effects of the conductor surface roughness in microstrip lines [65]. As the root-mean-square roughness value increases, the insertion losses (a,b) get several times higher than in smooth conductor surfaces, and the effective dielectric constant slightly increases (c,d). This impact is more pronounced as the frequency increases (for the losses) and the dielectric gets thin.

model with previous work since it is broadly used in data sheets of the most known manufacturers [115]. This parameter is defined in (4.23) for a line L, which height distribution $y(t)$ has a mean $\bar{y}$ along N measured points.

$$R_q = \sqrt{\frac{1}{N}\int_L (y-\bar{y})^2\,dt} \tag{4.23}$$

4.4.2.1 Loss and Phase in Transmission Lines: A Review

Let us define a two-port transmission line, e.g., microstrip line of length L, width W, over a dielectric of relative permittivity ε_r, loss tangent $\tan\delta$ and thickness H. The conductor trace has a conductivity σ_{bulk}, an average height greater than zero, e.g., 17.5 μm, and a root mean square value (RMS) roughness parameter R_q. For a frequency f, the associated wavelength is $\lambda_0 = c_0/f$, where c_0 is the light speed at the vacuum. Then, the performance of a 50-Ω two-port transmission line can be evaluated through the frequency-dependent parameter S_{21}, where the losses are related to its magnitude. That is because $Loss = 1 - |S_{11}|^2 - |S_{21}|^2$, and $|S_{11}|$ is zero for perfectly-matched transmission lines. The losses in a transmission line can be quantified through the attenuation constant α, which is:

$$\alpha = \alpha_c + \alpha_d + \alpha_r, \tag{4.24}$$

meaning that the total attenuation of a transmission line comes from the conductor (α_c), the dielectric (α_d), and radiation (α_r). Furthermore, accurate formulations for α_d and α_c are available in the literature [143]. Approximate expressions for α_d and α_c are defined in (4.25)–(4.26) [95]. The calculation of α_r is usually very complex, but for thin transmission lines ($H < \lambda_0/10$), it can be neglected, since $\alpha_r \propto (H/\lambda_0)^2$ [143].

$$\alpha_c \approx \frac{8.68 R_s}{Z_0 W}\ \text{dB/m} = \frac{298.28}{Z_0 W}\sqrt{\frac{1}{\sigma_{bulk}\lambda_0}}\ \text{dB/m} \tag{4.25}$$

$$\alpha_d \approx \frac{\beta \tan\delta}{2}\ \text{dB/m} = 27.3\frac{\varepsilon_r(\varepsilon_e - 1)}{\sqrt{\varepsilon_e}(\varepsilon_r - 1)}\frac{\tan\delta}{\lambda_0}\ \text{dB/m}, \tag{4.26}$$

where $R_s = \sqrt{\pi f \mu_0/\sigma_{bulk}}$ is the conductor surface resistance, Z_0 is the line characteristic impedance, β is the phase constant; and ε_e, its effective permittivity. From (4.25)–(4.26), the relations $\alpha_c \propto \sqrt{f}$ and $\alpha_d \propto f$ are true.

From (4.25), it is observed that the conductor losses get more significant as thinner is the transmission line since W is proportional to H. For such thin lines, α_c can be greater than α_d. Therefore, the skin depth δ plays an important role in the losses of a transmission line, as $R_s = 1/(\sigma_{bulk}\delta)$. Considering a conductive trace characterized by its constitutive parameters $(\varepsilon_c, \mu_c, \sigma)$, the value of δ can be calculated as:

$$\delta = \frac{\sqrt{2}}{\omega\sqrt{\mu_c\varepsilon_c}}\left\{\sqrt{1+\left(\frac{\sigma}{\omega\varepsilon_c}\right)^2}-1\right\}^{-0.5} \approx \sqrt{\frac{2}{\omega\mu_c\sigma}} \tag{4.27}$$

The accuracy of the last approximation in (4.27) depends on the relation $(\sigma/(\omega\varepsilon_c))^2 \gg 1$, which decreases with lower conductivity and higher frequency. Even so, the approximation given in (4.27) gives errors less than 0.02% with $\sigma_{bulk} = 0.001\sigma_{Copper}$ at 300 GHz. Hence, the concept of good conductors can still be considered in mmWave. Since the roughness of the profile becomes comparable with δ in mmWave and above, its impact on the conductor losses becomes more prominent.

The total loss of a transmission line can be modeled as in (4.24) and extracted from the magnitude of S_{21}. In addition, the phase of a transmission line can be modeled as in (4.28) [144], and extracted from the phase of S_{21}.

$$\beta = \frac{\angle S_{21}}{L} = \frac{2\pi f}{c_0}\sqrt{\varepsilon_e} \tag{4.28}$$

Depending on the conductor foiling process, the conductor surface may be classified from standard profile to very-low profile [144]. Moreover, electrodeposited foils have typical values of R_q of 1.8 μm, while rolled foils have R_q values around 0.3 μm [115]. The upcoming lines review the impact of the surface roughness in the losses and phase of transmission lines.

4.4.2.2 Impact of the Surface Roughness in the Conductor Loss of Transmission Lines

The effect of the conductor surface roughness in the conductor loss can be numerically modeled as an increase of the conductor attenuation constant at zero roughness, α_c, by a factor K_r [95]. This factor is primarily a function of the RMS height roughness R_q. Thus, the corrected conductor attenuation constant α_{cr} can be expressed as in (4.29), which can be used to estimate the total losses as in (4.24). Diverse strategies from previous work explore the impact of the conductor surface roughness to estimate the value of K_r from an empirical, analytical and statistical perspective.

$$\alpha_{cr} = K_r \alpha_c \tag{4.29}$$

Empirical formulations provide the fastest way to include the conductor foil roughness in transmission lines. Morgan and Hammerstad [59] developed a formulation using the Finite Element Method, and based on the assumption that the conductor profile has a saw-tooth shape, getting consequently a closed-form expression K_{r-MH} (4.30). Then, Groiss [60] developed a computer-aided model for cavity resonators, providing the known factor K_{r-G} (4.31) used to estimate the conduction losses in rough conductors. Both expressions have a maximum value of 2, as plotted in Fig. 4.8a. However, later experimental results [145] showed that the loss factor might be more than 2, making both formulations not convenient to characterize the effects of electrodeposited conductors at mmWave frequencies and above.

$$K_{r-MH} = 1 + \frac{2}{\pi} \arctan\left[1.4\left(\frac{R_q}{\delta}\right)^2\right] \tag{4.30}$$

$$K_{r-G} = 1 + \exp\left[-\left(\frac{\delta}{2R_q}\right)^{1.6}\right] \tag{4.31}$$

Analytical formulations have allowed the inclusion of the conductor foil roughness from its internal structure. Huray [61] proposed a roughness model using the superposition principle to solve the Maxwell equations. The foil was assumed to be composed of random-size spheres, or *snow balls*, where the effective radius and the concentration of spheres are the parameters for that model. This model does not present that asymptotic limit value at 2. Nonetheless, it requires a characterization for each sample, which requires physical observation through a microscope.

This *snowball* model was later modified [64], considering all the spheres identical and forming 11 spheres per cell –a *cannonball*– along the foil area, as illustrated in Fig. 4.8b. Having a more defined geometry, Simonovich [64] derived the factor K_{r-HS} (4.32) to calculate the increased insertion losses in rough conductors. The terms r_{eq} (4.33) and A_{eq} (4.34) in (4.32) are the *cannonball* radius and area, respectively. They are related to R_q [64]. This formulation is more realistic and closer to observed roughness profiles than the former empirical models. However, the height distribution still does not follow the widely observed Gaussian pattern [146], especially in electrodeposited foils.

$$K_{r-HS} = 1 + 84\frac{\pi r_{eq}^2}{A_{eq}}\left[1 + \frac{\delta}{r_{eq}} + \frac{1}{2}\left(\frac{\delta}{r_{eq}}\right)^2\right]^{-1}, \tag{4.32}$$

where

$$r_{eq} = \frac{R_q}{2\left(\frac{2\sqrt{6}}{3} + 1\right)} \tag{4.33}$$

$$A_{eq} = 6r_{eq}^2\sqrt{3}\left(\frac{1}{\sqrt{3}} + 1\right)^2, \tag{4.34}$$

which can be simply expressed as $r_{eq} = 0.19R_q$, $A_{eq} = 0.9324R_q^2$; and in (4.32), $r_{eq}^2/A_{eq} = 0.0387$.

From the statistical perspective, the concept of equivalent conductivity was introduced in the last decade [147]. It states that a rough conductor with bulk

conductivity σ_{bulk} can be modeled as an equivalent smooth conductor σ_{eq}. Moreover, σ_{eq} can be related to the increasing-loss factor K_r as $\sigma_{eq} = \sigma_{bulk}/K_r^2$ [148], after replacing (4.25) in (4.29) for σ_{bulk} and σ_{eq}.

To achieve this, the foil depth y is considered a variable to characterize the conductivity distribution $\sigma(y)$, a model known as the Gradient Model [147]. In smooth conductors, $\sigma(y) = 0,\ \forall y < 0$; and $\sigma(y) = \sigma_{bulk},\ \forall y \geq 0$. Meanwhile, for rough conductors, $\sigma(y)$ follows a zero-mean cumulative Gaussian distribution with standard deviation R_q. Then, the concept of equivalent conductivity can be developed as follows [66]: first, numerically solve (4.35) [149], which is based on the Maxwell equations for H-field along the x-axis (plot in Fig. 4.9), i.e., H_x; then, by calculating the power density from H_x; and finally, by comparing the dissipated power with the one from an equivalent smooth conductor of conductivity σ_{eq}.

$$\frac{d^2H_x}{dy^2} = (j\omega\mu_0\sigma - \omega^2\mu_0\varepsilon_0)H_x - \frac{1}{\sigma + j\omega\varepsilon_0}\frac{d\sigma}{dy}\frac{dH_x}{dy} \tag{4.35}$$

The expression (4.35) is solved for each point in angular frequency ω, as followed in [63, 66, 67]. The conductor is assumed to have permittivity ε_0 and permeability μ_0. This strategy is currently implemented in the simulation software SIMULIA™ CST, showing great correlation with measurements [63, 66]. This strategy may be extended to design microwave devices with an accurate response [67]. Nevertheless, the computer-aid mathematical implementation involves dense programming and several loops, which can be reduced through an equivalent algebraic model for σ_{eq}.

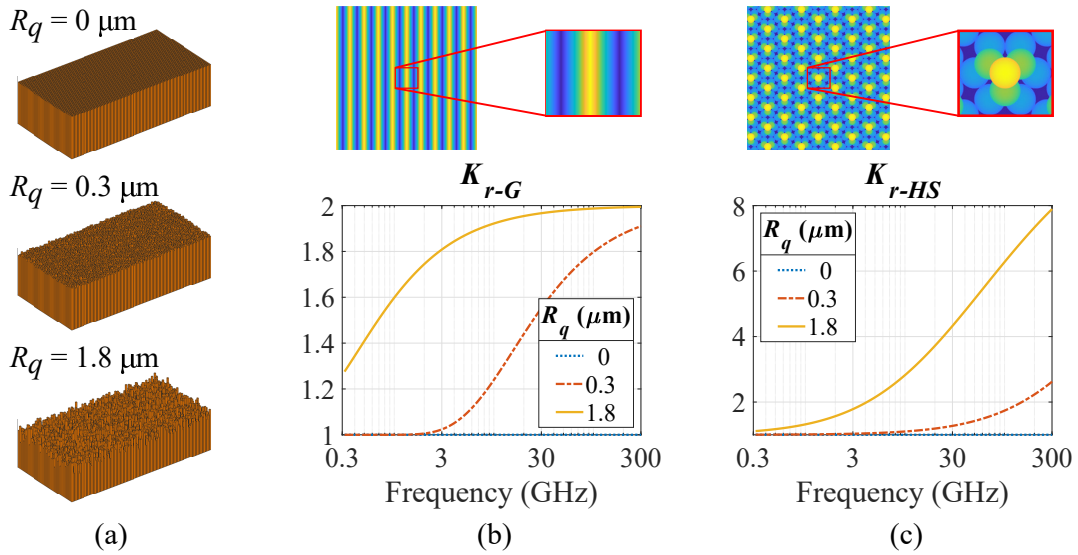

Figure 4.8: Geometrical roughness models for conductor foils.
Roughness typical profile (a) and two known roughness models: (b) Groiss [60] and (c) Huray [62] (modified by [64]). The geometries are shown at the top and left. Both models are geometry-based formulations and include an insertion-loss increase factor plotted between 0.3 GHz and 300 GHz.

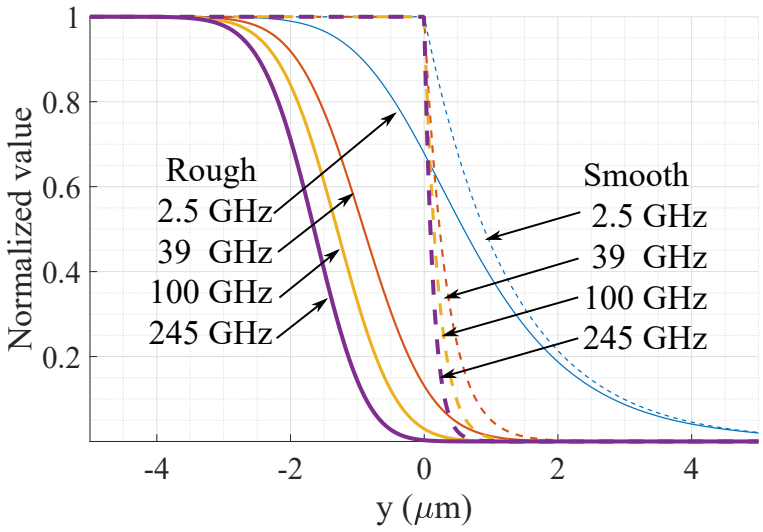

Figure 4.9: Equivalent distribution of magnetic fields for 1 μm rough copper.
According to the Gradient, Model [147], a gradual variation of the magnetic field (4.35) occurs from the space outside the conductor (y <0) up to the inner structure of the conductor (y >0) as the depth y increases. Then, a concept of an equivalent conductor can be built to model this field gradient.

4.4.2.3 Impact of the Surface Roughness in the Phase of Transmission Lines

The conductor surface roughness has been observed to increase the phase delay along the entire analysis range between 0.3 GHz and 300 GHz. However, it is more noticeable at frequencies above 30 GHz. The effect of the conductor surface roughness in the phase of transmission lines can be numerically assessed by the design dielectric constant, called Dk from now. The value of Dk can be extracted from (4.28) as in (4.36). This value is close to the relative permittivity of the substrate, ε_r. This value considers the interaction between the dielectric and conductor traces, which is geometry-dependent.

$$Dk = \left(\frac{\beta}{2\pi f/c_0}\right)^2 = \left(\frac{\angle S_{21}}{L}\frac{c_0}{2\pi f}\right)^2 \tag{4.36}$$

The impact of the conductor surface roughness in Dk is illustrated in Fig. 4.10c for striplines. Fig. 4.10a shows a 50 Ω stripline filled with a Rogers™ 3003 substrate ($\varepsilon_r = 3$, $h = 5$ mils, $t = 17.5$ μm or 0.5 oz/ft^2). At low frequencies, less than 3 GHz, an increase of Dk is observed in contrast to higher frequencies, even in the case of zero-roughness transmission lines. As the conductor surface roughness increases, the value of Dk also does, although the increase factor varies with frequency. These trends have also been observed in previous work [65, 144]. Then, this work aims to propose a mathematical model to quantify the variations of Dk while developing the formulations of the equivalent conductivity σ_{eq} to be used in smooth-conductor equivalent transmission lines that produces the same phase that the counterpart geometry with roughness.

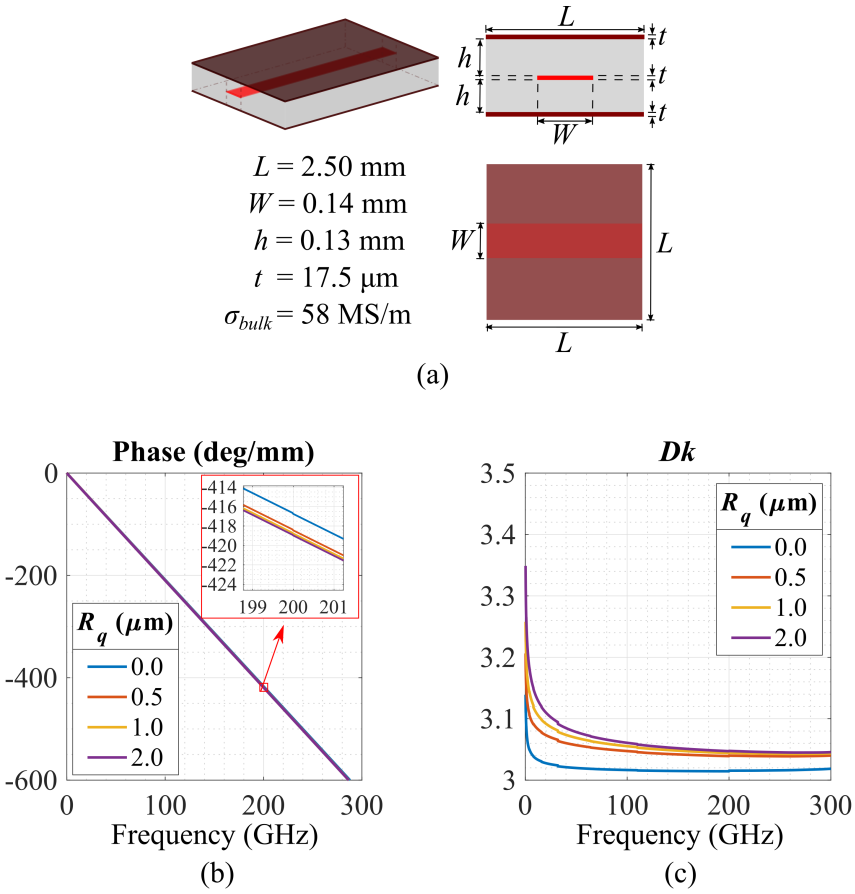

Figure 4.10: Impact of the conductor surface roughness in the phase delay. This figure exemplifies the phase delay in a stripline with rough copper traces up to 300 GHz. Simulations made with SIMULIA™ CST 2021. (a) Stripline geometry, (b) Phase delay from S_{21}, (c) Effect on Dk (4.36). With an increasing surface roughness, the phase delay is also increased, but with an inverse correlation with the frequency.

4.4.3 Consequences in EM Modeling of mmWave and Sub-THz Antennas

This section thoroughly reviews the effect of the geometrical characteristics (thickness and roughness) of conductor traces in MSPA modeling, especially for operating frequency in the mmWave and sub-THz bands. The proposed strategies to consider both geometrical features in modeling MSPAs above 30 GHz are listed as follows:

- Feeding adjustment: To ensure that the feeding line (embedded microstrip) has a characteristic impedance set to 50 Ω regardless of frequency and trace thickness, the line width W_f is adjusted before modeling PC-MSPAs. For PF-MSPAs, the coaxial line is scaled in frequency to ensure accurate line impedance. The effect of this strategy is reflected in the proposed MSPA models in Chapter 5.
- Model reformulation to include the conductor trace thickness: As discussed, an effective trace thickness can be calculated to model the patch's RLC resonant frequency accurately. This strategy consists in analytically formulating a concept of an effective dielectric thickness, which includes part of the trace thickness. This strategy is detailed in Chapter 5.
- Equivalence roughness model: This strategy aims to formulate a geometrical model that includes analytical formulations of the equivalent conductivity and design dielectric constant that replicates the same effects in loss and phase for transmission lines with rough conductor foils. This strategy is developed in the next section.

4.5 Equivalency Model to Assess the Impact of the Surface Roughness on Microstrip Lines and Striplines

This work proposes a mathematical model to assess the impact of the conductor surface roughness. This model postulates that a rough geometry, e.g., a transmission line, can be substituted by an equivalent smooth geometry so that the magnitude and phase of S_{21} are the same. This equivalency is pictured in Fig. 4.11. Therefore, this section details the analytical expressions for the equivalent conductivity σ_{eq} and introduces a new formulation for the design dielectric constant Dk for striplines.

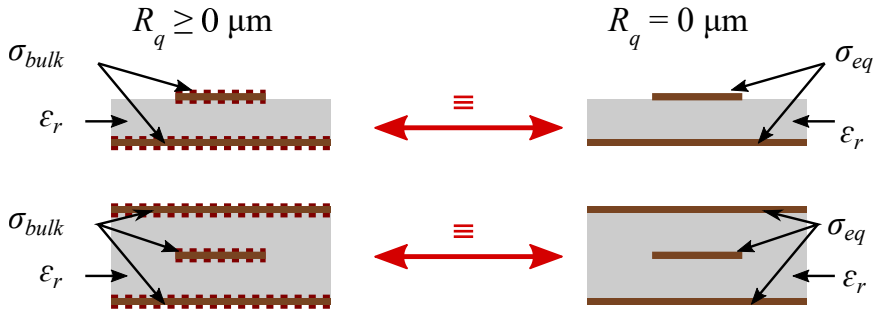

Figure 4.11: Equivalence model for transmission lines with rough conductors. A rough conductor can be replaced with a smooth and equivalent conductor to replicate the insertion loss caused by the conductor's surface roughness. Consequently, the design dielectric constant Dk changes so that it is equivalent to replicating the phase delay coming from the rough conductor.

The geometry equivalency can be mathematically described as follows: Let be a 50-Ω transmission line ($|S_{11}| \rightarrow 0$), where the substrate's relative permittivity ε, the substrate's loss tangent $\tan\delta$, and the trace conductivity σ are variable. The rest of the parameters and dimensions remain invariable. Then, the total loss and phase can be rewritten from (4.24) and (4.28) as:

$$\alpha \approx \frac{\zeta_1}{\sqrt{\sigma}} + \zeta_2 \tan\delta\sqrt{\varepsilon} \tag{4.37}$$

$$\beta = \zeta_3\sqrt{Dk}, \tag{4.38}$$

where ζ_1, ζ_2, and ζ_3 account for the invariable parameters and dimensions of the transmission line. Then, the geometry equivalency is expressed as in (4.39) and (4.40), which are related to the magnitude and the phase of S_{21}. In these equations, σ_{eq} is written as $\sigma_{eq} = \sigma_{bulk}K_\sigma$, where K_σ is a coefficient that depends on frequency and R_q. Besides, the design dielectric constant is written as $Dk|_{\sigma,\ Rq}$, showing dependency on conductivity and roughness.

$$\alpha_{\text{Original rough}} \equiv \alpha_{\text{Equivalent smooth}}$$

$$\frac{\zeta_1}{\sqrt{\sigma_{bulk}K_\sigma}} + \zeta_2 \tan\delta\sqrt{\varepsilon_r} \equiv \frac{\zeta_1}{\sqrt{\sigma_{eq}}} + \zeta_2 \tan\delta\sqrt{\varepsilon_r} \tag{4.39}$$

$$\beta_{\text{Original rough}} \equiv \beta_{\text{Equivalent smooth}}$$
$$\zeta_3\sqrt{Dk|_{\sigma=\sigma_{bulk},\ Rq\neq 0}} \equiv \zeta_3\sqrt{Dk|_{\sigma=\sigma_{eq},\ Rq=0}} \tag{4.40}$$

The variables σ_{eq} and ε_r are coupled variables, as observed in (4.39). This coupling may increase the formulation complexity of Dk if both equations are analytically solved. However, decoupling is possible by making $\tan\delta = 0$, allowing independent models for σ_{bulk} and Dk. The model for σ_{bulk} is built by comparing the magnitude of S_{21} from rough and smooth transmission lines, considering lossless substrates and variable conductivity media. Also, the model for Dk is created from the phase comparison of S_{21} from rough and smooth transmission lines with constant conductivity media.

4.5.1 Equivalent Conductivity

An straightforward formulation for σ_{eq} is built to be easily used as an equivalent smooth conductive boundary for rough conductors.

Let be a conductor characterized by its bulk conductivity σ_{bulk} (in MS/m) and its RMS roughness height R_q (in μm). The skin depth for the rough conductor, δ, defined in (4.27), can be rewritten as in (4.41), considering its bulk conductivity σ_{bulk}. Notice that the bulk conductivity is normalized to copper, where $\sigma_{Cu} =$ 58 MS/m. The frequency f is in GHz.

$$\delta = 2.09\sqrt{\frac{1}{f\ \sigma_{bulk}/\sigma_{Cu}}}\ \mu m \tag{4.41}$$

The roughness value R_q can be related to the skin depth δ by Δ_q as:

$$\Delta_q = \frac{R_q}{\delta} = \frac{R_q}{2.09}\sqrt{f\frac{\sigma_{bulk}}{\sigma_{Cu}}} \tag{4.42}$$

Let be the expression σ_{eq} in (4.43) as the equivalent conductivity for a rough conductor characterized by R_q and σ_{bulk}. The function f, defined as $\mathrm{f}(\xi, \upsilon, \Delta_q) = e^{\xi e^{-1.4(\Delta_q)^{-\upsilon}}}$, quantifies the conductivity degradation in the equivalent model. The coefficients ξ and υ in the function f are frequency independent, since δ is already function of frequency.

$$\sigma_{eq} = \frac{\sigma_{bulk}}{\mathrm{f}(\xi, \upsilon, \Delta_q)} = \frac{\sigma_{bulk}}{e^{\xi e^{-1.4(\Delta_q)^{-\upsilon}}}} \tag{4.43}$$

Then, by replacing (4.42) in (4.43), σ_{eq} can be expressed as:

$$\sigma_{eq} = \sigma_{bulk}\ e^{-\xi e^{-1.4(\Delta_q)^{-\upsilon}}} = \sigma_{bulk}\ e^{-\xi e^{-1.4\left(\frac{R_q}{2.09}\sqrt{f\frac{\sigma_{bulk}}{\sigma_{Cu}}}\right)^{-\upsilon}}}, \tag{4.44}$$

where $\xi = 4.6 - 0.1R_q$, $\upsilon = 0.6262 + 0.03R_q$, R_q is in μm, f is in GHz, and σ_{bulk} is in MS/m. For values of $R_q \in [0, 4]$ μm and frequencies between 30 GHz and 300 GHz, the terms R_q in ξ and υ can be ignored, i.e., $\xi = 4.6$, and $\upsilon = 0.6262$. The coefficients ξ and υ have been obtained as follows: first, by comparing the magnitude of S_{21} between simulated striplines with rough and smooth conductors, performed in SIMULIA™ CST 2021; then, by obtaining the conductivity and frequency in the intersect points; and finally, by applying the curve-fitting technique [69] to the data points, as illustrated in Fig. 4.12a. This proposed model is compared to previous work as shown in Fig. 4.12c.

Given σ_{bulk} and σ_{eq}, the factor K_r for additional conductor loss due to the roughness, can be rewritten as K_{r-eq} in (4.45), for R_q given in μm, and f specified in GHz. This value is plotted in Fig. 4.14b. for $R_q \in [0; 2]$ μm.

$$\begin{aligned} K_{r-eq} = \sqrt{\frac{\sigma_{bulk}}{\sigma_{eq}}} &= \sqrt{\mathrm{f}(\xi, \upsilon, \Delta_q)} = \sqrt{e^{\xi e^{-1.4(\Delta_q)^{-\upsilon}}}} \\ &= e^{0.5\xi e^{-1.4\left(\frac{R_q}{2.09}\sqrt{f\frac{\sigma_{bulk}}{\sigma_{Cu}}}\right)^{-\upsilon}}} \end{aligned} \tag{4.45}$$

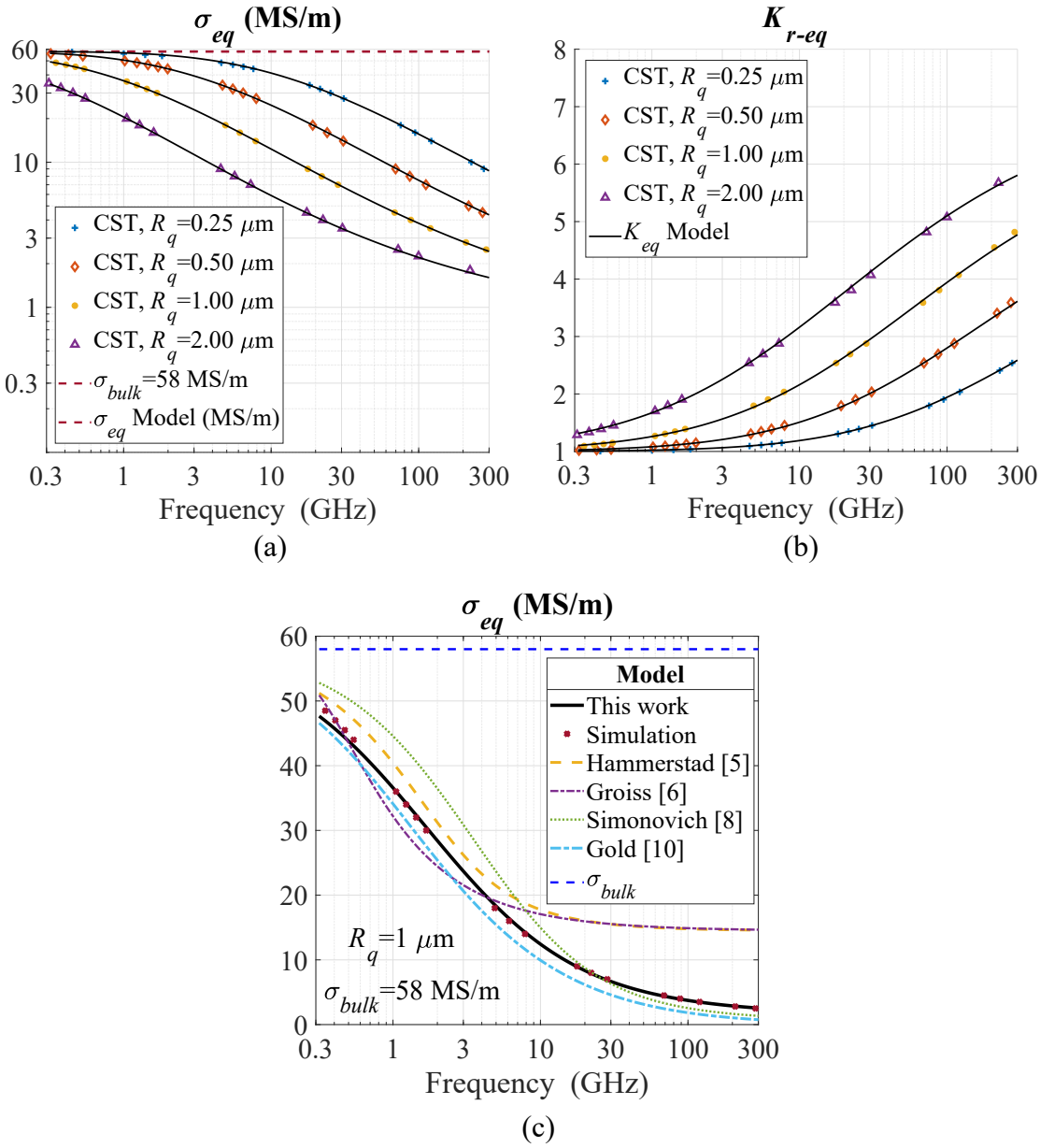

Figure 4.12: Variations of the equivalent conductivity over frequency.
(a) Proposed model, (b) Loss-increase factor, (c) Comparison with previous work. This enhanced model provides high accuracy with simulations while keeping a formulation easy to implement. The comparison with previous work shows a panoramic view of the different quantification outcomes from the conductor surface roughness up to the sub-THz bands.

4.5.2 Equivalent Design Dielectric Constant

This subsection introduces a mathematical model to assess the impact of the roughness in the phase of striplines. The value of Dk can be modeled as in (4.46). This function is constituted of a base value B and an increase factor F_{Dk}. The increase factor has an amplitude p_0, a zero p_1, and the poles p_2 and p_3. This mathematical formulation has been inspired by the multi-pole Debye model for permittivity dispersion [137].

$$Dk = B\ F_{Dk} = B\left[1 + p_0 \frac{(f + p_1)}{(f + p_2)(f + p_3)}\right] \tag{4.46}$$

In (4.46), f is in GHz. The coefficient B includes the value of ε_r. The coefficients B, p_0, p_1, p_2, and p_3 are described as in (4.47)–(4.51). where R_q is expressed in μm.

$$B = \varepsilon_r(1.012 - 0.007e^{-4R_q}) \tag{4.47}$$

$$p_0 = 0.98 - 0.85e^{-1.5R_q} \tag{4.48}$$

$$p_1 = 1.725 + e^{-1.25R_q}[0.2\cos(1.25R_q) - \sin(1.25R_q)] \tag{4.49}$$

$$p_2 = 0.61 - 0.25e^{-1.31R_q^2} \tag{4.50}$$

$$p_3 = 10\{2 + e^{-2.5R_q}[2.25\sin(2.5R_q) - 0.95\cos(2.5R_q)]\} \tag{4.51}$$

The numerical coefficients in (4.47)–(4.51) have been determined considering the geometry of Fig. 4.10a, considering a Rogers™ 3003 substrate ($\varepsilon_r = 3, h =$ 0.127 mm) and copper thickness of 17.5 μm. The model and accuracy assessment are illustrated in Fig. 4.13 for roughness values R_q up to 2 μm. The errors below 1 % show that the multi-pole formulation can be applied to estimate Dk in smooth and rough conductors. The expression of (4.46) can then be extended in future work for different substrate and conductor thicknesses to describe a more generalized pattern of the phase delay.

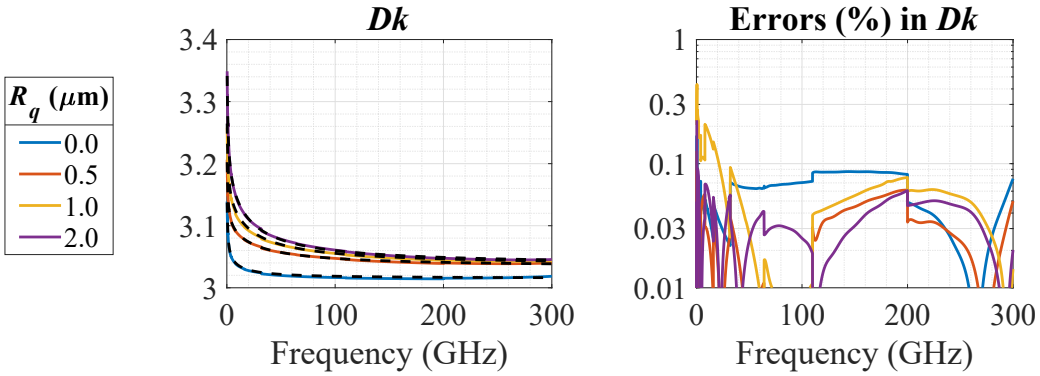

Figure 4.13: Variations of the design dielectric constant over frequency.
(a) Proposed model vs. simulation, (b) Percent errors. The data source comes from the copper stripline of Fig. 4.12, which is 0.14 mm wide and 17.5 μm thick, between two 0.13 mm-thick Rogers™ dielectrics ($\varepsilon_r = 3$). This introductory model provides a high estimation accuracy compared with simulations while keeping a formulation easy to implement.

4.5.3 Validation of the Proposed Model

The proposed model is validated by comparing the magnitude and phase of S_{21} and following the equivalency principle illustrated in Fig. 4.11. Thus, the model is validated with simulated data from the insertion losses and the phase coming from a microstrip transmission line and a stripline. Besides, the model is validated with measured magnitude and phase of S_{21} from a microstrip line.

4.5.3.1 Validation Methodology

The validation of this work aims to demonstrate the model equivalency. Thus, it is required to have the values of S_{21} from a rough transmission line made of lossy and rough materials and the values of S_{21} from a smooth transmission line made of the equivalent materials from the proposed model. The S_{21} solutions from the rough transmission lines are considered the ground truth to validate the proposed model. Also, measured results support the validity of the ground truth, which has also been demonstrated in previous work [66, 147].

The following designs were used for validation:

- Design 1 is a microstrip transmission line of width 0.392 mm, over a Rogers™ 5880 Duroid substrate with $\varepsilon_r = 2.2$, $\tan\delta = 0.0009$ and 5 mils thick. The conductor used has a bulk conductivity of 58 MS/m (copper).
- Design 2 is a stripline of width 0.144 mm and thickness 17.5 μm, between two Rogers™ 3003 substrates with $\varepsilon_r = 3.0$, $\tan\delta = 0.001$ and 5 mils thick each one. The conductors have a bulk conductivity of 41 MS/m between gold and aluminum.

Every conductor trace is 17.5 μm thick. The RMS roughness is defined as $R_q = 1$ μm. The transmission lines are 2.5 mm, 4 mm, and 6.5 mm long. In addition to the RMS roughness $R_q = 1$ μm used in the designs for Fig. 4.14, two additional variations ($R_q = 0.3$ μm and 1.8 μm) are analyzed.

The simulation data for the ground truth is obtained in SIMULIA™ CST. The designs were drawn using lossy and rough metals. The available settings that simulate the effects of the conductor roughness are based on the conductor gradient model [147]. Besides, these designs were replicated in Ansys™ HFSS with the equivalent material as on (4.44).

4.5.3.2 Simulated Results

A multi-frequency response is pictured in Fig. 4.14, comprising the mmWave and sub-THz bands. The comparisons of Fig. 4.14b,c overlap simulated responses (S_{21} in dB/mm for magnitude, and deg/mm for phase) of the aforementioned designs with both rough conductor and its smooth equivalent material (4.44). Then, the numerical accuracy of the model is listed in Table 4.5 and Table 4.6. The comparison is made at 39 GHz, 100 GHz, and 245 GHz, and with RMS roughness of 0.3 μm, 1 μm, and 1.8 μm.

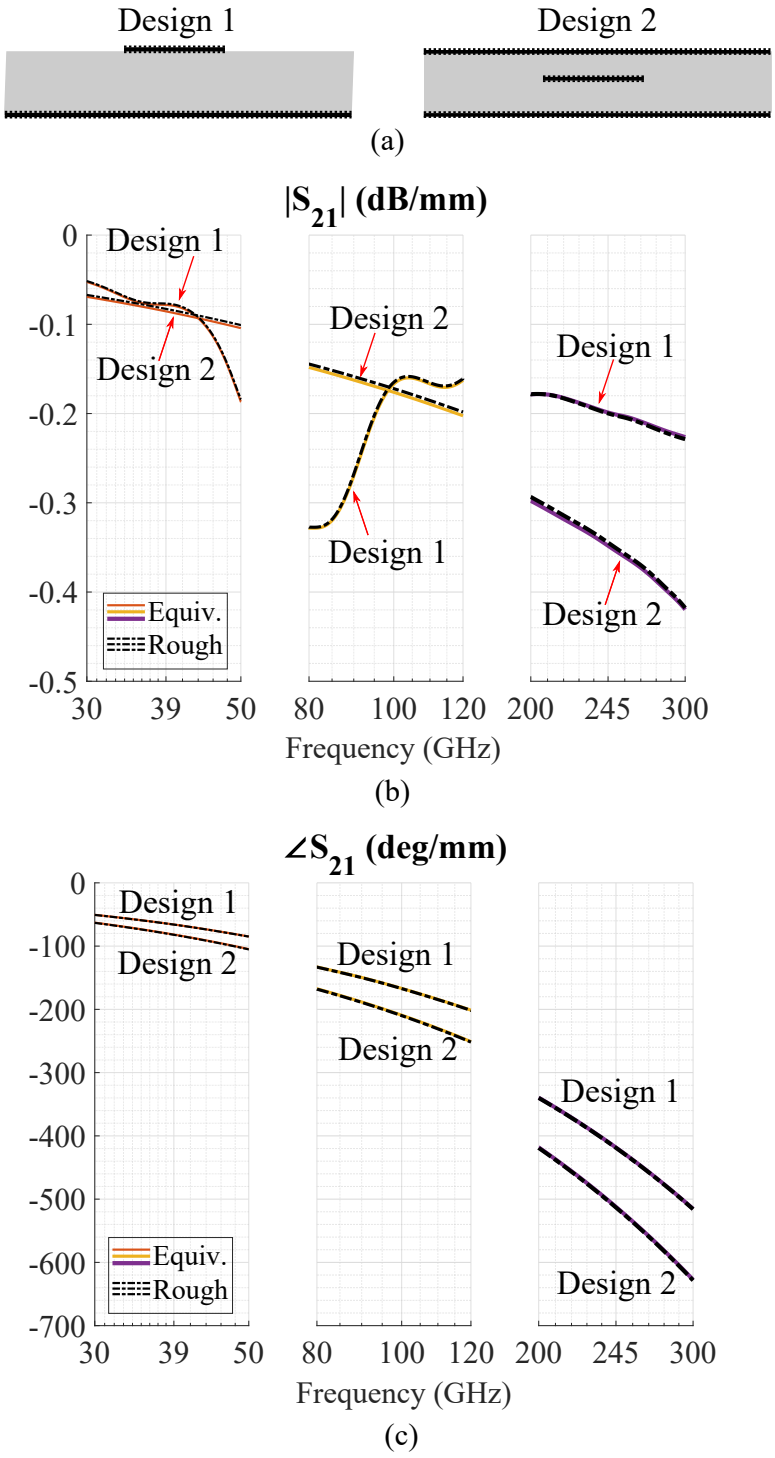

Figure 4.14: Simulated results for rough microstrip lines and striplines. (a) cross-sectional view of the lines, (b) simulated magnitudes, (c) simulated phases. A surface roughness $R_q = 1$ μm is considered in SIMULIA™ CST 2021. These results show the high accuracy of the proposed model in this work.

Table 4.5: A comparison of insertion losses (in dB/mm) and unwrapped phase (in degrees/mm) in microstrip transmission lines between rough conductors and modeled smooth equivalent conductors.

f_o (GHz)	R_q (μm)	Magnitude (dB/mm)			Phase (deg/mm)		
		Rough	Equiv.	% error	Rough	Equiv.	% error
39	0.3	-0.059	-0.060	1.25	-65.84	-65.68	0.247
	1.0	-0.077	-0.078	1.96	-66.01	-65.82	0.286
	1.8	-0.089	-0.090	2.03	-66.07	-65.90	0.266
100	0.3	-0.126	-0.128	1.51	-166.9	-166.6	0.189
	1.0	-0.165	-0.167	1.23	-167.2	-166.9	0.198
	1.8	-0.186	-0.188	1.18	-167.3	-167.0	0.153
245	0.3	-0.130	-0.131	0.46	-418.5	-418.0	0.130
	1.0	-0.200	-0.199	0.52	-418.9	-418.4	0.114
	1.8	-0.232	-0.231	0.43	-419.0	418.7	0.088

Table 4.6: A comparison of insertion losses (in dB/mm) and unwrapped phase (in degrees/mm) in strip transmission lines between rough conductors and modeled smooth equivalent conductors.

f_o (GHz)	R_q (μm)	Magnitude (dB/mm)			Phase (deg/mm)		
		Rough	Equiv.	% error	Rough	Equiv.	% error
39	0.3	-0.048	-0.050	2.48	-81.78	-81.47	0.380
	1.0	-0.083	-0.086	3.39	-82.14	-81.73	0.494
	1.8	-0.107	-0.111	3.37	-82.30	-81.91	0.470
100	0.3	-0.102	-0.104	2.66	-209.3	-208.7	0.281
	1.0	-0.172	-0.176	2.38	-209.9	-209.2	0.315
	1.8	-0.214	-0.219	2.48	-210.1	-209.6	0.260
245	0.3	-0.216	-0.219	1.72	-512.4	-511.4	0.205
	1.0	-0.345	-0.348	1.02	-513.2	-512.3	0.187
	1.8	-0.409	-0.410	0.34	-513.5	-512.7	0.152

The model equivalency looks pretty well in magnitude and phase, according to the plots shown in Fig. 4.14. The insertion losses in both transmission lines have an average error of less than 5 % at 39 GHz, 100 GHz, and 245 GHz. This difference is slightly more noticeable in the stripline (Design 2) than in the microstrip line (Design 1). Since the transmission lines used for antennas between 30 GHz and

300 GHz are in the order of a few millimeters, the total insertion losses may not exceed 1 dB. All this evidence shows that the proposed model provides an accurate equivalency to the entire analytical model of (4.35) [63, 67] based on Maxwell's equations while keeping it straightforward to implement in computational tools.

From a quantitative perspective, Table 4.5 and Table 4.6 show a high model accuracy in replicating the effects of the conductor surface roughness in the insertion loss and phase delay of transmission lines. The insertion losses and phase delay are higher in Design 2 because of the lower conductivity, higher loss tangent, and higher permittivity in Design 2 than in Design 1. The variable errors in the insertion losses (Design 1 and Design 2) indicate a high sensibility in the fabrication accuracy required to design, estimate, and verify the losses in transmission lines. However, the errors in the insertion loss do not exceed 2 % in microstrip lines and 3.5 % in striplines. The phase errors are kept in the tenth percent over frequency and roughness values, not exceeding 0.5 %.

4.5.3.3 Measurement Strategy

The S_{21} parameter of a 50-Ω microstrip transmission line is measured to validate the experimental roughness ground truth from the simulated design.

The following equipment has been used for this experimental validation:

1. A 50-Ω Signal Microwave™ (product code 044-044-1Fn) 1-in microstrip transmission line. This test board comprises a 0.127-mm (4.9 mils) thick Isola™ Astra MT77 laminate ($\varepsilon_r = 3$, $\tan\delta = 0.001$) with a 50 μm copper and gold low-profile cladding ($R_z = 2.50$ μm, equivalent to $R_q = 0.36\mu$m). On the edges, there are transitional structures to adapt the impedance matching differences between coaxial and microstrip transmission lines. Fig. 4.16a illustrate them in the close-up view. These transitions allow the operational frequency to in-

crease up to 110 GHz. Underneath this laminate is a 1.5-mm (60 mils) FR4 supporting board that allows appropriate mechanical handling.

2. A 50-Ω Signal Microwave™ (product code 044-044-2Fn) 2-in microstrip transmission line with the exact characteristics of the 1-in microstrip transmission described above.
3. Two Southwest Microwave™ (product code 2492-04A-6) mmWave connectors with the following characteristics: 1-mm (W, 110 GHz) end launch, jack, female, and standard Block (0.5 inches). These connectors present a 0.127-mm (5 mils) pin diameter, slightly thinner than the 7-to-11-mils microstrip line.
4. A Keysight™ N5225B performance network analyzer (PNA) with operation frequency from 10 MHz to 50 GHz.
5. A Keysight™ N5295AX03 frequency extender up to 120 GHz. This accessory allows using the PNA for the validation proposed in this work.
6. A Keysight™ 85059B 1-mm calibration kit. This product covers the frequency range from DC to 120 GHz. It contains 15 calibration devices: open-circuit terminations, short-circuit terminations, load terminations, and adap-ters, both with male and female variations.
7. Supportive equipment, such as positioning sliders, table, computer supplies, mechanical tools, and office supplies.

These items are part of the current equipment available at the mmWave and sub-THz laboratory in the Advanced Radar Research Center. This fixture is illustrated in Fig. 4.15e. The microstrip transmission lines (devices under test) are shown in Fig. 4.15a,b, with a close up in the connector in Fig. 4.15c,d.

The measured results are obtained by computing the net microstrip transmission line between the two microstrip test boards under the experiment. This approach is described as follows:

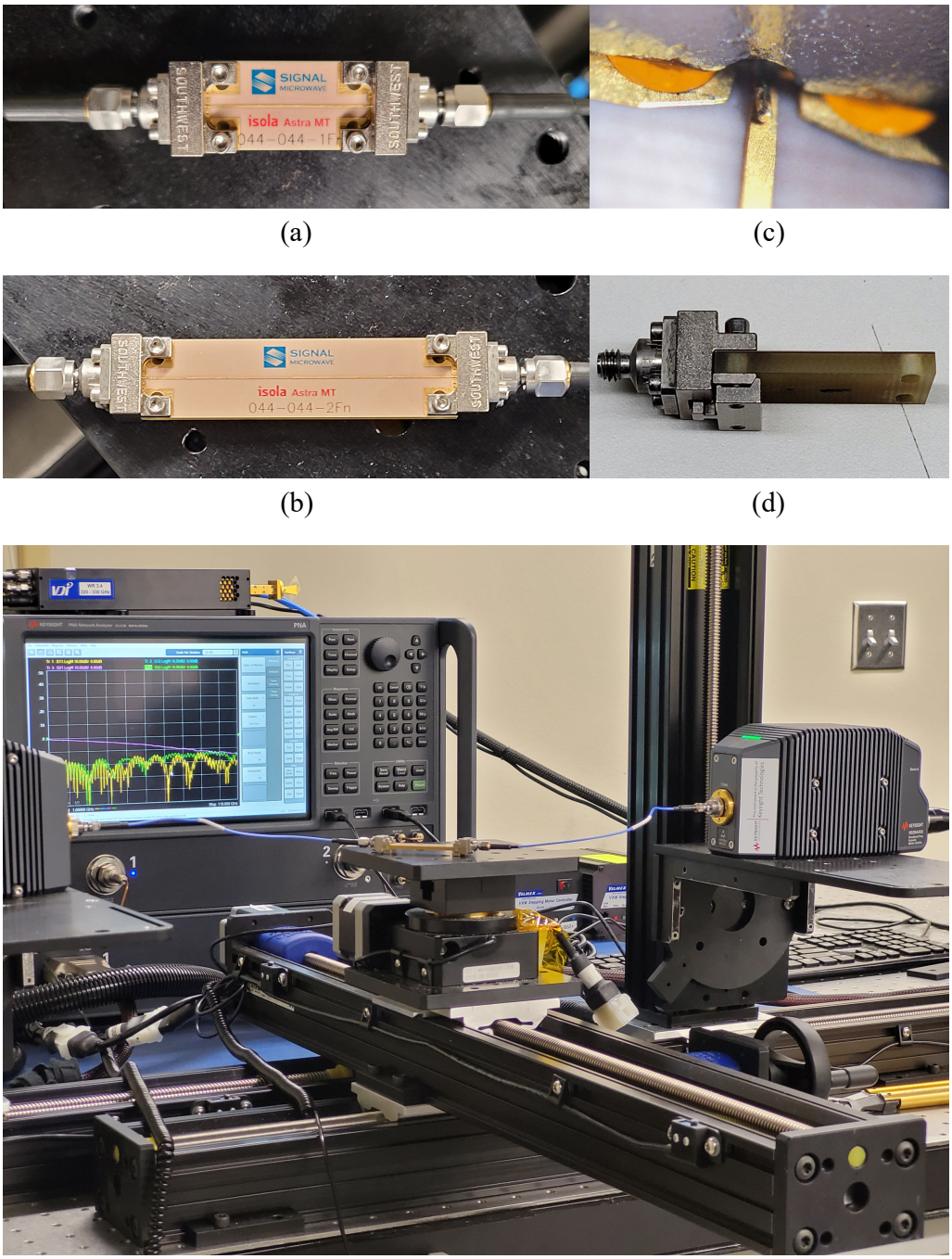

Figure 4.15: Electrical setup for experimental validation of microstrip lines. (a) Top view of 1-in microstrip line with 1-mm connectors and coaxial cables, (b) Top view of 2-in microstrip line with 1-mm connectors and coaxial cables, (c) A close-up of the connection, (d) A profile of the 1-in microstrip line and connector, (e) Experimental fixture (Keysight™ PNA, positioners, and supporting equipment).

The 1-in microstrip transmission line is connected with the PNA through two edge launch connectors and two low-loss coaxial cables. All these devices are operational up to 110 GHz. Then, the insertion loss (in dB) and unwrapped phase delay (in degrees) can be written as:

$$|S_{21}^{(T1)}| = 2|S_{21}^{(C)}|+2|S_{21}^{(ELC)}|+2|S_{21}^{(TR)}|+|S_{21}^{(u1)}| \tag{4.52a}$$

$$\angle S_{21}^{(T1)} = 2\angle S_{21}^{(C)} + 2\angle S_{21}^{(ELC)} + 2\angle S_{21}^{(TR)} + \angle S_{21}^{(u1)}, \tag{4.52b}$$

where the superscript $(T1)$ means 'total' for the 1-in board under test, (C) refers to the coaxial cables, (ELC) is associated with the edge launch connectors. Also, (TR) accounts for the transitions between the coaxial interface and microstrip transmission line –as seen in Fig. 4.16a– and $(u1)$ stands for the microstrip line itself. This formulation tells that the total insertion loss and total phase delay come from all the elements just described. The practical portion of the test board that is a microstrip line is 23.36 mm, less than 1 inch.

The 2-in microstrip line presents a measured insertion loss and unwrapped phase delay that can be written as in (4.53a)-(4.53b), where the superscript $(T2)$ refers to the 'totals' for the 2-in board under test. The length of the microstrip line without the transition is 48.76 mm, slightly less than 2 inches.

$$|S_{21}^{(T2)}| = 2|S_{21}^{(C)}|+2|S_{21}^{(ELC)}|+2|S_{21}^{(TR)}|+|S_{21}^{(u2)}| \tag{4.53a}$$

$$\angle S_{21}^{(T2)} = 2\angle S_{21}^{(C)} + 2\angle S_{21}^{(ELC)} + 2\angle S_{21}^{(TR)} + \angle S_{21}^{(u2)}, \tag{4.53b}$$

The effects of the coaxial cables, connectors, and transitions are considered equal in both formulations. Consequently, there may be a slight shift in the losses and phase delay up to the uncertainty of the adjustments in the different interfaces of the experiment setup.

Therefore, by subtracting (4.53a) from (4.52a), the result is a net 1-in microstrip line, which insertion loss can be expressed in dB as:

$$|S_{21}^{(T2)}|-|S_{21}^{(T1)}| = |S_{21}^{(u2)}|-|S_{21}^{(u1)}|= |S_{21}^{(u)}|, \tag{4.54}$$

where the superscript (u) is the net microstrip transmission line, which has a length of 48.76 mm−23.36 mm, equal to 1 inch. This value is also the length difference between the two microstrip test boards. Similarly, the unwrapped phase of the net 1-in microstrip line is expressed in degrees as:

$$\angle S_{21}^{(T2)} - \angle S_{21}^{(T1)} = \angle S_{21}^{(u2)} - \angle S_{21}^{(u1)} = \angle S_{21}^{(u)}, \tag{4.55}$$

Consequently, it is possible to get the magnitude and phase of a 1-in microstrip line from the measured S-parameters of the 2-in and 1-in microstrip-line test boards and their accessories. Moreover, since S_{21} are complex numbers, they can be divided as $S_{21}^{(T2)}/S_{21}^{(T1)}$ to replicate the formulations of (4.54)–(4.55). Then, the phase can be directly plotted in degrees without unwrapping.

4.5.3.4 Experimental Results

Two microstrip transmission lines were measured as illustrated in the setup of Fig. 4.16a, and as described above. A 1-in microstrip line was simulated without transitional structures and with wave ports. The simulation was performed in SIMULIA™ CST 2021, considering the specifications described in the first item of Section 4.5.3.3.

The plots of Fig. 4.16b,c compare the magnitude and phase between the net 1-in microstrip line from measured results and the simulated 1-in microstrip line. The comparison is made between 55 GHz and 110 GHz, which considers both the mmWave and sub-THz bands.

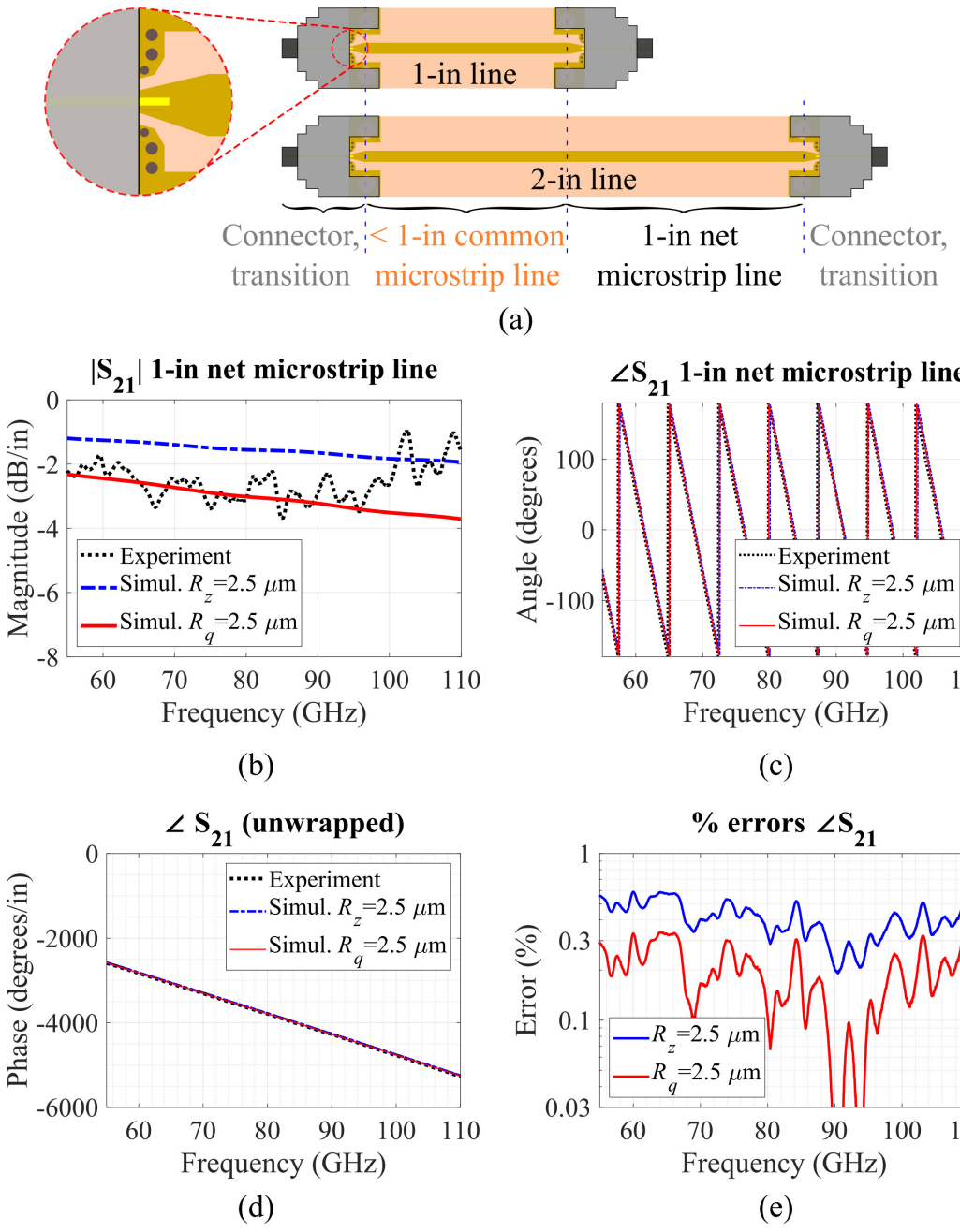

Figure 4.16: Measured results for rough microstrip lines up to 110 GHz. (a) measurement setup, (b) measured net magnitude, (c) measured net phase, (d) measured unwrapped phase, and (e) percent differences with simulated phase. Subtracting the losses and phases produced by the connector and transition in both lines, the net result is a 1-in microstrip line. Simulations in SIMULIA™ CST 2021 were executed to compare with the measurements. These results show a fair magnitude replication between simulation and measurement, with a great agreement in the phases.

The experimental validation shows a fair agreement between the net microstrip and the simulated counterpart. When simulating the microstrip line with the nominal roughness value provided in the data sheet ($R_z = 2.5$ μm, equivalent to $R_q = 0.36$ μm), the magnitudes have around 1 dB uniform discrepancy in the mmWave band, getting close from 100 GHz. A clear cause for this discrepancy was not found, but the following reason may have contributed to producing this difference:

1. The nominal roughness may have changed from $R_q = 0.36$ μm to a higher value. A closer agreement was found if $R_q = 2.50$ μm.
2. The calibration may include the adapter losses, which range between 0.2 dB and 0.4 dB between 55 GHz and 110 GHz.
3. The cable sizes and electrical connections may not be completely equal in both extremes of the tested microstrip lines. This effect may also be the main reason for the differences in the phase delay, which range between 15° to 25° over frequency, which is in the order of tenths percent.

When setting the simulations with $R_q = 2.50$ μm, the measured net insertion loss and the simulated insertion loss have a more significant agreement in the mmWave band. The differences start to be more noticeable in the sub-THz band. Neither Isola™ Group nor Dassault Systems™ provided further clarification in the units for roughness. However, it seems that a unit standardization and a more descriptive material characterization may allow solving this discrepancy.

The measured phase delay and the simulation of the 1-in net microstrip line present a great agreement between them. This close results happened with both simulation setups ($R_z = 2.50$ μm and $R_q = 2.50$ μm). Since all the plots look the same, the unwrapped phase was obtained, and the percent difference was calculated and plotted in Fig. 4.16d,e. Once again, although the difference is

minimal, there is a noticeable trend of the value $R_q = 2.5$ μm being more accurate for this specific application.

4.6 Summary

This chapter has presented a thorough overview of the impact of advanced material characteristics on the accuracy of current EM models for microstrip patch antennas. This impact includes challenges, trade-offs, and limitations of the available antenna models when the operation frequency is set in the mmWave and sub-THz bands.

As reviewed in the first sections of this chapter, the material characterization for antennas is typically performed by describing their constitutive parameters. These parameters are electric permittivity, magnetic permeability, and electric conductivity. An additional parameter for dielectric losses included in the technical specifications is the loss tangent, generally in the order of a thousandth. The most frequent and desired antennas for mmWave frequencies and above are purely metallic, purely dielectric, or contain both types of material. Advanced material characteristics, such as dielectric frequency dispersion, anisotropy, conductor thickness, and roughness, are required to model MSPAs accurately in the mmWave and sub-THz bands. As the frequency increases, the smaller material dimensions and imperfections become more noticeable in electrical length.

This chapter has provided a detailed analysis of the dielectric and conductor advanced characteristics and the consequences of EM modeling. The effect of the dielectric anisotropy may include the variation of the fringe fields, the patch' resonant frequency, and beyond. Including the frequency dispersion by a frequency-dependent relative permittivity provides a more realistic impedance estimation for MSPAs. The conductor trace thickness is usually ignored for MSPAs

with operating frequencies below 30 GHz. However, this dimension affects the impedance matching and patch's resonant frequency in the mmWave and sub-THz bands, which presents meaningful consequences in modeling MSPAs that will be developed in Chapter 5 through a new concept of effective substrate thickness.

The impact of the conductor surface roughness has been analyzed in this chapter, providing an enhanced model. The main impact of the conductor surface roughness is the increase of the insertion losses in devices with conductive traces such as transmission lines. A secondary effect of the roughness is the increase of the phase delay over frequency, quantified in branded laminates as an increase of the design dielectric constant.

This work has provided an equivalency model to accurately account for the effects of the conductor roughness in transmission lines. This approach considers the main advantages of empirical formulations (practical to implement) and the Gradient model (currently the most accurate physical model). A set of mathematical expressions is formulated to accurately replicate the effects of the conductor roughness by a close-form of the equivalent conductivity that replaces the original traces with a smooth equivalent conductor. Also, an unforeseen model for estimating the design dielectric constant has been introduced for striplines with rough conductors.

The validation of the equivalency model has shown high accuracy in simulated transmission lines and has presented a fair agreement in the experimental validation. The analytical expression of the equivalent conductivity has demonstrated great replication accuracy of the insertion losses and phase delays in microstrip lines and striplines between 30 GHz and 300 GHz. The experimental validation has shown that further clarification on the units set in the roughness characterization and models can provide reliable results that can be appropriately correlated

with measurements. Future work aims to pursue an advanced model with more roughness parameters that can be verified with experimental material characterization.

This chapter provides the foundations for the enhanced models presented in Chapter 5. As observed, model equivalencies and reformulations need to consider including these properties. Also, this study suggests accurately characterizing the materials for antenna design, emphasizing dielectric frequency dispersion and roughness.

Chapter 5

Enhanced EM Modeling for Microstrip Patch Antennas up to the Sub-THz Band

Science is fun. Science is curiosity.
We all have natural curiosity. Science is a process of investigating.
It's posing questions and coming up with a method. It's delving in. —Sally Ride

Antenna design in the mmWave and sub-THz bands is progressively increasing and enhancing towards the development of the upcoming 6G communication systems [14]. Despite the solid progress on design, prototyping and implementation usually constitute challenges due to the strict fabrication tolerances, being especially true above 100 GHz [15]. Analytical modeling of antennas plays a crucial role in developing strategic design guidelines since the formulations that support them permit to follow definite trends for the design features to optimize or prioritize. For antenna modeling above 30 GHz, these fabrication tolerances become more noticeable. For instance, the material's imperfections and small dimensions, such as copper thickness and roughness, must be included in the formulations.

As discussed in the preceding pages –in Chapter 2, Chapter 3, and Chapter 4–, previous work in modeling MSPAs shows the capability to estimate their behavior with good accuracy. The first models for these antennas [41] revealed that the impedance response of an MSPA could be modeled by an electric circuit composed

of an RLC parallel resonator in series with a lumped element. As detailed in Chapter 2, the resonator and the lumped element account for the patch and the feed, respectively.

In the cavity model [24], the patch, the ground plane, and the substrate between both forms a cavity resonator. One of the main parameters in the cavity resonator is the patch's resonant frequency of the dominant propagation mode f_{0p}, which is also the resonant frequency of the RLC circuit resonator. This parameter can be calculated as in (2.100) and (3.20) for PF-MSPAs and PC-MSPAs, respectively. The formulations for PF-MSPAs provide an accurate estimation of f_{0p} with errors less than 1 % for PF-MSPAs with substrates having dielectric constants up to 6.15 and thickness less than $0.1\lambda_0$ at operating frequencies less than 10 GHz. Also, several unprecedented modeling formulations for PC-MSPAs have been presented in detail in Chapter 3, showing errors in f_{0p} of less than 1 %. As demonstrated in Chapter 3, this accuracy is crucial to accurately model MSPAs, since all the parameters of the antenna equivalent circuit (quality factor, resonant resistance, and feeding reactance) depend on f_{0p}. Although this parameter is very accurate at frequencies less than 10 GHz, it begins to be out of track at frequencies above 100 GHz, as shown in Section 5.1 in this chapter. As explained in Chapter 4, this inaccuracy is mainly because the conductor foil thickness has been assumed negligible, which is not valid in millimeter-wave frequencies and higher.

The dielectric and conductor analysis in Chapter 4 demonstrated the importance of including the advanced electric and geometrical properties in the current MSPA model as reformulations to make them suitable up to the mmWave and sub-THz bands. The studies showed that the MSPA modeling assumptions –namely flat conductors, 50 Ω feed, and impedance reference– need to be evalu-

ated above 30 GHz. The model formulations in this chapter include the use of the frequency-dependent effective dielectric constant, the equivalence model for rough conductors, reformulations from the effect of the patch and feeding thickness, and evaluations of the MSPA modeling assumptions.

The previous work shows that the current models for MSPAs are not accurate for frequencies above 100 GHz. Then, as the first step in this chapter, a set of geometrical and mathematical modeling methods is proposed. They aim to improve the calculation of the resonant frequency of MSPAs by considering the conductor dimensions in the calculation. An updated circuit model for MSPAs will follow this enhancement.

This chapter also contributes novel methods to compute the RLC and feeding parameters of PF-MSPAs and PC-MSPAs in the mmWave and sub-THz bands. The upcoming sections provide updated formulations to model the patch's quality factor, resonant resistance, and feed impedance for PF-MSPAs and PC-MSPAs. Section 5.4 assesses the models with diverse antenna designs up to the sub-THz band, including a case with rough conductors. This chapter concludes with a discussion of the results and a summary of the findings.

5.1 Modeling Capability up the Sub-THz Band

The existing models for MSPAs, including the ones developed in this work in Chapter 3, are functional as long as the wavelength is several times the most diminutive dimensions of the patch and feeding structures. This section assesses the current EM models for PF-MSPAs and PC-MSPAs and lists modeling strategies to broaden the operational frequency up to 300 GHz.

5.1.1 Frequency Analysis

The previous chapters have covered the most recent EM models for estimating the impedance response of MSPAs, showing high accuracy in the radio frequency and lower microwave bands. Section 2.4 in Chapter 2 has covered the most recent EM model for PF-MSPAs. In addition, Section 3.4 provided the formulations for the new EM model for PC-MSPAs. These models process the geometrical and electrical properties of the materials to get circuit parameters computed to calculate the impedance response over frequency.

The accuracy of current EM models for MSPAs presents variations in the mmWave and sub-THz. As introduced in Chapter 4, modeling MSPA works under three fundamental assumptions:

- The conductor traces have an infinitesimal thickness; therefore, it does not play any role in the model response.
- The feeding transmission line is designed and set to 50 Ω.
- The impedance is delivered at a given location outside the patch.

The first assumption ignores the thickness of the conductors, especially from the patch. For PC-MSPAs, the feed thickness is also deemed negligible. At 3.5 GHz, a typical copper foil with a thickness of 17.5 μm represents 0.02 % the wavelength or $\lambda_0/5000$. However, at 286 GHz, this thickness represents 1.67 % the wavelength or $\lambda_0/60$. This thickness may be as significant as the dielectric substrate thickness. Hence, a frequency analysis is needed to assess the model working range and limitations in the mmWave bands and higher.

The second assumption ensures an accurate characterization of the return loss over frequency. It also helps avoid the complex calculations related to the feeding line's characteristic impedance towards estimating the S-parameters.

Since the standard port impedance is 50 Ω, the feeding line impedance is adjusted to keep a value of 50 ± 1 Ω up to 300 GHz and 35 μm trace thickness. This procedure has been illustrated in Table 4.3 in Chapter 4 for PC-MSPAs. The probe radius is scaled to keep the same relation with the dielectric radius. For a PTFE-based dielectric ($\varepsilon_r = 2.08$), the inner radius (probe) is proportional to 0.615 mm, and the external radius (dielectric) is proportional to 2.05 mm.

The third assumption is crucial to present the results accurately. For PF-MSPAs, the reference is between the coaxial feeding and the probe connecting the patch. For PC-MSPAs, the impedance reference is located in the feeding line and underneath the patch's edge that overlaps the feeding. Otherwise, if evaluated at the beginning of the feed, it would be necessary to determine the losses from the dielectric and the conductor for the associated embedded microstrip line, which models currently need to be made available, especially at sub-THz frequencies.

This section provides a frequency analysis of the current EM models for PF-MSPAs and PC-MSPAs. Since a frequency analysis has been introduced for PF-MSPAs in Section 4.4.1, this section focuses on PC-MSPAs. The model assessment is performed by comparing the impedance responses between the model and the simulation of designed PC-MSPAs in Ansys HFSS™. Because of the first assumption, two simulation setups are performed: ① by 3D-drawing the conductors for the patch, feeding line, the ground plane, with copper and 17.5 μm thick (Fig. 5.1), and ② by 2D-drawing (zero thickness) the same conductors and setting a copper-like conductivity boundary to them (Fig 5.2). A patch's resonant frequency analysis is also provided in Fig. 5.3 to compare the modeling accuracy for this parameter in both MSPA types.

The comparison in Fig. 5.1 shows an increasing shift in the patch's resonance parameters: resonant frequency, quality factor, and resonant resistance. Conse-

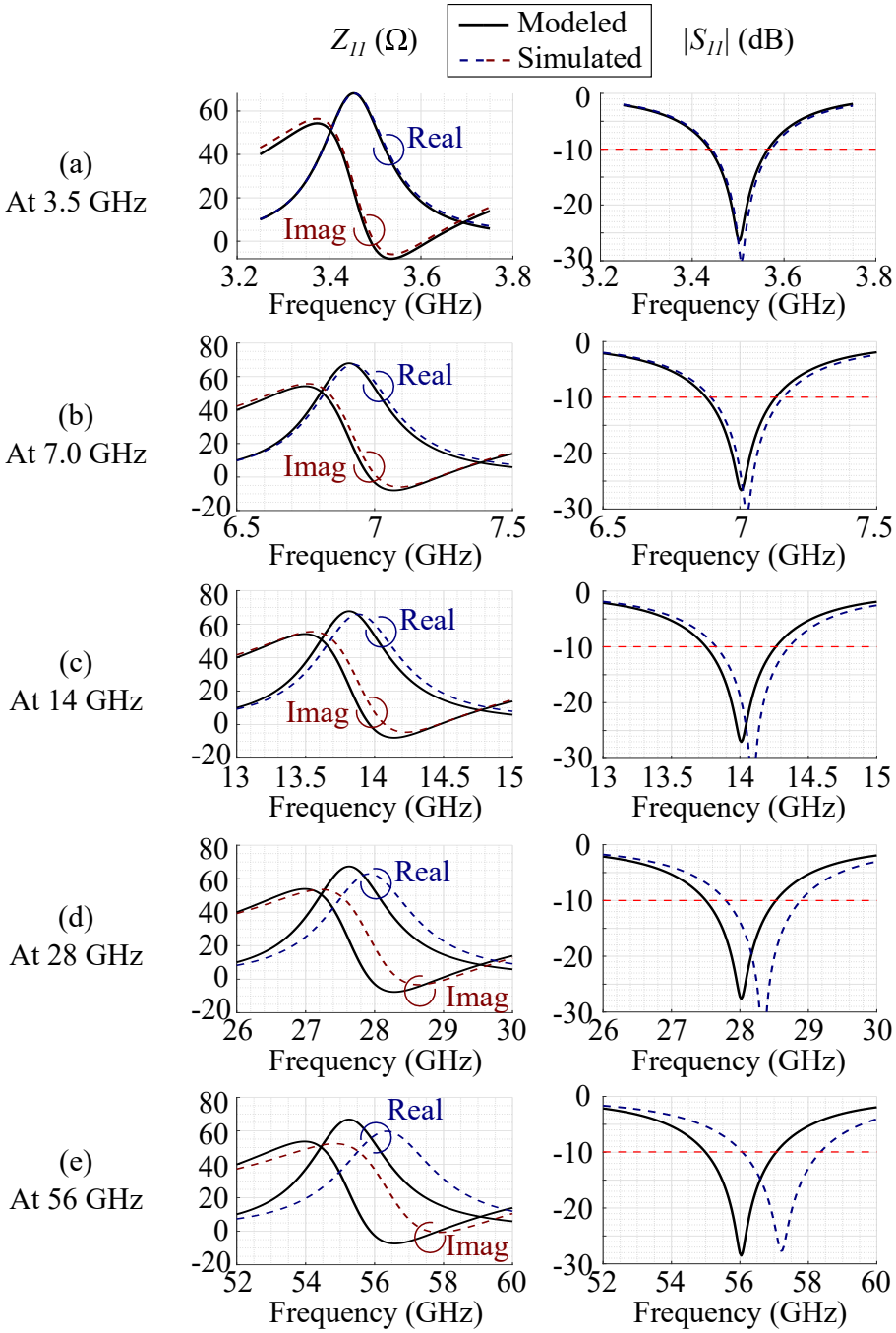

Figure 5.1: Performance of the most recent EM modeling method in thick-conductor PC-MSPAs up to the mmWave band.
Comparison between modeled and simulated impedance responses Z_{11} (left column), and S_{11} (right column). The designed PC-MSPAs have dimensions: $L = W = 0.448\lambda_0/\sqrt{\varepsilon_r}$, $\varepsilon_r = 2.20$, $t_p = t_f = 17.5$ μm, $h = 0.037\lambda_0$, $r_x = 0.32$. Antenna geometry as on Fig. 5.10. The latest PC-MSPA model (Section 3.4) performs great at frequencies below 10 GHz. This chapter extends its working range by defining a new concept: the effective dielectric thickness.

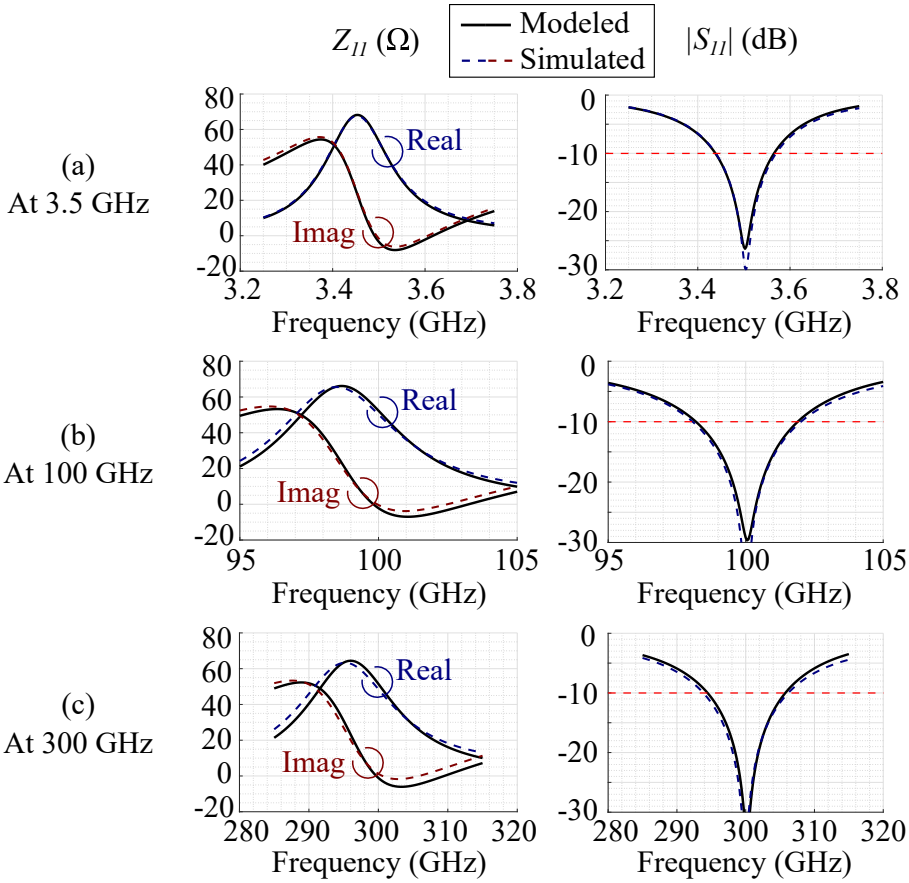

Figure 5.2: Performance of the most recent EM modeling method in zero-thickness-conductor PC-MSPAs up to the sub-THz band.
Comparison between modeled and simulated impedance responses Z_{11} (left column), and S_{11} (right column). The designed PC-MSPAs have dimensions: $L = W = 0.448\lambda_0/\sqrt{\varepsilon_r}$, $\varepsilon_r = 2.20$, $t_p = t_f = 0$ μm, $h = 0.037\lambda_0$, $r_x = 0.32$. Antenna geometry as on Fig. 5.10. If the conductor thickness is set to zero, the PC-MSPA model of Section 3.4 performs great even at 300 GHz.

quently, there is also an increasing discrepancy in estimating the operating frequency bands for PC-MSPAs in the mmWave band. These results show that the model works well up to 28 GHz when the traces are 17.5 μm thick. However, this model works with high accuracy up to 300 GHz if the traces' thicknesses are physically omitted, as shown in Fig. 5.3.

As observed in the results from Fig. 5.1 and Fig. 5.2, there are divergences in the results between the antenna simulations with 2D and 3D geometry. These

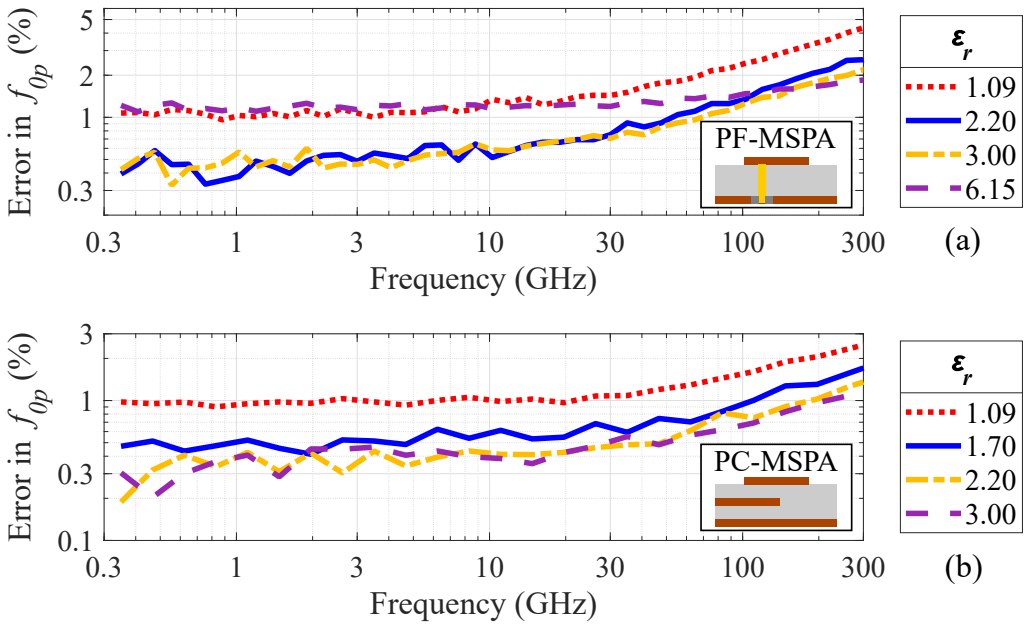

Figure 5.3: Effect of the conductor thickness in the modeling accuracy of the patch's resonant frequency in MSPAs up to the sub-THz band.
Estimation errors in PF-MSPAs (a), and in PC-MSPAs (b). The designed MSPAs have dimensions: $L = W \approx 0.45\lambda_0/\sqrt{\varepsilon_r}$, $t = t_p + t_f = 17.5$ μm, $h = 0.037\lambda_0$, $r_x = 0.32$. Antenna geometry as on Fig. 5.6 and Fig. 5.10. As the patch's and feed's thicknesses become electrically larger, the effect on the estimation accuracy of f_{0p} gets more significant. Therefore, the rest of resonator parameters (Q_p, R_p) and the estimation of the input response become less accurate over frequency.

differences are negligible at 3.5 GHz, but very notorious above 50 GHz. The comparison between the model and simulation in Fig. 5.2 shows that the assumption of zero-thickness conductors can still be valid even at 300 GHz if such a thickness is physically realizable. For the standard thickness in the conductors, the model accuracy gets very limited in the mmWave band, as illustrated in Fig. 5.1. Since actual thickness exists in real fabricated antennas and 2D sheets with thickness applied and the copper conductivity boundary is too idealistic, the model needs to work in antennas with actual 3D copper geometries and the corresponding thickness. In consequence, the first assumption of the model about the infinitesimal conductor thickness is no longer applicable, and it is then required to consider the actual conductor thickness. The other two assumptions about the 50 Ω feeding

line impedance and the impedance reference location remain valid up to the sub-THz band.

The work developed in this chapter aims to overcome this issue by extending the model up to 300 GHz. From these presented results, it is observed that the current EM MSPA models have accuracy limitations in estimating the impedance response in the mmWave band and that the errors increase with frequency. It is also noticed that the assumption of infinitesimal conductor thickness mainly causes these errors. As this assumption is no longer valid at these frequencies, further analysis is needed to determine the impact of the geometrical parameters on the patch's resonator parameters. The upcoming section provided a thorough analysis of the impact of modeling the MSPAs resonator parameters by geometrical scaling and its relation with the conductor trace thickness and model accuracy.

5.1.2 Geometry Analysis

The most updated EM model for MSPAs includes diverse material geometrical and electrical properties to accurately model behavioral response over frequency, such as the input impedance and return loss. As explored in Chapter 4, MSPAs comprise metallic and dielectric materials. Among the material properties in the metallic parts are the bulk conductivity and relative magnetic permeability of the patch, feed, and ground plane. In the dielectric, the relative electric permittivity, loss tangent, and thickness provide the necessary characterization to model MSPAs in the current models accurately.

The current models provide an accurate response in the radio frequency and microwave bands, specifically up to 30 GHz, with errors that remain constant over frequency. Nevertheless, these errors increase with frequency, being over 2 % in the sub-THz band. The main reason for these errors is the insufficient inclusion

of advanced characteristics of the metallic portions in MSPAs. As demonstrated in Chapter 4, the conductor's surface roughness can be modeled by an equivalent material replicating the roughness's effects. Also, the conductor's thickness contributes to modifying the characteristic impedance of microstrip transmission lines, which ultimately modifies the conditions and accuracy for EM modeling of MSPAs.

Overcoming these limitations requires analyzing and developing new methods to include the conductor thickness to account for the different impedance conditions that impact modeling performance. The study performed in this section provides diverse analysis using the mainstream conductor thickness from manufacturers, which are typical for the mmWave band, namely 8.75 μm (0.25 oz/ft^2), 17.5 μm (0.5 oz/ft^2), 35 μm (1 oz/ft^2). As the electrical thickness of conductors increases over frequency, the effects on the frequency response also get more noticeable. Then, the conductor thickness is kept constant over frequency in the analysis made in this section.

Frequency scaling has traditionally allowed antenna design at any frequency from a known geometry and known operation frequency, including for MSPAs. In both cases, the original design and the scaled design preserve the electrical thickness, keeping the exact shape of the frequency response, just multiplied by the scaling factor. Nonetheless, at mmWave and sub-THz bands, the conductor thickness and roughness may constitute a modifier in the response. The skin depth and the relative rough profile may impact the conductors' adequate electrical thickness of the most diminutive dimensions.

The patch's resonator RLC parameters are the most significant modeling source for impedance estimation. As explored in Chapter 2 (Section 2.4), the resonant frequency can be extracted from the Z_{11} response as the frequency where the maximum value of the Z_{11}'s real part occurs. The quality factor is extracted from

the frequencies where Z_{11}'s real part is half of Z_{11}'s real part at resonance, i.e., half of the maximum value. In addition, the resonant resistance is this maximum value of Z_{11}'s real part.

Then, this section analyzes the effects of the design scaling strategy in the MSPA RLC parameters, specifically in the resonant frequency and quality factor. As demonstrated later, the resonant resistance is proportional to the dielectric thickness, not the conductor thickness. The scaling is performed by comparing both RLC parameters in 'direct' and 'scaled' PF-MSPA designs. The base design operates at 3.5 GHz and has patch's size $L = W = 26.25$ mm, dielectric constant $\varepsilon_r = 2.2$, dielectric thickness $h = 3.15$ mm, and patch's thickness $t = 17.5$ μm. These dimensions represent an electrical thickness of $L = W = 0.448\lambda_0/\sqrt{\varepsilon_r}$, and $h = 0.0368\lambda_0$. The loss parameters σ_{bulk} and $\tan\delta$ are analyzed and vary from 58 MS/m to infinity (PEC) and from 0 to 0.0009, respectively. The patch's thickness t is set constant over frequency.

The 'direct' design considers λ_0 at the analysis frequency, including the scaling factor in the dimensions. For example, an MSPA designed at 280 GHz is 80 times smaller than the equivalent at 3.5 GHz and is designed with such small dimensions while keeping the patch's thickness to 8.75 μm, 17.5 μm, or 35 μm. In this example, the scaling factor is 80. For these designs, the simulations are carried at 3.5 GHz times the scaling factor, which is 280 GHz in this case. The frequency sweep analysis is made from 3.25 GHz to 3.75 GHz times the scaling factor, which is in this case from 260 GHz to 300 GHz.

The 'scaled' designs consider the base PF-MSPA design with an operating frequency of 3.5 GHz, but with a patch's thickness multiplied by the scaling factor necessary to emulate the scaled frequency. For example, for the 280 GHz case with a scaling factor of 80, the 'scaled' design has dimensions $L = W =$

26.25 mm, dielectric constant $\varepsilon_r = 2.2$, dielectric thickness $h = 3.15$ mm, and patch's thickness $t = 1.4$ mm. This value of t is 80 times the nominal thickness of 17.5 μm. This design is 80 times bigger than the 'direct' design at 280 GHz with a patch 17.5 μm thick. The frequency sweep analysis is then performed from 3.25 GHz to 3.75 GHz.

In both cases, the sweep analysis cover 5001 points and a maximum error in the S-parameters $\Delta S = 0.0005$ for advanced accuracy, especially in obtaining the conductor and dielectric quality factor. The upcoming lines discuss the consequences of MSPA scaling in estimating the patch's RLC parameters and its relation with EM modeling by comparing the results of both the 'direct' and 'scaled' designs. This analysis demonstrates that the indirect scaling of MSPAs may be used to formulate the model extensions up to 300 GHz, keeping accuracy at such frequencies while optimizing the use of computational resources in the modeling generation.

5.1.2.1 Effect of MSPA Scaling in the Patch's Resonant Frequency

This section scrutinizes the effect of considering a scaled design of an MSPA instead of the real-size version with the small dimensions associated with a patch's high resonant frequency (f_{0p}). Table 5.1 lists the scaling errors in PF-MSPAs in the mmWave and sub-THz bands. Fig. 5.4 illustrates the patch's resonant frequency trends over scaling factor and frequency bands between 35 GHz and 280 GHz.

The values of f_{0p} in Table 5.1 consider different geometrical and electrical variations for a complete study. The patch's thickness varies from 8.75 μm to 35 μm. Three variations inside each case were performed, with lossy materials ($\sigma_{bulk} = 58$ MS/m, $\tan\delta = 0.0009$), lossless dielectric and copper patch ($\sigma_{bulk} = 58$ MS/m, $\tan\delta = 0$), and lossless materials ($\sigma_{bulk} \to \infty$, $\tan\delta = 0$). The obtained

Table 5.1: Accuracy of patch's resonant frequency in scaled MSPAs.
The 'direct' PF-MSPAs have dimensions as a function of the free-space wavelength λ_0 as: $L = W = 0.448\lambda_0/\sqrt{\varepsilon_r}$, $\varepsilon_r = 2.20$, $t = 17.5$ μm, $h = 0.037\lambda_0$, $r_x = 0.32$. The 'scaled' PF-MSPAs considers λ_0 at 3.5 GHz and $t = 17.5$ μm times the scaling factor. Antenna geometry as on Fig. 5.6.

Scaling factor	Operating f_o (GHz)	t (μm)	Direct f_{0p} (GHz)	Scaled f_{0p} (GHz)	Converted f_{0p} (GHz)	Scaling error (%)
×10	35	8.75	34.26	3.4273	34.27	0.03
		17.5	34.20	3.4207	34.21	0.03
		35.0	34.09	3.4080	34.08	0.02
×14	49	8.75	47.93	3.4233	47.93	0.00
		17.5	47.81	3.4160	47.82	0.03
		35.0	47.60	3.4007	47.61	0.01
×20	70	8.75	68.38	3.4212	68.42	0.07
		17.5	68.15	3.4094	68.19	0.06
		35.0	67.79	3.3906	67.81	0.04
×28	98	8.75	95.59	3.4155	95.63	0.05
		17.5	95.19	3.4003	95.21	0.02
		35.0	94.55	3.3784	94.59	0.05
×40	140	8.75	136.3	3.4085	136.3	0.03
		17.5	135.6	3.3903	135.6	0.05
		35.0	134.4	3.3616	134.5	0.04
×56	196	8.75	190.3	3.4012	190.5	0.10
		17.5	189.0	3.3784	189.2	0.08
		35.0	187.1	3.3434	187.2	0.07
×80	280	8.75	271.0	3.3902	271.2	0.07
		17.5	268.8	3.3619	269.0	0.08
		35.0	265.3	3.3193	265.6	0.11

values of f_{0p} presented of less than 0.1 % for all cases. From a physical perspective, the invariability of f_{0p} among material loss parameters are correlated to the patch's cavity model in the fundamental expression of the resonant frequency of (2.79), which does not contain the patch's electrical conductivity nor the dielectric's loss tangent. Therefore, the values presented in Table 5.1 are the average values of these specific numbers.

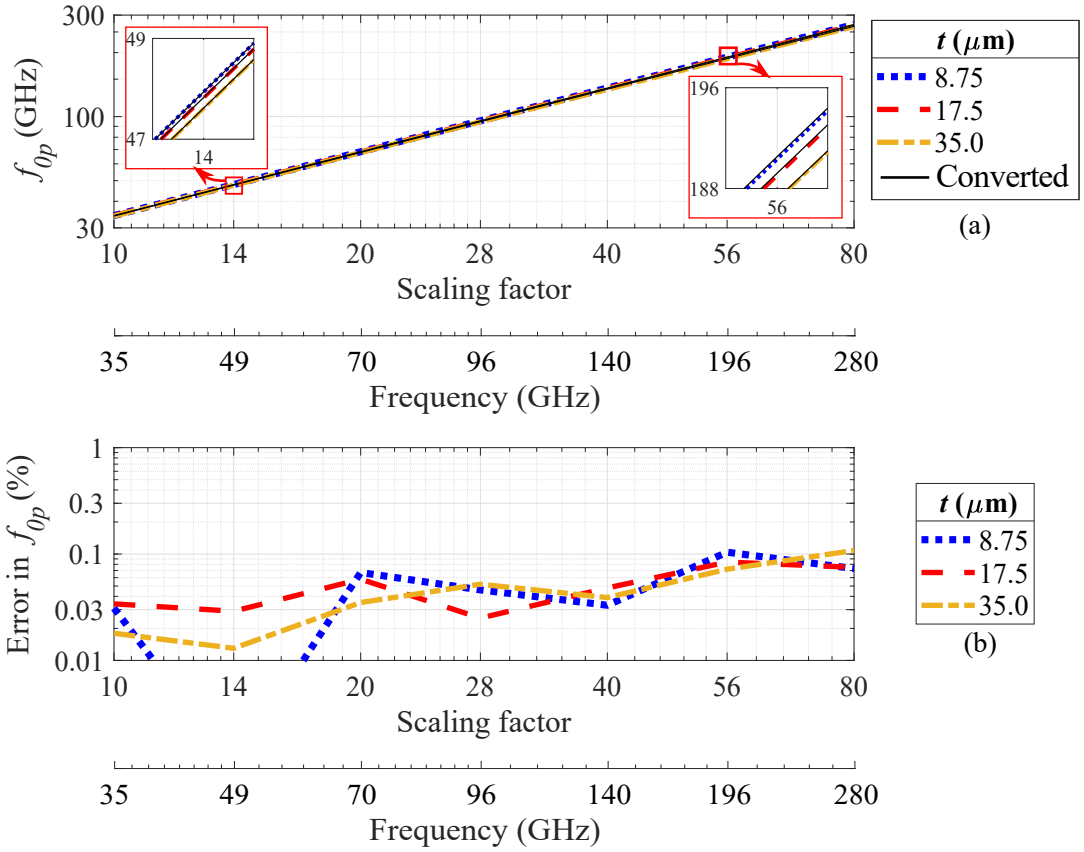

Figure 5.4: Patch's resonant frequency in scaled and thick MSPAs.
(a) Values of f_{0p} in simulated PF-MSPAs with and without geometry scaling. (b) Errors in f_{0p} in simulated PF-MSPAs due to the geometry scaling. The 'direct' PF-MSPAs have dimensions as a function of the free-space wavelength λ_0 as: $L = W = 0.448\lambda_0/\sqrt{\varepsilon_r}$, $\varepsilon_r = 2.20$, $t = 17.5$ μm, $h = 0.037\lambda_0$, $r_x = 0.32$. The 'scaled' PF-MSPAs considers λ_0 at 3.5 GHz and $t = 17.5$ μm times the scaling factor. Antenna geometry as on Fig. 5.6. Geometry scaling does not constitute error source even in the sub-THz band.

The first columns that conform to this table include the scaling factor, the operating frequency, and the patch's thickness t. The following columns list the values of f_{0p} for the 'direct' designs at the respective operating frequency, the values of f_{0p} for the 'scaled' designs at 3.5 GHz, the 'converted' values of f_{0p} by multiplying the 'scaled' values by the scaling factor, and the scaling percent errors between the 'direct' values and the 'converted' values.

The patch's resonant frequency f_{0p} follows definite patterns over the operating frequency band, patch's thickness, and design strategy. The values of f_{0p} tend to decrease as the patch's thickness increases. This effect is more notorious in the high sub-THz band than in the low mmWave band, as seen in the last and first rows of Table 5.1, respectively. This trend is also perceived in the 'scaled' values of f_{0p} with multiples of 17.5 μm in the patch's thickness. The 'converted' values of f_{0p} reflect the same patterns as in the 'direct' values. These trends are rigorously followed, with errors less than 0.11 % up to 280 GHz and 35 μm-thick patches.

The trends of f_{0p} in Fig. 5.4 illustrate an accurate estimation equivalency of the patch's resonant frequency from 'scaled' data. Fig. 5.4a overlaps the values of f_{0p} for different patch thicknesses and design strategies. Despite looking similar in the macroscopic view, the zoom-in around 49 GHz and 196 GHz show differences in the values of f_{0p} across the patch's thickness. These differences look more noticeable at 196 GHz, as in the zoom-in boxes around these two frequencies. Moreover, the error comparison in Fig. 5.4b indicates minimum errors due to the design strategy, which are also uncorrelated to the patch's thickness.

In all these cases, the scaling strategy does not affect the value of f_{0p}. Consequently, it is possible to accurately model f_{0p} with scaled antenna designs and then convert for the equivalent values. The main advantage of performing 'scaled' designs over 'direct' designs is the versatile availability of modeling data over frequency. For example, Table 5.1 covers seven frequency points. However, as seen later in Section 5.2 and Section 5.3, modeling the conductor trace thickness requires the values of the RLC parameters over numerous frequency points in the order of several tens of samples. Simulating each frequency point in a different project reduces the computation efficiency as it requires significantly more time and memory resources to perform the required simulations. With this observa-

tion, it is observed that the values of f_{0p} can be obtained for several operating frequency points on the same file, dramatically reducing resource consumption without affecting modeling accuracy. Nonetheless, this conclusion may not be correct for estimating the quality factor and resonant resistance. Therefore, a similar analysis is performed and discussed in the next sections.

5.1.2.2 Effect of MSPA Scaling in the Patch's Quality Factor

The effects of the MSPA design strategy are inspected in the mmWave and sub-THz bands. Similarly to the initial analysis of the patch's resonant frequency f_{0p}, the design scaling strategy plays a role in the accuracy of the values of the patch's quality factor Q_p. For this section, the variable Q_p will also be called *total quality factor*, making a difference from the material-based quality factors, namely dielectric quality factor Q_d and the conductor quality factor Q_c. The additive combination between the radiation quality factor Q_{rad} and the surface-wave quality factor Q_{sw} will be called *effective radiation quality factor* Q_{rs}. Since the total quality factor depends on the loss characteristics of the antenna material, the performed analysis includes 'lossy' and 'lossless' PF-MSPA designs. The 'lossy' PF-MSPAs consider copper traces and PTFE loss tangent (σ_{bulk} = 58 MS/m, $\tan\delta = 0.0009$). Conversely, the 'lossless' PF-MSPAs have parameters $\sigma_{bulk} \to \infty$ (PEC) and $\tan\delta = 0$. Table 5.2 lists the total quality factor for lossy and lossless PF-MSPAs, for both the 'direct' and 'scaled' antenna designs. Fig. 5.5 illustrates the trends and errors for Q_p due to the antenna scaling design strategy for both lossy and lossless MSPAs. The values of Q_p in Table 5.2 indicate scaling errors that grow with frequency for lossy PF-MSPAs. At 35 GHz, the scaling errors are 1.4 %, while at 280 GHz, they increases up to about 4.5 %. However, there are no significant scaling errors in Q_p for lossless MSPAs. Both trends happen for all

the analyzed patch thicknesses, between 8.75 μm and 35 μm.

Table 5.2: Accuracy of patch's quality factor in scaled MSPAs.
The 'direct' PF-MSPAs have dimensions as a function of the wavelength at free space λ_0 as: $L = W = 0.448\lambda_0/\sqrt{\varepsilon_r}$, $\varepsilon_r = 2.20$, $t = 17.5$ μm, $h = 0.037\lambda_0$, $r_x = 0.32$. The 'scaled' ones consider λ_0 at 3.5 GHz and $t = 17.5$ μm times the scaling factor. The 'lossy' antennas have copper traces ($\sigma_{bulk} = 58$ MS/m) and substrate loss-tangent $\tan\delta = 0.0009$, while the 'lossless' ones have PEC traces and $\tan\delta = 0$. Antenna geometry as on Fig. 5.6.

Scaling factor	Operating f_o (GHz)	t (μm)	Direct Q_p		Scaled Q_p		Scaling error (%)	
			Lossy	Lossless	Lossy	Lossless	Lossy	Lossless
×10	35	8.75	17.27	17.87	17.51	17.88	1.44	0.03
		17.5	17.22	17.80	17.44	17.78	1.25	0.07
		35.0	17.06	17.61	17.33	17.64	1.60	0.13
×14	49	8.75	17.21	17.84	17.48	17.89	1.59	0.28
		17.5	17.06	17.72	17.38	17.72	1.90	0.01
		35.0	16.86	17.49	17.18	17.50	1.86	0.04
×20	70	8.75	17.09	17.79	17.43	17.79	2.00	0.02
		17.5	16.91	17.64	17.27	17.62	2.13	0.13
		35.0	16.61	17.32	17.00	17.29	2.35	0.18
×28	98	8.75	16.91	17.72	17.36	17.77	2.64	0.24
		17.5	16.70	17.50	17.14	17.51	2.65	0.02
		35.0	16.31	17.07	16.71	17.05	2.43	0.13
×40	140	8.75	16.72	17.66	17.31	17.62	3.49	0.21
		17.5	16.44	17.33	16.96	17.31	3.20	0.13
		35.0	15.90	16.72	16.39	16.68	3.12	0.20
×56	196	8.75	16.50	17.53	17.15	17.51	3.90	0.11
		17.5	16.10	17.06	16.72	17.05	3.83	0.04
		35.0	15.32	16.20	15.89	16.17	3.70	0.16
×80	280	8.75	16.17	17.32	16.96	17.30	4.90	0.10
		17.5	15.66	16.67	16.36	16.68	4.43	0.07
		35.0	14.58	15.49	15.18	15.44	4.13	0.29

Fig. 5.5a shows an excellent agreement between 'direct' and 'scaled' values of Q_p for lossless MSPAs. The estimation errors due to the scaling design strategy are less than 0.3 %, as seen in Fig. 5.5c. Meanwhile, the values of Q_p in lossy MSPAs get divergent as the frequency increases. These trends are illustrated in Fig. 5.5b for different patch thicknesses. The scaling errors are from 1.25 % and show a consistent increase over frequency.

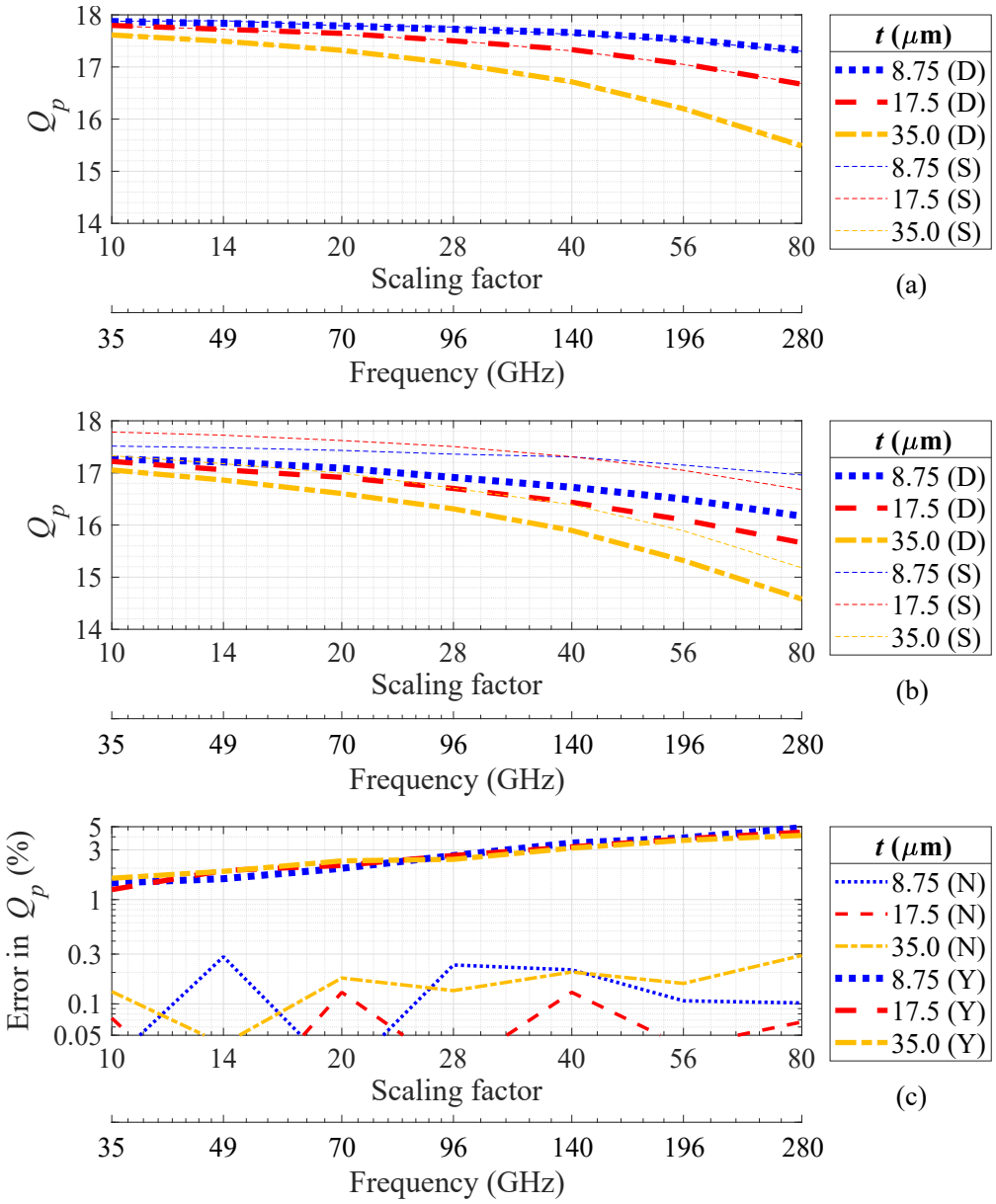

Figure 5.5: Patch's quality factor in scaled and thick MSPAs.
(a) Values of Q_p in lossless PF-MSPAs with and without geometry scaling. (b) Values of Q_p in lossy PF-MSPAs with and without geometry scaling. (c) Errors in Q_p in PF-MSPAs due to the geometry scaling. The 'direct' (D) PF-MSPAs have dimensions as a function of the free-space wavelength λ_0 as: $L = W = 0.448\lambda_0/\sqrt{\varepsilon_r}$, $\varepsilon_r = 2.20$, $t = 17.5$ μm, $r_x = 0.32$, $h = 0.037\lambda_0$. The 'scaled' (S) ones consider λ_0 at 3.5 GHz and $t = 17.5$ μm times the scaling factor. The 'lossy' (Y) MSPAs have substrate loss-tangent $\tan\delta = 0.0009$ and copper traces ($\sigma_{bulk} = 58$ MS/m), while the 'lossless' (N) ones have PEC traces and $\tan\delta = 0$. Antenna geometry as on Fig. 5.6. These plots suggest great scaling properties for the patch quality factor in lossless PF-MSPAs.

The estimation discrepancies discussed in these first observations suggest better strategies than scaling MSPAs to accurately model the patch's total quality factor with lossy materials. However, since the scaling strategy becomes appropriate for lossless MSPAs, a method can be developed to use the scaling design strategy and still get an accurate estimation of Q_p. The following lines provide further analysis of the components that comprise the total quality factor, coming from the dielectric, conductor, and effective radiation.

The values of Q_d, Q_c, and Q_{rsw} for an MSPA can be obtained from the extracted Q_p values coming from the impedance response of that MSPA with three different settings, described as follows:

1. Lossless MSPA:

   Considering a dielectric with loss tangent $\tan\delta = 0$, and patch's electrical conductivity $\sigma_{bulk} \to \infty$ (PEC), then:

$$\begin{aligned} Q_{p1}^{-1} &= Q_{d1}^{-1} + Q_{c1}^{-1} + Q_{rsw1}^{-1} \\ Q_{p1}^{-1} &= Q_{rsw}^{-1}, \end{aligned} \tag{5.1}$$

   which means that the total quality factor in lossless MSPAs only comprises the effective radiation quality factor.

2. Lossless-dielectric MSPA:

   Considering a dielectric with loss tangent $\tan\delta \neq 0$, and patch's electrical conductivity $\sigma_{bulk} \to \infty$ (PEC), then:

$$\begin{aligned} Q_{p2}^{-1} &= Q_{d2}^{-1} + Q_{c2}^{-1} + Q_{rsw2}^{-1} \\ Q_{p2}^{-1} &= Q_{d}^{-1} + Q_{rsw}^{-1}, \end{aligned} \tag{5.2}$$

   which means that the total quality factor in lossless-dielectric MSPAs comprises the effective radiation and dielectric quality factors.

3. Lossy MSPA:

   Considering a dielectric with loss tangent $\tan\delta \neq 0$, and patch's electrical conductivity $\sigma_{bulk} < \infty$ (non PEC), then:

$$Q_{p3}^{-1} = Q_{d3}^{-1} + Q_{c3}^{-1} + Q_{rsw3}^{-1}$$
$$Q_{p3}^{-1} = Q_{d}^{-1} + Q_{c}^{-1} + Q_{rsw}^{-1}, \tag{5.3}$$

   which means that the total quality factor in lossy MSPAs comprises all three components: the effective radiation quality factor, the dielectric quality factor, and the conductor quality factor.

Since the three variations keep the same geometry, dimensions, and electrical properties, then the values of Q_d, Q_c, and Q_{rsw} in (5.1)–(5.2) remain the same. The extraction of Q_{p1}, Q_{p2}, and Q_{p3} is performed by applying its definition in electric circuits, coming from the real part of the input impedance response. Then, the values of Q_d, Q_c, and Q_{rsw} can be extracted as follows:

$$Q_d^{-1} = Q_{p2}^{-1} - Q_{p1}^{-1}, \qquad \text{by subtracting (5.2) − (5.1)} \tag{5.4a}$$
$$Q_c^{-1} = Q_{p3}^{-1} - Q_{p2}^{-1}, \qquad \text{by subtracting (5.3) − (5.2)} \tag{5.4b}$$
$$Q_{rsw}^{-1} = Q_{p1}^{-1}, \qquad \text{directly from (5.1)} \tag{5.4c}$$

These extracted values of Q_d, Q_c and Q_{rsw} are listed in Table 5.3, Table 5.4, and Table 5.5, respectively. Table 5.3 presents a survey of the values of the dielectric quality factor, while Table 5.4 lists the values of the conductor quality factor. These values are calculated from the values of Q_p at lossy and lossless material variations. Table 5.5 lists the values of Q_{rs}, which primarily impacts the values of Q_p. For all the cases, the frequency coverage ranges from the low mmWave band to the high sub-THz band.

- **Dielectric quality factor Q_d**

  The values of Q_d from Table 5.3 are above 1000, which is expected for a low loss-tangent dielectric as Rogers™ 5880 ($\tan\delta = 0.0009$). The theoretical value of Q_p is the inverse of $\tan\delta$, which is 1111. The values of Q_d are unrelated to the patch's thickness or the scaling design strategy. The harmonic average values are around 20 % above the nominal value of 1111. It is important to notice that the inverse of these values is in the order of less than a thousandth, and estimating them with high accuracy requires strict simulation tolerances. Even so, it can be concluded that the dielectric quality factor is independent of the patch's thickness, uncorrelated to the scaling design strategy, and so high that the impact on the total quality factor is minimum.

- **Conductor quality factor Q_c**

  The conductor quality factor Q_c follows a much more defined pattern than Q_d, as observed in Table 5.4. The values of Q_c from 'direct' and 'scaled' PF-MSPA designs are entirely different. On the 'direct' scaling approach, there is a decreasing trend of Q_c as the frequency increases. Conversely, Q_c looks constant to around 2500 in all the scaling factors, with values several times the ones from the 'direct' approach.

  This outcome is related to the definition of Q_c (2.102) in Chapter 2. The skin depth is inversely proportional to the square root of the frequency, while the thickness between conductors is inversely proportional to the frequency. This difference in proportionality induces errors when using the 'scaled' approach. Therefore, it is necessary to use the 'direct' scaling strategy to calculate the values of Q_c accurately. Since the values of Q_c look independent from the patch's thickness, the formulation at radio frequency can still be used in the mmWave and sub-THz bands. As demonstrated later in Section 5.2.2, the

Table 5.3: Accuracy of patch's dielectric quality factor in scaled MSPAs.
The 'direct' PF-MSPAs have dimensions as a function of the wavelength at free space λ_0 as: $L = W = 0.448\lambda_0/\sqrt{\varepsilon_r}$, $\varepsilon_r = 2.20$, $t = 17.5$ μm, $h = 0.037\lambda_0$, $r_x = 0.32$, $\tan\delta = 0.0009$. The 'scaled' ones consider λ_0 at 3.5 GHz and $t = 17.5$ μm times the scaling factor. Antenna geometry as on Fig. 5.6.

Scaling factor	Operating f_o (GHz)	t (μm)	Direct Q_d	Average value	Scaled Q_d	Average value	Scaling error (%)	Nominal error (%)
×10	35	8.75	1280	1353	1270	1372	1.44	21.7
		17.5	1417		1236			
		35.0	1368		1695			
×14	49	8.75	1522	1308	1171	1297	0.82	17.7
		17.5	1263		1355			
		35.0	1184		1389			
×20	70	8.75	1661	1410	1302	1376	2.41	26.9
		17.5	1346		1324			
		35.0	1278		1521			
×28	98	8.75	1390	1381	1216	1198	13.3	24.3
		17.5	1355		1181			
		35.0	1400		1196			
×40	140	8.75	1170	1283	1366	1367	6.51	15.5
		17.5	1328		1148			
		35.0	1370		1691			
×56	196	8.75	1370	1399	1691	1299	7.13	25.9
		17.5	1602		1258			
		35.0	1285		1269			
×80	280	8.75	1356	1416	1115	1232	13.0	27.4
		17.5	1496		1330			
		35.0	1402		1272			

value of Q_c is independent of the conductor thickness, and no effective dielectric thickness is necessary to model this parameter.

- **Effective radiation quality factor Q_{rs}**

  The combined quality factor from radiation and surface waves Q_{rs} also follow a clear pattern, as listed in Table 5.2. The values of Q_{rs} decrease over frequency and patch thickness. This trend is similar to the ones of f_{0p}, as in Table 5.1. Furthermore, the scaling errors are also minimum, at less than 0.3 %. This evidence is supported in the formulation of (5.3) and Fig. 5.5b, as the value of Q_{rs} extracted from lossless and lossy materials are related to the MSPA's

Table 5.4: Accuracy of patch's conductor quality factor in scaled MSPAs. The 'direct' PF-MSPAs have dimensions as a function of the wavelength at free space λ_0 as: $L = W = 0.448\lambda_0/\sqrt{\varepsilon_r}$, $\varepsilon_r = 2.20$, $t = 17.5$ μm, $h = 0.037\lambda_0$, $r_x = 0.32$, $\sigma_{bulk} = 58$ MS/m. The 'scaled' ones consider λ_0 at 3.5 GHz and $t = 17.5$ μm times the scaling factor. Antenna geometry as on Fig. 5.6.

Scaling factor	Operating f_o (GHz)	t (μm)	Direct Q_c	Average value	Scaled Q_c	Average value	Scaling error	Nominal error (%)
×10	35	8.75	843.4	860.6	2700	2722	3.16:1	2.35
		17.5	850.0		3151			
		35.0	889.9		2412			
×14	49	8.75	722.6	734.7	2287	2578	3.51:1	1.28
		17.5	713.4		2733			
		35.0	770.5		2775			
×20	70	8.75	591.5	588.8	2556	2680	4.55:1	4.97
		17.5	587.0		2581			
		35.0	587.8		2936			
×28	98	8.75	503.3	500.6	2023	2492	4.97:1	4.65
		17.5	500.0		2781			
		35.0	498.6		2857			
×40	140	8.75	432.7	425.1	3358	2784	6.54:1	3.05
		17.5	418.4		3236			
		35.0	424.6		2124			
×56	196	8.75	341.8	355.8	2386	2519	7.08:1	3.80
		17.5	309.6		2611			
		35.0	357.2		2571			
×80	280	8.75	297.3	304.1	3880	2920	9.60:1	1.47
		17.5	312.3		2232			
		35.0	303.1		3110			

electrical thickness. Hence, it is possible to accurately model Q_{sw} by using the 'scaled' design strategy for lossless MSPAs up to 300 GHz.

From the values of the quality factor in MSPAs, it is observed that the scaling strategy can be partially used to estimate this patch's resonator parameter. The value of Q_p needs to be modeled from its three components: Q_d, Q_c, and Q_{rs}. For Q_d, the inverse of the loss-tangent can be used to compute this value. Future work can help better understand the differences with the theoretical values, which may be caused by either the numerical simulation settings or additional effects related to the mmWave and sub-THz bands. For Q_c, it is necessary to use the

Table 5.5: Accuracy of patch's radiation quality factor in scaled MSPAs.
The 'direct' PF-MSPAs have dimensions as a function of the wavelength at free space λ_0 as: $L = W = 0.448\lambda_0/\sqrt{\varepsilon_r}$, $\varepsilon_r = 2.20$, $t = 17.5$ μm, $h = 0.037\lambda_0$, $r_x = 0.32$. The 'scaled' ones consider λ_0 at 3.5 GHz and $t = 17.5$ μm times the scaling factor. Antenna geometry as on Fig. 5.6.

Scaling factor	Operating f_o (GHz)	t (μm)	Direct Q_{rs}	Scaled Q_{rs}	Scaling error (%)
×10	35	8.75	17.87	17.88	0.03
		17.5	17.80	17.78	0.07
		35.0	17.61	17.64	0.13
×14	49	8.75	17.84	17.89	0.28
		17.5	17.72	17.72	0.01
		35.0	17.49	17.50	0.04
×20	70	8.75	17.79	17.79	0.02
		17.5	17.64	17.62	0.13
		35.0	17.32	17.29	0.18
×28	98	8.75	17.72	17.77	0.24
		17.5	17.50	17.51	0.02
		35.0	17.07	17.05	0.13
×40	140	8.75	17.66	17.62	0.21
		17.5	17.33	17.31	0.13
		35.0	16.72	16.68	0.20
×56	196	8.75	17.53	17.51	0.11
		17.5	17.06	17.05	0.04
		35.0	16.20	16.17	0.16
×80	280	8.75	17.32	17.30	0.10
		17.5	16.67	16.68	0.07
		35.0	15.49	15.44	0.29

corresponding designs at each frequency to model this value accurately. The model for Q_p is revised and updated in Section 5.2.2. Only Q_{rs} can be accurately modeled using the 'scaled' design approach in lossless MSPAs. Since Q_{rs} is the dominant component in Q_p, a model reformulation is proposed in Section 5.2.2 using the concept of effective dielectric thickness.

5.1.3 Modeling Strategy above 30 GHz

Extending the functionality of the MSPA EM models up to the sub-THz band requires considering advanced material characteristics, as discussed in Chapter 4.

It is then hypothesized that an appropriate accountability of the conductor thickness permits establishing a generalized model for the patch's resonator parameters over frequency, correcting the shifting and amplitude errors in the real and imaginary parts of MSPAs' input impedance response up to 300 GHz. The modeling strategy includes these advanced characteristics as effective material geometrical and electrical properties. The following specific strategies are proposed to extend the validity of current MSPA models up to 300 GHz:

1. Frequency-dependent effective dielectric constant:

   This formulation –provided in (4.17) in Chapter 4– covers a broader frequency range than the expression of (2.76) in Chapter 2. The frequency-dependent effective dielectric constant can also be used to accurately model the effect of the dielectric frequency dispersion on MSPAs. This concept is included in the formulations and comparisons made in this chapter.

2. Equivalent electric conductivity:

   The effect of the conductor surface roughness is included in the model by replacing the material's bulk conductivity with the equivalent conductivity formulation of (4.44). As demonstrated in Fig. 4.14, the effect of conductor roughness in MSPAs can be replicated by replacing every rough conductor with the equivalent smooth conductors for antenna design, including the patch, the feed, and the ground plane.

3. Effective substrate thickness:

   A part of the patch's and feed's thickness can be considered part of the effective substrate thickness to compute the RLC parameters for MSPAs. This strategy is formulated in detail in this chapter. For PC-MSPAs, the substrate thickness ratio formulation r_h is reformulated by including this concept for thick feeds.

4. Feeding parametric scaling:

   The effect of the copper thickness is considered in PC-MSPA design by a function-based width scaling over frequency, following the example provided in Table 4.3 in Chapter 4. This width is parameterized to keep a characteristic impedance of 50±2 Ω over frequency and thickness. Although the feeding width is not part of the model, an appropriate feeding setup is meaningful for accurate antenna modeling.

About 4000 antenna designs are designed and simulated between 0.3 GHz and 300 GHz with lossless materials, using the scaling approach for a base design at 3.5 GHz, and multiplying the conductor thickness by the corresponding scaling factor. Since this approach does not count the dielectric nor the conductor quality factor, the information from Table 5.3 and Table 5.4 is used, which come from non-scaled designs.

The next sections provide modeling formulations for MSPAs, aiming to extend the operating range up to 300 GHz. The formulations primarily focus on the conductor thickness, while the rest of the strategies are implicitly included. The assessments include variations in dielectric permittivity and thickness, as well as conductor thickness. Finally, a comparison of MSPA frequency response with a rough conductor is provided to assess model equivalency.

5.2 Modeling Extension for Probe-fed MSPAs

This section provides modeling updates extending the equivalent electric circuit model for PF-MSPAs up to 300 GHz. This model has been detailed in Section 2.4.4, covering the expressions (2.97)–(2.109) and the associated circuit of Fig. 2.12a. The equivalent circuit for a PF-MSPA is composed of a parallel RLC resonator (R_p, L_p, C_p) in series with an inductor (L_{TF}).

Extending the EM model for PF-MSPAs with thick patches comprises the following reformulations:

- The cavity-model base equation to calculate the patch's resonant frequency.
- The patch's effective radiation quality factor.
- The revision of the patch's resonant resistance and feed reactance.

The patch's thickness is included through a new concept of *effective substrate thickness*. This concept includes the dielectric thickness and a portion of the patch thickness, called from now as *effective patch thickness*. Then, this modeling method uses the effective substrate thickness in the mathematical formulations that provide the patch's RLC resonator parameters. The upcoming lines describe the modeling methodology, geometry, and formulations for the extended model for PF-MSPAs.

The formulation to extract the effective patch thickness is performed for PF-MSPAs with patch thickness up to 35 μm. Diverse PF-MSPA design sets are simulated, covering a permittivity range between 1.09 and 9.20 and substrate thickness from $0.025\lambda_0$ to $0.05\lambda_0$. Each set of PF-MSPA designs is evaluated at 46 frequency samples equally distributed in the logarithmic scale between 0.3 GHz and 300 GHz. The PF-MSPAs were designed at 3.5 GHz, and the patch's thickness ranged accordingly with the frequency sample points, following the 'scaled' design strategy discussed in Section 5.1.

The patch's resonant frequency and effective radiation quality factor were calculated for each data set. Then, a numerical sweep of values for the effective substrate thickness was evaluated, computing the estimation errors over the 46 frequency points. A value of the effective substrate thickness was found for each data set so that the modeling estimation errors remained approximately constant over frequency. Hence, the formulations that account for patch effective thickness

for this model have been empirically determined by applying the curve-fitting technique [69] to the values of the effective substrate thickness obtained through the antenna design variations along dielectric constant and patch thickness.

5.2.1 Patch Resonant Frequency

Let be a probe-fed MSPA, composed of a substrate with relative permittivity ε_r, and thickness h, with copper foils of thickness t above and under the substrate. The patch is on the top foil, with length L and width W. The ground plane is located on the bottom foil and has a length $2\lambda_0$, where λ_0 is the free-space wavelength at the operating frequency f_o. The geometry and dimensions of this antenna are shown in Fig. 5.6.

The patch's dominant-mode resonant frequency f_{0p} is calculated from the cavity model as in (2.100). This parameter depends on the patch's length L, the effective dielectric constant ε_{rep}, and the fringe-field equivalent extension length ΔL. Both quantities depend primarily on h and ε_r. Since the copper foil is thick enough not to assume negligible at mmWave frequencies, it needs to be included in the calculations for f_{0p}. This effect may arise from the electric fields between the patch, and the ground plane departing at different heights relative to the ground plane, as shown in Fig. 5.6a.

Consequently, the variables of ε_{rep} and ΔL get shifted, modifying the calculation in (2.100). Then, a portion k_t of the foil thickness t is added to the substrate thickness h to have a total thickness h_T, as in (5.6) and Fig. 5.6b. This effective thickness may be used in (2.100) to calculate f_{0p}. The value of k_t is expressed in (5.5), and it is shown in Fig. 5.6c for substrate dielectric constants ranging from 1 to 10.

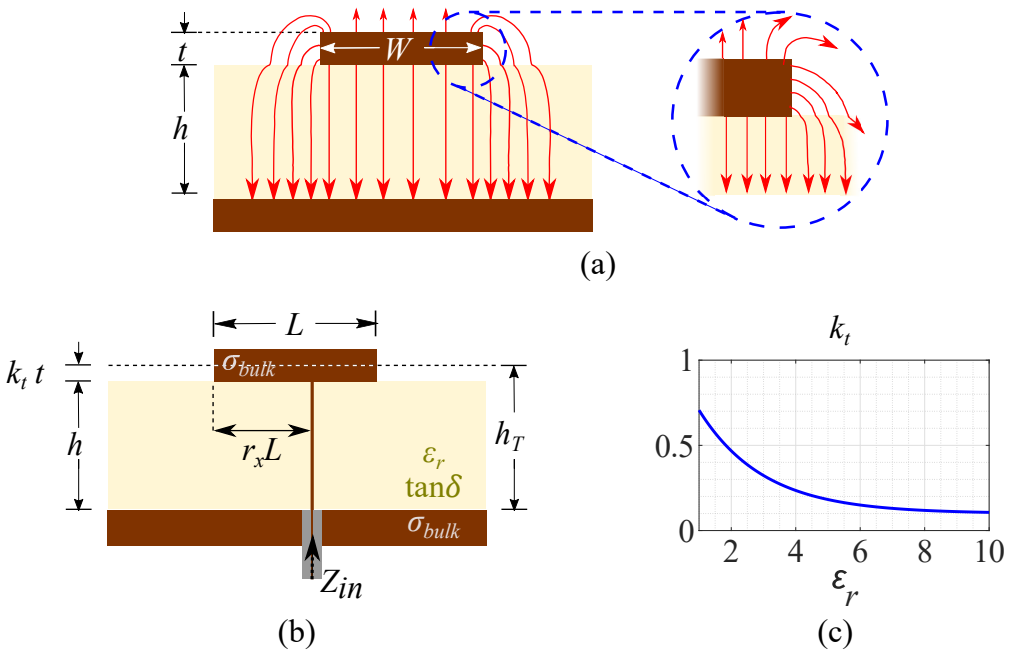

Figure 5.6: Geometrical formulation for modeling PF-MSPAs with thick conductors up to the sub-THz band.
(a) Cross-sectional view and field distribution, (b) longitudinal view and illustration of effective substrate thickness h_T, (c) variations of effective conductor-trace coefficient k_t over dielectric constant ε_r. This geometry considers the patch's thickness to accurately model PF-MSPAs up to the sub-THz band.

$$k_t = 0.1 + e^{-\varepsilon_r/2} \tag{5.5}$$

$$h_T = h + k_t\ t \tag{5.6}$$

This formulation updates the dielectric thickness h by replacing it with h_T for all the subsequent calculations that deliver the value of f_{0p}. As discussed in Section 5.1.3, this model utilizes the frequency-dependent effective dielectric constant (4.17) to calculate ε_{rep} and ΔL. An alternative value of k_t has been identified if the non-frequency-dependent formulation of ε_{re} (2.76) is used to calculate ε_{rep} and ΔL. It is defined as $k_t = 0.1225 + 1.035e^{-0.351\varepsilon_r}$, and is also valid for the range $\varepsilon_r \in [1.09; 9.20]$ $t \leq 35$ μm.

Therefore, the steps to accurately model the patch's resonant frequency in rectangular PF-MSPAs operating up to 300 GHz are as follows:

1. Identify the necessary information about the PF-MSPA's geometrical and electrical properties: L, W, ε_r, h, and t.
2. Compute the effective dielectric thickness h_T by following the formulation of (5.6). This value replaces the value of h in the subsequent steps.
3. Calculate the patch's associate microstrip frequency-dependent relative permittivity, expressed as in (5.7), where $\varepsilon_{rc} = \varepsilon_r$ for single substrate MSPA, and the values of ε_{e0}, f_a, and m are further detailed in (4.18a)–(4.18g) in Section 4.3.3.

$$\varepsilon_{re}(f) = \varepsilon_{rc} - \frac{\varepsilon_{rc} - \varepsilon_{e0}}{1 + (f/f_a)^m} \tag{5.7}$$

4. Evaluate the patch's relative dielectric constant ε_{rep} (2.97) as:

$$\varepsilon_{rep} = 0.5\varepsilon_r + 0.5\varepsilon_{re} \tag{5.8}$$

5. Compute the fringe-field equivalent length extension ΔL as in (5.9), where the values of ζ_1 through ζ_5 can be determined in (2.99a)–(2.99e).

$$\Delta L = h_T \ \zeta_1\zeta_3\zeta_5/\zeta_4 \tag{5.9}$$

6. Finally, evaluate f_{0p} as in (5.10), considering the values of ε_{rep} and ΔL (in meters) calculated in the previous steps.

$$f_{0p} = \frac{0.3}{2(L + 2\Delta L)\sqrt{\varepsilon_{rep}}} \text{ GHz} \tag{5.10}$$

This formulation is tested by comparing the estimated values of f_{0p} with the extracted values of f_{0p} from simulated MSPAs. The estimation of f_{0p} comes from using (5.10) and the effective substrate thickness of (5.6). The extraction of the f_{0p} values derives from the real part of the impedance responses from simulated PF-MSPAs at 46 frequency samples between 0.3 GHz and 300 GHz.

The designed MSPAs have dimensions $L = W = 0.448\lambda_0/\sqrt{\varepsilon_r}$, $h = 0.0368\lambda_0$, $t = 17.5$ μm, $\varepsilon_r = 2.2$, being designed for operating frequencies along the analysis range. Fig. 5.7 illustrates the method performance, including variations in ε_r, t, and h to include several geometrical and electrical conditions. The errors are reported using the logarithmic scale to provide an enhanced view.

The proposed modeling method with the concept of effective substrate thickness works excellently over the entire frequency analysis range, including the mmWave and sub-THz bands. The plots of Fig. 5.7 show the high accuracy of the proposed method to calculate f_{0p} up to 300 GHz. As seen in Fig. 5.7a the inclusion of k_t consistently improves the accuracy of f_{0p} above 10 GHz, reducing the errors from 3 % to 0.3 % at 300 GHz. Moreover, the line slope in the error curve from the previous model changes to a horizontal trend, indicating model stability in this range.

This modeling method works with diverse design conditions, such as substrate dielectric constant, substrate thickness, and patch thickness. The proposed method allows estimating f_{0p} with errors less than 1 % in the permittivity range between 1.7 and 6.15, according to Fig. 5.7b. As shown in Fig. 5.7c, the method works with an accuracy almost independently from the foil thickness when it is up to 35 μm thick. Finally, Fig. 5.7d reveals that the method works very well in substrates with thickness up to $0.05\lambda_0$, with errors less than 1 % in all the cases and up to 300 GHz.

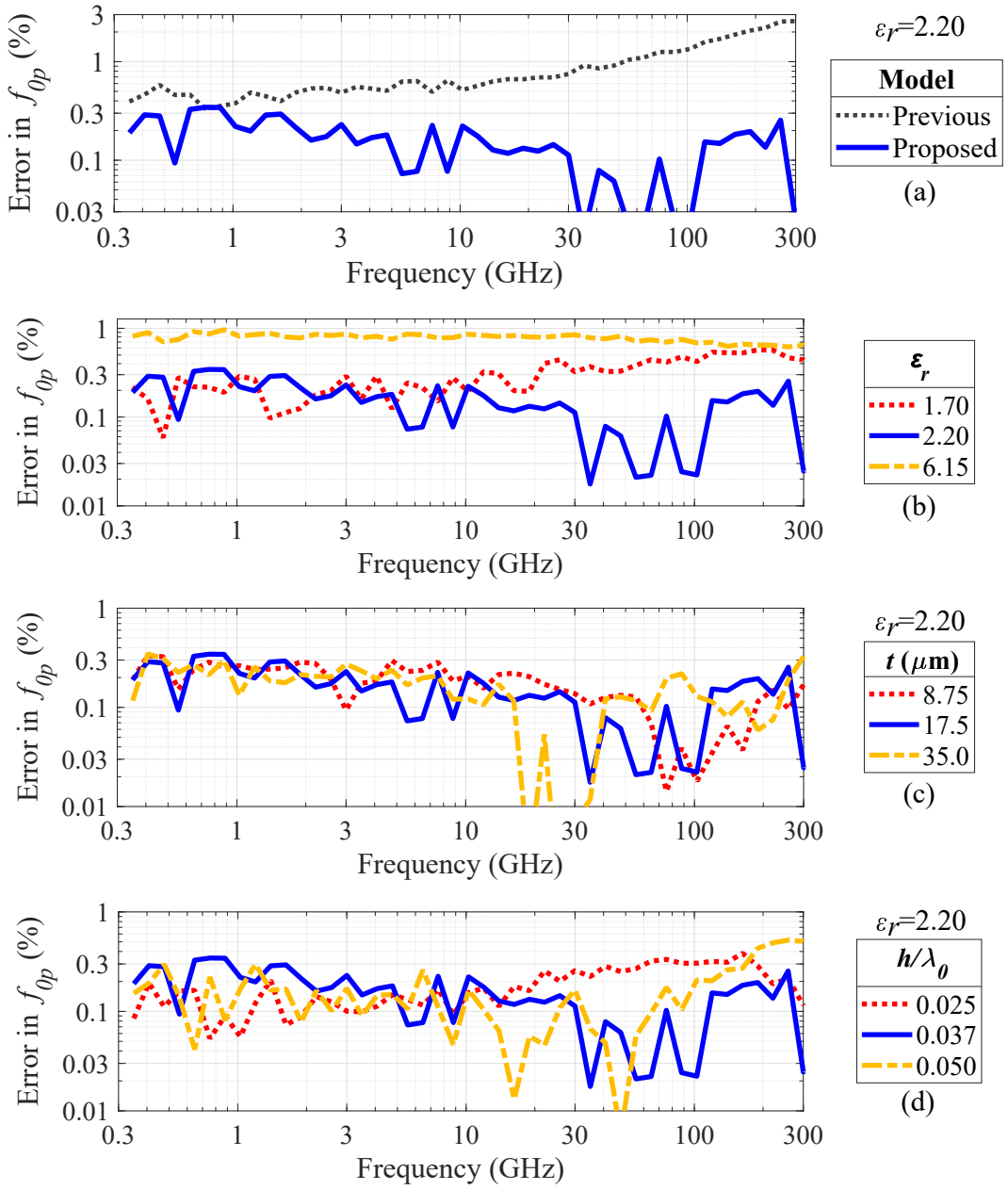

Figure 5.7: Estimation accuracy of patch's resonant frequency in PF-MSPAs up to the sub-THz and with thick conductors.
Errors between simulation and modeling in PF-MSPAs between 300 MHz and 300 GHz. Comparisons made by modeling method (a), by substrate's relative permittivity (b), by patch's and feed's thickness (c), and by feeding and patch substrate's thickness (d). The proposed modeling method produces a highly accurate estimation of the patch's quality factor f_{0p} in PF-MSPAs up to 300 GHz, under several geometrical and electrical conditions.

This new concept presents a promising impact on modeling MSPAs, which is further explored in the upcoming sections. The fact of accurately replicating the values of f_{0p} with a single equation makes this strategy especially useful to model this antenna. The versatility of this modeling method is noticed as it can be extended to estimate the patch quality factor and characterize the patch RLC parameters for PC-MSPAs. Furthermore, an accurate model of f_{0p} brings enhanced accuracy of Q_p and R_p, since these parameters are very dependent on the wavelength calculated at f_{0p}, as seen in (2.102) and (2.104b). The upcoming lines formulate the values of Q_p for PF-MSPAs up to 300 GHz.

5.2.2 Patch Quality Factor

Let us consider a PF-MSPA with the geometry and dimensions defined in Section 5.2.1 and Fig. 5.6. The loss-related material characteristics are now included in the formulation for the patch's quality factor Q_p. The loss tangent $\tan\delta$ characterizes the dielectric losses in the antenna substrate, while the bulk electrical conductivity σ_{bulk} describes the losses in the patch. The proposed formulation for modeling Q_p is divided by its components: conductor (Q_c), dielectric (Q_d), and the combination of radiation and surface waves (Q_{rs}).

Each component presents a unique formulation strategy, and they are described as follows:

5.2.2.1 Conductor Quality Factor Q_c

The value of Q_c depends on the distance between conductors h, resonant frequency f_{0p}, and electric conductivity σ_{bulk}, as expressed in (2.102). The value of Q_c is proportional to $hf_{0p}^{0.5}$ for a given conductor. Since the MSPA dimensions are proportional to the inverse of frequency (f_{0p}^{-1}), this decrease occurs at a higher

exponent than $f_{0p}^{0.5}$. The total effect is a decreasing value of Q_c over frequency for MSPAs with the same electrical thickness. This effect is observed in Fig. 5.8.

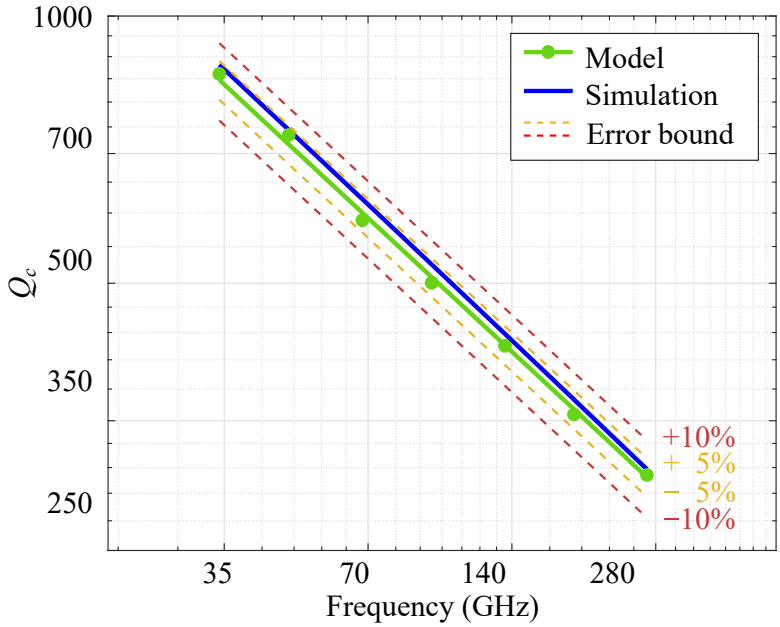

Figure 5.8: Patch's conductor quality factor in thick MSPAs.
The designed PF-MSPAs have dimensions as a function of the free-space wavelength λ_0 as: $L = W = 0.448\lambda_0/\sqrt{\varepsilon_r}$, $\varepsilon_r = 2.20$, $t = 17.5$ μm, $r_x = 0.32$, $h = 0.037\lambda_0$, $\sigma_{bulk} = 58$ MS/m. Antenna geometry as on Fig. 5.6. Modeling Q_c does not require adding the patch's thickness, keeping the estimation errors lower than 5 %.

Modeling Q_c does not include the patch's thickness, while the equivalent conductivity replaces the bulk conductivity for rough foils. The definition of conductor quality factor does not change with the patch's thickness, as seen in the modeling data (blue curve) in Fig. 5.8. In other words, the thickness required to compute this quality factor is the separation between the patch and the ground plane, which happens to be the substrate thickness h. The estimation errors for Q_c do not exceed 5 %, as shown in the error bounds in Fig. 5.8. Besides, the conductor roughness effect in the patch and ground plane on the losses needs to be accounted for Q_d. From the equivalency model, modeling this effect is possible by replacing the bulk conductivity σ_{bulk} with the equivalent value σ_{eq} of (4.44).

For the ideal case of a smooth patch, both values get congruent ($\sigma_{eq} = \sigma_{bulk}$). Hence, the expression for Q_c is written as:

$$Q_c = h\sqrt{\pi f_{0p}\mu\sigma_{eq}} \tag{5.11}$$

5.2.2.2 Dielectric Quality Factor Q_d

The theoretical value of Q_d is solely characterized by the substrate loss tangent $\tan\delta$, as discussed in Section 2.4.4.1 and expressed in (2.102) as $Q_d = 1/\tan\delta$. The comparison provided in Table 5.3 showed that the simulated values of Q_d are overestimated from the theoretical value, with an average error of 22.8 %. Even though the origin of this difference is not specific, the impact of these values on Q_d can be quantified.

For the designs made for Table 5.3 ($\tan\delta = 0.0009$), the theoretical value of Q_d is 1111.1, which is almost two orders of magnitude superior to Q_p. At 49 GHz, the values of Q_{rs} and Q_c are 17.5 and 500, respectively. For $Q_d = 1111.1$, the resulting value of Q_p is 16.655. The 5 %-error bound for Q_p occurs at $Q_d = 1663$ and $Q_d = 832$. Then, if Q_d is overestimated in 50 %, the impact on Q_p is 5 %. At 280 GHz, the values of Q_{rs} and Q_c are 16.5 and 300, respectively. A 56 %-overestimated value of Q_d would be necessary to produce 0.5 % error in the resulting value of Q_p. Since the estimation errors in Q_d are less than 25 %, the expected impact on Q_p is less than 0.5 %. This minimum impact occurs because of the high values of Q_d for low-loss dielectrics such as PTFE. Therefore, the dielectric quality factor for modeling MSPAs up to 300 GHz is expressed as:

$$Q_d = \frac{1}{\tan\delta} \tag{5.12}$$

5.2.2.3 Radiation and Surface-Wave Quality Factor Q_{rs}

The quality factor from the combined effect between radiation and surface waves, Q_{rs}, is typically the dominant value and significantly impacts the patch's quality factor Q_p. The value of Q_{rs} is exclusively geometry-dependent as expressed in (2.102). The variable Q_{rs} is a function of the patch's radiating cavity's electrical thickness, permittivity, and permeability under the cavity model. In this formulation, the substrate's electrical thickness h_T/λ_{0p} plays an important role, being the leading cause of forming broad bands in MSPAs.

As listed in Table 5.5a, the values of Q_p strongly depend on the patch thickness. At 280 GHz, the values of Q_p drops from 17.32 to 15.49 for a patch's thickness between 8.75 μm and 35 μm. Therefore, extending the current formulation of Q_{rs} up to the mmWave and sub-THz bands is performed using the concept of effective dielectric thickness. An effective patch's thickness of 25 % of its physical thickness has been found to match best with the simulated values of Q_{rs} for the ranges $\varepsilon_r \in [1.09; 9.20]$, $t \in [8.75; 35]$ μm, and $h \in [0.025; 0.050]\lambda_0$. This value has been found by analyzing PF-MSPAs in the described ranges and using the same strategy as in the formulations for f_{0p}, as detailed in Section 5.2.1. Thus, an accurate estimation of Q_{rs} up to 300 GHz and for $t < 35$ μm is possible by considering the patch's thickness through the effective substrate thickness h_e as formulated in (5.13). The resulting value of Q_{rs} is then expressed as in (5.14).

$$h_e = h + t/4 \tag{5.13}$$

$$Q_{rs} = \frac{3}{16}\frac{\varepsilon_r}{pc_1}\frac{\lambda_{0p}}{h_e}\frac{L_e}{W_e}\left[1 + \frac{3}{4}\pi\frac{k_{0p}h_T}{c_1}\left(1 - \frac{1}{\varepsilon_r}\right)^3\right]^{-1}, \tag{5.14}$$

where the values of p, c_1, L_e, W_e, and k_{0p} are described in (2.103a) through (2.103c) applied to f_{0p} of (5.10).

5.2.2.4 Assessment of the Patch's Quality Factor Q_p

By integrating the quality factor from each source: conductor (Q_c), dielectric (Q_d), and radiation (Q_{rs}), the value of Q_p can be determined as in (5.15). This equation comes from the formulations made in (5.11), (5.12), and (5.14).

$$\begin{aligned} Q_p &= [Q_c^{-1} + Q_d^{-1} + Q_{rs}^{-1}]^{-1} \\ &= \left[\frac{1}{h\sqrt{\pi f_{0p}\mu\sigma_{eq}}} + \tan\delta + \frac{16}{3}\frac{pc_1}{\varepsilon_r}\frac{h_e}{\lambda_{0p}}\frac{W_e}{L_e}\left(1 + \frac{3}{4}\pi\frac{k_{0p}h_e}{c_1}\left(1 - \frac{1}{\varepsilon_r}\right)^3\right)\right]^{-1}, \end{aligned} \tag{5.15}$$

This formulation is verified by comparing the estimated values of Q_p with the extracted values of Q_p from simulated lossless MSPAs up to 300 GHz. The calculations of Q_p are made by using (5.15) and the associated components. The extraction of the Q_p values derives from the real part of the impedance responses from simulated PF-MSPAs at 46 frequency samples between 0.3 GHz and 300 GHz. The designed MSPAs have dimensions $L = W = 0.448\lambda_0/\sqrt{\varepsilon_r}$, $h = 0.0368\lambda_0$, $t = 17.5$ μm, and $\varepsilon_r = 2.2$. They are designed for operating frequencies along the analysis range. Fig. 5.9 displays the model performance, including variations in ε_r, t, and h.

The proposed modeling method estimates errors of less than 7 % in the mmWave and sub-THz bands. The plots of Fig. 5.9 show the high accuracy of the proposed method to calculate f_{0p} up to 300 GHz. Then, this method improves the accuracy by a factor of two compared with the most recent model for Q_p from previous work. As seen in Fig. 5.7a, the inclusion of the patch's thickness provides an accuracy of f_{0p} above 20 GHz, reducing the errors from 14 % to 5 % at 300 GHz. However, the upward line slope in the error curve from the previous model changes to a downward trend, indicating a potential model limitation at terahertz frequencies.

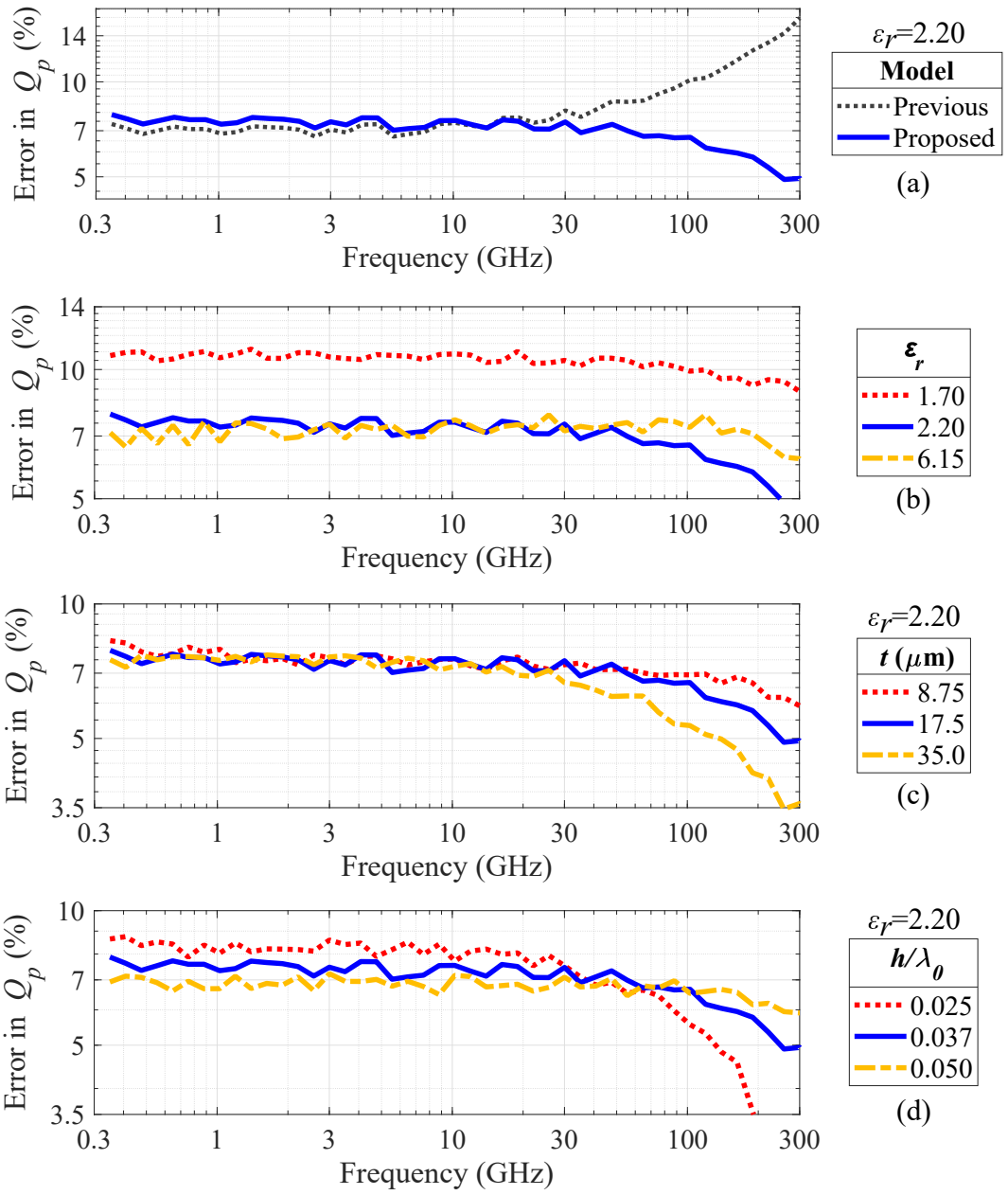

Figure 5.9: Estimation accuracy of patch's quality factor in PF-MSPAs up to the sub-THz and with thick conductors.
Errors between simulation and modeling in PF-MSPAs between 300 MHz and 300 GHz. Comparisons made by modeling method (a), by substrate's relative permittivity (b), by patch's and feed's thickness (c), and by feeding and patch substrate's thickness (d). The proposed modeling method produces a highly accurate estimation of the patch's quality factor Q_p in PF-MSPAs up to 300 GHz, under several geometrical and electrical conditions.

This model extension also performs excellently with diverse design conditions, such as substrate dielectric constant, substrate thickness, and patch thickness. The method allows estimating Q_p with errors less than 11 % in the permittivity range between 1.7 and 6.15, according to Fig. 5.9b. This method is especially accurate for a range of substrate's dielectric constants between 2.20 to 6.15, with errors less than 8 %. As shown in Fig. 5.9c, the method works with high accuracy for foil thicknesses up to 35 μm thick. However, the potential limitations above 300 GHz are more noticeable for thick patches, as seen in the more prominent downward slopes of the error curves. Finally, Fig. 5.9d reveals that the method works very well in substrates with thickness up to $0.05\lambda_0$ despite the potential limitations at terahertz frequencies.

5.2.3 Patch Resonant Resistance

The patch's resonant resistance R_p is a function that involves modeling the patch, the associated cavity underneath, and the excitation geometry. This patch's resonator parameter depends on the other two previously modeled parameters: the resonant frequency (f_{0p}) and the quality factor (Q_p). Besides, the feeding location modifies the value of R_p through the probe location along the patch r_xL and the probe height h. Since the probe contacts the patch in its bottom face, no effective patch thickness is included. However, the value of R_p is indirectly modified by the patch's thickness from f_{0p} and Q_p. Thus, the value for R_p as part of the modeling extension for PF-MSPA is expressed as in (5.16).

$$R_p = \frac{4}{\pi}(\mu_r\eta_0)Q_p\frac{L}{W}\frac{h}{\lambda_{0p}}\cos^2\left(\pi\frac{r_xL+\Delta L}{L+2\Delta L}\right) \tag{5.16}$$

This approach is tested by assessing the proportionality of R_p from the values of f_{0p} and Q_p that indirectly modifies R_p in PF-MSPAs with a thick patch.

Let be a set of square PF-MSPAs ($L_e = W_e$), where the only difference in

each design is the patch's thickness. The value of R_p gets proportional to Q_p/λ_{0p}, i.e. $R_p \propto Q_p f_{0p}$, according to the formulation given in (5.16). This relation is evaluated. The parameters' values f_{0po}, Q_{po}, and R_{po} for the PF-MSPA with a patch thickness $t = 0$ μm are found and set as the base reference. As t increases, the values of f_{0p} and Q_p decreases, as demonstrated in the trends of Fig. 5.4 and Fig. 5.5. The updated values of f_{0p} and Q_p are then used to compute R_p using the proportional relation $R_p = R_{po}(f_{0p}/f_{0po})(Q_p/Q_{po})$. If this relation is correct, then the errors between these computed values and the values of R_p extracted from the simulated PF-MSPAs must be ideally zero. The assessment of proportionality listed in Table 5.6 and Table 5.7 shows estimation errors less than 5 % for a patch thickness up to 35 μm, frequencies up to 280 GHz, and dielectric constants between 1.09 and 9.20. These results validate the proposed formulation in (5.16) for PF-MSPA with a thick patch.

Table 5.6: Assessment of accuracy estimation of the patch's resonant resistance for PF-MSPAs at different conductor thickness as a proportional relation with patch's parameters and dimensions.

ε_r	t (μm)	f_{0p} (GHz)	Q_p	R_p (Ω)	Prop. R_p (Ω)	Error (%)
1.09	0	272.0	15.30	60.00	60.00	–
	8.75	267.4	14.77	55.50	56.93	2.58
	17.5	263.8	14.18	51.57	53.94	4.59
	35.0	259.0	12.85	44.86	47.98	6.95
3.00	0	273.9	20.03	78.84	78.84	–
	8.75	271.3	19.20	73.40	74.84	1.97
	17.5	269.7	18.40	68.96	71.30	3.40
	35.0	266.9	17.03	62.30	65.31	4.83
9.20	0	275.7	33.09	127.5	127.5	–
	8.75	275.4	30.73	116.2	118.2	1.73
	17.5	275.2	28.98	108.5	111.4	2.73
	35.0	274.6	26.65	98.25	102.2	4.06

"–": the errors consider the resistance data with zero thickness ($t = 0$ μm) as the ground reference.

Table 5.7: Assessment of accuracy estimation of the patch's resonant resistance for PF-MSPAs at different operating frequencies as a proportional relation with patch's parameters and dimensions.

ε_r	h (mm)	f_{0p} (GHz)	Q_p	R_p (Ω)	Prop. R_p (Ω)	Error (%)
1.09	3.150	3.401	15.30	60.21	60.21	–
	0.630	16.96	15.26	59.62	59.89	0.46
	0.158	67.36	15.06	57.76	58.69	1.61
	0.039	263.8	14.18	51.57	54.11	4.93
3.00	3.150	3.425	20.14	79.20	79.20	–
	0.630	17.10	20.00	78.45	78.53	0.11
	0.158	68.14	19.62	76.00	76.75	0.99
	0.039	269.7	18.40	68.96	71.22	3.27
9.20	3.150	3.446	33.17	127.9	127.9	–
	0.630	17.23	32.98	126.3	127.2	0.70
	0.158	68.90	31.93	121.2	123.1	1.55
	0.039	275.2	28.98	108.5	111.5	2.83

"–": the errors consider the resistance data at a frequency $f_o = 3.5$ GHz as the ground reference.

5.2.4 Probe Feeding

The impedance produced by the probe feeding is modeled as an inductive reactance that adds to the patch's resonator impedance. Therefore, the reactance X_{TF} is frequency dependent. Moreover, the associated inductor L_{TF} is frequency dependent, as written in (2.108). Considering PF-MSPAs operating in the mmWave or sub-THz band, the typical analysis frequency is expressed in GHz, and the probe's radius a_f is in the order of tenths of a millimeter. Hence, for a set of frequencies f in GHz, a substrate thickness h in mm, and a probe radius a_f in mm, the expression for L_{TF} and X_{TF} are written as follows:

$$L_{TF} = 0.2\mu_r h\left[\ln\left(\frac{300}{\pi f a_f\sqrt{\varepsilon_r\mu_r}}\right) - 0.577\right]\cos^2\left(\pi\frac{|r_x L - L/2|}{L+\Delta L}\right)\text{nH} \tag{5.17}$$

$$X_{TF} = j0.4\pi\mu_r f h\left[\ln\left(\frac{300}{\pi f a_f\sqrt{\varepsilon_r\mu_r}}\right) - 0.577\right]\cos^2\left(\pi\frac{|r_x L - L/2|}{L+\Delta L}\right)\ \Omega \tag{5.18}$$

5.3 Modeling Extension for Proximity-coupled MSPAs

This section delivers a reformulated model for PC-MSPAs with thick patches and feeds. This update extends the EM model proposed and discussed in Chapter 3 up to the mmWave and sub-THz bands. The equivalent circuit for PC-MSPAs for modeling its input impedance comprises an RLC parallel resonator in series with an inductor and a capacitor. Similarly to PF-MSPAs, the RLC resonator models the patch's impedance, while the LC segment accounts for the proximity-coupled feeding when $r_x < 0.75$. The value of r_x is illustrated in Fig. 5.10.

The architecture of a PC-MSPA is composed of metallic and dielectric materials, as illustrated in Fig. 5.10a. The patch, feed, and ground plane conform to the metallic portions of the PC-MSPA, characterized by an electrical conductivity σ_{bulk}. The patch's thickness is defined as t_p, while the feed presents a thickness t_f. The feed finishes at the location $r_x L$, where r_x is the feed-to-patch overlap ratio. The dielectric fills the volume between the patch and the ground plane surrounding the feed. The thickness of this substrate presents two portions, having a thickness h_2 above the feed and h_1 underneath it. Both thicknesses are related through the substrate thickness ratio r_h. The substrate is characterized by its dielectric constant ε_r and loss tangent $\tan\delta$.

Extending the current model for PC-MSPAs requires defining effective dimensions, as demonstrated in the formulations for PF-MSPAs. Similarly to PF-MSPAs, the field lines depart from the feed to the patch and the ground plane, as displayed in Fig. 5.10a. Then, considering a feeding transmission line with thickness t_f, an effective portion is added to the substrate thicknesses h_1 and h_2 to form the effective thicknesses h_{1e} and h_{2e}. This division considers a coefficient k_f (5.19) and is illustrated in Fig. 5.10b,c. Then, an effective substrate thickness ratio r_{he} (5.22) is defined. Also, the effective patch's thickness $k_t t_p$ is added to

form an effective substrate thickness h_T (5.23a). For modeling Q_p, an effective thickness h_{Te} (5.23b) is defined, presenting an analogous formulation as in (5.13). As in PF-MSPAs, the patch's thickness t_p is not considered to model R_p and the feeding parameters. Therefore, the following effective dimensions are formulated:

- Feed-thickness division coefficient k_f:

$$k_f = 0.5 + 0.0766(\varepsilon_r - 1)(h_2/h_1)^{1.25} \tag{5.19}$$

  The formulation followed to get this equation is analogous to k_t in PF-MSPAs. This equation has been formulated by applying the curve-fitting technique to the data points representing the effective portions of the patch's thickness that produce constant errors of f_{0p} over frequency up to 300 GHz.

- Patch-thickness division coefficient k_t, previously defined in (5.5) as $k_t = 0.1 + e^{\varepsilon_r/2}$ for a given substrate with dielectric constant ε_r.

- Effective bottom substrate thickness:

$$h_{1e} = h_1 + k_f t_f \tag{5.20}$$

- Effective top substrate thickness:

$$h_{2e} = h_2 + (1 - k_f)t_f \tag{5.21}$$

- Effective substrate thickness ratio:

$$r_{he} = h_{2e}/h_{1e} \tag{5.22}$$

- Effective total substrate thickness:

$$\begin{aligned} h_T &= h_{1e} + h_{2e} + k_t t_p \\ &= h_1 + h_2 + t_f + k_t t_p, \text{ for modeling } f_{0p}. \end{aligned} \tag{5.23a}$$

$$\begin{aligned} h_{Te} &= h_{1e} + h_{2e} + t_p/4 \\ &= h_1 + h_2 + t_f + t_p/4, \text{ for modeling } Q_p. \end{aligned} \tag{5.23b}$$

$$h_{To} = h_{1e} + h_{2e}$$
$$= h_1 + h_2 + t_f, \text{ for modeling } R_p. \tag{5.23c}$$

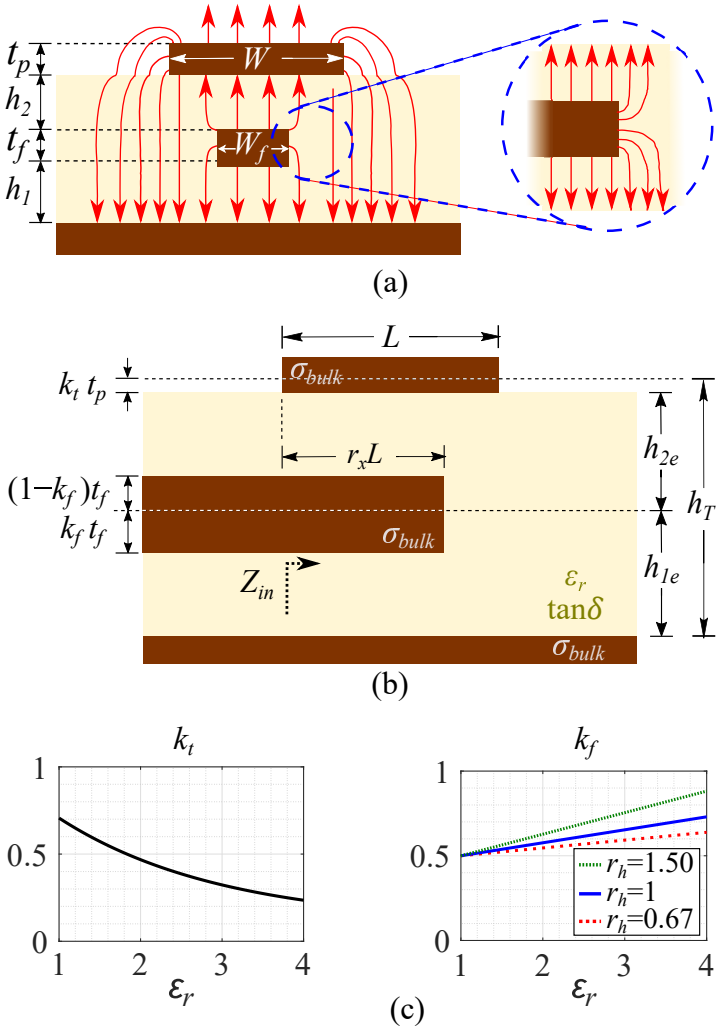

Figure 5.10: Geometrical formulation for modeling PC-MSPAs with thick conductors up to the sub-THz band.
(a) Cross-sectional view and field distribution, (b) longitudinal view and illustration of effective substrate thicknesses (h_{1e}, h_{2e}), (c) variations of effective conductor-trace coefficients (k_f, k_t) over dielectric constant ε_r. This geometry considers the patch's and feed's thicknesses to accurately model PC-MSPAs up to the sub-THz band.

The following sections describe the formulations to model PC-MSPAs up to the mmWave and sub-THz bands.

5.3.1 Patch Resonant Frequency

The determination of the patch's resonant frequency f_{0p} in PC-MSPAs is divided into two stages, as proposed in Section 3.4.1: the base resonant frequency f_{0r}, and the frequency shift factor F_{f0}.

Let be the PC-MSPA geometry of Fig. 5.10. The value of f_{0r} (5.24) is computed from the formulations for PF-MSPAs with a thickness h_T, where ε_{rep} and ΔL are calculated as in (5.8) and (5.9), respectively.

$$f_{0r} = \frac{0.3}{2(L + 2\Delta L)\sqrt{\varepsilon_{rep}}} \text{ GHz} \tag{5.24}$$

The shifting factor f_{F0} accounts for the effect of proximity coupling feeding into the patch's resonant frequency. This value is expressed in (5.25) and includes the effective substrate thickness ratio r_{he} in the required steps.

$$F_{f0} = 1.02 - \frac{0.045}{\sqrt{\varepsilon_r}} + \left(\frac{h_T}{\lambda_{0r}} - 0.005\right)\frac{1}{\sqrt{\varepsilon_r}}\left(\frac{0.7376}{r_{he}} + 0.4754\right) \tag{5.25}$$

Thus, the value of f_{0p} for PC-MSPAs is calculated as in (5.26).

$$f_{0p} = f_{0r}F_{f0} \text{ GHz} \tag{5.26}$$

The proposed formulation has been verified in several simulated PC-MSPAs at 25 operating frequency samples from 0.3 GHz up to 300 GHz. The designed MSPAs have dimensions $L = W = 0.454\lambda_0/\sqrt{\varepsilon_r}$, $\varepsilon_r = 2.2$, $h_1 = h_2 = 0.0184\lambda_0$, $t_f = t_p = 8.75$ μm. Fig. 5.11 illustrates the model performance, including variations in ε_r, $t_f + f_p$, $h_1 + h_2$, and r_h to include several geometrical and electrical conditions.

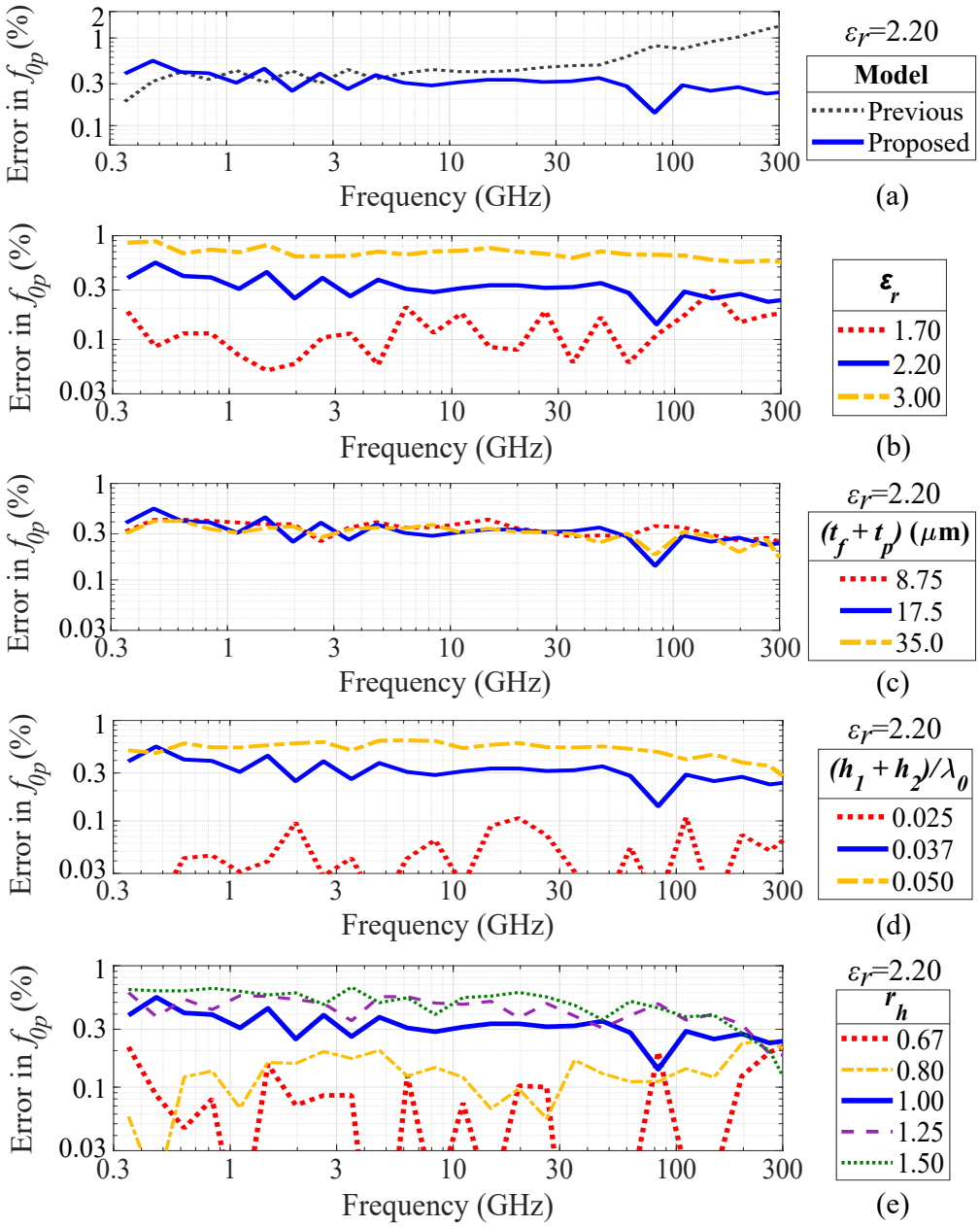

Figure 5.11: Estimation accuracy of patch's resonant frequency in PC-MSPAs up to the sub-THz and with thick conductors.
Errors between simulation and modeling in PC-MSPAs between 300 MHz and 300 GHz. Comparisons made by modeling method (a), by substrate's relative permittivity (b), by patch's and feed's thickness (c), by feeding and patch substrate's thickness (d), and by substrate thickness ratio (e).
The proposed modeling method produces a highly accurate estimation of the patch's resonant frequency f_{0p} in PC-MSPAs up to 300 GHz, under several geometrical and electrical conditions.

The proposed modeling method works with high accuracy, up to 300 GHz. Fig. 5.11a shows that including k_f and k_t in the model calculations consistently improves the accuracy of f_{0p} above 10 GHz, reducing the errors from 1.4 % to 0.3 % at 300 GHz. Although the previous modeling errors of f_{0p} are more than 1 % from 200 GHz, they are comparably lower to the ones for PF-MSPAs (Fig. 5.7a), indicating a robust formulation of the PC-MSPA model proposed in Chapter 3. Moreover, the line slope in the error curve from the previous model changes to a horizontal trend, indicating the high stability of this model extension across frequency.

This modeling method works with diverse design conditions, such as substrate dielectric constant, substrate thickness, substrate thickness ratio, and conductor thickness. The method allows estimating f_{0p} with errors less than 1 % in the permittivity range between 1.7 and 3, according to Fig. 5.11b. As shown in Fig. 5.11c, the method works with an accuracy almost independently from the foil thickness when $t_f = t_p = t/2$ and t is up to 35 μm thick. The plots of Fig. 5.11d reveals that the method works very well in substrates with thickness $h_1 = h_2 = h/2$ up to $h = 0.05\lambda_0$. Finally, the proposed model works appropriately with diverse substrate thickness ratio ranges, from 2/3 to 3/2, producing errors of less than 1 % in all the cases, as indicated in Fig. 5.11e.

5.3.2 Patch Quality Factor

Modeling the patch's quality factor Q_p for PC-MSPAs includes the quality factor values from the dielectric Q_d, conductor Q_c, radiation, and surface waves Q_{rs}. As in PF-MSPAs, the combined quality factor from radiation and surface waves are the most significant value on the determination of Q_p.

The expression for Q_p in PC-MSPAs with the extension up to 300 GHz is formulated in (5.27). As analyzed for PF-MSPAs in Section 5.2.2, the value of Q_d solely depends on the substrate's tangent loss $\tan\delta$. Besides, the conductor quality factor Q_c is not affected by the patch's thickness, so this term is a function of the distance between the patch and the ground plane, $h_{To} = h_1 + h_2 + t_f$. The value of Q_{rs} for PC-MSPAs is included from (3.40) and modified with the effective dimensions h_{Te} (5.23b) and r_{he} (5.22).

$$Q_p = \frac{1}{\tan\delta + \frac{1}{h_{To}\sqrt{\pi f_{0p}\mu\sigma_{eq}}} + {r_{he}}^{0.24}\frac{16}{3}\frac{pc_1}{\varepsilon_r}\frac{h_{Te}}{\lambda_{0p}}\frac{W_e}{L_e}\left(1+\frac{3}{4}\pi\frac{k_{0p}h_{Te}}{c_1}\left(1-\frac{1}{\varepsilon_r}\right)^3\right)} \tag{5.27}$$

In this expression, μ has a value of $4\pi \times 10^{-7}$ H/m. The variable σ_{eq} represents the equivalent electric conductivity for rough metallic foils, as defined in (4.44) from the bulk conductivity σ_{bulk} and RMS roughness value R_q. The values of p, c_1, L_e, W_e, and k_{0p} are described in (2.103a)–(2.103c) applied to f_{0p} (5.26).

The described formulation is assessed by comparing modeled and simulated values of Q_d in PC-MSPAs at 25 operating frequency samples from 0.3 GHz up to 300 GHz. Fig. 5.12 illustrates the model performance, including variations in ε_r, $t_f + f_p$, $h_1 + h_2$, and r_h to include several geometrical and electrical conditions. The designed MSPAs have dimensions $L = W = 0.454\lambda_0/\sqrt{\varepsilon_r}$, $\varepsilon_r = 2.2$, $h_1 = h_2 = 0.0184\lambda_0$, $t_f = t_p = 8.75$ μm.

The proposed modeling method works with high accuracy up to the mmWave band. Fig. 5.11a shows an enhanced accuracy in the entire frequency range up to 300 GHz with half errors compared with the previous method. The method allows estimating Q_p with errors less than 7 % for values of ε_r between 1.7 and 3, according to Fig. 5.11b. As shown in Fig. 5.11c, the method works better for low-profile conductor thickness, having errors less than 7 % when $t_f = t_p = t/2$ and t

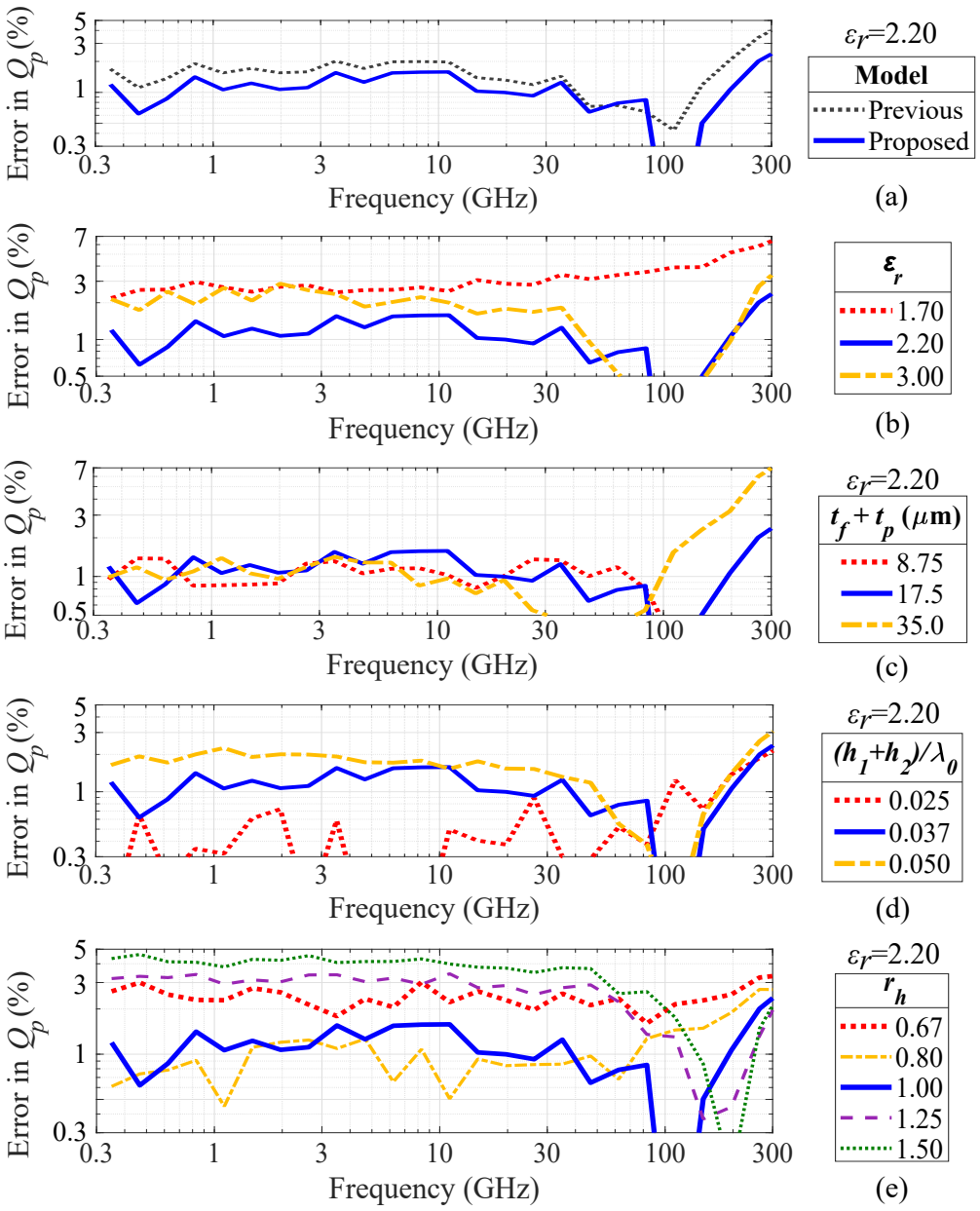

Figure 5.12: Estimation accuracy of patch's quality factor in PC-MSPAs up to the sub-THz and with thick conductors.

Errors between simulation and modeling in PC-MSPAs between 300 MHz and 300 GHz. Comparisons made by modeling method (a), by substrate's relative permittivity (b), by patch's and feed's thickness (c), by feeding and patch substrate's thickness (d), and by substrate thickness ratio (e).

The proposed modeling method produces a highly accurate estimation of the patch's quality factor Q_p in PC-MSPAs up to 300 GHz, under several geometrical and electrical conditions.

is up to 35 μm thick. The plots of Fig. 5.11d indicate that the method works very well in substrates with thickness $h_1 = h_2 = h/2$ up to $h = 0.05\lambda_0$. This method also works appropriately with diverse substrate thickness ratio ranges, from 2/3 to 3/2, producing errors of less than 5 % in all the cases, as indicated in Fig. 5.11e.

5.3.3 Patch Resonant Resistance

The formulation of the patch's resonant resistance R_p for PC-MSPAs includes determining the resistance at the edge and the amplitude function due to the feed's open-end location. As discussed in Section 3.4.1, the value of R_p is a function of the patch's resonant frequency f_{0p} and quality factor Q_p. In addition, there are two terms, K_R and F_{Rp}, which are shape factors that account for the feed's geometrical distribution with the patch and ground plane. The value of R_p for PC-MSPAs up to 300 GHz is expressed in (5.28) and the following equations. In this updated formulation, the effective dimensions h_{To} and r_{he} are included, λ_{0r} derives from f_{or} in (5.24), W, L, r_x are defined in Fig. 5.10, and μ_r is the relative permeability, deemed unity.

$$R_p = \frac{4}{\pi}(\mu_r \eta_0) Q_p \frac{L}{W} \frac{h_{To}}{\lambda_{0p}} K_R F_{Rp} \tag{5.28}$$

$$K_R = 1.1 \varepsilon_r^{-0.02\lambda_{0p}/h_{To}} (W/L)^{0.75} r_{he}^{-0.8+4.44\sqrt{h_{To}/(\varepsilon_r \lambda_{0p})}} \tag{5.29}$$

$$F_{Rp} = A e^{-p_1 r_x} + (1 - A) e^{-p_2 r_x}, \tag{5.30}$$

where:

$$A = 0.58 - 1.8 e^{-270 \frac{h_{To}}{\lambda_{0r}} \frac{1}{\varepsilon_r}} + \Big[0.173 + 130.8\Big(\frac{h_{To}}{\lambda_{0r}} \frac{1}{\varepsilon_r} - 0.03135\Big)^2\Big] \ln r_{he} \tag{5.31}$$

$$p_1 = 2[(h_{To}/\lambda_{0r})\sqrt{\varepsilon_r} + 0.035]^{-1} \tag{5.32}$$

$$p_2 = 1.35 r_{he}^{0.75} \Big[1 - 1.25 e^{-50 \frac{h_{To}}{\lambda_{0r}} \varepsilon_r^{-0.63}}\Big] \tag{5.33}$$

The proportionality of R_p is assessed from the parameters that indirectly modify R_p in PC-MSPAs with thick patches. This analysis is similar to the one in Section 5.2.3 for PF-MSPAs, but adding this time the shape factors K_R and F_{Rp}. As seen in (5.28), the value of R_p gets proportional to $Q_p/\lambda_{0p}K_RF_{Rp}$, i.e. $R_p \propto Q_p f_{0p} K_R F_{Rp}$. The base reference values f_{0po}, Q_{po}, R_{po}, K_{Ro} and F_{Rpo} for the PC-MSPA variation with a patch thickness $t_f = t_p = 0$ μm are found and set as the base reference. The values of f_{0p}, Q_p, K_R and F_{Rp} are then used to compute R_p in the PC-MSPAs with $t_f + t_p > 0$ using proportionality. The assessment is listed in Table 5.8 and Table 5.9. Estimation errors less than 10 % are observed for a combined value of patch and feed thickness up to 35 μm ($t_f = t_p$), frequencies up to 280 GHz, and dielectric constants between 1.70 and 3. These results validate the proposed formulation in (5.16) for PC-MSPA with a thick patch.

5.3.4 Proximity-coupled Feeding

The proximity-coupled feeding adds an impedance to the patch's resonator, completing the EM model to compute the input impedance for PC-MSPAs. As discussed in Section 3.4.2, the feeding impedance is composed of both inductive and capacitive reactance. From the equivalent inductor L_t and capacitor C_T given in (3.31a) and (3.31b), the total reactance X_{TF} is expressed as in (5.34). As seen in this formulation, there is no impact from the conductor thicknesses on this value.

$$\begin{aligned} X_{TF} &= j2\pi f L_T + \frac{1}{j2\pi f C_T} \\ &= j\left\{2.937\left(\frac{f}{f_{0p}}\right)e^{4.551r_x} - 4.913\left(\frac{f_{0p}}{f}\right)\frac{1}{0.1634-(r_x-0.4534)^2}\right\}\ \Omega \end{aligned} \tag{5.34}$$

Table 5.8: Assessment of accuracy estimation of the patch's resonant resistance for PC-MSPAs at different conductor thicknesses as a proportional relation with patch's parameters and dimensions.

ε_r	$t_f + t_p$ (μm)	f_{0p} (GHz)	Q_p	R_p (Ω)	h_T (mm)	K_R	F_{Rp}	Prop. R_p (Ω)	Error (%)
1.70	0	280.8	19.10	68.00	39.38	0.8295	0.2347	68.00	–
	8.75	276.5	16.91	62.95	43.75	0.8493	0.2252	64.73	2.83
	17.5	273.1	15.01	59.47	48.13	0.8663	0.2175	61.49	3.40
	35.0	267.0	12.27	53.69	56.88	0.8931	0.2059	56.69	5.58
2.20	0	276.0	20.55	70.00	39.38	0.7228	0.2688	70.00	–
	8.75	272.5	18.08	64.00	43.75	0.7498	0.2544	66.32	3.62
	17.5	269.2	16.04	60.71	48.13	0.7726	0.2432	63.00	3.77
	35.0	263.5	12.90	53.75	56.88	0.8093	0.2270	57.30	6.61
3.00	0	276.0	22.60	74.00	39.38	0.6210	0.3342	74.00	–
	8.75	272.3	19.70	67.39	43.75	0.6533	0.3101	69.00	2.39
	17.5	269.4	17.15	62.88	48.13	0.6816	0.2913	64.08	1.91
	35.0	263.6	13.75	56.95	56.88	0.7268	0.2650	57.62	1.18

"–": the errors consider the resistance data with no thickness as ground reference.

Table 5.9: Assessment of accuracy estimation of the patch's resonant resistance for PC-MSPAs at different operating frequencies as a proportional relation with patch's parameters and dimensions.

ε_r	h (mm)	f_{0p} (GHz)	Q_p	R_p (Ω)	h_T (mm)	K_R	F_{Rp}	Prop. R_p (Ω)	Error (%)
1.70	3.150	3.510	19.10	68.00	3150	0.8295	0.2347	68.00	–
	0.630	17.50	18.79	67.20	638.8	0.8277	0.2260	64.98	3.30
	0.158	69.64	17.91	64.50	166.3	0.8368	0.2240	64.29	0.33
	0.039	273.1	15.01	59.47	48.13	0.8663	0.2175	61.49	3.40
2.20	3.150	3.450	20.55	70.00	3150	0.7228	0.2688	70.00	–
	0.630	17.22	20.29	69.00	638.8	0.7163	0.2530	65.24	5.45
	0.158	68.48	19.37	66.80	166.3	0.7290	0.2508	65.04	2.64
	0.039	269.2	16.04	60.71	48.13	0.7726	0.2432	63.00	3.77
3.00	3.150	3.450	22.60	74.00	3150	0.6210	0.3342	74.00	–
	0.630	17.20	22.20	72.46	638.8	0.6053	0.3055	65.48	9.64
	0.158	68.52	20.90	69.66	166.3	0.6227	0.3019	64.98	6.72
	0.039	269.4	17.15	62.88	48.13	0.6816	0.2913	64.08	1.91

"–": the errors consider the resistance data at 3.50 GHz as ground reference.

5.4 Analysis of Model Accuracy up to 300 GHz

Modeling MSPAs in the mmWave and sub-THz bands have involved analyzing and including the most diminutive dimensions and electrical properties that comprise the architecture of these planar antennas. The modeling extension for PF-MSPAs has provided several reformulations in the patch's RLC resonator parameters, including the patch's thickness and roughness. Similarly, the modeling extension for PC-MSPAs updates the definition of substrate thickness ratio by including the feed and patch thickness. The formulations along Section 5.2 and Section 5.3 showed to perform accurately up to 300 GHz.

This section analyzes nine design cases in the sub-THz band with different electrical properties and dimensions. Section 5.4.1 assesses PF-MSPAs, while Section 5.4.2 analyzes PC-MSPAs. In addition, the effect of the conductor roughness is modeled and evaluated in Section 5.4.3. The model validation for both MSPA types is performed by analyzing the input impedance. The upcoming lines also provide an accuracy analysis, discussing the findings associated with the frequency response.

5.4.1 PF-MSPA Modeling Assessment

The modeling estimation accuracy for the input impedance and reflection coefficient in PF-MSPAs is analyzed in this section. The input impedance for a PF-MSPA is calculated from the values of f_{0p} (5.10), Q_p (5.15), R_p (5.16) and X_{TF} (5.18) as $Z_{11} = Z_{in}$ expressed in (2.109). The value of the S_{11} parameter, also the reflection coefficient, is calculated from Z_{11} and 50 Ω port as $S_{11} = (Z_{11} - 50)/(Z_{11} + 50)$.

Four PF-MSPAs are designed to assess the model accuracy between 100 GHz and 300 GHz. The geometrical and electrical specifications for these design cases

are listed in Table 5.10. The designs D1, D2, D3, and D4 operate at different frequency ranges along the sub-THz band. The conductors used to design the patch and ground plane cover the main metallic elements: copper (σ_{bulk} = 58 MS/m), silver (σ_{bulk} = 63 MS/m), and gold (σ_{bulk} = 41 MS/m). The dielectrics used to design the substrate possess dielectric constants ε_r in the range from 1.7 to 3 and loss tangents $\tan\delta$ that vary between 0.9 and 2 thousandths. The substrate thickness is chosen to cover different electrical thicknesses, fluctuating between $0.027\lambda_o$ ($\lambda_o/37$) to $0.046\lambda_o$ ($\lambda_o/21.7$). The patch's thicknesses are selected to cover diverse values between 5 μm (0.14 oz/ft^2) to 35 μm (1 oz/ft^2).

The patch dimensions (L, W) were set to obtain a PF-MSPA operation frequency at 140 GHz, 200 GHz, 240 GHz, and 300 GHz for the given dimensions for D1, D2, D3, and D4, respectively. The feeding location is set around 30 % relative length from the patch's left edge, as illustrated in Fig. 5.6b. The probe radius a_f is designed to an electrical length around $0.007\lambda_o$, ranging from 6.8 μm to 15.4 μm. The ground plane size is approximately two times the free-space wavelength at the given operating frequencies f_o.

Table 5.10: Sub-THz PF-MPSAs' design specifications.
The antenna's geometry and dimensions are defined in Fig. 5.6.

Specification	Unit	D1	D2	D3	D4
f_o	GHz	140	200	240	300
σ_{bulk}	MS/m	41	63	58	58
ε_r	–	1.7	2.2	2.2	3.0
$\tan\delta$	–	0.0020	0.0009	0.0009	0.0013
h	μm	97.5	40	45	35
t	μm	8.75	35	17.5	5
L, W	μm	728	455	375	260
r_x	-	0.28	0.31	0.32	0.30
a_f	μm	15.38	10.25	8.80	6.80
L_g, W_g	mm	4.50	3.00	2.57	2.00
h_T	λ_0	0.046	0.027	0.036	0.035

The model assessment results are reported in Table 5.11 and Fig. 5.13. The parameters f_{0p}, Q_p, and R_p are listed in the first three rows of Table 5.11, and they are extracted from the real part of Z_{11}. Similarly, the parameters f_o and $\%BW$ are obtained from the magnitude of S_{11} in dB. The plots drawn in Fig. 5.13 show the real and imaginary part of Z_{11} in the left column and the magnitude of S_{11} in the right column.

Table 5.11: Resonance modeling performance on sub-THz PF-MSPAs. Comparison between modeled and simulated antenna's electric-circuit parameters from the impedance and reflection response. The proposed model accurately delivers these properties in PF-MSPAs up to 300 GHz.

Parameter	Source	D1	Error (%)	D2	Error (%)	D3	Error (%)	D4	Error (%)
f_{0p} (GHz)	Model	135.5	0.318	197.6	0.061	235.6	0.183	295.4	0.206
	Simul.	135.1		197.7		235.2		296.0	
Q_p	Model	13.84	10.25	19.64	1.465	16.31	3.530	18.69	2.005
	Simul.	12.56		19.93		15.75		18.32	
R_p (Ω)	Model	88.89	1.985	61.17	0.971	59.87	0.670	82.95	1.025
	Simul.	87.16		61.77		60.27		83.81	
f_o (GHz)	Model	139.8	0.228	200.0	0.100	239.7	0.067	301.4	0.397
	Simul.	140.1		200.2		239.5		302.6	
$\%BW$	Model	5.034	0.663	3.379	0.165	3.488	0.414	3.769	0.452
	Simul.	5.697		3.544		3.902		4.221	

Table 5.11 shows a high estimation accuracy for sub-THz PF-MSPAs' resonator and bandwidth parameters. The errors in f_{0p} are less than 0.5 % in all the cases, showing the best accuracy in D2, and the least in D1. The errors in both cases are correlated with the substrate electrical thickness h/λ_0, but they are still minimal compared with $\%BW$. The estimation of Q_p presents high accuracy in all the design cases except D1. The electrically thick and lossy substrate may be the main variables that make the errors rise to 10.25 % in this case, while the rest of the designs show errors less than 3.53 %. Similar error patterns for R_p, f_o, and $\%BW$ showing highly accurate estimation values with errors less than 1.1 %.

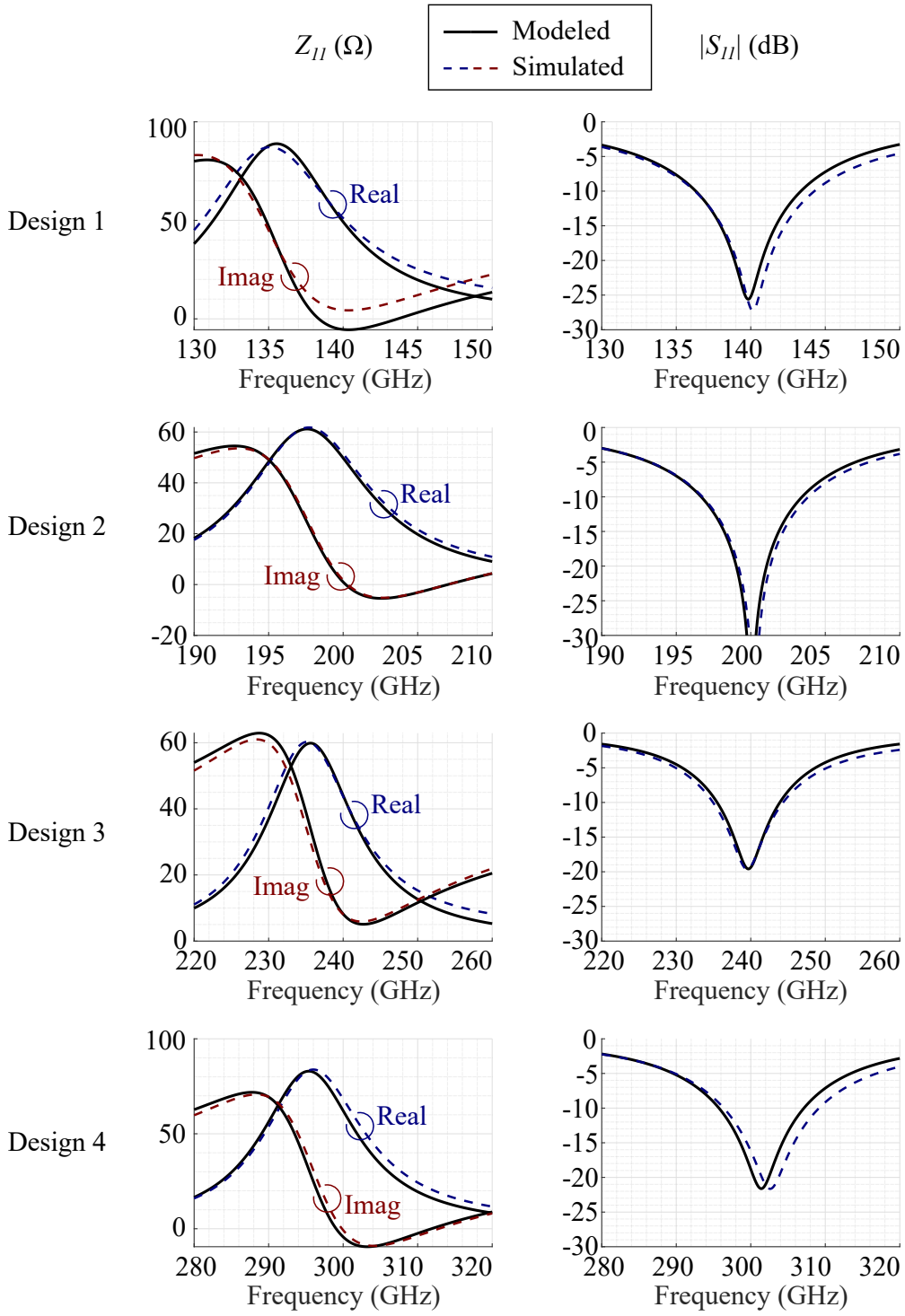

Figure 5.13: Extended-model performance on PF-MSPAs up to 300 GHz. Comparison between modeled and simulated impedance responses $Z_{11}(\Omega)$, on the left column; and S_{11} (dB), on the right column. There is an excellent agreement between the frequency responses for PF-MSPAs up to 300 GHz.

The comparison plots in Fig. 5.13 show an excellent agreement between modeling and simulation. The real parts of the modeled and simulated input impedance overlap for the four design cases. The best accurate estimation in the real part over the entire design frequency analysis is seen in design 2 and design 3. Also, the four cases show an excellent agreement between the model and simulation for the real part of Z_{11} in the frequencies around resonance. The feeding reactance is accurately estimated, with a remarkable convergence for design 2, design 3, and design 4. In case design 1, there is a 10-Ω difference around resonance and above, which may be due to the probe's high electrical height. The impedance bandwidth is accurately estimated for all the design cases, as seen in the S_{11} plots from 140 GHz to 300 GHz.

5.4.2 PC-MSPA Modeling Assessment

The input impedance and reflection coefficient are modeled and compared with the simulated impedance data to assess the model accuracy for sub-THz PC-MSPAs. The input impedance for a PC-MSPA is calculated from the values of f_{0p} (5.26), Q_p (5.27), R_p (5.28) and $Z_{feed} = X_{TF}$ (5.34) as $Z_{11} = Z_{in}$ expressed in (3.19). The value of S_{11} is also calculated from Z_{11} as $S_{11} = (Z_{11} - 50)/(Z_{11} + 50)$.

Four different design cases are analyzed to assess the model in PC-MSPAs. The design specifications are listed in Table 5.12. The designs cover operating frequencies between 140 GHz and 300 GHz, electrical thickness from $0.026\lambda_o$ ($\lambda_o/38.4$) to $0.048\lambda_o$ ($\lambda_o/20.8$), dielectric constants in the range from 1.7 to 3, PTFE-like loss tangents, and conductor thicknesses up to 39.4 μm (1.13 oz/ft$_2$). The substrate thickness distribution (h_1 and h_2) is chosen to provide different thickness ratios between 4/5 and 5/4. Also, the feed length, patch size, and ground plane size values are determined to set antenna operating frequencies at 140 GHz, 200 GHz,

240 GHz, and 300 GHz for the design cases D5, D6, D7, and D8, respectively.

Table 5.12: Sub-THz PC-MPSAs' design specifications.
The antenna's geometry and dimensions are defined in Fig. 5.10.

Specification	Unit	D5	D6	D7	D8
f_o	GHz	140	200	240	300
σ_{bulk}	MS/m	58	41	63	58
$\varepsilon_1, \varepsilon_2$	–	2.2	3.0	1.7	2.2
$\tan\delta$	–	0.0009	0.00013	0.0005	0.0009
h_1	μm	39.5	21.2	26.5	18.0
h_2	μm	39.5	16.9	29.2	22.5
r_h	–	1.00	0.80	1.10	1.25
t_f	μm	17.5	1	4.375	5
t_p	μm	17.5	8.75	35	10
L, W	μm	645	405	406	296
r_x	-	0.70	0.70	0.65	0.63
L_f	mm	1.928	1.297	1.407	0.852
W_f	μm	93.5	48	85	45
L_g, W_g	mm	4.5	3.0	2.5	2.0
h_T	λ_0	0.045	0.026	0.048	0.046

The impedance and reflection-coefficient resonance parameters are compared to determine model accuracy. The resonance modeling performance on sub-THz PC-MSPAs is listed as percent errors in Table 5.13. The results show high accuracy in the parameter estimation in the four PC-MSPA cases in the sub-THz band. The resonant frequency f_{0p} is estimated with errors less than 0.2 %, while the quality factor Q_p and resonant resistance R_p present estimation errors up to 5.5 %. This accuracy is as great as in the microwave frequencies obtained with the previous EM model in Chapter 3. The extended PC-MSPA model allows estimating f_{0p} and $\%BW$ with errors less than 0.5 %, which confirms the functionality of the model extension up to the mmWave and sub-THz bands.

The modeled and simulated values of Z_{11} and S_{11} are plotted and compared in Fig. 5.14 for the four sub-THz PC-MSPA designs. The real and imaginary parts of the input impedance overlap for all the diversely designed antenna geometries. In

Table 5.13: Resonance modeling performance on sub-THz PC-MSPAs. Comparison between modeled and simulated antenna's electric-circuit parameters from the impedance and reflection response. The proposed model accurately delivers these properties in PC-MSPAs up to 300 GHz.

Parameter	Source	D5	Error (%)	D6	Error (%)	D7	Error (%)	D8	Error (%)
f_{0p} (GHz)	Model	137.6	0.169	197.5	0.146	237.6	0.063	297.4	0.028
	Simul.	137.8		197.7		237.8		297.4	
Q_p	Model	15.27	0.586	26.83	0.626	12.77	5.478	14.01	0.492
	Simul.	15.36		27.00		12.11		14.08	
R_p (Ω)	Model	60.41	3.783	84.44	2.919	51.23	5.450	48.17	1.568
	Simul.	58.21		86.98		48.59		47.43	
f_o (GHz)	Model	139.8	0.100	200.0	0.354	240.7	0.200	300.3	0.043
	Simul.	140.0		200.7		240.2		300.2	
$\%BW$	Model	4.421	0.072	2.640	0.158	5.153	0.271	4.569	0.129
	Simul.	4.348		2.798		5.424		4.441	

addition, the perfectly overlapping plots of the reflection coefficient magnitudes indicate an accurate impedance bandwidth identification. This accuracy level was obtained in Fig. 3.11 for frequencies below 10 GHz and negligible conductor thickness. However, this high accuracy is now replicated in sub-THz PC-MSPAs with different substrate thicknesses and dielectric constants, as well as thick feeds and patches.

The proposed PC-MSPA model developed in Section 5.3 permits keeping the RLC-LC equivalent circuit as the characteristic model for this antenna even in the sub-THz band. The most significant benefit of the proposed model is the accurate identification of the resonant frequency, even at frequencies above 300 GHz, as suggested in Fig. 5.11a. Future work in extending the operating frequency range of the model for Q_p may be helpful to complete advanced accuracy for terahertz PC-MSPA and electrically-thick sub-THz PC-MSPAs.

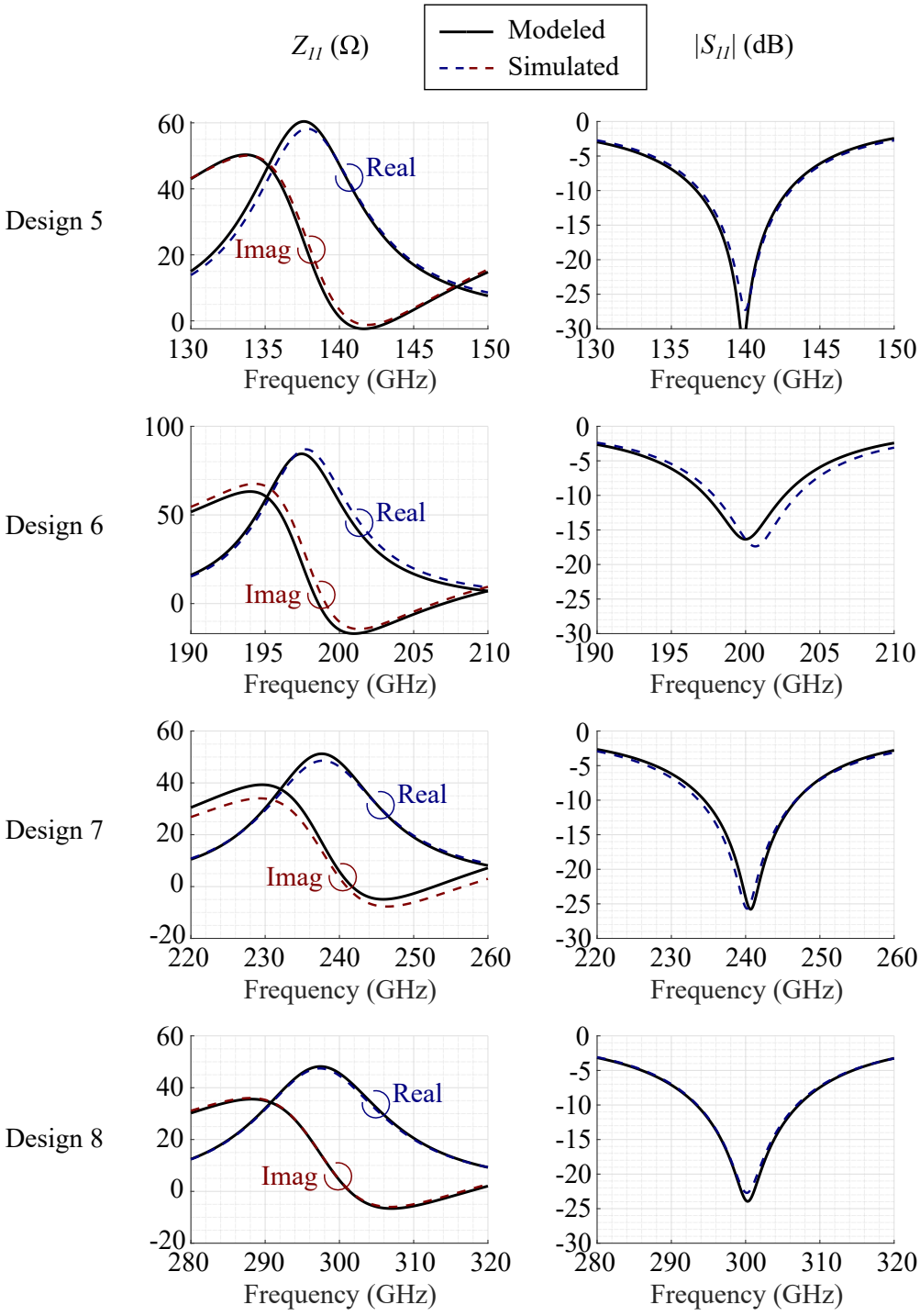

Figure 5.14: Extended-model performance on PC-MSPAs up to 300 GHz. Comparison between modeled and simulated impedance responses $Z_{11}(\Omega)$, on the left column; and S_{11} (dB), on the right column. There is an excellent agreement between the frequency responses for PC-MSPAs up to 300 GHz.

5.4.3 Rough-Conductor MSPAs Modeling Assessment

The previous sections have listed the modeling extension for MSPAs up to 300 GHz, showing high estimation accuracy in the frequency response (both Z_{11} and S_{11}). The impact of the conductor thickness in MSPAs' impedance response can be modeled by including part of this thickness in the total height between the patch and the ground plane. However, the surface roughness in the patch produces further changes to the impedance response in MSPAs. The proposed model extension covers the effect of the surface roughness by using an equivalent conductivity that replicates the losses in MSPAs through the quality factor. This section reviews the model accuracy of this formulation by analyzing a rough-conductor MSPA at 200 GHz.

Let be the PF-MSPA of Design 2, which specifications are listed in Table 5.10. Surface roughness is added in the patch and the ground plane, with R_q values of 0 μm (smooth conductor), 0.3 μm (typical value for rolled copper), and 1 μm (typical for low-profile electrodeposited copper). Silver-made (σ_{bulk} = 63 MS/m) traces are defined. At 200 GHz, the equivalent conductivity σ_{eq} is 9.28 MS/m and 2.98 MS/m for $R_q = 0.3$ μm and $R_q = 1$ μm, respectively. These updated values are considered in Section 5.2 model formulations, and the impedance response is evaluated. In addition, the conductivity equivalency is verified by simulating the same MSPAs with smooth conductors with the frequency-dependent equivalent conductivity at the given R_q values.

The modeling assessment is reported in Table 5.14 and Fig. 5.15. The patch's resonator parameters f_{0p}, Q_p, and R_p are extracted from the MSPAs' impedance response Z_{11}. The impedance-response data comes from the EM model developed in this work, simulation with the equivalent conductivity proposed in Chapter 4, and simulation with rough silver. After calculating S_{11} from Z_{11} for a 50-Ω port,

the bandwidth parameters f_o and $\%BW$ are obtained, which are listed in the last two rows of Table 5.14. The impedance response and reflection coefficient from the three data sources are plotted and displayed in Fig. 5.15 for each case.

Table 5.14: Resonance modeling performance on sub-THz PF-MSPAs under the presence of surface roughness in the patch and ground plane.
Comparison between modeled and simulated patch resonator parameters from the equivalent circuit and frequency response. Geometry and dimensions as in Fig. 5.6 and Table 5.10 (Design 2), respectively.
The proposed model delivers an accurate characterization of the patch circuit properties in low-profile PF-MSPAs in the sub-THz band.

Parameter	Source	R_q 0 μm	Error (%)	R_q 0.3 μm	Error (%)	R_q 1 μm	Error (%)
f_{0p} (GHz)	Model	197.6	0.002	197.6	0.825	197.6	1.104
	Simul. Equiv.	197.6	0.000	196.8	0.408	196.1	0.343
	Simul. Rough	197.6	–	196.0	–	195.4	–
Q_p	Model	19.64	0.333	17.65	0.057	15.68	1.678
	Simul. Equiv.	19.57	0.000	17.67	0.042	15.72	1.923
	Simul. Rough	19.57	–	17.66	–	15.43	–
R_p (Ω)	Model	61.17	0.368	54.99	2.196	48.86	4.012
	Simul. Equiv.	61.39	0.000	55.86	0.642	50.58	0.630
	Simul. Rough	61.39	–	56.22	–	50.90	–
f_o (GHz)	Model	200.0	0.000	200.0	0.816	200.0	1.081
	Simul. Equiv.	200.0	0.000	199.2	0.393	198.5	0.323
	Simul. Rough	200.0	–	198.4	–	197.9	–
$\%BW$	Model	3.379	0.150	3.499	0.196	3.519	0.290
	Simul. Equiv.	3.529	0.000	3.678	0.016	3.791	0.018
	Simul. Rough	3.529	–	3.695	–	3.809	–

"–": the errors consider the simulation-with-roughness data as the reference.

The proposed model provides an accurate resonance estimation when rough conductors are added to MSPAs. This study case with the 200-GHz rough-silver PF-MSPA shows that the conductor equivalency works by estimating the quality factor and resonant resistance with errors less than 2 %. When applying the model with the equivalent conductor, the estimation errors in both parameters do not exceed 4 %. The estimation errors for f_{0p}, f_o, and $\%BW$ are less than 1.1 %, where this value occurs for $R_q = 1$ μm.

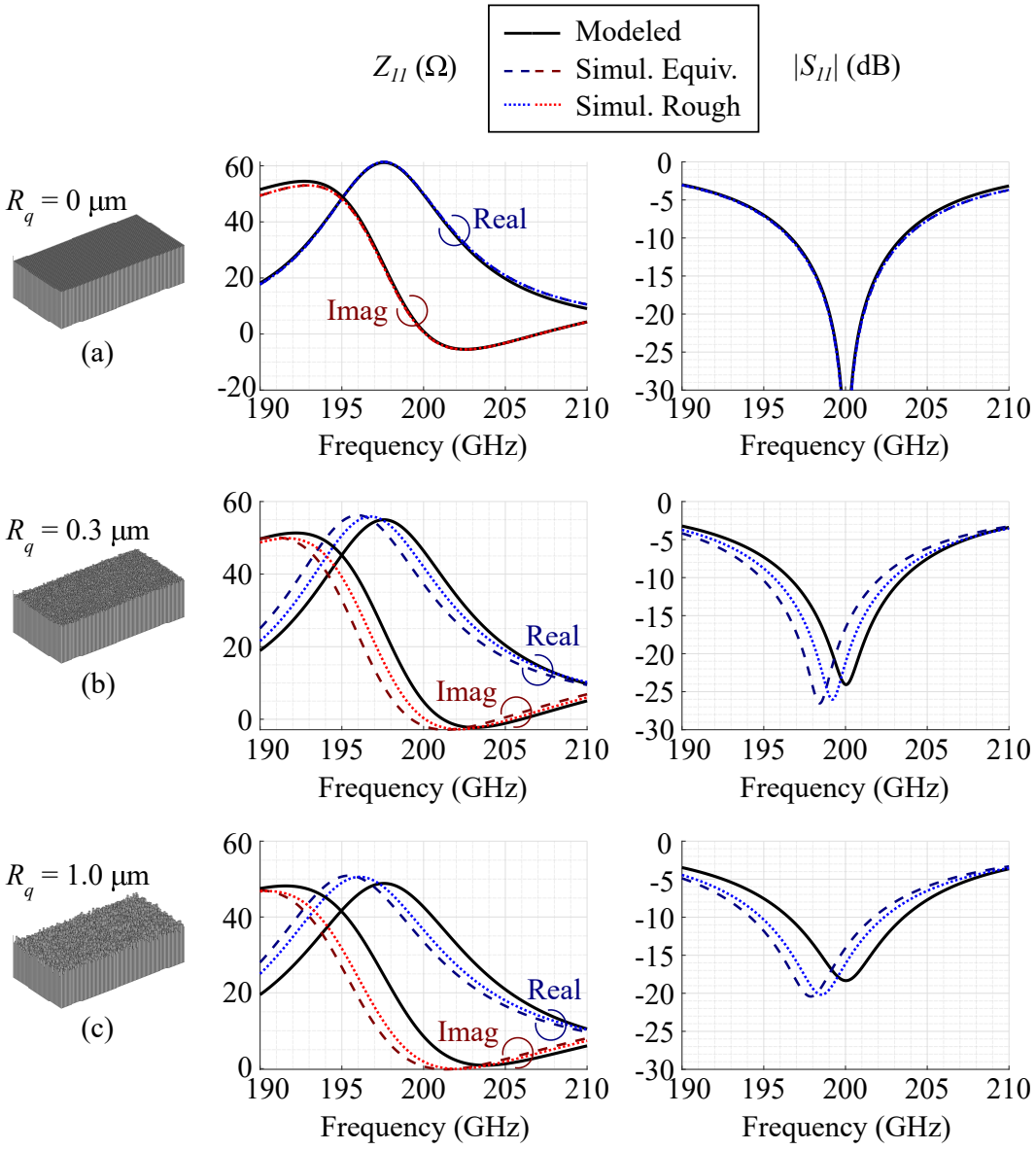

Figure 5.15: Extended-model performance on sub-THz PF-MSPAs under the presence of surface roughness in the patch and ground plane.
Comparison between modeled and simulated impedance responses $Z_{11}(\Omega)$, on the left column; and S_{11} (dB), on the right column. Geometry and dimensions as in Fig. 5.6 and Table 5.10 (Design 2), respectively. These results show a fair agreement between the frequency responses, despite the progressive differences in the estimation of the resonant frequency. Future work on analyzing the surface impedance on rough conductors will help to improve the accuracy of these results.

The plots in Fig. 5.15 reveal a progressive shift in the resonant frequency and impedance amplitude. Even though this difference is slight, this effect is noticed, and the actual resonance happens at lower frequencies for increasing roughness values. This shift can be explained by the effect of the conductor roughness in the design dielectric constant Dk, as introduced in Section 4.5.2. As R_q increases, so do Dk, the effective permittivity also gets shifted upwards, and it produces a lower value of f_{0p}, as expressed in (5.10). This difference can be addressed by including a generalized formulation of Dk for MSPAs, which constitutes an extension of the work developed in Section 4.5 and an opportunity for future research.

5.5 Summary

This chapter has discussed an unprecedented, straightforward, and accurate method to calculate the dominant mode's resonant frequency, quality factor, and resonant resistance for MSPAs. This new formulation considers the conductor foil thickness on the existing metallic parts. This method aims to extend the applicability of previous MSPA models to the mmWave and sub-THz frequency bands.

A new strategy to estimate the patch-dominant-mode resonant frequency f_{0p} of MSPAs has been developed. In contrast to previous work, this formulation allows to model MSPAs up to 300 GHz. The proposed formulation works for PF-MSPAs and PC-MSPAs over the range of substrate's dielectric constants between 1.70 and 6.15, thicknesses up to $0.05\lambda_0$, foil thicknesses up to 35 μm (1 oz/ft^2), and substrate thickness ratio between 0.67 and 1.50 in PC-MSPAs. In all these cases, the error between modeled and simulated dominant-mode patch resonant frequency is less than one percent. This error level remains constant along the frequency range from 0.3 GHz to 300 GHz, which indicates a possible working range extension up to terahertz frequencies. When the conductor surface roughness is

included in PF-MSPAs at 200 GHz, the errors in the patch resonant frequency are less than 1 % for roughness values R_q up to 1 μm.

A revised formulation for the patch's quality factor Q_p for MSPAs has been proposed as part of the model extension up to 300 GHz. An analysis of the dielectric quality factor showed that this value produces an impact of less than 1 % in the total quality factor for substrates with loss tangents similar to PTFE materials. The analysis of the conductor quality factor revealed that the patch's thickness does not impact its value. Still, the patch's roughness needs to be included through the equivalent conductivity value developed in Chapter 4. The study of the combined quality factor from radiation and surface waves demonstrated to depend on the patch's thickness and the rest of the MSPA's geometrical properties. The proposed formulation showed an accurate characterization of the patch's quality factor in PF-MSPAs and PC-MSPAs up to the sub-THz band, with errors up to 11 % for PF-MSPAs, and 7 % for PC-MSPAs.

The proposed modeling extension also included revising the patch's resonant resistance R_p and feeding impedance X_{TF} for MSPAs with probe feeding and proximity-coupled feeding. The proportionality analysis revealed that the reformulated values of f_{0p} and Q_p rectify the value of R_p in thick-patch MSPAs. This evidence allowed the model to use the current formulation for the resonant resistance without further modification. As demonstrated in Section 5.3, the feeding impedance is not affected by the patch's thickness in both MSPA feeding types.

The model assessment showed a remarkable performance of the proposed model extensions for PF-MSPAs and PC-MSPAs up to 300 GHz. The model agreed with simulated results for the input impedance and reflection coefficients over frequency by including the conductor thickness in the patch and feed. The models showed an enhanced performance for electrically thin PF-MSPAs, while

the estimation accuracy remained excellent for all the analyzed thicknesses in PC-MSPAs. This evidence confirms the high model accuracy of the PC-MSPA model developed in Chapter 3 and extended in this chapter up to the sub-THz band. The assessment with MSPA under the presence of rough conductors revealed a slight shift in the values of the patch's resonance parameters, which were less than 4 % for RMS roughness values R_q up to 1 μm. A generalization of the introduced formulations for the design dielectric constant Dk in Chapter 4 may successfully address these modeling differences. Overall, the proposed models significantly impact future research in MSPA analysis and design for the upcoming 6G technology era.

Chapter 6

Conclusions

All that I saw and learned was a new delight to me. —Marie Curie

Analytically modeling MSPAs in the mmWave and sub-THz bands allows an efficient design process, which may benefit developing future 6G communication systems and radars above 30 GHz. Since the existing MSPA models have been limited to frequency and feeding type, this work aimed to build a new mathematical framework to model MSPAs up to 300 GHz accurately. Different causes are associated with the lack of accurate MSPA models up to the mmWave and sub-THz bands, among them the modeling process, equipment, antenna materials, research scope, logistics, and physical environment. This work has addressed some of these aspects, specifically the geometrical and electrical limitations of current models over frequency. The diverse models developed in this work have shown that an accurate characterization of the materials that compose MSPAs is the base for developing reliable EM models for frequency ranges up to 300 GHz. From the information of these material properties, equivalent circuit models allowed estimation of the impedance response of MSPAs with probe feeding and proximity-coupled feeding with an excellent agreement with simulation and measurements.

This chapter overviews the research developed in this work, delivering an insightful analysis of the contributions, limitations, findings, and opportunities for future research in this topic.

6.1 Research Summary

This work has developed a new mathematical framework to accurately model MSPAs with probe feeding (PF) and proximity-coupled (PC) feeding up to 300 GHz. The developed formulations required various studies of the impedance response of these antennas, including the impact of the geometrical and electrical properties of the conductor and dielectric that comprises MSPAs. A new model has been produced for PC-MSPAs up to 10 GHz. This work provided an enhanced model for estimating the effects of the conductor surface roughness. Then, several reformulations were proposed, aiming to extend the operating range of PF-MSPA and PC-MSPA models up to the mmWave and sub-THz band.

This research work started by exploring different EM models for conventional antennas in radio frequency. Chapter 2 has provided an overview of EM modeling techniques for wired antennas and MSPAs. As the EM theory and the electric-circuit theory are connected, this chapter showed that an equivalent electric circuit could model the impedance behavior of MSPAs. Moreover, the impedance contribution from the patch presents the shape of the frequency response of an RLC parallel resonator. The model formulations for PF-MSPAs demonstrated that the RLC parameters for the patch could be computed as either circuit-concentrated or resonating-cavity parameters. An updated expression for the patch's effective permittivity was empirically determined to improve the accuracy of the patch's resonant frequency in PF-MSPAs. Lastly, the research done in this chapter identified different feeding techniques, noticing the absence of an EM model for PC-

MSPAs.

An unprecedented EM model for PC-MSPAs was formulated, covering formulations from the impedance bandwidth to differentially-fed PC-MSPAs. Chapter 3 described and discussed an advanced EM modeling framework for PC-MSPAs in radio frequency and microwaves. The diverse parametric simulations performed to optimize the bandwidth in PC-MSPAs enabled designing a set of guidelines to design these antennas efficiently. Two geometrical parameters were identified as crucial in PC-MPSA design: the feed-to-patch overlap ratio and the substrate thickness ratio. A new design strategy has been developed to maximize the bandwidth of these antennas by formulating the optimum substrate thickness ratio. In addition, a closed-form expression was proposed and validated to estimate the impedance bandwidth for PC-MSPAs designed with the proposed guidelines. The models were demonstrated to behave accurately with simulated and measured PC-MSPA between 3 GHz and 10 GHz.

An equivalent electric-circuit model has been formulated to estimate the impedance response for PC-MSPAs up to 10 GHz accurately. The analysis of trends in the input impedance of PC-MSPA over frequency and feeding length revealed that the patch's resonant frequency keeps invariant from the feeding size. In contrast, the patch's resonant resistance decreases with the feeding length in a non-cosinusoidal variation. The same analysis showed a progressive increase of the input impedance's imaginary part as the feeding becomes more prominent, a variation that an inductor could model. Also, this analysis found that the input impedance's reactance is strongly capacitive for PC-MSPAs with short feeding lengths. This evidence constituted the basis for formulating an unforeseen equivalent electric circuit composed of the RLC resonator explored in PF-MSPAs in series with an inductor-capacitor load that characterizes the feed impedance. The

proposed model and the derived mathematical formulations provided highly accurate estimations of the antenna's input impedance and reflection coefficient over the S-, C-, and X- bands. In addition, the proposed EM model was extended for PC-MSPAs with differential feeding, showing a shift in the patch's resonant parameters that could be accurately modeled by brand-new modeling formulations that depend on the materials' geometrical and electrical properties.

This research work has also thoroughly reviewed the design trade-offs for MSPA EM modeling up to the sub-THz band. MSPAs have been identified as one of the most suitable radiating elements for 6G applications in the mmWave and sub-THz band. Since MSPAs are composed of conductor and dielectric materials, Chapter 4 analyzed the effects of their geometrical and electrical properties to model these antennas from 30 GHz. An enhanced equivalency model was formulated to assess the impact of the conductor surface roughness on microstrip lines and striplines. A close-form expression of the equivalent electrical conductivity was built to replicate the effects of the conductor RMS roughness. In addition, this work introduced a new concept and formulation of the equivalent design electric constant to describe the effect of the conductor roughness on the phase of transmission lines. The proposed equivalent-conductivity formulation allowed replicating the insertion losses and phase of simulated transmission lines up to 245 GHz. The experimental results revealed that an enhanced description of the roughness description method and units helps correlate and agree between the model, simulation, and measurements. Overall, the proposed equivalent-conductor model constitutes a tool to accurately account for conductor losses in EM devices such as transmission lines and, ultimately, MSPAs.

The research work reached its ultimate goal by supplying a set of reformulations that updates and extends MSPA models up to 300 GHz. Chapter 5 analyzed

the conductor thickness and its effect on MSPA's impedance response, constituting the basis for formulating the model updates. The analysis of the impact of the patch thickness revealed that including a portion of this thickness into the substrate height leads to accurately computing the patch's resonator parameters. Therefore, this work delivered a closed-form expression of the effective amount of the patch and feed thickness that optimizes the modeling accuracy of the patch's resonant frequency, quality factor, and resonant resistance. The dielectric frequency dispersion and conductor surface roughness were considered in the reformulated models by using the frequency-dependent effective dielectric constant and equivalent conductivity, respectively. The proposed model achieved highly accurate impedance responses in sub-THz PF-MSPAs and PC-MSPAs with different patch and feed thicknesses, conductivity, substrate thickness, and dielectric constants.

6.2 Contribution Overview

As MSPAs operate at higher frequencies and their dimensions get miniaturized, more reliable models are demanded for strategic design for the upcoming 6G devices. This work has contributed a modeling framework composed of several mathematical formulations and concepts that permit an accurate characterization of the impedance frequency response of MSPAs up to 300 GHz. The most significant benefit of this contribution is that the models allow an instant estimation of the antenna impedance behavior, facilitating its design for any frequency band up to 300 GHz. Since these models are fully analytical, they can be implemented as algorithm commands to perform the calculations. This contribution makes it possible to understand MSPAs more efficiently and may facilitate the analysis and design of more sophisticated microstrip antennas.

The following research lines have been identified from the contribution made in this work: antenna modeling, antenna design, material characterization, and 6G communications systems. The following specific contributions have been developed in this work:

1. **An advanced EM model for PC-MSPAs:** This contribution comprises analytically-based design guidelines, a closed-form expression to estimate the impedance bandwidth, and an equivalent electric circuit and formulations (resistances, inductors, and capacitors) for PC-MSPAs with single feeding and differential feeding. This model can be used to design PF-MSPAs analytically, including the possibility of optimizing the impedance bandwidth based on the feeding substrate thickness. It also can be used to estimate the impedance response and bandwidth. This contribution can be used to accurately design and estimate the impedance behavior of these antennas up to 10 GHz. These models are described in Chapter 3, Section 3.1.5, Section 3.2.1, Section 3.4.1, Section 3.4.2, Section 3.4.3, and Section 3.5.1. The research lines associated with these contributions are antenna modeling and antenna design.

2. **An updated review of MSPA's trade-offs in the mmWave and sub-THz bands:** It provides an overview of mmWave and sub-THz antennas, identifies MSPA's relevant characteristics, lists materials and fabrication process, and analyzes the effect of material properties in MSPA EM modeling. The information supplied in this contribution permits a panoramic knowledge of the role of MSPAs in sub-THz band applications and trade-offs. Chapter 4 contains this contribution, specifically in Section 4.2, Section 4.3, and Section 4.4. The identified research lines associated with this contribution are material characterization and 6G communication systems.

3. **A new analytical formulation to equalize the effects of surface roughness in conductors:** This model contributes with a closed form for the equivalent conductivity that replicated the losses in rough conductors and with a method to estimate the design dielectric constant in strip lines. The MPSA models can use this equivalent-conductivity formula to replicate the effect of the losses due to the conductor roughness. This value can also simulate MSPAs and transmission lines with smooth conductors where this equivalent conductivity replaces the original rough conductor. These models are described in Chapter 4, Section 4.5.1 and Section 4.5.2. This contribution is related to the material characterization research field.

4. **Two extended EM models for PF-MSPAs and PC-MSPAs up to 300 GHz:** This contribution consists of a new concept of effective conductor thickness, the associated formulations, and the modifications in the current MSPA models with the effective antenna height based on the effective conductor thickness considered. The effective conductor thickness can accurately model MSPAs with probe feeding and proximity-coupled feeding operating at frequencies up to 300 GHz. The extended MSPA EM models permit an instant and accurate estimation of the impedance response for conductor thickness up to 35 μm and RMS roughness values R_q up to 1 μm. These enhanced models are listed in Chapter 5, Section 5.2, and Section 5.3. Two relevant research fields connected with this contribution are antenna modeling and 6G communication systems.

6.3 Research Limitations

The research developed in this work included exploration, description, comprehension, and integration of diverse model formulations to synthesize the MSPA

models in radio frequency, microwave, mmWave, and sub-THz bands. The explored models in Chapter 2 and the PC-MSPA model provided in Chapter 3 were scoped up to 10 GHz. This work performed double validation for the PC-MSPA models with a single feed to assess model accuracy for the bandwidth and impedance model. The equivalency model for conductor roughness was formulated up to 300 GHz but experimentally validated up to 110 GHz. Finally, the MSPA models in the mmWave and sub-THz bands were validated with simulation. During the development of this work and the formulated models, the following limitations have been found:

- MSPA models are limited by the substrate electrical thickness, typically up to 0.05 times the free-space wavelength at the operating frequency. This limitation is especially true for PF-MSPAs since the current model for probe impedance ignores the probe resistance.
- The PC-MSPA models are delimited for feeding lengths that overlap from 5 % to 75 % of the patch's length, i.e., for $r_x \in [0.05; 0.75]$. This limitation occurs because the patch's resonator properties are no longer frequency-invariant for feed that ends near the patch edges. A similar effect happens in PF-MSPAs, where the probe connects the patch near its center.
- The proposed MSPA models assume isotropic materials up to the sub-THz band. Accuracy limitations may occur in anisotropic dielectrics, such as crystals, and anisotropic surface conductors, such as graphene.
- The proposed MSPA models are currently limited to a maximum conductor thickness of 35 μm, equivalent to an electrodeposition of one ounce per square foot. For PC-MSPAs, the limitation applies to the combined thickness of the patch and feed, and model accuracy limitations may occur for thicker patches and feeds. Moreover, since the proximity-coupled feeding line width is inversely

correlated with its thickness and substrate's dielectric constant, design limitations are very likely for PC-MSPAs with a dielectric constant of more than three.

- The modeled equivalent conductivity produced surface impedances with an argument of 45 degrees. In other words, the conductor's surface reactance numerically equals its resistance. Thus, there is a potential opportunity to enhance the proposed equivalency model by analyzing and modeling the conductor's surface reactance and its effect on the design dielectric constant.
- A limitation in the availability of reliable roughness information was found in this research work. More specifically, there is limited information on the roughness values in the laminates' drum and matte sides. The information about the measuring method and standard (R_q, R_a, R_z, etc.) is also limited in both the material datasheets and the documentation currently available in Simulia™ CST software.
- Even though the enhanced MSPA model works well up to 300 GHz, there are potential accuracy limitations for frequencies in the near range above 300 GHz. Then, an opportunity for future research is identified to enhance this work and extend its functionality to frequencies beyond 300 GHz.
- The enhanced EM MSPA model is limited for RMS roughness values up to 1 μm. Although this model accurately estimates the patch's quality factor and resonant resistance with errors less than 10 %, the value of the patch's resonant frequency gets shifted, with errors that may exceed 1 % for roughness RMS values R_q more than 1 μm.

Even though the identified limitations do not affect the model accuracy inside the scope of this research, addressing them constitutes an opportunity for future research that can enhance the current models and research conditions.

6.4 Research Findings

The diverse models developed in this work and the high accuracy observed in the validation confirm that the frequency response of MSPAs can be accurately modeled by an electric circuit whose element values are computed from the antenna's geometrical and electrical properties. The following findings have been identified in this research work:

1. An effective dielectric constant for MSPAs with a value equal to the average between the substrate's dielectric constant and the microstrip's effective dielectric constant makes the patch's resonant frequency estimated with errors below 0.5 %.
2. The impedance behavior in PC-MSPAs with a given patch and height is mainly governed by the feed-to-patch overlap ratio and the substrate thickness ratio. The feed-to-patch overlap ratio is the primary variable that affects impedance matching in PC-MSPAs. The substrate thickness ratio is the primary variable for bandwidth optimization for PC-MSPAs.
3. The impedance bandwidth for PC-MSPAs is a function that depends on the substrate thickness ratio on a logarithmic basis.
4. The resonant frequency and quality factors in PC-MSPAs are invariant for feed-to-patch overlap ratio below 75 %.
5. The impedance response of PC-MSPAs can be modeled by an electric circuit composed of a resistor-inductor-capacitor (RLC) parallel resonator connected in series with a second inductor and a second capacitor.
6. The path's resonator parameters in PC-MSPAs shift from the ones with equivalent PF-MSPA. The substrate thickness ratio is the main geometrical feature that causes these shifts.
7. The impedance response of PC-MSPAs with differential feeding can also be

modeled with an RLC parallel resonator in series with an inductor-capacitor impedance block. However, the RLC parameter values get shifted by the differential feeding.

8. Rough conductors increase loss and phase delay compared with smooth conductors. The effect of the conductor surface roughness can be replicated by an equivalent smooth conductor and an effective design dielectric constant.
9. Thicker MSPA conductors (patch and proximity-coupled feed) reduce the patch's resonant frequency and radiation quality factor, but not the conductor and dielectric quality factors. The concept of effective conductor thickness can be used to model the patch's resonator parameters up to 300 GHz accurately. The feeding reactance is not affected by the conductor thickness in MSPAs up to 300 GHz. For PC-MSPAs, the thicker conductor also reduces the necessary feeding width to have a 50-Ω line impedance.
10. Rougher MSPA conductors (patch and proximity-coupled feed) also reduce the patch's resonant frequency and quality factor. The resonant frequency is reduced because of the effect of the conductor roughness on the effective design dielectric constant. Meanwhile, the reduction of the quality factor results from the higher losses, which are modeled by a lower equivalent conductivity.

These findings reveal the significant impact of material geometrical and electrical properties in modeling MSPAs, especially at operating frequencies between 30 GHz and 300 GHz.

6.5 Future Research

The following future work is recommended to enhance further the EM models developed in this work:

1. Generalize the formulation for the effective dielectric constant for MSPAs and

extend the MPSA models for anisotropic materials.

2. Extend the EM model for PC-MSPAs with an electrical thickness over 10 % of the free-space wavelength, with substrate dielectric constants less than 1.7, and feed-to–patch overlap ratios over 75 %.
3. Enhance the formulation of the shape factors in PC-MSPA's resonant resistance across feeding length and substrate geometrical and electrical properties (thickness, thickness ratio, and dielectric constant).
4. Model the impact of the differential feeding in the input reactance of PC-MSPAs.
5. Generalize the equivalency model for rough conductors in the design dielectric constant and surface impedance. Then, use this formulation to update the MSPA EM model and further improve the patch's resonant frequency accuracy.

The proposed work can be initiated by identifying the MSPA behavioral patterns and how the material properties affect them. More information about the material's advanced characteristics will significantly support the model formulation and validation. Completing this recommended work will allow consolidating the EM models developed in this work towards a reliable and strategic design of future technology, including antennas for 6G communication systems and beyond.

References

[1] T. S. Rappaport *et al.*, "Wireless Communications and Applications Above 100 GHz: Opportunities and Challenges for 6G and Beyond," *IEEE Access*, vol. 7, pp. 78 729–78 757, 2019.

[2] E. Ezhilarasan and M. Dinakaran, "A review on mobile technologies: 3g, 4g and 5g," in *2017 Second International Conference on Recent Trends and Challenges in Computational Models (ICRTCCM)*, 2017, pp. 369–373.

[3] WorldTimeZone.com. "4g LTE World Coverage Map - LTE, WiMAX, HSPA+, 3G, GSM Country List." (2022), [Online]. Available: https://www.worldtimezone.com/4g.html (visited on 11/01/2022).

[4] R. Singh, W. Lehr, D. Sicker, and K. M. Saidul-Huq, "Beyond 5G: The Role of THz Spectrum," *SSRN Electronic Journal*, Aug. 2019, ISSN: 1556-5068.

[5] W. Hong *et al.*, "The Role of Millimeter-Wave Technologies in 5G/6G Wireless Communications," *IEEE Journal of Microwaves*, vol. 1, no. 1, pp. 101–122, 2021.

[6] M. H. Alsharif, A. H. Kelechi, M. Albreem, S. A. Chaudhry, M. S. Zia, and S. Kim, "Sixth Generation (6G) Wireless Networks: Vision, Research Activities, Challenges and Potential Solutions," *Symmetry*, vol. 12, no. 4, 2020, ISSN: 2073-8994.

[7] M. Z. Chowdhury, M. Shahjalal, S. Ahmed, and Y. M. Jang, "6G Wireless Communication Systems: Applications, Requirements, Technologies, Challenges, and Research Directions," *IEEE Open Journal of the Communications Society*, vol. 1, pp. 957–975, 2020.

[8] I. F. Akyildiz, A. Kak, and S. Nie, "6G and Beyond: The Future of Wireless Communications Systems," *IEEE Access*, vol. 8, pp. 133 995–134 030, 2020.

[9] I. F. Akyildiz, C. Han, Z. Hu, S. Nie, and J. M. Jornet, "Terahertz Band Communication: An Old Problem Revisited and Research Directions for the Next Decade," *IEEE Transactions on Communications*, vol. 70, no. 6, pp. 4250–4285, 2022.

[10] Institute of ELectrical and Electronics Engineers, "IEEE Standard Letter Designations for Radar-Frequency Bands," *IEEE Std 521-2019 (Revision of IEEE Std 521-2002)*, pp. 1–15, 2020.

[11] V. Petrov, T. Kurner, and I. Hosako, "IEEE 802.15.3d: First Standardization Efforts for Sub-Terahertz Band Communications toward 6g," *IEEE Communications Magazine*, vol. 58, no. 11, pp. 28–33, 2020.

[12] Nippon Telegraph and Telephone Corporation (NTT) Docomo, *White Paper: 5G Evolution and 6G*, 2020.

[13] W. Saad, M. Bennis, and M. Chen, "A Vision of 6G Wireless Systems: Applications, Trends, Technologies, and Open Research Problems," *IEEE Network*, vol. 34, no. 3, pp. 134–142, 2020.

[14] M. A. Jamshed, A. Nauman, M. A. B. Abbasi, and S. W. Kim, "Antenna Selection and Designing for THz Applications: Suitability and Performance Evaluation: A Survey," *IEEE Access*, vol. 8, pp. 113 246–113 261, 2020.

[15] Y. Zhang and J. Mao, "An Overview of the Development of Antenna-in-Package Technology for Highly Integrated Wireless Devices," *Proceedings of the IEEE*, vol. 107, no. 11, pp. 2265–2280, 2019.

[16] M. J. Marcus, "Progress in Opening Access to Spectrum above 100 GHz," *IEEE Wireless Communications*, vol. 26, no. 2, pp. 2–3, 2019.

[17] A. Y. Nashashibi, A. Alaqeel, K. Sarabandi, and H. Shaman, "Calibration of Fully Polarimetric Wideband FMCW Instrumentation Radar at Sub-TeraHertz Frequencies," in *2018 USNC-URSI Radio Science Meeting (Joint with AP-S Symposium)*, 2018, pp. 143–144.

[18] HFSS, *version 2021 R1*. Canonsburg, Pensilvania: Ansys Inc., 2021.

[19] CST, *version 2021*. Johnston, Rhode Island: Dassault Systems Simulia Corp., 2021.

[20] S. N. Makarov, *Antenna and EM Modeling with MATLAB*. John Wiley and Sons Inc., 2002, p. 284, ISBN: 0471218766.

[21] MATLAB, *version 9.9.0 (release R2020b)*. Natick, Massachusetts: The MathWorks Inc., 2020.

[22] PCAAD, *version 7.0*. Leverett, Massachusetts: Antenna Design Associates, Inc., 2014.

[23] R. Garg, P. Bhartia, I. Bahl, and A. Ittipiboon, *Microstrip Antenna Design Handbook*. Artech House, 2001, p. 845, ISBN: 0890065136.

[24] C. A. Balanis, *Antenna Theory: Analysis and Design*. John Wiley & Sons, 2015, p. 1072, ISBN: 9781118642061.

[25] A. Bourdoux, A. Noll Barreto, B. van Liempd, C. de Lima, D. Dardari, and D. et. al., *6G White Paper on Localization and Sensing*, 2020.

[26] R. Singh and D. Sicker, "Beyond 5G: THz Spectrum Futures and Implications for Wireless Communication," International Telecommunications Society (ITS), 30th European Regional ITS Conference, Helsinki 2019 205213, 2019.

[27] S .Lepeshov, A. Gorodetsky, A. Krasnok, E. Rafailov, and P. Belov, "Enhancement of Terahertz Photoconductive Antenna Operation by Optical Nanoantennas," *Laser & Photonics Reviews*, vol. 11, no. 1, p. 1 600 199, 2017. eprint: https://onlinelibrary.wiley.com/doi/pdf/10.1002/lpor.201600199.

[28] T. Nagatsuma *et al.*, "A 120-GHz Integrated Photonic Transmitter," in *International Topical Meeting on Microwave Photonics MWP 2000 (Cat. No.00EX430)*, 2000, pp. 225–228.

[29] H. Vettikalladi, W. T. Sethi, A. F. B. Abas, W. Ko, M. A. Alkanhal, and M. Himdi, "Sub-THz Antenna for High-Speed Wireless Communication Systems," *International Journal of Antennas and Propagation*, vol. 2019, p. 9 573 647, Mar. 2019, ISSN: 1687-5869.

[30] G. Chattopadhyay, M. Alonso-del Pino, N. Chahat, D. Gonzalez-Ovejero, C. Lee, and T. Reck, "Terahertz Antennas and Feeds," in *Aperture Antennas for Millimeter and Sub-Millimeter Wave Applications*, A. Boriskin and

R. Sauleau, Eds. Cham: Springer International Publishing, 2018, pp. 335–386, ISBN: 978-3-319-62773-1.

[31] T. Nagatsuma *et al.*, "Giga-bit Wireless Link Using 300–400 GHz Bands," in *2009 International Topical Meeting on Microwave Photonics*, 2009, pp. 1–4.

[32] G. Varshney, A. Verma, V. S. Pandey, R. S. Yaduvanshi, and R. Bala, "A Proximity Coupled Wideband Graphene Antenna with the Generation of Higher Order TM Modes for THz Applications," *Optical Materials*, vol. 85, pp. 456–463, Nov. 2018, ISSN: 09253467.

[33] A. Boriskin and R. Sauleau, *Aperture Antennas for Millimeter and Sub-Millimeter Wave Applications*. Springer International, 2018, p. 490, ISBN: 9783319627724.

[34] T. Nagatsuma and G. Carpintero, "Recent Progress and Future Prospect of Photonics-Enabled Terahertz Communications Research," *IEICE Transactions on Electronics*, vol. E98.c, no. 12, pp. 1060–1070, 2015.

[35] M. Mitolo and R. Araneo, "A Brief History of Maxwell's Equations," *IEEE Industry Applications Magazine*, vol. 25, no. 3, pp. 8–13, 2019.

[36] A. G. Deschamps, "Microstrip Microwave Antennas," *Third USAF Symposium on Antennas*, 1953, ISSN: 0018-926x.

[37] H. Gutton and G. Baissinot, "Flat Aerial for Ultra High Frequencies," *French Patent No. 703 113*, 1955, ISSN: 0018-926x.

[38] Y. Liu *et al.*, *Some Recent Developments of Microstrip Antenna*, en, Review Article, 2012.

[39] N. Liu, S. Gao, L. Zhu, L. Ji, L. Yang, and H. Zheng, "Low-profile Microstrip Patch Antenna with Simultaneous Enhanced Bandwidth, Beamwidth, and Cross-polarisation Under Dual Resonance," *IET Microwaves, Antennas Propagation*, vol. 14, no. 5, pp. 360–365, 2020.

[40] D. Sun, Z. Zhang, and X. Yan, "A Wideband Dual-polarized Patch Antenna," in *Proceedings of 2014 3rd Asia-Pacific Conference on Antennas and Propagation*, Jul. 2014, pp. 84–86.

[41] K. Carver and J. Mink, "Microstrip Antenna Technology," *IEEE Transactions on Antennas and Propagation*, vol. 29, no. 1, pp. 2–24, Jan. 1981, ISSN: 1558-2221.

[42] D. M. Pozar and B. Kaufman, "Increasing the Bandwidth of a Microstrip Antenna by Proximity Coupling," *Electronics letters*, vol. 23, no. 8, pp. 368–369, 1987.

[43] J. James, P. Hall, C. Wood, and A. Henderson, "Some Recent Developments in Microstrip Antenna Design," *IEEE Transactions on Antennas and Propagation*, vol. 29, no. 1, pp. 124–128, 1981.

[44] G. Splitt and M. Davidovitz, "Guidelines for Design of Electromagnetically Coupled Microstrip Patch Antennas on Tow-layer Substrate," *IEEE Trans. Antennas Propagat.*, vol. 38, no. 7, pp. 1136–1140, 1990, ISSN: 0018-926x.

[45] F. Abboud, J. P. Damiano, and A. Papiernik, "Accurate Model for the Input Impedance of Coax-fed Rectangular Microstrip Antenna With and Without Airgaps," in *1989 Sixth International Conference on Antennas and Propagation, ICAP 89 (Conf. Publ. No.301)*, 1989, 102–106 vol.1.

[46] P. Sullivan and D. Schaubert, "Analysis of an Aperture Coupled Microstrip Antenna," *IEEE Transactions on Antennas and Propagation*, vol. 34, no. 8, pp. 977–984, 1986.

[47] N. C. Karmakar and A. Bhattacharyya, "Electromagnetically Coupled Patch Antenna - Theoretical and Experimental Investigations," *Microwave and Optical Technology Letters*, vol. 5, pp. 115–118, Mar. 1992.

[48] D. Guha, "Resonant Frequency of Circular Microstrip Antennas With and Without Air Gaps," *IEEE Transactions on Antennas and Propagation*, vol. 49, no. 1, pp. 55–59, 2001.

[49] D. R. Jackson, J. T. W. S. A. Long, and V. B. Davis, "Computer-aided Design of Rectangular Microstrip Antennas," in *Advances in Microstrip and Printed Antennas*, ser. Wiley Series in Microwave and Optical Engineering, W. C. K. F. Lee, Ed., New York, NY, USA: John Wiley ans Sons Inc., 1997, ch. 5, pp. 223–272.

[50] D. G. Fang, *Antenna Theory and Microstrip Antennas*. Taylor & Francis group, 2010, p. 311, ISBN: 9781315218311.

[51] A. K. Singh, R. K. Gangwar, and B. K. Kanaujia, "Bandwidth Enhancement of L-probe Proximity-fed Annular Ring Microstrip Slot Antenna," in *2013 6th IEEE/International Conference on Advanced Infocomm Technology (ICAIT)*, Jul. 2013, pp. 195–197.

[52] M. K. M. Amin, M. F. Mansor, N. Misran, and M. T. Islam, "28/38GHz Dual Band Slotted Patch Antenna with Proximity-Coupled Feed for 5G Communication," in *2017 International Symposium on Antennas and Propagation (ISAP)*, 2017, pp. 1–2.

[53] A. K. Awasthi *et al.*, "Ultra-Wideband Patch Antenna Array With an Inclined Proximity Coupled Feed for Small Unmanned Aircraft RADAR Applications," *IEEE Open Journal of Antennas and Propagation*, vol. 2, pp. 1079–1086, 2021.

[54] K. F. Lee, *Microstrip Patch Antennas*. Imperial College Press, London, 2011, p. 1072, ISBN: 9781118642061.

[55] D. Pozar and D. Schaubert, *Microstrip Antennas: The Analysis and Design of Microstrip Antennas and Arrays*. IEEE Press, New York, 1995, p. 1072, ISBN: 9781118642061.

[56] D. R. Jackson and N. G. Alexopoulos, "Simple Approximate Formulas for Input Rresistance, Bandwidth, and Efficiency of a Resonant Rectangular Patch," *IEEE Trans. on Antennas and Propagat.*, vol. 39, no. 3, pp. 407–410, Mar. 1991, ISSN: 0018-926x.

[57] R. C. Johnson, *Antenna Engineering Handbook*. New York: McGraw-Hill, 1993, p. 1512, ISBN: 9781118642061.

[58] G. Kumar and I. Ray, *Broadband Microstrip Antennas*. Artech House, London, 2003, p. 432, ISBN: 9781118642061.

[59] E. Hammerstad and O. Jensen, "Accurate Models for Microstrip Computer-Aided Design," in *1980 IEEE MTT-S International Microwave symposium Digest*, 1980, pp. 407–409.

[60] S. Groiss, I. Bardi, O. Biro, K. Preis, and K. R. Richter, "Parameters of Lossy Cavity Resonators Calculated by the Finite Element Method," *IEEE Transactions on Magnetics*, vol. 32, no. 3, pp. 894–897, 1996.

[61] P. G. Huray *et al.*, "Fundamentals of a 3-D "snowball" Model for Surface Roughness Power Losses," in *2007 IEEE Workshop on Signal Propagation on Interconnects*, 2007, pp. 121–124.

[62] P. G. Huray, "Surface Roughness," in *The Foundations of Signal Integrity*. John Wiley & Sons, Ltd, 2009, ch. 6, pp. 216–276, ISBN: 9780470543481. eprint: https://onlinelibrary.wiley.com/doi/pdf/10.1002/9780470543481.ch6.

[63] G. Gold and K. Helmreich, "Effective Conductivity Concept for Modeling Conductor Surface Roughness," in *DesignCon*, vol. 01, Jan. 2014.

[64] B. Simonovich, "Practical Method for Modeling Conductor Surface Roughness Using Close Packing of Equal Spheres," *Signal Integrity*, Jul. 2016.

[65] J. Coonrod. "Choosing Copper Foils for High-Frequency PCBs." (2016), [Online]. Available: https://pcdandf.com/pcdesign/index.php/magazine/11120-high-frequency-design-1610 (visited on 04/20/2021).

[66] G. Gold and K. Helmreich, "A Physical Surface Roughness Model and Its Applications," *IEEE Transactions on Microwave Theory and Techniques*, vol. 65, no. 10, pp. 3720–3732, 2017.

[67] B. Huang and Q. Jia, "Accurate Modeling of Conductor Rough Surfaces in Waveguide Devices," *Electronics*, vol. 8, no. 3, 2019, ISSN: 2079-9292.

[68] The MatWorks Inc. "Channel Model." (2020), [Online]. Available: https://www.mathworks.com/discovery/channel-model.html (visited on 11/15/2020).

[69] S. L. Arlinghaus, *Practical Handbook of Curve Fitting*. CRC Press, 1994, p. 272, ISBN: 978-0849301438.

[70] N. Aboserwal, N. R. Ccoillo Ramos, Z. Qamar, and J. L. Salazar-Cerreno, "An Accurate Analytical Model to Calculate the Impedance Bandwidth of a Proximity Coupled Microstrip Patch Antenna (PC-MSPA)," *IEEE Access*, vol. 8, pp. 41 784–41 793, 2020. eprint: https://doi.org/10.1109/ACCESS.2020.2976750.

[71] N. R. Ccoillo Ramos, N. Aboserwal, Z. Qamar, and J. L. Salazar-Cerreno, "Assessment of the Impedance Bandwith of a Proximity-Coupled Mi-

crostrip Patch Antenna," in *2020 IEEE International Symposium on Antennas and Propagation and North American Radio Science Meeting*, 2020, pp. 153–154. eprint: https://doi.org/10.1109/IEEECONF35879.2020.9330497.

[72] N. R. Ccoillo-Ramos, N. Aboserwal, J. Salazar-Cerreno, and Z. Qamar, "Improved Analytical Model for a Proximity Coupled Microstrip Patch Antenna (PC-MSPA)," *IEEE Transactions on Antennas and Propagation*, vol. 69, no. 10, pp. 6244–6252, 2021. eprint: https://doi.org/10.1109/TAP.2021.3082570.

[73] N. R. Ccoillo Ramos and J. L. Salazar-Cerreno, "A New Impedance Model for Differentially-fed Proximity-Coupled Microstrip Patch Antennas," in *2022 IEEE Texas Symposium on Wireless and Microwave Circuits and Systems (WMCS)*, 2022, pp. 1–5. eprint: https://doi.org/10.1109/WMCS55582.2022.9866490.

[74] N. R. Ccoillo Ramos and J. L. Salazar-Cerreno, "An Enhanced Method to Estimate the Resonant Frequency in mmWave Microstrip Patch Antennas," in *2022 IEEE International Symposium on Antennas and Propagation and North American Radio Science Meeting*, 2022, pp. 1178–1179.

[75] N. R. Ccoillo Ramos, J. Salazar-Cerreno, and N. Aboserwal, "The Role of Patch Antennas in 6G Communications: Modeling, Analysis, and Design Trade-offs," *IEEE Transactions on Antennas and Propagation, submitted*, 2022.

[76] N. R. Ccoillo Ramos, J. Salazar-Cerreno, and N. Aboserwal, "An Accurate Model to Assess the Impact of the Surface Roughness on Microstrip and Striplines for mmWave Applications," *IEEE Transactions on Antennas and Propagation, submitted*, 2022.

[77] C. A. Balanis, *Advanced Engineering Electromagnetics*. John Wiley & Sons, 2012, p. 1040, ISBN: 9780470589489.

[78] X. Chen and Y. Liu, *Finite Element Modeling and Simulation with ANSYS Workbench*. Taylor & Francis Group, 2018, p. 471, ISBN: 978-1351045872.

[79] M. E. Benlakehal, A. Hocini, D. Khedrouche, T. A. Denidni, *et al.*, "Design and Analysis of Novel Microstrip Patch Antenna Array Based on Photonic Crystal in THz," *Optical and Quantum Electronics*, vol. 54, no. 5, pp. 1–16, 2022.

[80] W. Hackbusch, *Integral Equations*. Birkhäuser Basel, 1995, p. 362, ISBN: 9783764328719.

[81] P. Ufimtsev, *Theory of Edge Diffraction in Electromagnetics: Origination and Validation of the Physical Theory of Diffraction*. Birkhäuser Basel, 2009, p. 444, ISBN: 9781891121661.

[82] J. Ramsay, "Highlights of Aantenna History," *IEEE Antennas and Propagation Society Newsletter*, vol. 23, no. 6, pp. 7–20, 1981.

[83] A. E. Zahran, M. A. Abdalla, and M. H. A. El-Azeem, "Single/dual band reconfigurable metamaterial dipole loaded antenna for wireless applications," in *2016 IEEE International Symposium on Antennas and Propagation (APS-URSI)*, Jun. 2016, pp. 457–458.

[84] T. M. Khalid, "Combined fractal dipole wire antenna," in *2007 2nd International ITG Conference on Antennas*, Mar. 2007, pp. 176–180.

[85] N. Nguyen-Trong, S. X. Ta, M. Ikram, K. Bertling, and A. M. Abbosh, "A low-profile wideband tri-polarized antenna," *IEEE Transactions on Antennas and Propagation*, pp. 1–1, 2018, ISSN: 0018-926X.

[86] E. S. Pires, G. Fontgalland, M. A. B. Melo, R. R. M. Valle, and S. E. Barbin, "Metamaterial-inspired wire antennas," *IEEE Transactions on Magnetics*, vol. 49, no. 5, pp. 1893–1896, May 2013, ISSN: 0018-9464.

[87] S. Kumar, J. L. Buckley, A. Di Serio, and B. O'Flynn, "Comparative analysis of circuit and finite element models for a linear wire dipole antenna," in *2018 29th Irish Signals and Systems Conference (ISSC)*, Jun. 2018, pp. 1–6.

[88] F. Sagnard and D. Ton, "Analysis of the transient waveforms radiated by a combination of thin-wire antennas-part i: Modeling," *IEEE Antennas and Wireless Propagation Letters*, vol. 5, pp. 209–212, 2006, ISSN: 1536-1225.

[89] N. A. Aboserwal, J. L. Salazar, J. A. Ortiz, J. D. Díaz, C. Fulton, and R. D. Palmer, "Source Current Polarization Impact on the Cross-Polarization Definition of Practical Antenna Elements: Theory and Applications," *IEEE Transactions on Antennas and Propagation*, vol. 66, no. 9, pp. 4391–4406, Sep. 2018, ISSN: 0018-926x.

[90] A. Ludwig, "The Definition of Cross Polarization," *IEEE Transactions on Antennas and Propagation*, vol. 21, no. 1, pp. 116–119, Jan. 1973, ISSN: 0018-926x.

[91] W. Richards, Yuen Lo, and D. Harrison, "An Improved Theory for Microstrip Antennas and Applications," *IEEE Transactions on Antennas and Propagation*, vol. 29, no. 1, pp. 38–46, Jan. 1981, ISSN: 1558-2221.

[92] E. O. Hammerstad, "Equations for Microstrip Circuit Design," in *1975 5th European Microwave Conference*, 1975, pp. 268–272.

[93] M. Kirschning, R. H. Jansen, and N. H. L. Koster, "Accurate Model for Open End Effect of Microstrip Lines," *Electronics Letters*, vol. 17, no. 3, pp. 123–125, 1981.

[94] D. Guha, M. Biswas, and J. Y. Siddiqui, "Harrington's Formula Extended to Determine Accurate Feed Reactance of Probe-fed Microstrip Patches," *IEEE Antennas and Wireless Propagation Letters*, vol. 6, pp. 33–35, 2007.

[95] D. M. Pozar, *Microwave Engineering, 4th Edition.* Wiley, 2011, ISBN: 9781118213636.

[96] A. Ittipiboon, R. Oostlander, Y. M. M. Antar, and M. Cuhaci, "A Modal Expansion Method of Analysis and Measurement on Aperture-Coupled Microstrip Antenna," *IEEE Transactions on Antennas and Propagation*, vol. 39, no. 11, pp. 1567–1574, 1991.

[97] M. Tsai, F. Flaviis, O. Fordham, and N. Alexopoulos, "Modeling Planar Arbitrarily Shaped Microstrip Elements in Multilayered Media," *IEEE Trans. Microwave Theory and Tech.*, vol. 45, no. 3, pp. 330–336, 1997, ISSN: 0018-926x.

[98] R. Garg, I. Bahl, and M. Bozzi, *Microstrip Lines and Slotlines.* Artech House, 2013, p. 603, ISBN: 9781608075355.

[99] M. K. Hammood, "Impedance of Stripline," *Tikrit Journal of Pure Science*, vol. 17, no. 4, pp. 144–147, 2012.

[100] The Institute for Printed Circuits, *Design Guide for High-speed Controlled Impedance Circuit Boards* (Standard). 2004, ISBN: 9781580982443.

[101] K. F. Lee and K. F. Tong, "Microstrip Patch Antennas," in *Handbook of Antenna Technologies*. Singapore: Springer Singapore, 2016, pp. 787–852, ISBN: 978-981-4560-44-3.

[102] D. Guha and J. Siddiqui, "Computer Aided Design of Microstrip Antennas," in *Microstrip and Printed Antennas: New Trends, Techniques and Applications*, ser. Wiley Series in Microwave and Optical Engineering, Y. A. D. Guha, Ed., West Sussex, UK: John Wiley ans Sons Inc., 2010, ch. 2, pp. 35–64.

[103] S. V. Hum and H. Y. Xiong, "Analysis and Design of a Differentially-Fed Frequency Agile Microstrip Patch Antenna," *IEEE Transactions on Antennas and Propagation*, vol. 58, no. 10, pp. 3122–3130, 2010.

[104] Y. Zhang and J. Wang, "Theory and Analysis of Differentially-driven Microstrip Antennas," *IEEE Transactions on Antennas and Propagation*, vol. 54, no. 4, pp. 1092–1099, 2006.

[105] Z. Tong, A. Stelzer, and W. Menzel, "Improved Expressions for Calculating the Impedance of Differential Feed Rectangular Microstrip Patch Antennas," *IEEE Microwave and Wireless Components Letters*, vol. 22, no. 9, pp. 441–443, 2012.

[106] R. Xu *et al.*, "A Review of Broadband Low-Cost and High-Gain Low-Terahertz Antennas for Wireless Communications Applications," *IEEE Access*, vol. 8, pp. 57 615–57 629, 2020.

[107] K. R. Jha and G. Singh, *Terahertz Planar Antennas for Next Generation Communication*. Springer International Publishing, 2014, p. 207, ISBN: 9783319023403.

[108] Isola Group. "Presentation: PCB Material Selection for RF, Microwave and Millimeter-wave Design." (2018), [Online]. Available: https://www.isola-group.com/wp-content/uploads/PCB-Material-Selection-for-RF-Microwave-and-Millimeter-wave-Designs-1.pdf (visited on 11/27/2020).

[109] J. Luo *et al.*, "A Sub-terahertz Multi-Pixel Imaging System with Surface Wave Resonator for Isolation," in *2017 IEEE Asia Pacific Microwave Conference (APMC)*, 2017, pp. 422–425.

[110] T. A. Nisamol, K. K. Ansha, and P. Abdulla, "Design of Sub-THz Beam Scanning Antenna Using Luneburg Lens for 5G Communications or Beyond," *Progress In Electromagnetics Research C*, vol. 99, pp. 179–191, 2020, ISSN: 19378718.

[111] G. Di Massa, S. Costanzo, A. Borgia, F. Venneri, and I. Venneri, "Innovative Dielectric Materials at Millimeter-Frequencies," in *2010 Conference Proceedings ICECom, 20th International Conference on Applied Electromagnetics and Communications*, 2010, pp. 1–4.

[112] T. Tasaki, A. Shiotani, T. Yamaguchi, and K. Sugimoto, "The Low Dk/Df Polyimide Adhesives for Low Transmission Loss Substrate," in *2016 IEEE 37th International Electronics Manufacturing Technology (IEMT) 18th Electronics Materials and Packaging (EMAP) Conference*, 2016, pp. 1–6.

[113] M. Lahti, K. Kautio, M. Karppinen, K. Keränen, J. Ollila, and P. Karioja, "Review of LTCC Technology for Millimeter Waves and Photonics," *International Journal of Electronics and Telecommunications*, vol. vol. 66, no. No 2, pp. 361–367, 2020.

[114] U. Ullah, N. Mahyuddin, Z. Arifin, M. Z. Abdullah, and A. Marzuki, "Antenna in LTCC Technologies: A Review and the Current State of the Art," *IEEE Antennas and Propagation Magazine*, vol. 57, no. 2, pp. 241–260, 2015.

[115] Rogers Corp. "Copper Foils for High Frequency Materials." (2021), [Online]. Available: https://rogerscorp.com/-/media/project/rogerscorp/documents/advanced-electronics-solutions/english/properties---detailed-characteristics/copper-foils-for-high-frequency-circuit-materials.pdf (visited on 10/08/2021).

[116] S. Dash and A. Patnaik, "Material Selection for THz Antennas," *Microwave and Optical Technology Letters*, vol. 60, no. 5, pp. 1183–1187, 2018.

[117] B. Marinho, M. Ghislandi, E. Tkalya, C. E. Koning, and G. de With, "Electrical Conductivity of Compacts of Graphene Multi-wall Carbon Nanotubes, Carbon Black, and Graphite Powder," *Powder Technology*, vol. 221, pp. 351–358, 2012, Selected papers from 2010 AIChE Annual Meeting, ISSN: 0032-5910.

[118] L. Rizzi, A. Zienert, J. Schuster, M. Köhne, and S. E. Schulz, "Electrical Conductivity Modeling of Graphene-based Conductor Materials," *ACS Applied Materials & Interfaces*, vol. 10, no. 49, pp. 43 088–43 094, 2018.

[119] M. Köhne and L. Rizzi, "Can Graphene-based Conductors Compete with Copper in Electrical Conductivity?," Feb. 2021.

[120] C. H. Chan, "Thz Antennas – Design, Fabrication and Testing," in *2019 13th European Conference on Antennas and Propagation (EuCAP)*, 2019, pp. 1–4.

[121] Leiterplatten-Kopierfräsen Laser & Electronics Inc. "LPKF Proto Laser U4: Micromachining With the LPKF ProtoLaser U4." (2020), [Online]. Available: https://www.lpkf.com/en/industries-technologies/research-in-house-pcb-prototyping/produkte/lpkf-protolaser-u4 (visited on 11/26/2020).

[122] Fast Radius Inc. "CNC Machining." (2020), [Online]. Available: https://www.fastradius.com/capabilities/cnc-machining/ (visited on 11/26/2020).

[123] Stratasys Inc. "Stratasys Objet30 Scholar." (2020), [Online]. Available: https://www.stratasys.com/3d-printers/objet30 (visited on 11/26/2020).

[124] A. Ali, J. Yun, H. J. Ng, D. Kissinger, F. Giannini, and P. Colantonio, "Sub-thz On-Chip Dielectric Resonator Antenna with Wideband Performance," in *2019 49th European Microwave Conference (EuMC)*, 2019, pp. 912–915.

[125] Y. Hao, "Silicon-based MEMS Fabrication Techniques and Standardization," *Indian Journal of Pure & Applied Physics*, vol. 45, no. 4, pp. 317–320, 2007.

[126] J. A. Leon *et al.*, "Rapid Fabrication of Bilayer Graphene Devices Using Direct Laser Writing Photolithography," *Journal of Vacuum Science & Technology B*, vol. 29, no. 2, p. 021 204, 2011. eprint: https://doi.org/10.1116/1.3556978.

[127] D. Phillips, S. Simpson, and S. Hanna, "Optomechanical Microtools and Shape-Induced Forces," in Elsevier Inc., May 2017, pp. 65–98, ISBN: 9780081022481.

[128] C. Gu, S. Gao, and B. Sanz-Izquierdo, "Low-cost Wideband Low-THz Antennas for Wireless Communications and Sensing," in *2017 10th UK-Europe-China Workshop on Millimetre Waves and Terahertz Technologies (UCMMT)*, 2017, pp. 1–4.

[129] Plasma-Therm Inc. "Deep Reactive Ion Etching (DRIE)." (2020), [Online]. Available: https://corial.plasmatherm.com/en/technologies/drie-deep-reactive-ion-etching (visited on 11/26/2020).

[130] M. Ohring, "Chapter 5 - Plasma and Ion Beam Processing of Thin Films," in *Materials Science of Thin Films (Second Edition)*, M. Ohring, Ed., Second Edition, San Diego: Academic Press, 2002, pp. 203–275, ISBN: 978-0-12-524975-1.

[131] A. Lamminer, J. Saarilahti, P. Pursula, M. Kantanen, and V. Ermolov, "Impact of Fabrication Process Tolerances on Characteristics of Sub-THz Silicon Micromachined Filters," in *2018 48th European Microwave Conference (EuMC)*, 2018, pp. 284–287.

[132] E. Garcia-Marin, J. L. Masa-Campos, and P. Sanchez-Olivares, "Diffusion Bonding Manufacturing of High Gain w-Band Antennas for 5G Applications," *IEEE Communications Magazine*, vol. 56, no. 7, pp. 21–27, 2018.

[133] P. Dankov, M Iliev, and V. Levcheva, "Bi-axial Dielectric Anisotropy of Crystalline Materials and its Characterization by Resonance Microwave Methods," *Bulgarian Chemical Communications*, vol. Volume 50, pp. 126–134, Dec. 2018.

[134] J. C. Rautio, "Measurement of Uniaxial Anisotropy in Rogers RO3010 Substrate Material," in *2009 IEEE International Conference on Microwaves, Communications, Antennas and Electronics Systems*, 2009, pp. 1–4.

[135] C. D. Morales Peña, C. Morlaas, A. Chabory, R. Pascaud, M. Grzeskowiak, and G. Mazingue, "Additive Manufacturing of a Uniaxial Anisotropic Dielectric Material for Antenna Applications," in *16èmes Journées de Caractérisation Microondes et Matériaux*, Toulouse (virtuel), France: IET, Nov. 2020.

[136] J. Perruisseau-Carrier, "Graphene for Antenna Applications: Opportunities and Challenges from Microwaves to THz," in *2012 Loughborough Antennas Propagation Conference (LAPC)*, 2012, pp. 1–4.

[137] S. G. Pytel *et al.*, "Dielectric Modeling, Characterization, and Validation up to 40 GHz," in *11th IEEE Workshop on Signal Propagation on Interconnects*, Los Alamitos, CA, USA: IEEE Computer Society, May 2007.

[138] Keysight Technologies. "Presentation: Basics of Measuring the Dielectric Properties of Materials." (2020), [Online]. Available: https://www.keysight.com/us/en/assets/7018-01284/application-notes/5989-2589.pdf (visited on 11/28/2020).

[139] R. E. Collin, *Foundations for Microwave Engineering*. Artech House, 1992, p. 944, ISBN: 9780780360310.

[140] Y. J. Yoon and B. Kim, "A New Formula for Effective Dielectric Constant in Multi-Dielectric Layer Microstrip Structure," in *IEEE 9th Topical Meeting on Electrical Performance of Electronic Packaging (Cat. No.00TH8524)*, 2000, pp. 163–167.

[141] K. R. Jha and G. Singh, "Analysis and Design of Rectangular Microstrip Antenna on Two-Layer Substrate Materials at Terahertz Frequency," *Journal of Computational Electronics*, vol. 9, no. 2, pp. 68–78, Jun. 2010, ISSN: 1572-8137.

[142] D. Whitehouse, "Profile and Areal (3D) Parameter Characterization," in *Surfaces and Their Measurement*, D. Whitehouse, Ed., Oxford: Kogan Page Science, 2002, pp. 48–95, ISBN: 978-1-903996-01-0.

[143] G. Kompa, *Practical Microstrip Design and Applications*. Artech House, Jan. 2005, pp. 194–201, ISBN: Isbn1-58053-980-7.

[144] X. Guo, D. R. Jackson, M. Y. Koledintseva, S. Hinaga, J. L. Drewniak, and J. Chen, "An Analysis of Conductor Surface Roughness Effects on Signal Propagation for Stripline Interconnects," *IEEE Transactions on Electromagnetic Compatibility*, vol. 56, no. 3, pp. 707–714, 2014.

[145] A. F. Horn, J. W. Reynolds, P. A. LaFrance, and J. C. Rautio, "Effect of Conductor Profile on the Insertion Loss, Phase Constant, and Dispersion in Thin High Frequency Transmission Lines," in *DesignCon 2010*, 2010, pp. 1–22.

[146] J. A. Marshall, "Measuring Copper Surface Roughness for High Speed Applications," in *Proc. IPC*, 2015, pp. 1–6.

[147] G. Gold and K. Helmreich, "A Physical Model for Skin Effect in Rough Surfaces," in *2012 7th European Microwave Integrated Circuit Conference*, 2012, pp. 631–634.

[148] H. Braunisch, X. Gu, A. Camacho-Bragado, and L. Tsang, "Off-chip Rough-Metal-Surface Propagation Loss Modeling and Correlation with Measurements," in *2007 Proceedings 57th Electronic Components and Technology Conference*, 2007, pp. 785–791.

[149] R. LeVeque, *Finite Difference Methods for Ordinary and Partial Differential Equations: Steady-State and Time-Dependent Problems (Classics in Applied Mathematics*. Usa: Society for Industrial and Applied Mathematics, 2007, ISBN: 0898716292.

Appendix A

EM Modeling Source Codes in MATLAB™

This appendix contains the MATLAB™ source codes for the models proposed in this work. The programs are organized in input information, e.g., antenna dimensions, then the program performs initial calculations, which are followed with the model's calculations. Each program decribes the functionality and the location of the associated theory in this dissertation.

A.1 Design of a PC-MSPA in RF and Microwaves

This code delivers the dimensions of a PC-MSPA from an initial information about the substrate dielectric constant ε_r, the feed substrate thickness h_1, and the desired performance in operating frequency and percent bandwidth. The theory related to this code is detailed in Chapter 3, on Section 3.1.

```
%% PC-MSPA designer for optimum bandwidth
% Feb 7, 2020 by Nim R. Ccoillo Ramos
clear;clc;close all
%% Initial requirements
er=   2.20; % Feeding substrate dielectric constant
h1_mil=  125; % Feeding substrate thickness in mils
fo_GHz= 3; % Operating frequency desired by user
pBW=  7;  % Percent bandwidth desired by user
```

```
%% Unit conversions
h1=h1_mil*25.4/1e6; % h1 in meters
fo=fo_GHz*1e9;   % f0 in Hertz
%% Physical constants
e0=1/(36*pi)*1e-9;
u0=4*pi*1e-7;
c0=1/sqrt(e0*u0);
%% Verfying the feed substrate
%- Wavelengths and relatives
lr=c0/fo*1/sqrt(er); % relative wavelength in meters
h1_lr=h1/lr;
%- A_bw coefficients
a1=98840*exp(-2.145*sqrt(er))+533.6;
a2=-0.3252*exp(-0.8037*sqrt(er))+0.1231;
%- Finding the solution
%-- Maximum possible bandwidth
Abw_p=a1.*(h1_lr.^2-.5*(1+tanh(1e3*(h1_lr-a2))).*(h1_lr-a2).^2);

if Abw_p≥pBW % then, it is possible
    %- keep the operating frequency,
    %- keep h1_lr, go to the next step
    else % then, get a new solution, find h1_lr<0.1
    disp('Design not possible with the desired bandwidth.')
    disp('Modifying the operation frequency.')
    %- Starting with 100 points between 0 to 0.1h1_lr
    H1_LR_m=linspace(0,0.1,101);
    Abw_m=a1.*(H1_LR_m.^2-1/2*(1+tanh(1000*(H1_LR_m-a2)))...
    .*(H1_LR_m-a2).^2);
    %- Finding the new solution
    h1_lr=H1_LR_m(find(Abw_m≥pBW,1)); % Feed substrate thickness
    pBW=Abw_m(find(Abw_m≥pBW,1)); % Percent bandwidth found
    if isempty(h1_lr)
```

```
41          disp('Design not possible with lower operation ...
                frequency.')
42          disp('Decrease the desired bandwidth and try again.')
43          return
44          else
45          lr=h1/h1_lr; % Modified relative wavelength in meters
46          fo=c0/lr*1/sqrt(er); % new operating frequency in Hz
47      end
48  end
49  %% Designing the patch substrate
50  %- r_h-opt coefficients
51  T1=1.379*exp(-0.7*er)+0.3682;
52  T2=0.5182*exp(-0.4078*er)+0.6912;
53  T3=128*exp(-0.925*er)+25.4;
54  T4=-0.0446*exp(-0.6077*er)+0.05295;
55  T5=0.2694*exp(-0.15*er)+0.2903;
56  T6=96.43*exp(-0.9577*er)+16.98;
57  %- r_h-opt value
58  rh_opt=T1+T2*tanh(T3*(h1_lr-T4))+T5*cos(T6*h1_lr);
59  %- Patch substrate
60  h2=h1*rh_opt;
61  %- Total substrate thickness
62  hT=h1+h2;
63  %% Designing the feed overlapping section
64  %- r_x-opt coefficients
65  KP_3=73.75*er.^2-834.9*er+3129;
66  KP_2=-149.9-257.1*exp(-0.1708*er.^2);
67  KP_1=0.2772*er.^2-2.489*er+8.502;
68  KP_0=0.89;
69  %- r_x-opt value
70  rx_opt=KP_3.*h1_lr.^3+KP_2.*h1_lr.^2+KP_1.*h1_lr+KP_0;
71
```

```
%% Designing the patch
Wp0=c0/(2*fo)*sqrt(2/(er+1)); % Initial patch width
Wp_h=Wp0/hT; % Ratio width-height on patch
ereff=(er+1)/2+(er-1)/2*(1+12/Wp_h)^(-0.5); % Effective er
dL=0.412*hT*(ereff+0.300)/(ereff-0.258)...
*(Wp_h+0.264)/(Wp_h+0.800); % Fringe-field length
L=c0/(2*fo*sqrt(ereff))-2*dL; % Patch length
W=L; %Patch width (square patch)
%% Completing the feed design
%- Feed overlapping length
x0=rx_opt*L;
%- Total feeding length
Lf=c0/fo-L/2+x0*L;
%- Feed width (50-Ohm microstrip line)
syms Wh
ereff=(er+1)/2+(er-1)/2*(1+12/Wh)^(-0.5); % Effective er
F1=6+(2*pi-6)*exp(-(30.666/Wh)^0.7528);
Z01=60*log(F1/Wh+sqrt(1+(2/Wh)^2));
Wf_h1=vpasolve(Z01==50);
Wf=Wf_h1*h1;
%% Displaying the antenna dimensions
fprintf('Assuming matching at fo= %f GHz and er= %f;\n',fo/1e9,er)
fprintf('The predicted bandwidth is: %f\n',pBW)
disp('Dimensions:')
fprintf('Patch L=W= %f mm\n',1000*L)
fprintf('Substrates h1= %f mils, and h2= %f mils\n',...
h1*1e6/25.4,h2*1e6/25.4)
fprintf('Feed Lf= %f mm and Wf= %f mm\n',1000*Lf,1000*Wf)
```

A.2 Impedance Bandwidth of a PC-MSPA up to 30 GHz

This program provides an instant estimation of the bandwidth for PC-MSPAs in radiofrequency and microwave bands. It requires the antenna geometry, and then it performs the calculations to deliver its percent impedance bandwidth. It also gives the conditions to get maximum bandwidth from the given geometry information. The theory related to this code is detailed in Chapter 3, on Section 3.2.

```
%% %BW predictor for PC-MSPAs
% Feb 7, 2020 by Nim R. Ccoillo Ramos
clear;clc;close all
%% Antenna geometry
er=   2.20; % Substrate dielectric constant (feed and patch)
h1_mil=  125; % Feeding substrate thickness in mils
h2_mil=  125; % Patch substrate thickness in mils
L_mm=  29.4; % Square patch size, W=L
%% Unit conversions
h1=h1_mil*25.4/1e6; % h1 in meters
h2=h2_mil*25.4/1e6; % h2 in meters
L=L_mm/1000;    % L in meters
%% Physical constants
e0=1/(36*pi)*1e-9;
u0=4*pi*1e-7;
c0=1/sqrt(e0*u0);
%% Basic calculations
%- Substrate thickness ratio
rh=h2/h1;
%- Operating frequency
W=L;    %width for square patch
hT=h1+h2;  %total substrate thickness
Wp_h=W/hT; % Ratio width-height on patch
ereff=(er+1)/2+(er-1)/2*(1+12/Wp_h)^(-0.5); % Effective er
```

```
25 dL=0.412*hT*(ereff+0.300)/(ereff-0.258)...
26 *(Wp_h+0.264)/(Wp_h+0.800); % Fringe-field length
27 Le=L+2*dL;
28 fo=c0/(2*Le*sqrt(ereff)); % operating frequency
29 lr=c0/(fo*sqrt(er)); % relative wavelength
30 h1_lr=h1./lr;
31 %- Condition of operability - overlapping feeding ratio
32 %- r_x-opt coefficients
33 KP_3=73.75*er.^2-834.9*er+3129;
34 KP_2=-149.9-257.1*exp(-0.1708*er.^2);
35 KP_1=0.2772*er.^2-2.489*er+8.502;
36 KP_0=0.89;
37 %- r_x-opt value
38 rx=KP_3.*h1_lr.^3+KP_2.*h1_lr.^2+KP_1.*h1_lr+KP_0;
39 %- Conversion from vector to matrices
40 [RH_m,H1_LR_m]=meshgrid(rh,h1_lr);
41 %% Bandwidth model coefficients
42 %- A_bw coefficients
43 a1=98840*exp(-2.145*sqrt(er))+533.6;
44 a2=-0.3252*exp(-0.8037*sqrt(er))+0.1231;
45 %- r_h-opt coefficients
46 T1=1.379*exp(-0.7*er)+0.3682;
47 T2=0.5182*exp(-0.4078*er)+0.6912;
48 T3=128*exp(-0.925*er)+25.4;
49 T4=-0.0446*exp(-0.6077*er)+0.05295;
50 T5=0.2694*exp(-0.15*er)+0.2903;
51 T6=96.43*exp(-0.9577*er)+16.98;
52 %- r_h=opt
53 rh_opt=T1+T2*tanh(T3*(H1_LR_m-T4))+T5*cos(T6*H1_LR_m);
54 %- Ka coefficients and Ka
55 k1=0.7682*exp(-0.3526*er)+0.4086;
56 k2=2.299*exp(-0.5975*er)+0.2538;
```

```
k3=80.32*exp(-1.028*er)+42.36;
k4=-0.06715*exp(-0.771*er)+0.04963;
k5=1.271*exp(-0.5736*er)+0.07257;
k6=311.6*exp(-1.406*er)+18.96;
Ka=k1+k2*tanh(k3*(H1_LR_m-k4))+k5*cos(k6*H1_LR_m);
%- Kbw coefficient
Kbw=Ka./rh_opt+sqrt(4+(Ka./rh_opt).^2);
%% Bandwidth amplitude
Abw=a1.*(H1_LR_m.^2-.5*(1+tanh(1e3*(H1_LR_m-a2)))...
    .*(H1_LR_m-a2).^2);
%% Substrate-ratio's geometrical distance
Y8=log2(RH_m./rh_opt);%ratio log value
K8=log2(Kbw)-1; %elipsis 'radius'
%% %BW Calculation
BW=Abw.*sqrt(1-(Y8./K8).^2);
BW(abs(imag(BW))>0) = 0;
%% Displaying the results
fprintf('Assuming matching at fo= %f GHz, er= %f, and rx= ...
   %f;\n',fo/1e9,er,rx)
fprintf('The predicted bandwidth BW is %f \n',BW)
fprintf('This value is considering h1= %f mils, and h2= %f ...
   mils \n',h1_mil,h2_mil)
fprintf('For h2= %f mils, BW increases to %f\n',rh_opt*h1_mil,Abw)
```

A.3 Impedance Response of a PC-MSPA up to 30 GHz

This script implements the equivalent model for PC-MSPAs proposed in this work. It employs the formulations provided in the related theory of Chapter 3, Section 3.4. The input information comprises the antenna geometry and material electrical properties. This program delivers the impedance response over fre-

quency, up to the radiofrequency and microwave bands.

```
%% Equivalent Circuit Model of PC-MSPA Impedance
% Oct 10, 2020 by Nim R. Ccoillo Ramos
clc;clear;close all;
%% Antenna dimensions and setup
%- Substrates
er=2.2; tanD=0.0009;
h1=125/1000*25.4/1000; %bottom substrate thickness
h2=125/1000*25.4/1000; % top substrate thickness
%- Patch
L=27.7/1000; % patch length
W=L; % patch width
ur=1;
sig_cu=5.8*1e7;
%- Feed
rx=0.25; % Overlap ratio (rx=x0/L)
%- Frequency sweep
f=1*1e+09*linspace(2.5,3.5,1001);
%% Physical constants
e0=1/(36*pi)*1e-09;
u0=1*( 4*pi)*1e-07;
c0=1/sqrt(e0*u0);
z0=sqrt(u0/e0);
%% Dimension Equivalents
rh=h2/h1;
hT=h2+h1;
WhT=W/hT;
%% Effective permittivity
ere=(er+1)/2+(er-1)/2*(1+10/WhT)^(-0.5);
erep=0.5*er+0.5*ere;
%% Delta length
```

```
zi1=0.4349*(erep^0.81+0.260)/(erep^0.81-0.189)...
*(WhT^0.8544+0.236)/(WhT^0.8544+0.870);
zi2=1+(WhT^0.371)/(1+2.358*er);
zi3=1+0.5274*atan(0.084*WhT^(1.9413/zi2))/erep^0.9236;
zi4=1+0.0377*atan(0.067*WhT^1.456)*(6-5*exp(0.036*(1-er)));
zi5=1-0.218*exp(-7.5*WhT);
dL0=hT*zi1*zi3*zi5/zi4;
%% PF effective dimensions
dW0=dL0;
Le0=L+2*dL0;  We0=W+2*dW0;
%% PF Resonant frequency
f0r=c0/(2*Le0*sqrt(erep));
l0r=c0/f0r;
k0r=2*pi/l0r;
hT_l0r=hT/l0r;
%% PC-MSPA Resonant frequency
F0=1.02-0.045/sqrt(er);
F1=(0.7376/rh+0.4754)/sqrt(er);
Ff0=F0+(hT_l0r-0.005)*F1;
f0p=f0r*Ff0;
l0p=c0/f0p;
k0p=2*pi/l0p;
hT_l0p=hT/l0p;
%% PC-MSPA effective dimensions
Le=c0/(2*f0p*sqrt(erep));
dL=0.5*(Le-L);
dW=0.25*dL;
Le=L+2*dL;
We=W+2*dW;
%% Quality factor
p=1-0.001*(16.605*(k0p*We)^2-0.229*(k0p*We)^4+...
18.283*(k0p*Le)^2-0.217*(k0p*We)^2*(k0p*Le)^2);
```

```
c1=1-1/(er*ur)+0.4/(er*ur)^2;
er_hed=(1+3*pi/4*k0p*hT/c1*(1-1/er)^3)^(-1);
Qp=(tanD+1/(hT*sqrt(pi*f0p*u0*ur*sig_cu))+...
16/3*(p*c1)/er*hT_l0p*We/Le*1/er_hed)^(-1);
%% Resonant resistance
RpM=4/pi*(ur*z0)*Qp*L/W*hT_l0p*(cos(pi*dL/Le))^2;
mfull=1;
if mfull==1 %Full estimation
    A=sqrt(rh)*(-0.66*exp(-97.13*hT_l0p)+...
    0.74*exp(-4.505*hT_l0p));
    p1=1.544/(hT_l0p+0.01456);
    p2=rh^(0.75)*(1.456-1.698*exp(-32.18*hT_l0p));
    Frp=A*exp(-p1*rx)+(1-A)*exp(-p2*rx);
else %Fast estimation
    Frp=32.38*(1-rx^0.005)+0.14;
end
Rp=RpM*Frp;
%% PC-MSPA Feeding
L_T=1*1e-09*0.4674./(f0p/1e9).*exp(4.551*rx);
C_T=1*1e-12*1.0000./(f0p/1e9)*(-32.395*(rx-0.4534)^2+5.2925);

%% Building the circuit and estimating the impedance response
%-- Synthetize response
Rpa=Rp;
Cpa=Qp./(2*pi*f0p.*Rpa);
Lpa=Rpa./(2*pi*f0p.*Qp);
fprintf('PC Resonant resistance Rp=%f Ohm\n',Rp)
fprintf('Resonant frequency f0p=%f GHz\n',f0p/1e9)
fprintf('Res. Quality factor Qp=%f \n',Qp)
Z_ptch=1./(1./Rpa+1i*2*pi*f.*Cpa-1i./(2*pi*f.*Lpa));
Z_feed=1i*2*pi*f.*L_T-1i./(2*pi*f.*C_T);
Zin_m=Z_ptch+Z_feed;
```

```
95  %-- Reflection coefficient
96  Z0sm=50;
97  Gamma_m=(Zin_m-Z0sm)./(Zin_m+Z0sm);
98  Gamma_m_dB=mag2db(abs(Gamma_m));
99  %% Plotting
100 %- Impedance Z11
101 figure; hold on
102 plot(f/1e9,real(Zin_m),'b','Linewidth',3)
103 plot(f/1e9,imag(Zin_m),'r','Linewidth',3)
104 hold off;grid on;grid minor;xlabel('Frequency (GHz)');
105 set(gca,'FontName','Times','FontSize',24)
106 %- Reflection coefficient S11
107 figure; hold on
108 plot(f/1e9,Gamma_m_dB,'b','Linewidth',3)
109 hold off;grid on;grid minor;xlabel('Frequency (GHz)');
110 set(gca,'FontName','Times','FontSize',24)
111 yticks([-30 -25 -20 -15 -10 -5 0])
112 ylim([-30 0])%axis([-Inf Inf -30 0])
113 %- Smith chart
114 figure;
115 sm=smithplot(f,Gamma_m);sm.LineWidth=3;
116 grid on;
117 set(gca,'FontName','Times','FontSize',24);
```

A.4 Equivalency Model for Conductor Foil Surface Roughness

This source code implements the equivalent conductor model proposed in this work. This model is complemented with the calculation of the impedance and losses in microstrip transmission lines. The code employs the formulations pro-

vided in the related theory of Chapter 4, from Section 4.3 through 4.5. The input information comprises the microstrip line geometry and materials' electrical properties. This program delivers the equivalent conductivity over frequency, conductor-loss increase factor, microstrip-line characteristic impedance, and estimation of losses in dB.

```
%% Equivalency Model for Conductive Materias with Roughness
% Sep 19, 2022 by Nim R. Ccoillo Ramos
clc;clear;close all;
%% Conductor Specifications and Setup
Rq_um=0.15; % Rq (RMS) roughness, in microns.
sig_bulk_MS_m=58; % Bulk conductivity, in MS/m.
f0_GHz=100; % Frequency, in GHz.
% It can be also a vector. Example: linspace(50,150,101)
%% Microstrip Line Dimmensions (to estimate losses)
W_mils=15.48; % line width, in mils
L_in=1; % line length, in inches
t_um=17.5; % line thickness, in microns
er=2.20; % substrate's dielectric constant. It can be also ...
    vector as f0_GHz.
tanD=0.0009; % substrate's loss tangent. It can be also ...
    vector as f0_GHz.
h_mils=5; % substrate's thickness, in mils
%% Physical constants
e0=1/(36*pi)*1e-09;
u0=1*( 4*pi)*1e-07;
c0=1/sqrt(e0*u0);
z0=sqrt(u0/e0);
%% Basic calculations
%- Unit conversions
W=W_mils/1000*25.4/1000; % line width, in meters
```

```
24      L=L_in*25.4/1000; % line length, in meters
25      t=t_um*1e-6; % line thickness, in meters
26      h=h_mils/1000*25.4/1000; % substrate's thickness, in meters
27      %- Skin depth, in microns
28      sd=2.09*sqrt(1./(f0_GHz*sig_bulk_MS_m/58));
29      Rq_sd=Rq_um./sd; % Roughness over skin depth
30      %% Equivalent Conductivity
31      xi=4.6-0.1*Rq_um;
32      nu=0.6262+0.03*Rq_um;
33      fct=exp(xi.*exp(-1.4*(Rq_Δ).^(-nu)));
34      sig_eq_MS_m=sig_bulk_MS_m./fct;
35      %% Additional Attenuation Constant for Conductor Losses
36      Kr_eq=sqrt(fct);
37      %% Microstrip Line Characteristic Impedance
38      %- Normalized width without conductor thickness
39      u=W./h;
40      %- Normalized width with conductor thickness
41      uo=u+1/pi*t./h.*log(1+4*exp(1)...
42      ./(t./h.*(coth(sqrt(6.517*u))).^2));
43      uz=u+(uo-u)/2.*(1+1./(cosh(sqrt(er-1))));
44      %- Effective dielectric constant at DC
45      a=1+1/49*log((uz.^4+(uz/52).^2)./(uz.^4+0.432))...
46      +1/18.7*log(1+(uz/18.1).^3);
47      b=0.564*((er-.9)./(er+0.3)).^0.053;
48      ere0=(er+1)/2+(er-1)/2.*(1+10./uz).^(-a.*b);
49      %- Effective dielectric constant over frequency
50      erT=ere0;
51      WhT=uz;
52      hT=h;
53      Feh=(0.02*(erT-1)*(1-WhT).^2).*(WhT<1);
54      ere0=(erT+1)/2+(erT-1)/2*(1+12./WhT)^(-0.5)+...
55      Feh-0.217*(erT-1)*t/sqrt(W.*hT);
```

```
56      fb=47.746/((1000*hT)*sqrt(erT-ere0))...
57      *atan(erT*sqrt((ere0-1)./(erT-ere0)));
58      fa=fb/(0.75+(0.75-0.332*erT^(-1.73)).*WhT);
59      m0=1+1/(1+sqrt(WhT))+0.32*(1+sqrt(WhT)).^(-3);
60      mc=(WhT>0.7)+(1+1.4/(1+WhT)...
61      *(0.15-0.235*exp(-0.45*f0_GHz/fa))).*(WhT≤0.7);
62      m=m0*mc;
63      %-- consolidated value
64      ere=erT-(erT-ere0)./(1+(f0_GHz./fa).^m);
65      %- Calculation of the Characteristic Impedance
66      F1=6+(2*pi-6)*exp(-(30.666./uz).^0.7528);
67      Z0=z0./(2*pi*sqrt(ere)).*log(F1./uz+sqrt(1+4./uz.^2));
68      %% Approximate Insertion Loss in Microstrip Lines
69      %- Normalized substrate thickness
70      lbd0_mm=300./f0_GHz;
71      h_lbd0=h./(lbd0_mm/1000);
72      %- Conductor losses
73      alpha_c0=298.28./(Z0.*W)...
74      .*sqrt(1./(sig_bulk_MS_m.*(1000*lbd0_mm)));
75      alpha_cr=alpha_c0.*Kr_eq;
76      alpha_c=alpha_cr*L;
77      %- Dielectric losses
78      alpha_d0=27.3*er.*(ere-1)...
79      ./(sqrt(ere)*(er-1))*tanD./(lbd0_mm/1000);
80      alpha_d=alpha_d0*L;
81      %- Estimated total losses (radiation losses are ignored)
82      alpha=alpha_c+alpha_d;
83      %% Reporting results
84      if length(f0_GHz)==1
85      % Print results in the command window
86      disp('Given the following information:')
87      fprintf('Bulk conductivity sigma= %f MS/m\n',sig_bulk_MS_m)
```

```
88      fprintf('Frequency freq= %f GHz\n',f0_GHz)
89      fprintf('The equivalent conductivity is sigma_eq= %f ...
           MS/m\n',sig_eq_MS_m)
90      fprintf('It increases the conductor losses by %f ...
           times\n',Kr_eq)
91      disp('Loss estimation: Given the microstrip line dimensions')
92      fprintf('The characteristic impedance is %f Ohms\n',Z0)
93      fprintf('The substrate''s electrical thickness is %f ...
           lambda_0\n',h_lbd0)
94      if max(h_lbd0)>0.1
95      disp('The microstrip line is thick, the losses may be higher')
96      end
97      fprintf('The conductor loss is %f dB\n',alpha_c)
98      fprintf('The dielectric loss is %f dB\n',alpha_d)
99      fprintf('The  total  loss is %f dB\n',alpha)
100     else
101     % Generate plots
102     %- Equivalent conductivity and increase factor
103     figure;
104     %-- Equivalent conductivity
105     yyaxis left
106     plot(f0_GHz,sig_eq_MS_m,'LineWidth',2);hold on
107     plot(f0_GHz,sig_bulk_MS_m*f0_GHz.^0,'--',...
108     'Color',[0 0.4470 0.7410],'LineWidth',2);hold off
109     %--- Axis properties
110     ylabel('\sigma_{eq} (MS/m)')
111     ylim([0.9*min(sig_eq_MS_m) 10*ceil(0.101*sig_bulk_MS_m)])
112     ax = gca;
113     set(ax, 'YScale', 'log')
114     ax.YMinorTick = 'on';
115     yt=[0.2:0.4:1 2:4:10 20:20:60];
116     ax.YTick=yt;
```

```
117     %-- Conductor Loss Increase factor
118     yyaxis right
119     plot(f0_GHz,Kr_eq,'LineWidth',2)
120     %--- Axis properties
121     ylabel('K_{r-eq}')
122     %-- General properties
123     grid on; grid minor
124     ylim([1 2*ceil(1.05/2*max(Kr_eq))])
125     title('Characteristic impedance')
126     xlabel('Frequency (GHz)')
127     set(gca,'FontName','Times','FontSize',25)
128     %- Characteristic Impedance
129     figure;
130     plot(f0_GHz,Z0,'LineWidth',2)
131     grid on; grid minor
132     ylim([0 10*ceil(0.105*max(Z0))])
133     title('Characteristic impedance')
134     xlabel('Frequency (GHz)')
135     ylabel('Resistance (\Omega)')
136     set(gca,'FontName','Times','FontSize',25)
137     %- Negative of Insertion Losses (S21 magnitude)
138     figure;
139     plot(f0_GHz,-alpha_c,'LineWidth',2);hold on
140     plot(f0_GHz,-alpha_d,'LineWidth',2);
141     plot(f0_GHz,-alpha, 'LineWidth',2);
142     tk=find(h_lbd0>0.05);
143     %   plot(f0_GHz(tk),-alpha_c(tk),'--b','LineWidth',2);
144     %   plot(f0_GHz(tk),-alpha_d(tk),'--r','LineWidth',2);
145     %   plot(f0_GHz(tk),-alpha(tk), '--y','LineWidth',2);hold off
146     v1 = [f0_GHz(tk(1)) ...
            -ceil(1.05*max(alpha(tk)));f0_GHz(tk(1)) 0;...
147     f0_GHz(tk(end)) 0;f0_GHz(tk(end)) -ceil(1.05*max(alpha(tk)))];
```

```
148     f1 = [1 2 3 4];
149     c1 = [1 1 0];
150     patch('Faces',f1,'Vertices',v1,'FaceColor',c1,...
151     'EdgeColor','None','FaceAlpha',0.15)
152     hold off
153     grid on; grid minor
154     ylim([-ceil(1.05*max(alpha(tk))) 0])
155     title('Estimated losses')
156     xlabel('Frequency (GHz)')
157     ylabel('Magnitude (dB)')
158     legend('-\alpha_{cond}','-\alpha_{diel}',...
159     '-\alpha_{total}','Location','SW')
160     text(f0_GHz(tk(1)),-(1.05*max(alpha(tk))),...
161     '\alpha may be higher','FontName','Times','FontSize',15)
162     set(gca,'FontName','Times','FontSize',25)
163     end
```

A.5 Impedance Response of a PF-MSPA up to 300 GHz

This program implements the equivalent model for PF-MSPAs with extension and functionality up to 300 GHz, covering from radiofrequency to the mmWave and sub-THz bands. The commands used in the following lines uses the mathematical and geometrical formulations given in the related theory of Chapter 5, Section 5.2. This code includes the frequency-dependent effective dielectric constant, and the effects of the conductor surface roughness in the patch and ground plane. The program requires the antenna geometry and materials' electrical properties as input information. The program then delivers the antenna's impedance response over frequency.

```
%% Equivalent Circuit Model of PF-MSPA Impedance up to 300 GHz
% Oct 10, 2022 by Nim R. Ccoillo Ramos
clc;clear;close all;
%% Antenna dimensions and setup
%- Substrates
er=2.2;
tanD=0.0009;
h=40*1e-6; %substrate thickness
%- Patch
L=455*1e-6; % patch's length
W=L; % patch's width
t=35*1e-6; % patch's thickness
sig_cu=6.3*1e7; % patch's bulk conductivity
Rq=0.3*1e-6; % patch's and feed's roughness
ur=1;
%- Feed
rx=0.31; % Overlap ratio (rx=x0/L)
a_pf=10.25*1e-6; % Feed's radius
%- Frequency sweep
f=1*1e+09*linspace(190,210,1001);
%% Physical constants
e0=1/(36*pi)*1e-09;
u0=1*( 4*pi)*1e-07;
c0=1/sqrt(e0*u0);
z0=sqrt(u0/e0);
%% Dimension Equivalents
kt=0.1+exp(-0.5*er);
hTo=h; % With no patch thickness
hTp=h+kt*t; % With part of patch thickness
hTQ=h+0.25*t; % With fourth patch thickness
%% Equivalent conductivity
```

```
f_GHz=mean(f)/1e9; % Frequency, in GHz.
Rq_um=Rq/1e-6; % Rq (RMS) roughness, in microns.
sig_bulk_MS_m=sig_cu/1e6; % Bulk conductivity, in MS/m.
%- Skin depth, in microns
sd=2.09*sqrt(1./(f_GHz*sig_bulk_MS_m/58));
Rq_sd=Rq_um./sd; % Roughness over skin depth
% Equivalent Conductivity
xi=4.6-0.1*Rq_um;
nu=0.6262+0.03*Rq_um;
fct=exp(xi.*exp(-1.4*(Rq_sd).^(-nu)));
sig_eq_MS_m=sig_bulk_MS_m./fct;
sig_cu=sig_eq_MS_m*1e6;
%% Effective permittivity
hT=hTp; % With part of patch thickness
WhT=W./hT;
erT=er;
%-- calculations
Feh=(0.02*(erT-1)*(1-WhT).^2).*(WhT<1);
ere0=(erT+1)/2+(erT-1)/2*(1+12./WhT)^(-0.5)+...
Feh-0.217*(erT-1)*t/sqrt(W.*hT);
fb=47.746/((1000*hT)*sqrt(erT-ere0))...
*atan(erT*sqrt((ere0-1)./(erT-ere0)));
fa=fb/(0.75+(0.75-0.332*erT^(-1.73)).*WhT);
m0=1+1/(1+sqrt(WhT))+0.32*(1+sqrt(WhT)).^(-3);
mc=(WhT>0.7)+(1+1.4/(1+WhT)...
*(0.15-0.235*exp(-0.45*f0_GHz/fa))).*(WhT≤0.7);
m=m0*mc;
%-- consolidated value
ere=erT-(erT-ere0)./(1+(f0_GHz./fa).^m);
erep=0.5*er+0.5*ere;
%% Delta length
zi1=0.4349*(erep^0.81+0.260)/(erep^0.81-0.189)...
```

```
*(WhT^0.8544+0.236)/(WhT^0.8544+0.870);
zi2=1+(WhT^0.371)/(1+2.358*er);
zi3=1+0.5274*atan(0.084*WhT^(1.9413/zi2))/erep^0.9236;
zi4=1+0.0377*atan(0.067*WhT^1.456)*(6-5*exp(0.036*(1-er)));
zi5=1-0.218*exp(-7.5*WhT);
dL0=hT*zi1*zi3*zi5/zi4;
%% PF-MSPA effective dimensions
dW0=dL0;
Le=L+2*dL0;  We=W+2*dW0;
%% PF-MSPA Resonant frequency
f0p=c0/(2*Le*sqrt(erep));
l0p=c0/f0p;
k0p=2*pi/l0p;
%% Quality factor
hT=hTQ; % With fourth patch thickness
hT_l0p=hT./l0p;
hT_Qc=hTo; % With no patch thickness
p=1-0.001*(16.605*(k0p.*We).^2-0.229*(k0p.*We).^4+...
18.283*(k0p.*Le).^2-0.217*(k0p.*We).^2.*(k0p.*Le).^2);
c1=1-1./(er.*ur)+0.4./(er.*ur).^2;
er_hed=(1+3*pi/4*k0p.*hT./c1*(1-1./er).^3).^(-1);
Qp=(tanD+1./(hT_Qc.*sqrt(pi*f0p.*u0.*ur.*sig_cu))+...
16/3*(p.*c1)./er.*hT_l0p.*We./Le.*1./er_hed).^(-1);
%% Resonant resistance
hT=hTo; % With no patch thickness
hT_l0p=hT./l0p;
Rp=4/pi*(ur*z0).*Qp.*L./W.*hT_l0p.*(cos(pi*(rx*L+dL0)./Le)).^2;
%% PC-MSPA Feeding
hT=hTo; % With no patch thickness
L_Tf=1*1e-09*200*ur*hT*(log(2./(k0p*a_pf))-0.5772)...
.*(cos(pi*abs(rx*L-L/2)./Le)).^2;
%% Building the circuit and estimating the impedance response
```

```
%-- Synthetize response
Rpa=Rp;
Cpa=Qp./(2*pi*f0p.*Rpa);
Lpa=Rpa./(2*pi*f0p.*Qp);
fprintf('PF Resonant resistance Rp=%f Ohm\n',Rp)
fprintf('Resonant frequency f0p=%f GHz\n',f0p/1e9)
fprintf('Res. Quality factor Qp=%f \n',Qp)
Z_ptch=1./(1./Rpa+1i*2*pi*f.*Cpa-1i./(2*pi*f.*Lpa));
Z_feed=1i*2*pi*f.*L_Tf;
Zin_m=Z_ptch+Z_feed;
%-- Reflection coefficient
Z0sm=50;
Gamma_m=(Zin_m-Z0sm)./(Zin_m+Z0sm);
Gamma_m_dB=mag2db(abs(Gamma_m));
%% Plotting
%- Impedance Z11
figure; hold on
plot(f/1e9,real(Zin_m),'b','Linewidth',3)
plot(f/1e9,imag(Zin_m),'r','Linewidth',3)
hold off;grid on;grid minor;
xlabel('Frequency (GHz)');
set(gca,'FontName','Times','FontSize',24)
%- Reflection coefficient S11
figure; hold on
plot(f/1e9,Gamma_m_dB,'b','Linewidth',3)
hold off;grid on;grid minor;
xlabel('Frequency (GHz)');
set(gca,'FontName','Times','FontSize',24)
yticks([-30 -25 -20 -15 -10 -5 0])
ylim([-30 0])
%- Smith chart
figure;
```

```
128 sm=smithplot(f,Gamma_m);sm.LineWidth=3;
129 grid on;
130 set(gca,'FontName','Times','FontSize',24);
```

A.6 Impedance Response of a PC-MSPA up to 300 GHz

The source code contained in the upcoming lines performs the equivalent modeling for PC-MSPAs up to 300 GHz, which extends the functionality of the model provided in the appendix A.3 from radiofrequency to the mmWave and sub-THz bands. The related formulation has been presented in Chapter 5, Section 5.3. As part of the frequency extension, this program includes the frequency-dependent effective dielectric constant, and the effects of the conductor surface roughness in the patch, feed, and ground plane. The antenna geometry and materials' electrical properties are the input information necessary to run this source code, delivering the antenna's impedance response over frequency.

```
1  %% Equivalent Circuit Model of PC-MSPA Impedance up to 300 GHz
2  % Oct 18, 2022 by Nim R. Ccoillo Ramos
3  clc;clear;close all;
4  %% Antenna dimensions and setup
5  %- Substrates
6  er=2.2;
7  tanD=0.0009;
8  h1=18.0*1e-6; %bottom substrate thickness
9  h2=22.5*1e-6; % top substrate thickness
10 %- Patch
11 L=296*1e-6; % patch's length
12 W=L; % patch's width
13 tp=10*1e-6; % patch's thickness
```

```
14 sig_cu=5.8*1e7; % patch's and feed's bulk conductivity
15 Rq=0.3*1e-6; % patch's and feed's roughness
16 ur=1;
17 %- Feed
18 rx=0.63; % Overlap ratio (rx=x0/L)
19 tf=5*1e-6; % feed's thickness
20 %- Frequency sweep
21 f=1*1e+09*linspace(280,320,1001);
22 %% Physical constants
23 e0=1/(36*pi)*1e-09;
24 u0=1*( 4*pi)*1e-07;
25 c0=1/sqrt(e0*u0);
26 z0=sqrt(u0/e0);
27 %% Dimension Equivalents
28 kf=0.50*(1+0.1533*(er-1)*(h2/h1).^1.25);
29 kt=0.1+exp(-0.5*er);
30 h1e=h1+kf*tf;
31 h2e=h2+(1-kf)*tf;
32 rh=h2e./h1e;
33 hTo=h2e+h1e; % With no patch thickness
34 hTp=h2e+h1e+kt*tp; % With part of patch thickness
35 hTQ=h2e+h1e+0.25*tp; % With fourth patch thickness
36 %% Equivalent conductivity
37 f_GHz=mean(f)/1e9; % Frequency, in GHz.
38 Rq_um=Rq/1e-6; % Rq (RMS) roughness, in microns.
39 sig_bulk_MS_m=sig_cu/1e6; % Bulk conductivity, in MS/m.
40 %- Skin depth, in microns
41 sd=2.09*sqrt(1./(f_GHz*sig_bulk_MS_m/58));
42 Rq_sd=Rq_um./sd; % Roughness over skin depth
43 % Equivalent Conductivity
44 xi=4.6-0.1*Rq_um;
45 nu=0.6262+0.03*Rq_um;
```

```
fct=exp(xi.*exp(-1.4*(Rq_Δ).^(-nu)));
sig_eq_MS_m=sig_bulk_MS_m./fct;
sig_cu=sig_eq_MS_m*1e6;
%% Effective permittivity
hT=hTp; % With part of patch thickness
WhT=W./hT;
erT=er;
%-- calculations
Feh=(0.02*(erT-1)*(1-WhT).^2).*(WhT<1);
ere0=(erT+1)/2+(erT-1)/2*(1+12./WhT)^(-0.5)+...
Feh-0.217*(erT-1)*t/sqrt(W.*hT);
fb=47.746/((1000*hT)*sqrt(erT-ere0))...
*atan(erT*sqrt((ere0-1)./(erT-ere0)));
fa=fb/(0.75+(0.75-0.332*erT^(-1.73)).*WhT);
m0=1+1/(1+sqrt(WhT))+0.32*(1+sqrt(WhT)).^(-3);
mc=(WhT>0.7)+(1+1.4/(1+WhT)...
*(0.15-0.235*exp(-0.45*f0_GHz/fa))).*(WhT≤0.7);
m=m0*mc;
ere=erT-(erT-ere0)./(1+(f0_GHz./fa).^m);
erep=0.5*er+0.5*ere;
%% Delta length
zi1=0.4349*(erep^0.81+0.260)/(erep^0.81-0.189)...
*(WhT^0.8544+0.236)/(WhT^0.8544+0.870);
zi2=1+(WhT^0.371)/(1+2.358*er);
zi3=1+0.5274*atan(0.084*WhT^(1.9413/zi2))/erep^0.9236;
zi4=1+0.0377*atan(0.067*WhT^1.456)*(6-5*exp(0.036*(1-er)));
zi5=1-0.218*exp(-7.5*WhT);
dL0=hT*zi1*zi3*zi5/zi4;
%% PF effective dimensions
dW0=dL0;
Le0=L+2*dL0;  We0=W+2*dW0;

```

```
%% PF Resonant frequency
f0r=c0/(2*Le0*sqrt(erep));
l0r=c0/f0r;
k0r=2*pi/l0r;
hT=hTo; % With no patch thickness
hT_l0r=hT./l0r;
%% PC-MSPA Resonant frequency
F0=1.02-0.045/sqrt(er);
F1=(0.7376/rh+0.4754)/sqrt(er);
Ff0=F0+(hT_l0r-0.005)*F1;
f0p=f0r*Ff0;
l0p=c0/f0p;
k0p=2*pi/l0p;
%% PC-MSPA effective dimensions
Le=c0/(2*f0p*sqrt(erep));
dL=0.5*(Le-L);
dW=0.25*dL;
Le=L+2*dL;
We=W+2*dW;
%% Quality factor
hT=hTQ; % With fourth patch thickness
hT_l0p=hT./l0p;
hT_Qc=hTo; % With no patch thickness
p=1-0.001*(16.605*(k0p.*We).^2-0.229*(k0p.*We).^4+...
18.283*(k0p.*Le).^2-0.217*(k0p.*We).^2.*(k0p.*Le).^2);
c1=1-1./(er.*ur)+0.4./(er.*ur).^2;
er_hed=(1+3*pi/4*k0p.*hT./c1*(1-1./er).^3).^(-1);
Qp=(tanD+1./(hT_Qc.*sqrt(pi*f0p.*u0.*ur.*sig_cu))+...
16/3*(p.*c1)./er.*hT_l0p.*We./Le.*1./er_hed.*rh.^0.24).^(-1);
%% Resonant resistance
hT=hTo; % With no patch thickness
hT_l0p=hT./l0p;
```

```
RpM=4/pi*(ur*z0).*Qp.*L./W.*hT_l0p;
Kr=1.1*er.^(-0.02./hT_l0r).*(W./L).^0.75...
.*rh.^(-0.8+4.44*sqrt(hT_l0r./er));
A=0.58-1.8*exp(-270*hT_l0r./er)+...
log(rh).*(0.1732+130.8*((hT_l0r./er)-0.03135).^2);
p1=2./(hT_l0r.*sqrt(er)+0.035);
p2=1.35*rh.^(0.75).*(1-1.25*exp(-50*hT_l0r.*er.^-0.63));
Frp=Kr.*(A.*exp(-p1.*rx)+(1-A).*exp(-p2.*rx));
Rp=RpM.*Frp;
%% PC-MSPA Feeding
L_T=1*1e-09*0.4674./(f0p/1e9).*exp(4.551*rx);
C_T=1*1e-12*1.0000./(f0p/1e9)*(-32.395*(rx-0.4534)^2+5.2925);
%% Building the circuit and estimating the impedance response
%-- Synthetize response
Rpa=Rp;
Cpa=Qp./(2*pi*f0p.*Rpa);
Lpa=Rpa./(2*pi*f0p.*Qp);
fprintf('PC Resonant resistance Rp=%f Ohm\n',Rp)
fprintf('Resonant frequency f0p=%f GHz\n',f0p/1e9)
fprintf('Res. Quality factor Qp=%f \n',Qp)
Z_ptch=1./(1./Rpa+1i*2*pi*f.*Cpa-1i./(2*pi*f.*Lpa));
Z_feed=1i*2*pi*f.*L_T-1i./(2*pi*f.*C_T);
Zin_m=Z_ptch+Z_feed;
%-- Reflection coefficient
Z0sm=50;
Gamma_m=(Zin_m-Z0sm)./(Zin_m+Z0sm);
Gamma_m_dB=mag2db(abs(Gamma_m));
%% Plotting
%- Impedance Z11
figure; hold on
plot(f/1e9,real(Zin_m),'b','Linewidth',3)
plot(f/1e9,imag(Zin_m),'r','Linewidth',3)
```

```
142 hold off;grid on;grid minor;xlabel('Frequency (GHz)');
143 set(gca,'FontName','Times','FontSize',24)
144 %- Reflection coefficient S11
145 figure; hold on
146 plot(f/1e9,Gamma_m_dB,'b','Linewidth',3)
147 hold off;grid on;grid minor;xlabel('Frequency (GHz)');
148 set(gca,'FontName','Times','FontSize',24)
149 yticks([-30 -25 -20 -15 -10 -5 0])
150 ylim([-30 0])
151 %- Smith chart
152 figure;
153 sm=smithplot(f,Gamma_m);sm.LineWidth=3;
154 grid on;
155 set(gca,'FontName','Times','FontSize',24);
```

Appendix B

List of Publications

This appendix contains the list of publications associated to this dissertation. These publications are grouped by category: scientific journal, and conference proceedings; and the number of references are sorted by chronological order.

B.1 Journal Papers

[70] N. Aboserwal, N. R. Ccoillo Ramos, Z. Qamar, and J. L. Salazar-Cerreno, "An Accurate Analytical Model to Calculate the Impedance Bandwidth of a Proximity Coupled Microstrip Patch Antenna (PC-MSPA)," *IEEE Access*, vol. 8, pp. 41 784–41 793, 2020. eprint: https://doi.org/10.1109/ACCESS.2020.2976750.

[72] N. R. Ccoillo-Ramos, N. Aboserwal, J. Salazar-Cerreno, and Z. Qamar, "Improved Analytical Model for a Proximity Coupled Microstrip Patch Antenna (PC-MSPA)," *IEEE Transactions on Antennas and Propagation*, vol. 69, no. 10, pp. 6244–6252, 2021. eprint: https://doi.org/10.1109/TAP.2021.3082570.

[75] N. R. Ccoillo Ramos, J. Salazar-Cerreno, and N. Aboserwal, "The Role of Patch Antennas in 6G Communications: Modeling, Analysis, and Design Trade-offs," *IEEE Transactions on Antennas and Propagation, submitted*, 2022.

[76] N. R. Ccoillo Ramos, J. Salazar-Cerreno, and N. Aboserwal, "An Accurate Model to Assess the Impact of the Surface Roughness on Microstrip and Striplines for mmWave Applications," *IEEE Transactions on Antennas and Propagation, submitted*, 2022.

B.2 Conference Papers

[71] N. R. Ccoillo Ramos, N. Aboserwal, Z. Qamar, and J. L. Salazar-Cerreno, "Assessment of the Impedance Bandwith of a Proximity-Coupled Microstrip Patch Antenna," in *2020 IEEE International Symposium on Antennas and Propagation and North American Radio Science Meeting*, 2020, pp. 153–154. eprint: https://doi.org/10.1109/IEEECONF35879.2020.9330497.

[73] N. R. Ccoillo Ramos and J. L. Salazar-Cerreno, "A New Impedance Model for Differentially-fed Proximity-Coupled Microstrip Patch Antennas," in *2022 IEEE Texas Symposium on Wireless and Microwave Circuits and Systems (WMCS)*, 2022, pp. 1–5. eprint: https://doi.org/10.1109/WMCS55582.2022.9866490.

[74] N. R. Ccoillo Ramos and J. L. Salazar-Cerreno, "An Enhanced Method to Estimate the Resonant Frequency in mmWave Microstrip Patch Antennas," in *2022 IEEE International Symposium on Antennas and Propagation and North American Radio Science Meeting*, 2022, pp. 1178–1179.